Development of Bioinspired Nanostructured Materials for Photocatalytic CO_2 Reduction to Value-added Chemicals

Thesis Submitted in Partial Fulfilment of the Requirements
for the Award of the Degree of

DOCTOR OF PHILOSOPHY

by

Pramod Madhukar Gawal

Department of Chemical Engineering
Indian Institute of Technology Guwahati
Assam-781039, INDIA

August 2025

Dedicated

to

Almighty God, My parents and family, mentors, and well-wishers

DEPARTMENT OF CHEMICAL ENGINEERING
INDIAN INSTITUTE OF TECHNOLOGY GUWAHATI
GUWAHATI-781039
ASSAM, INDIA

DECLARATION

I hereby declare that the work embodied in this thesis entitled "**Development of Bioinspired Nanostructured Materials for Photocatalytic CO_2 Reduction to Value-added Chemicals"** is the outcome of original investigations carried out by me at the Indian Institute of Technology Guwahati, Assam, INDIA-781039, under the supervision of Prof. Animes Kumar Golder, Department of Chemical Engineering, IIT Guwahati. This thesis is submitted to the Indian Institute of Technology Guwahati for the award of the degree of Doctor of Philosophy.

In accordance with standard academic practice, due acknowledgements have been made wherever the work presented is based on the contribution or findings of other researchers.

Pramod Madhukar Gawal
Roll no.: 206107104
Department of Chemical Engineering
Indian Institute of Technology Guwahati
Guwahati, Assam, INDIA

DEPARTMENT OF CHEMICAL ENGINEERING
INDIAN INSTITUTE OF TECHNOLOGY GUWAHATI
GUWAHATI-781039
ASSAM, INDIA

CERTIFICATE

This is to certify that the thesis entitled "**Development of Bioinspired Nanostructured Materials for Photocatalytic CO_2 Reduction to Value-added Chemicals"** submitted by Mr. Pramod Madhukar Gawal to Indian Institute of Technology Guwahati, India, for the award of the degree of Doctor of Philosophy, has been carried out by him under my guidance and supervision.

We further certify that the work embodied in this thesis is an original contribution of the candidate and has not been submitted, either in part or in full, to any other university or institute for the award of any degree or diploma.

Animes Kumar Golder
(Thesis Supervisor)
Professor
Department of Chemical Engineering
Indian Institute of Technology Guwahati
Guwahati – 781039
Assam, INDIA

भारतीय प्रौद्योगिकी संस्थान गुवाहाटी
Indian Institute of Technology Guwahati

Acknowledgement

I owe a debt of gratitude to many people who have helped me in completing this research work directly and indirectly. I would like to acknowledge them all.

First and foremost, I would like to express my deepest gratitude to my supervisor, **Prof. Animes K. Golder**, for his constant guidance, support, and encouragement throughout the course of this research. His insightful suggestions and valuable feedback have played a crucial role in shaping this work.

I would like to thank my doctoral committee members, **Prof. Bishnupada Mandal** and **Prof. Mahuya De** (Department of Chemical Engineering), and **Prof. Kannan Pakshirajan** (Department of Bioscience & Bioengineering), for their valuable suggestions and constructive criticism during the project evolution, which helped me to make necessary improvements in various stages of my research work.

I am grateful to the faculty and staff members of the Department of Chemical Engineering, IIT Guwahati, for their constant help and support. I would also like to acknowledge the Department of Chemical Engineering, Central Instrument Facilities (CIF), for providing various analytical facilities essential for conducting my research. I place on record my sincere gratitude to the **Ministry of Education** (formerly known as the Ministry of Human Resource and Development), Government of India, for awarding me the **Prime Minister's Research Fellowship (PMRF)** and funding my research work. I am also thankful to the IIT Guwahati for providing state-of-the-art infrastructure to pursue advanced research.

I express my gratitude to the entire AKG Lab for our countless insightful discussions. I sincerely appreciate the valuable suggestions from my seniors, including Dr. Paulomi Bose, Dr. Smruti Ranjan Dash, Dr. Anirban Chowdhury, and Dr. Swagata Patra. I am also thankful to my lab members, Chandrabhan, Ravi, Biswajit Bhattacharjya, and Mrinal Kanti Dolai, for their supportive collaboration and enthusiastic company. I would like to thank my friends Ajay Kumar Shakya and Avinash Anand for their constant support.

I sincerely thank my parents and family members for their encouragement, blessings, and motivation at every step.

Last but not least, I thank the almighty God for giving me the strength to overcome difficulties that crossed my path and for being my pole star.

Pramod Madhukar Gawal

Abstract

The energy crisis and the greenhouse gas effect are recognized as two major future issues due to excessive consumption of non-renewable fossil fuels. Therefore, developing sustainable energy resources is highly imperative to meet energy demand and mitigate the greenhouse gas effect. The photocatalytic CO_2 reduction (PCO_2R) has been considered one of the most effective techniques for the utilization of CO_2. The reaction can be performed under solar light in an aqueous media to produce value-added chemicals such as methanol (CH_3OH), ethanol (C_2H_5OH), formic acid (HCOOH), methane (CH_4), carbon monoxide (CO), etc., in an environmentally friendly process. Therefore, photocatalytic reduction of CO_2 is like killing two birds with one stone to solve energy demand and environmental issues. The development of green pathways for the synthesis of nanoparticles (NPs) and their application in the photocatalytic reduction of CO_2 to value-added chemicals is a potential pathway for controlling industrial CO_2 emissions.

This doctoral work focuses on developing an environmentally benign process for synthesizing CdS NPs, nanorods and quantum dots (QDs), and they are further modified for enhanced PCO_2R. The resulting catalysts are applied for photocatalytic CO_2 reduction to value-added chemicals under visible light irradiation.

In the first study, bio-based CdS(bio) nanorods were synthesized using plant-based phytochemicals found in *Aegle marmelos* and carbon quantum dots (CQDs) using *orange peels*. CQDs (7 nm) were homogeneously incorporated into CdS(bio) nanorods via simple deposition, forming CQDs/CdS(bio) nanocomposites. The catalysts were thoroughly characterized using diffraction, microscopic, spectroscopic, and electrochemical techniques. CQDs/CdS(bio) composites had a diameter and length of 73 nm and 822 nm with 82.25 m^2/g specific surface area. CQDs/CdS(bio) composites showed a fourfold increase in both photocurrent density (0.38 $\mu A/cm^2$) and CO_2 adsorption capacity (0.292 mmol/g) compared to CdS(bio) nanorods alone. The conduction band of the composite (-0.92 eV) becomes more negative compared to CdS(bio) (-0.85 eV). Moreover, the composite formation notably improved decay time by 2.35-fold and reduced photoluminescence intensity by 59.23 % compared to CdS(bio), indicating enhanced charge separation and reduced charge carrier recombination. Furthermore, the photocatalytic activity of CQDs/CdS(bio) nanocomposites was investigated for CO_2 reduction to methanol under visible light (250 W, λ>420 nm, 2.2 W/m^2, 4.2719×10^{18} photons/m^2.s) without any sacrificial reagent. The effect of the mass

fraction of CQDs on CdS and catalyst loading on PCO_2R has been investigated. The optimal CQDs/CdS(bio) loading (0.50% w/w) exhibited the maximum methanol rate of 1060.52 μmol/g·h (apparent quantum yield (AQY) 7%) over 5 h. CQDs/CdS(bio) nanocomposites exhibited strong stability (test up to 25 h in five consecutive cycles), retaining the morphological (0.11 % variation in size) and structural (4.2% variation in crystallinity index) attributes. This work would provide valuable insights into the development of bio-based CdS-based composites for efficient PCO_2R into valuable chemicals.

Z-scheme In_2O_3/CdS(bio) heterostructures (25 nm, 217.0 m^2/g surface area) with a more negative conduction band, synthesized using phytochemicals present in *Aegle marmelos* with short microwave irradiation, inhibit CdS(bio) photocorrosion, forming SO_4^{2-}. In_2O_3/CdS(bio) increased photocurrent density (0.82 μA/cm^2) and CO_2 adsorption (0.431 mmol/g) significantly compared to CdS(bio) and In_2O_3(bio) NPs. Heterostructures increased decay time and reduced PL intensity by 46.28% and 61.80% over CdS(bio) and In_2O_3(bio) NPs. Density functional theory (DFT)-optimized geometry, band structure analysis, and density of state (DOS) studies indicate that the DOS of CdS is modified with In_2O_3 incorporation, enhancing charge separation. Optimal 0.4In_2O_3/CdS(bio) heterostructures exhibit remarkable CO_2 conversion to HCOOH/CO production of 514.4/162 μmol/g·h (AQY 4.44/2.45%), surpassing CdS(bio) and In_2O_3(bio) by 9 and 6.5 times, and retained its morphological and structural stability. In the subsequent study, bio-based CdS heterostructures were developed for PCO_2R to overcome limited redox potential alignment, restricting multi-electron transfer pathways and narrowing product selectivity.

This study presents both experimental and theoretical insights into CO_2 reduction to HCOOH using biomass-derived carbon dots embedded onto phytochemical-based CdS quantum dots. The 0D CDs/CdS QDs(bio) composites exhibit rich sulfur vacancies and a more negative conduction band, effectively inhibiting CdS photocorrosion (SO_4^{2-}) while enhancing CO_2 adsorption and photocurrent response. Additionally, it reduced PL intensity and increased decay time, suggesting enhancing charge separation and suppressing charge recombination. The optimal 0.4CDs/CdS QDs(bio) composite exhibited remarkable CO_2 reduction to HCOOH formation rate of 439.51 μmol/g·h (AQY 3.81%) while retaining its structural and morphological stability. DFT calculations reveal HCOO* as a key intermediate, confirming the thermodynamic preference for HCOOH formation over CO with a free energy change of -0.71 eV. This study introduces a novel bio-based CdS QDs composite modified with biomass-derived CDs, providing mechanistic insights into PCO_2R for sustainable fuel production.

This work studies on bio-based Z-scheme heterojunction photocatalysts for efficient reduction of CO_2 into value-added chemicals. A Z-scheme SnO_2/CdS heterojunction is synthesized (5.7 nm, 120.6 m^2/g) with a conduction band position of -0.96 eV using bio-analytes found in *Aegle marmelos* via microwave irradiation. The heterojunction synthesized could significantly enhance CO_2 adsorption capacity (0.4 mmol/g) and photocurrent response (0.74 $\mu A/cm^2$) in comparison to CdS QDs(bio) and SnO_2(bio). Additionally, it improves charge carrier dynamics as PL intensity is reduced by 60 and 56.1 %, and charge carrier lifetime is increased by 48.9 and 59.2%, respectively. The internal electric field generated by the Fermi level difference between CdS (- 4.51 eV) and SnO_2 (-5.52 eV) facilitates charge separation and transport, suppresses recombination, and prevents photocorrosion (SO_4^{2-}) of CdS QDs(bio). DFT analysis further confirms modifications in the density of states of CdS within the bandgap region due to SnO_2 incorporation, promoting efficient charge transfer at the interface. The optimized 0.50SnO_2/CdS QDs(bio) heterostructure exhibits remarkable photocatalytic activity for CO_2 reduction, achieving CH_3OH and hydrogen production rates of 675.9/139.5 μmol/g·h (AQY 3.51/0.24%) while maintaining its structural and morphological stability.

In this study, a bio-based zero-dimensional (0D) p–n heterojunction CuO/CdS photocatalyst (7.2 nm, 136.65 m^2/g) with a conduction band of -1.12 eV was synthesized using bio-analytes from *Aegle marmelos* via microwave irradiation. The p–n heterojunction enhanced CO_2 adsorption capacity (0.643 mmol/g) and photocurrent response (0.94 $\mu A/cm^2$) compared to CdS QDs(bio) and CuO QDs(bio). Additionally, it improved charge carrier dynamics by reducing PL intensity by 73% and 67% and increasing decay time by 74% and 54.6%, respectively. The internal electric field generated by the Fermi level difference between n-type CdS (- 4.21 eV) and p-type CuO (- 4.7 eV) enhanced charge separation and transport, suppressed recombination, and prevented photocorrosion (SO_4^{2-}) of CdS QDs(bio). DFT analysis revealed alterations in the DOS of CdS within the band gap region due to the incorporation of CuO, further facilitating efficient charge separation and transport at the local junctions. The optimal 0.50CuO/CdS QDs(bio) heterostructure exhibited remarkable photocatalytic performance for CO_2 reduction, achieving C_2H_5OH (C2 product) and CO production rates of 158.48/182.68 μmol/g·h (AQY 8.24/1.58%) while maintaining its structural and morphological stability. This work highlights the potential of bio-based p-n junction photocatalysts for efficient CO_2 reduction into value-added chemicals.

Keywords: Photocatalytic CO_2 reduction; Bio-based synthesis; CdS nanorods; Carbon quantum dots; CdS nanoparticles; CdS quantum dots; p-n junction; Z-scheme heterojunction; DFT calculation; Methanol formation; Formic acid formation; Ethanol formation; Carbon monoxide formation; Hydrogen production

Table of Contents

List of Table Captions

List of Figure Captions

CHAPTER 1

Introduction and Literature Review

This chapter provides a general introduction to CO_2 emissions, including the global and Indian scenarios, the fundamentals of CO_2 photoreduction, and an overview of various technologies for converting CO_2 into value-added chemicals. It also presents a concise review of the state-of-the-art literature on photocatalysts and their modifications for enhancing photocatalytic CO_2 reduction.

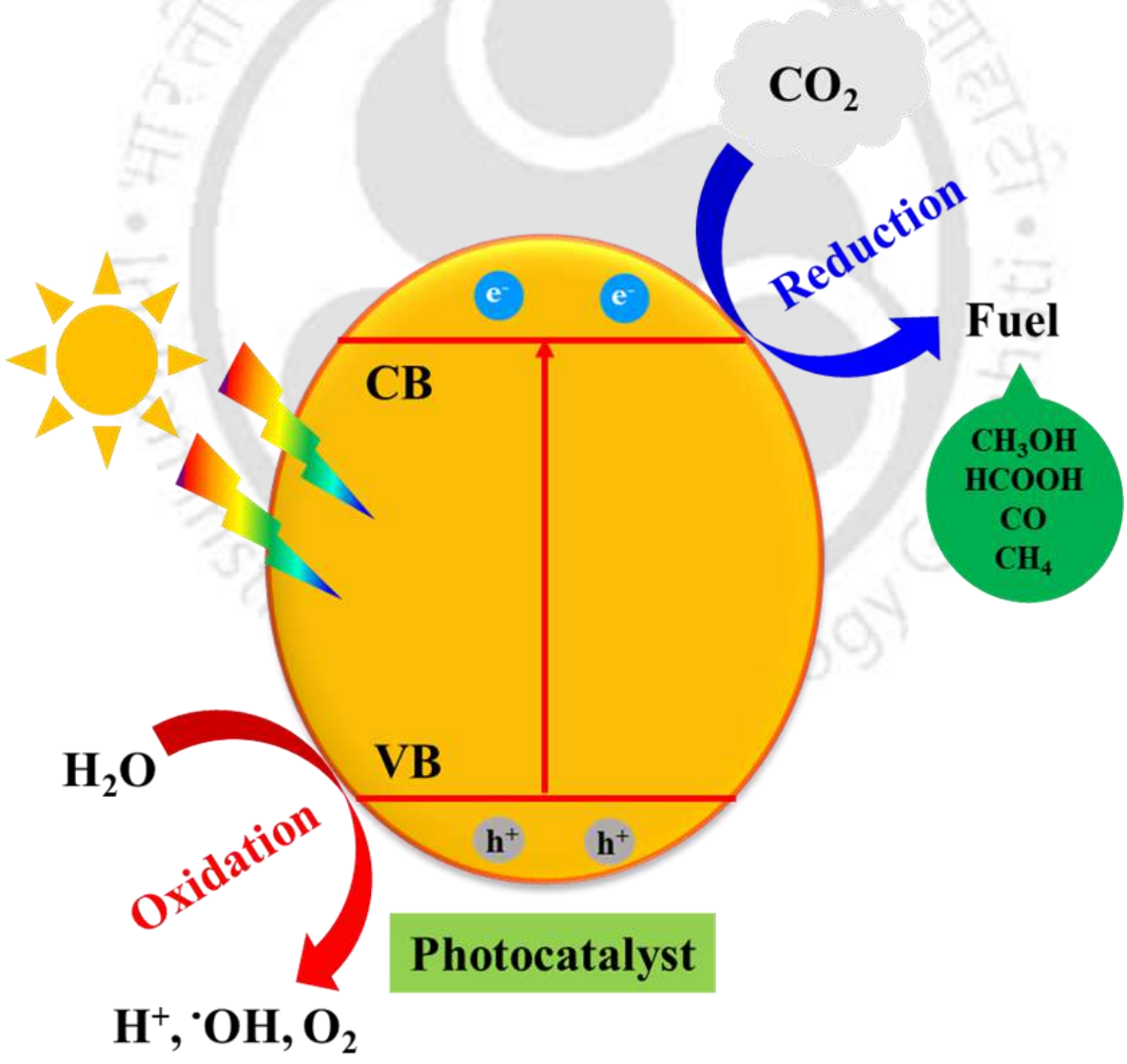

1.1 Overview

The global energy demand is increasing rapidly due to accelerated industrialization and rising living standards. Global energy consumption is projected to increase by 48% between 2012 and 2040 (Source: Energy Information Administration (EIA)). The rapid rise in global energy consumption and industrialization has resulted in the emission of significant amounts of greenhouse gases, causing serious harm to the environment and life on Earth [1]. Among these greenhouse gases, carbon dioxide (CO_2) is the primary contributor, accounting for approximately 76% of the total greenhouse effect, potentially causing severe and irreversible environmental changes that impact human health [2]. Global CO_2 emissions have now surpassed 40 gigatonnes annually, with atmospheric CO_2 concentrations reaching 429.6 ppm (Source: International Energy Review (IEA)).

Currently, most of the world's energy needs are met by burning non-renewable fossil fuels like coal, oil, petroleum, and natural gas. Continued dependence on these resources could lead to their eventual depletion [3–5]. Furthermore, the extensive combustion of fossil fuels is a major source of greenhouse gas emissions, which drive global warming, rising sea levels, ice melt, and numerous other environmental consequences.

1.1.1 CO_2 emission and its global scenario

Figure 1.1 depicts global CO_2 emissions across various sectors from the mid-18th century to the present. Emissions remained relatively low until the mid-19th century, reaching 6 billion tonnes by 1950. By 1990, this number had nearly quadrupled to over 22 billion tonnes. Since then, emissions have continued to increase rapidly, presently exceeding 40 gigatonnes per year.

CO_2 emissions originate from a range of sectors, including electricity and heat production, industry, transportation, residential, agriculture, and commercial and public services. **Figure 1.2** shows the global distribution of CO_2 emissions by sector from 1990 to 2019. The top three contributors, electricity and heat production, industry, and transportation, collectively account for about 82.77% of total emissions. The remaining 17.23% is related to residential, agricultural, commercial, and public service sector activities.

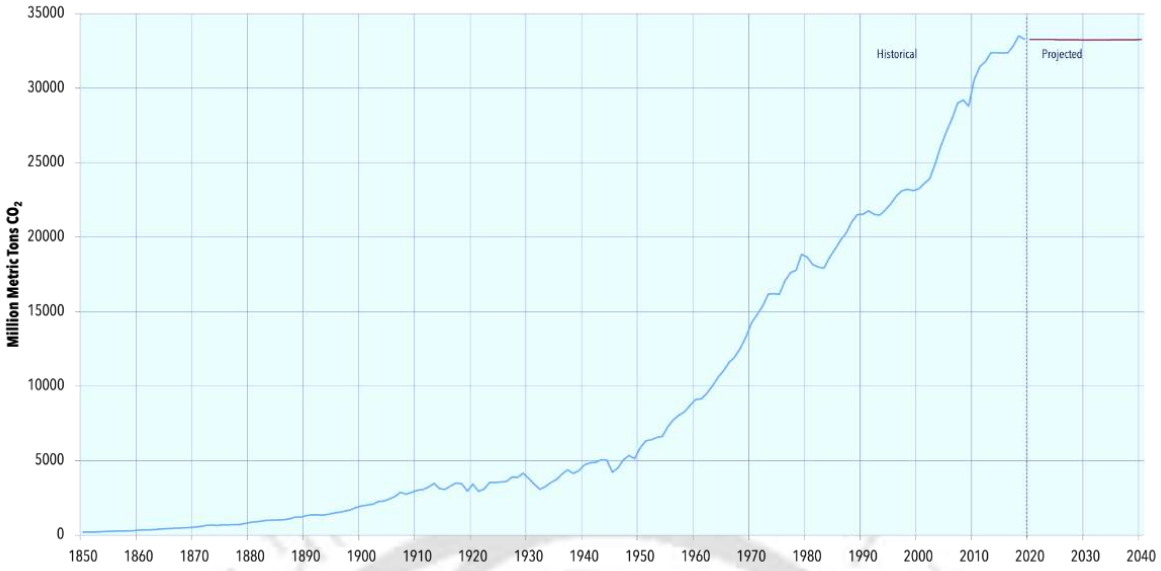

Figure 1.1. Global annual CO_2 emissions from the year 1850 to 2040 (Source: Center for Climate and Energy Solutions, available at www.c2es.org, accessed on 15 August 2025).

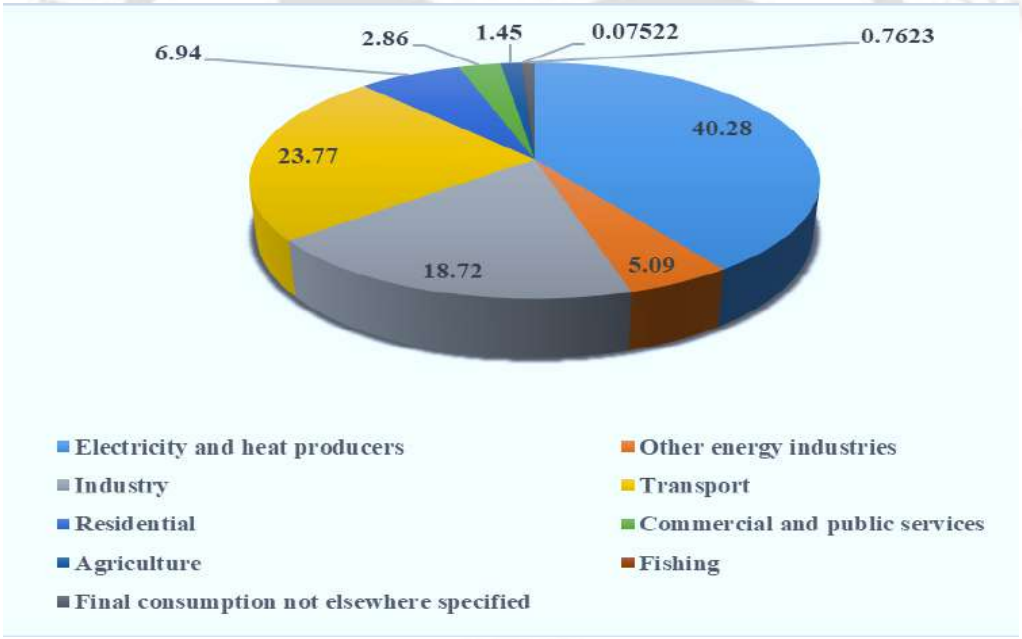

Figure 1.2. Global sector-wise CO_2 emissions annually from 1990 to 2019 (Source: International Energy Agency, available at www.iea.org, accessed on 15 August 2025).

Figure 1.3 illustrates the country-wise global CO_2 emission distribution. In 2020, China, the United States, and India were the top three emitters, accounting for approximately 28, 15, and 7% of total global emissions, respectively.

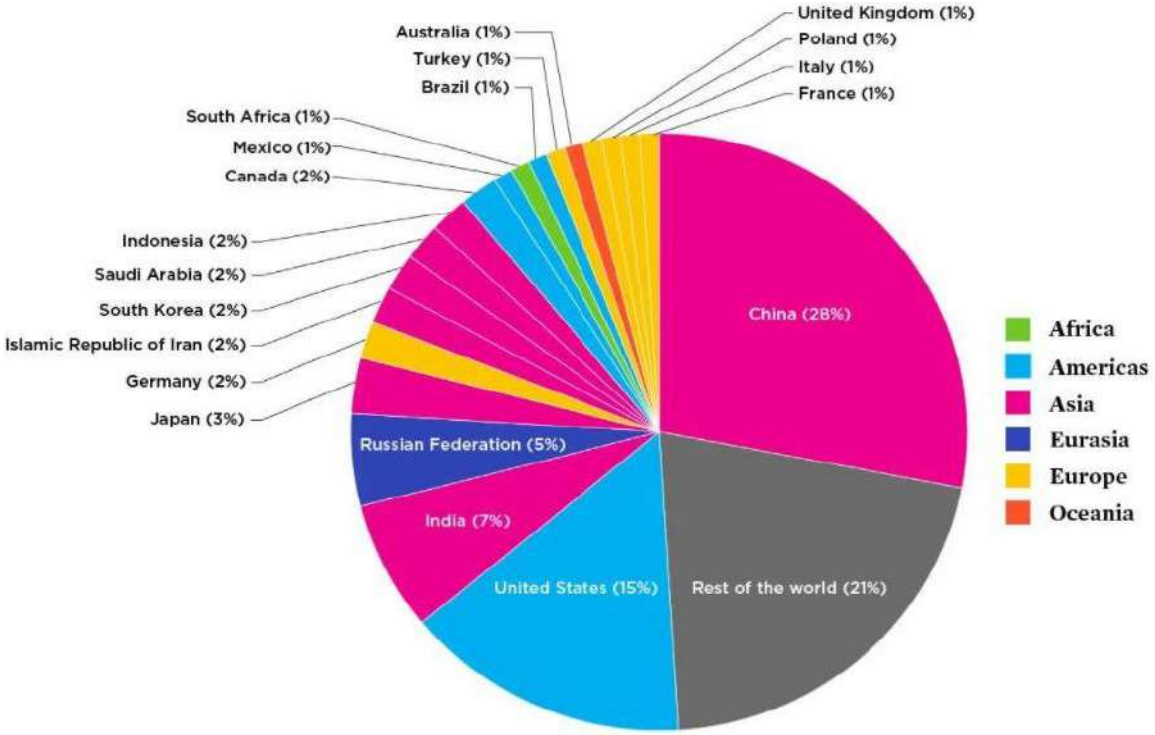

Figure 1.3. Global share of CO_2 emissions by country in the year 2020 (Source: International Energy Agency, available at the link www.ucsusa.org, accessed on 15 August 2025).

Since the Industrial Revolution, atmospheric CO_2 levels have steadily risen, reaching a record 412.5 ppm in 2020 (**Figure 1.4**), despite the temporary economic slowdown caused by the COVID-19 pandemic. Compared to 1960, this represents an increase of 95.5 ppm, or approximately 30.12%.

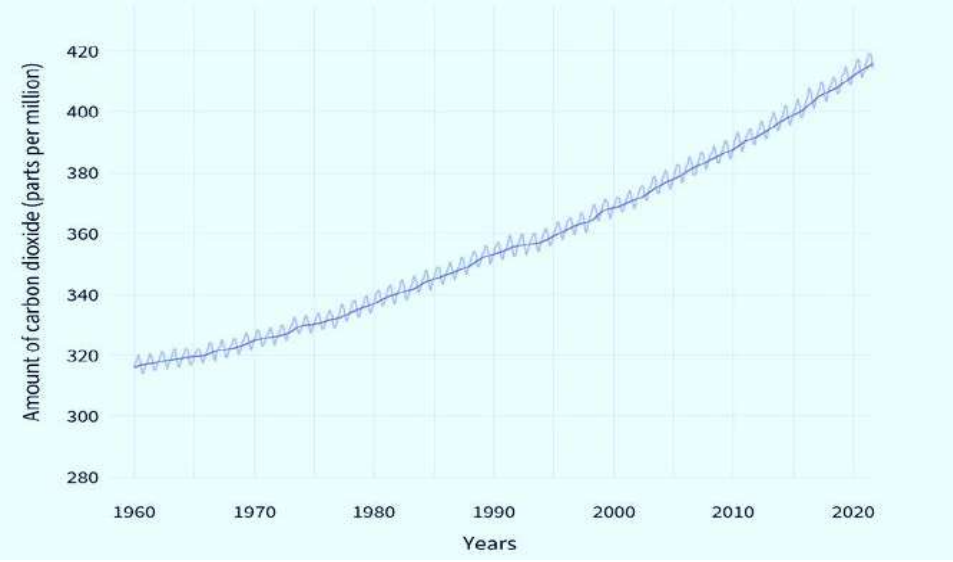

Figure 1.4. Atmospheric CO_2 concentration levels from 1960 to 2020 (Source: National Ocean and Atmospheric Administration, available at www.statista.com accessed on 15 August 2025).

1.1.2 Indian CO_2 emission scenario

India is the third-largest emitter of greenhouse gases globally, contributing nearly 7% of total global CO_2 emissions, primarily from fossil fuel combustion. Currently, India's CO_2 emissions have risen to approximately 3 gigatonnes, exceeding the 2019 level of 2.59 gigatonnes, a surge largely driven by increased coal usage. However, in the financial year 2019–20, the country experienced a rare decline in CO_2 emissions from coal, oil, and gas by about 30 million tonnes (1.4%), marking the first drop in four decades (**Figure 1.5**). This downward trend continued with estimated reductions of 15% in March 2020 and 30% in April 2020, largely due to the nationwide lockdown during the COVID-19 pandemic. Overall, India's total CO_2 emissions in 2020 fell by 9.7%, slightly surpassing the global average decline of 9.6%.

Figure 1.6 presents sector-wise CO_2 emissions in India from 1990 to 2019. The top three sectors—electricity and heat production, industry, and transport—collectively contribute around 86.76% of the total emissions. The remaining 13.24% originates from other sectors, including residential, agriculture, commercial, and public services.

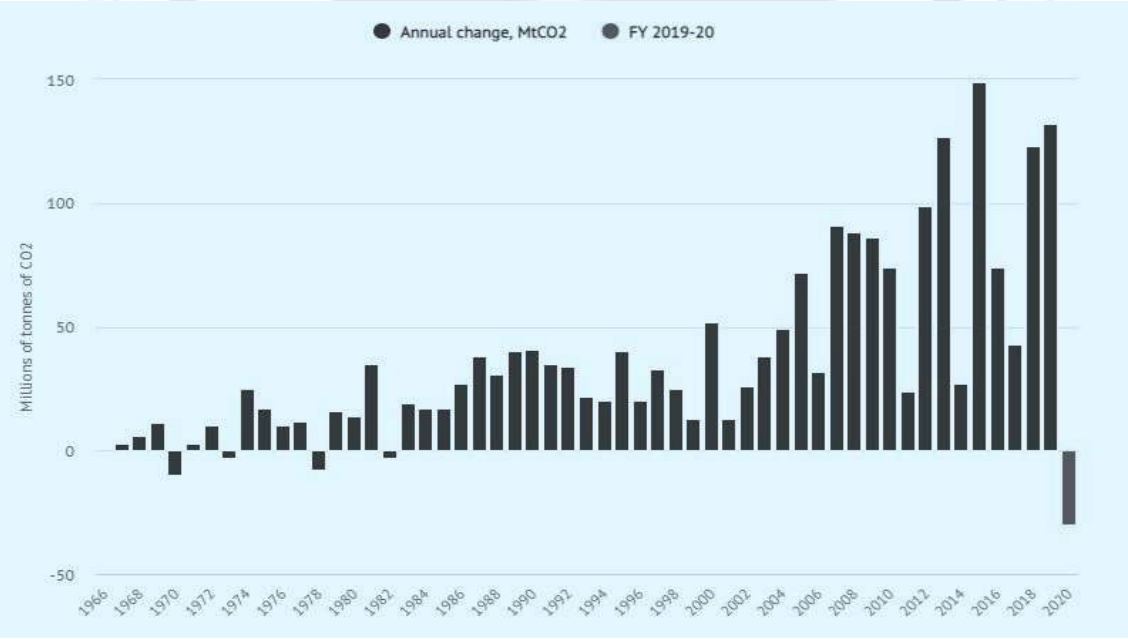

Figure 1.5. Annual CO_2 emissions in India from fossil fuel consumption during the period 1965 to 2020 (Source: Centre for Research on Energy and Clean Air, available at www.carbonbrief.org, accessed on 15 August 2025).

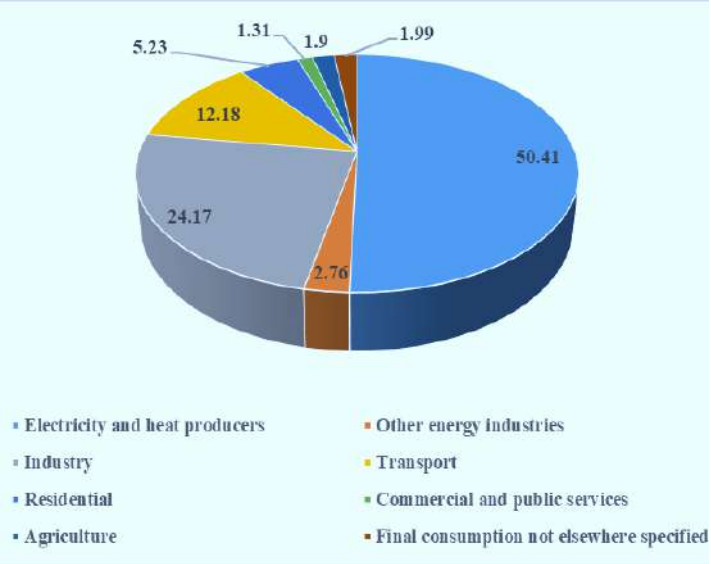

Figure 1.6. Sector-wise CO_2 emissions in India from 1990 to 2019 (Source: IEA, available at www.iea.org/ accessed on 15 August 2025).

1.2 Need for sustainable CO_2 utilization strategies

The development of sustainable renewable energy technologies is an urgent need of 21st century to meet energy demands while mitigating the greenhouse gas effect. Several approaches have been explored for CO_2 reduction, including carbon capture and storage (CCS), catalytic conversion, thermochemical conversion, electrochemical conversion, biological conversion, photoelectrocatalytic conversion, and photocatalytic conversion. However, each of these technologies comes with its own set of limitations and challenges.

CCS technologies have been widely employed with notable efficiency; however, their broader adoption is limited by challenges such as leakage risks, high compression costs, and the need for extensive transportation infrastructure [6]. Similarly, catalytic and thermochemical conversions of CO_2 into carbon monoxide (CO) and methane (CH_4) using transition metal catalysts are effective for commercial use [7]. However, they require high temperatures and pressures, making both capital and operational costs significantly high. Electrochemical conversion offers a route to reduce CO_2 into valuable chemicals using electrical energy, yet it faces limitations related to low efficiency and electrode stability [8]. Biological conversion, which utilizes microalgae to transform CO_2 into value-added products, also encounters challenges, including limited enzyme regeneration and low production yields [9].

Photocatalytic CO_2 reduction utilizes a semiconductor photocatalyst, light energy (solar or artificial light), and cost-effective water as a reducing agent to convert CO_2 into solar fuels such as CH_4, CO, methanol (CH_3OH), formic acid (HCOOH), ethanol (C_2H_5OH), and

formaldehyde (HCHO). This method is considered as one of the most promising, efficient, and environmentally friendly strategies for addressing both energy and climate challenges. It utilizes renewable solar light energy, operates mostly under ambient temperature and pressure, produces no toxic byproducts or residues, and results in zero carbon emissions [10,11].

1.3 Fundamentals of CO_2 photoreduction

1.3.1 Basic principle of CO_2 photoreduction

Photocatalytic reduction of CO_2 is a process that mimics natural photosynthesis in plants. In photosynthesis, green plants and photosynthetic bacteria convert atmospheric CO_2 into oxygen and energy-rich compounds like carbohydrates using light energy. Similarly, photocatalytic CO_2 reduction emulates this mechanism by using light, a semiconductor catalyst, and water to convert CO_2 into valuable fuels or chemicals [11,12] (**Figure 1.7**). In this process, the semiconductor photocatalyst absorbs ultraviolet or visible light, generating electron(e^-)/hole (h^+) pairs when the incident light energy equals or exceeds the bandgap energy (Eg) of the catalyst. The excited electrons are promoted to the conduction band (CB), while holes are left in the valence band (VB). The photogenerated holes oxidize water (H_2O), producing protons (H^+), hydroxyl radicals ($^{\bullet}OH$), or oxygen (O_2), while the photogenerated electrons reduce CO_2 adsorbed on the catalyst surface into value-added chemicals such as CO, CH_4, HCOOH, C_2H_5OH, and CH_3OH [13].

The photocatalytic reduction of CO_2 proceeds through five key sequential steps: light absorption, charge separation, CO_2 adsorption, surface redox reactions, and product desorption. This photoreduction process can be carried out in both liquid-phase and gas-phase systems [14].

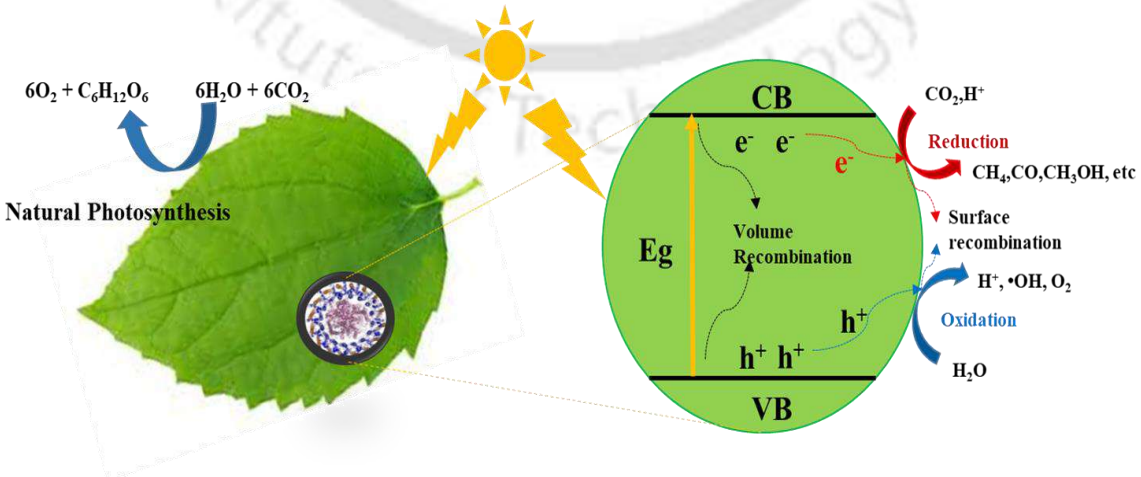

Figure 1.7. Schematic of photocatalytic CO_2 reduction.

CO_2 is a highly stable, linear, and symmetrical molecule, characterized by strong C=O double bonds with a bond energy of approximately 750 kJ/mol—significantly higher than that of typical single bonds such as C–O (327 kJ/mol), C–H (411 kJ/mol), and C–C (336 kJ/mol) [14]. This inherent stability poses a major challenge for its activation, as considerable energy is required to overcome the thermodynamic barrier and break the C=O bonds during photoreduction. In this context, solar energy emerges as a promising solution with an immense potential of around 1.3×10^5 TW. It provides a clean, sustainable, and abundant energy source to drive the conversion of CO_2 into value-added chemicals.

The reduction potential of photogenerated electrons plays a crucial role in providing the driving force required for CO_2 reduction. Photocatalytic CO_2 reduction follows a complex, multi-electron and multi-proton transfer pathway, typically involving 2, 6, or 8 electrons and protons [15]. This process can yield a variety of value-added products, including C_1 compounds such as CH_4, CO, CH_3OH, HCOOH, and HCHO, as well as C_2 compounds like C_2H_5OH, ethylene (C_2H_4), and acetic acid (CH_3COOH). The main reaction pathways and their corresponding redox potentials (E°) are summarized in **Table 1.1**. These theoretical reduction potentials are referenced to the normal hydrogen electrode (NHE) at pH 7.0 in aqueous solution.

Table 1.1. The main products of CO_2 reduction with the corresponding reduction potential (pH=7) [12].

Reaction	**Product**	**E^o (V vs. NHE)**
$CO_2 + e^- \rightarrow CO_2^{\bullet-}$	Carbonate anion radical	-1.90
$CO_2 + 2H^+ + 2e^- \rightarrow HCOOH$	Formic acid	-0.61
$CO_2 + 2H^+ + 2e^- \rightarrow CO + H_2O$	Carbon Monoxide	-0.53
$CO_2 + 4H^+ + 4e^- \rightarrow HCHO + H_2O$	Formaldehyde	-0.48
$CO_2 + 6H^+ + 6e^- \rightarrow CH_3OH + H_2O$	Methanol	-0.38
$CO_2 + 8H^+ + 8e^- \rightarrow CH_4 + H_2O$	Methane	-0.24
$2H^+ + 2e^- \rightarrow H_2$	Hydrogen	-0.41

As shown in **Table 1.1**, the direct one-electron reduction of CO_2 is highly unfavorable, owing to its extremely negative redox potential of –1.9 V vs. NHE at pH 7 [16]. To date, no known photocatalyst exhibits a conduction band potential negative enough to efficiently

facilitate this single-electron transfer. In contrast, proton-coupled multi-electron reduction pathways present a more feasible and energy-efficient alternative. These routes require significantly less negative redox potentials, making them more suitable for practical CO_2 conversion under photocatalytic conditions [12].

Considering these challenges, the development of a highly active, durable, low-cost, and multifunctional photocatalyst for CO_2 reduction requires careful attention to several critical factors. Firstly, the photocatalyst must have a suitable band structure capable of generating multiple e^-/h^+ pairs and facilitating efficient transfer of photogenerated electrons to CO_2. Specifically, the conduction band edge should be more negative than the redox potentials of CO_2 and its corresponding reduction products to ensure thermodynamic feasibility. Additionally, effective mass transport is essential; the reactants must readily access and adsorb onto the active sites, while the products must be able to diffuse away and desorb from the catalyst surface after the reaction. Finally, photoinduced holes should be rapidly consumed by a sacrificial agent or water to prevent charge recombination and maintain continuous photocatalytic activity [12,17].

1.3.2 Adsorption and activation of CO_2

The adsorption and activation of CO_2 on the photocatalyst surface are critical steps for facilitating its subsequent reduction and for suppressing the competing hydrogen evolution reaction (HER). Upon adsorption, CO_2 typically interacts with surface atoms to form a partially charged intermediate species, $CO_2^{\delta\bullet-}$ [18]. As illustrated in **Figure 1.8**, CO_2 can adsorb in various configurations, including carbon coordination, oxygen coordination, and mixed coordination modes.

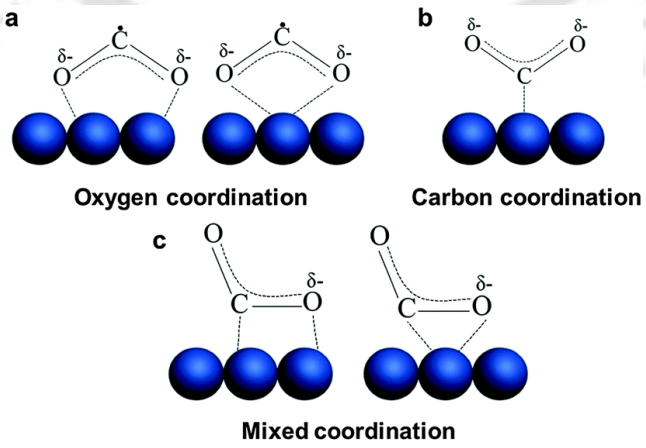

Figure 1.8. Possible structures of adsorbed $CO_2^{\delta\bullet-}$ on the photocatalyst (Reproduced with permission from [18], Copyright 2016, Royal Society of Chemistry).

In oxygen coordination, each oxygen atom of the CO_2 molecule donates its lone pair electrons to a Lewis acid site on the photocatalyst surface (**Figure 1.8a**). In carbon coordination, the carbon atom accepts electrons from surface species such as oxide ions, forming a carbonate-like intermediate (**Figure 1.8b**). In mixed coordination, both the carbon and oxygen atoms of CO_2 simultaneously function as an electron acceptor and donor, respectively, leading to a more complex interaction with the surface (**Figure 1.8c**).

In photocatalytic CO_2 reduction, the adsorption of CO_2 is widely considered as both the rate-determining and selectivity-controlling step. This process requires significant reorganization energy to convert the linear CO_2 molecule into a bent radical anion ($CO_2^{\bullet-}$), which can be facilitated through various strategies, such as increasing surface area, introducing surface defects, and optimizing surface configurations. Enhancing the surface area of photocatalysts promotes faster mass transfer, improves CO_2 adsorption, and provides more active sites for the reduction reaction [11]. To achieve this, a wide range of nanostructured materials has been engineered to offer high surface areas, including zero-dimensional (0D) nanoparticles, one-dimensional (1D) nanotubes, nanorods, and nanowires, two-dimensional (2D) nanosheets, and three-dimensional (3D) hierarchical micro/nanostructures. Additionally, porous and hollow materials with large surface-to-volume ratios and interconnected channels have been developed to further enhance photocatalytic CO_2 reduction performance [18].

Introducing surface defects in photocatalysts is another effective strategy to enhance CO_2 adsorption and activation. Defects such as oxygen and sulfur vacancies serve as highly reactive sites, particularly in metal oxide- and sulfide-based photocatalysts. Oxygen vacancies in metal oxides can significantly modify the catalyst's structure, as well as its electronic and chemical properties, thereby improving its ability to interact with and activate CO_2 molecules. Similarly, sulfur vacancies in sulfide-based photocatalysts can produce comparable effects, enhancing photocatalytic performance [11].

1.3.3 Mechanism of photocatalytic CO_2 reduction

Photocatalytic CO_2 reduction is a complex redox process involving multiple steps, including the transfer of electrons and protons, the breaking of C=O bonds, and the formation of new C–X bonds with various species. Throughout the reaction sequence, several radical intermediates may form and participate at different stages, contributing to the complexity of the overall process. The reaction outcome can vary significantly depending on experimental conditions such as light source, reactor design, and the nature of the photocatalyst. There are

three primary proposed pathways for CO_2 reduction: the formaldehyde pathway, the carbene pathway, and the glyoxal pathway. Each pathway involves distinct intermediate species, which are summarized along with their corresponding reaction mechanisms in **Table 1.2**.

In the formaldehyde pathway [11], the $CO_2^{\bullet-}$ radical anion is first attacked by a proton to form HCOOH. This is followed by the dehydration of a dihydroxymethyl intermediate, producing HCHO, which is subsequently reduced to CH_3OH and eventually to CH_4. In the carbene pathway [17], a proton reacts with $CO_2^{\bullet-}$ to break a C-O bond, forming CO. Through successive electron and proton transfers, CO is reduced to a carbon residue, which is further transformed into reactive intermediates such as $CH^{\bullet}$ and $CH_3^{\bullet}$, ultimately yielding CH_4. Methane can then react with hydroxyl radicals ($^{\bullet}OH$) to form CH_3OH. Alternatively, carbene intermediates may undergo reduction to form C_2H_4 and subsequently ethane (C_2H_6). This pathway involves only reduction steps, featuring the transfer of electrons and hydrogen atoms to form various radical and non-radical intermediates. In contrast, the glyoxal pathway [18] includes both oxidation and reduction steps. The proposed sequence of intermediates includes $CO_2^{\bullet-}$, HCOOH, $HCO^{\bullet}$, $C_2H_3O^{\bullet}$, $CH_3^{\bullet}$, CH_4, and CH_3OH, highlighting a more complex interplay between redox reactions throughout the CO_2 reduction process.

Table 1.2. CO_2 reduction reaction pathways and related reactions and products [19,20].

Pathways	**CO_2 reduction reaction and product formation**
Formaldehyde	$CO_2 + e^- \rightarrow CO_2^{\bullet-} + H^+ \rightarrow COOH^{\bullet} + e^- + H^+ \rightarrow HCOOH$ (formaldehyde) $+ e^- + H^+ \rightarrow H_3CO_2^{\bullet} + e^- + H^+ \rightarrow CH_2O + H_2O$ $CH_2O + e^- \rightarrow H_2CO^- + H^+ \rightarrow H_3CO^{\bullet} + e^- + H^+ \rightarrow CH_3OH + e^- + H^+ \rightarrow CH_3^{\bullet} + H_2O$ $CH_3^{\bullet} + e^- + H^+ \rightarrow CH_4$
Carbene	$CO_2 + e^- \rightarrow CO_2^{\bullet-} + e^- + H^+ \rightarrow CO + OH^-$ $CO + e^- \rightarrow CO^{\bullet-} + e^- + H^+ \rightarrow C + OH^-$ $C + e^- + H^+ \rightarrow CH^{\bullet} + e^- + H^+ \rightarrow CH_2$ (carbene) $+ e^- + H^+ \rightarrow CH_3^{\bullet} + e^- + H^+ \rightarrow CH_4$ or $CH_3^{\bullet} + e^- + H^+ + {}^{\bullet}OH \rightarrow CH_3OH$ $2CH_2 + 2e^- \rightarrow C_2H_4 + 2H^+ \rightarrow C_2H_6$
Glyoxal	$CO_2 + e^- \rightarrow CO_2^{\bullet-} + e^- + H^+ \rightarrow HCO_2^- + H^+ \rightarrow HCOOH + e^- \rightarrow HCO^{\bullet} + OH^-$ $HCO^{\bullet} + HCO^{\bullet} \rightarrow C_2H_2O_2$ (glyoxal) $+ e^- + H^+ \rightarrow C_2H_3O_2^{\bullet} + e^- + H^+ \rightarrow C_2H_4O_2 + e^- + H^+ \rightarrow C_2H_3O^{\bullet} + H_2O$

	$C_2H_3O^{\bullet} + e^- + H^+ \rightarrow C_2H_4O + H^+ \rightarrow C_2H_3O^{\bullet} + H^+$ $C_2H_3O^{\bullet} \rightarrow CH_3^{\bullet} + CO + e^- + H^+ \rightarrow CH_4$ or $CH_3^{\bullet} + CO + e^- + H^+ + {}^{\bullet}OH \rightarrow CH_3OH$

1.4 Technologies for CO_2 reduction to value-added chemicals

Several technologies have been developed for the reduction of CO_2, including carbon capture and storage (CCS), catalytic conversion, thermochemical conversion, electrochemical conversion, biological conversion, photoelectrocatalytic conversion, and photocatalytic conversion. These methods are illustrated in **Figure 1.9** [21]. A brief description of these methods is provided in the subsequent sub-sections.

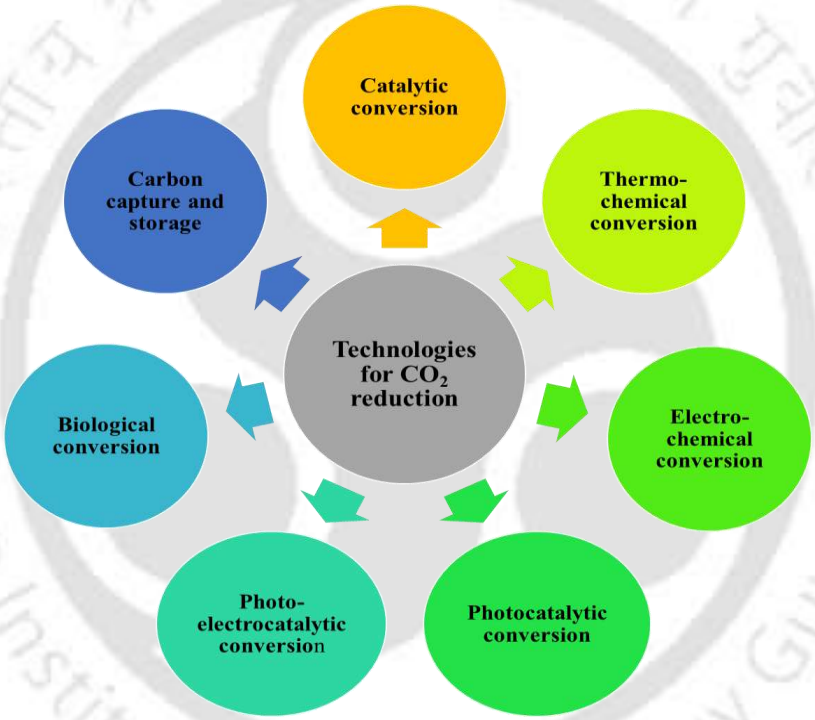

Figure 1.9. Technologies for CO_2 reduction.

1.4.1 Carbon capturing and storage (CCS)

Carbon capture and storage (CCS) is a process designed to capture CO_2 before they are released into the atmosphere. It involves three main steps: (i) CO_2 capture, (ii) CO_2 transportation, and (iii) CO_2 storage. This technology has the potential to capture up to 90% of CO_2 emissions generated from fossil fuel-based power generation and industrial activities such as cement production. CCS is considered as a promising solution for reducing CO_2 emissions within the energy sector and is often viewed as a key strategy for mitigating the impact of fossil fuels on global warming [6]. However, the widespread implementation of CCS is limited by

several challenges, including high costs, the risk of CO_2 leakage, and the expenses associated with compression and transportation. These factors have significantly constrained its large-scale adoption.

1.4.2 Biological conversion

This technique resembles photocatalytic conversion, as it utilizes solar energy to drive the transformation of CO_2 into chemical energy through natural photosynthesis, resulting in the production of biofuels. In this method, microalgae (photosynthetic microorganisms) convert CO_2 into biofuels or valuable chemicals in the presence of sunlight and water. It represents a promising and eco-friendly pathway for CO_2 reduction. However, scaling up this process for industrial applications remains challenging due to the low efficiency of CO_2 fixation. Additionally, harsh operating conditions such as high CO_2 concentrations, elevated temperatures, and high pH levels pose significant stress on microalgal species, adversely affecting both their growth and their ability to fix CO_2 effectively [9].

1.4.3 Catalytic conversion

The catalytic conversion of CO_2 into valuable products such as CO and CH_4 using transition metal catalysts is an effective technique with strong potential for commercial applications. This technology is generally categorized into two types: homogeneous and heterogeneous catalysis. Both approaches typically follow a three-step process: (i) adsorption of CO_2 onto the catalyst surface, (ii) decomposition or activation of the CO_2 molecule, and (iii) desorption of the resulting products. The catalytic reduction of CO_2 often involves its hydrogenation to produce CH_4, CH_3OH, or other hydrocarbons. However, the process usually requires high temperatures and pressures and is exothermic in nature. These factors, along with the associated high operating and capital costs, pose significant limitations to the widespread adoption of this technology [22].

1.4.4 Thermochemical conversion

This technology is closely related to catalytic conversion, where CO_2 is reduced through thermochemical processes to produce CO and CH_4 at high temperatures, typically ranging from 500 to 1000°C. These reactions are highly endothermic and can be driven by concentrated solar radiation. However, the implementation of this approach requires substantial initial investment, either for achieving and maintaining high temperatures or for installing solar concentrators to harness sufficient solar energy. Additionally, a comprehensive understanding of the catalyst's

morphology, surface chemistry, and structural changes under such extreme conditions remains limited, posing further challenges to the development and optimization of this technology [23].

1.4.5 Electrocatalytic conversion

Electrocatalytic conversion of CO_2 is an emerging technology that utilizes externally supplied electrical energy to drive redox reactions at electrode surfaces. In this process, water is oxidized at the anode to produce oxygen and protons. These protons then migrate through a proton exchange membrane to the cathode, where they participate in the reduction of CO_2 into value-added chemicals. This conversion can take place across various electrode and cell configurations, operating through 2-, 4-, 6-, or 8-electron transfer pathways in aqueous, non-aqueous, or gas-phase systems. The final products are highly dependent on several factors, including the pH of the reaction medium, CO_2 concentration, type of catalyst and electrolyte, electrode material, buffer strength, reaction environment, pressure, and temperature. Typical products of electrochemical CO_2 reduction include CO, HCOOH, HCHO, CH_3OH, C_2H_5OH, CH_4, and C_2H_4 [9]. The technology is appealing due to its on-demand operation, compactness, modularity, and scalability for both small- and large-scale applications. However, the reaction mechanism remains complex and not fully understood, posing challenges for further development and optimization.

1.4.6 Photocatalytic conversion

Photocatalytic reduction of CO_2 involves using a semiconductor photocatalyst, solar or artificial light, and economical water as a reductant to convert CO_2 into solar fuels such as CH_4, CO, CH_3OH, and HCOH. This process mimics the natural photosynthetic cycle and requires no additional energy input. Among the various CO_2 reduction technologies, this approach stands out as one of the most effective, promising, and environmentally friendly. It leverages abundant and renewable solar energy, operates primarily under ambient temperature and pressure, and produces no toxic byproducts or residues, resulting in zero carbon emissions. Since CO_2 and water serve as the primary reactants, this method offers a sustainable pathway for fuel generation while simultaneously addressing environmental concerns. In essence, photocatalytic CO_2 reduction offers a dual benefit—tackling both energy demand and climate change in a single step [11].

1.4.7 Photoelectrocatalytic conversion

The photoelectrocatalytic reduction of CO_2 is a hybrid technology that integrates photocatalytic and electrocatalytic processes to enhance CO_2 conversion efficiency. In this system, a semiconductor photoelectrode generates e^-/h^+ pairs through photoexcitation. The photogenerated holes at the anode react with water to produce oxygen and protons, while the protons migrate through a membrane to the cathode, where they participate in the reduction of CO_2. Simultaneously, the photogenerated electrons are directed toward the CO_2 at the cathode under the influence of an externally applied voltage, driving the reduction process. The application of external electric energy facilitates the directional movement of charge carriers, significantly improving the separation efficiency of e^-/h^+ pairs and enhancing the redox capability of the system. Moreover, when the semiconductor's band positions are not ideal for H_2O oxidation or CO_2 reduction, applying an appropriate bias voltage can help adjust the redox potential, making the process more effective [24]. This method reduces the overall external energy input while enabling the efficient use of renewable energy. However, challenges such as slow reaction kinetics and limited photoelectrode stability continue to hinder its widespread application. The advantages and disadvantages of various CO_2 reduction technologies are summarized in **Table 1.3**.

Table 1.3. Advantages and disadvantages of CO_2 reduction technologies.

Technologies for CO_2 reduction	**Advantage**	**Disadvantage**
Carbon Capture and Storage (CCS)	Remarkable efficiency, reduces the effect of climate change	Cost is High, Risk of leakage, cost of compression, and transportation have constrained its wide application
Electrocatalytic Conversion	Utilize a renewable source	Low energy efficiency, unfavorable product selectivity, unknown durability, and mass transfer limitations
Catalytic Conversion	Commercial available	High temperature and pressure, exothermic

		reaction, and high operating and capital costs limit the wide application
Thermochemical Conversion	Commercially available	Low productivity, slow kinetics, drastic conditions for heterogeneous catalysts, and a challenge to scale up homogeneous catalysts
Biological Conversion	Utilize solar energy	Low efficiency in CO_2 fixation, constrained production, and regeneration of enzymes.
Photoelectrocatalytic Conversion	Utilization of renewable sources, reduction the external energy, Rapid transfer of electrons	High cost and low stability of the catalyst, instability of the electrode, Less selectivity, poor production rate, and efficiency
Photocatalytic Conversion	Utilize solar energy	Low conversion rate, low photon efficiency of materials

Photocatalytic CO_2 reduction is a sustainable approach to mitigate greenhouse gas emissions while simultaneously producing value-added fuels and chemicals. It utilizes abundant solar energy and readily available water as an electron donor to convert CO_2 into products such as CH_4, CH_3OH, CO, and HCOOH under mild reaction conditions, mimicking the natural process of photosynthesis [11,25]. This method avoids the high energy demands of conventional CO_2 conversion technologies, making it environmentally and economically attractive. Moreover, it offers a pathway to close the carbon cycle by transforming CO_2 into renewable energy carriers, contributing to climate change mitigation towards a carbon-neutral future. Hence, the state-of-the art literature on photocatalytic CO_2 reduction is provided in the next section.

1.5 State-of-art literature on photocatalytic CO_2 reduction

1.5.1 Photocatalysts for CO_2 reduction

Various photocatalysts have been explored for the photocatalytic CO_2 reduction, including TiO_2 [22], ZnO [23], Cu_2O [24], g-C_3N_4 [29], CdS [12], and others. The bandgap structures, along with the advantages and limitations of these photocatalysts for CO_2 reduction, are summarized in **Table 1.4**.

Table 1.4. Common photocatalysts for the photocatalytic reduction of CO_2 with advantages and limitations.

Photocatalyst	Bandgap Structure vs. NHE			Advantage	Disadvantage
	CB (eV)	VB (eV)	Eg(eV)		
TiO_2	-0.5	+2.7	3.2	High thermal and chemical stability, high oxidation potential, high surface area, availability, and nontoxic	High surface recombination rate, high bandgap
ZnO	-0.61	+2.58	3.19	Rapid generation of photoexcited e^-/h^+ pairs, high excitation binding energy	Slow formation of carbonates, only UV-light utilization
CdS	-0.95	+1.45	2.4	Predominantly harvest the visible light, earth-abundant, suitable negative potential of CB	Oxidative photocorrosion, suffers from the recombination of photogenerated e^-/h^+ pairs
Cu_2O	-1.16	+0.85	2.01	Abundant oxygen defect, admirable redox ability, and low cost	Dual photocorrosion, low quantum efficiency

g-C_3N_4	-1.13	+1.57	2.7	Easy preparation, high thermal and chemical stability, low cost, a suitable negative potential energy of CB	Low charge transfer efficiency, high recombination issue, and stability issue

CB: Conduction band; VB: Valence band; Eg: Bandgap

Among these photocatalysts, CdS has been intensively studied for CO_2 reduction due to its suitable bandgap (2.4 eV) and conduction band potential (-0.95 V vs. NHE, pH 7), high solar energy conversion, and earth abundance [25,30]. However, CdS suffers from rapid e^-/h^+ pairs recombination and oxidative corrosion. To overcome these limitations, CdS can be modified to enhance its structural stability and e/h^+ recombination reduction for improved photocatalytic CO_2 reduction. A brief discussion of modification strategies is provided in the next section.

1.5.2 Catalyst modifications to boost photocatalytic CO_2 reduction reaction

A wide range of photocatalysts has been investigated for the photocatalytic CO_2 reduction. However, their overall conversion efficiency remains limited due to several challenges, including poor light-harvesting ability, rapid recombination of photogenerated e/h^+ pairs, low photostability, and catalyst corrosion. Therefore, it is crucial to develop effective strategies to overcome these limitations and enhance the efficiency of CO_2 reduction into value-added chemicals. To address these issues, researchers have employed various approaches such as elemental doping, surface modification, introduction of structural defects, and construction of heterostructures and Z-scheme systems. These strategies, illustrated in **Figure 1.10**, aim to improve charge separation, extend light absorption, and boost overall photocatalytic performance.

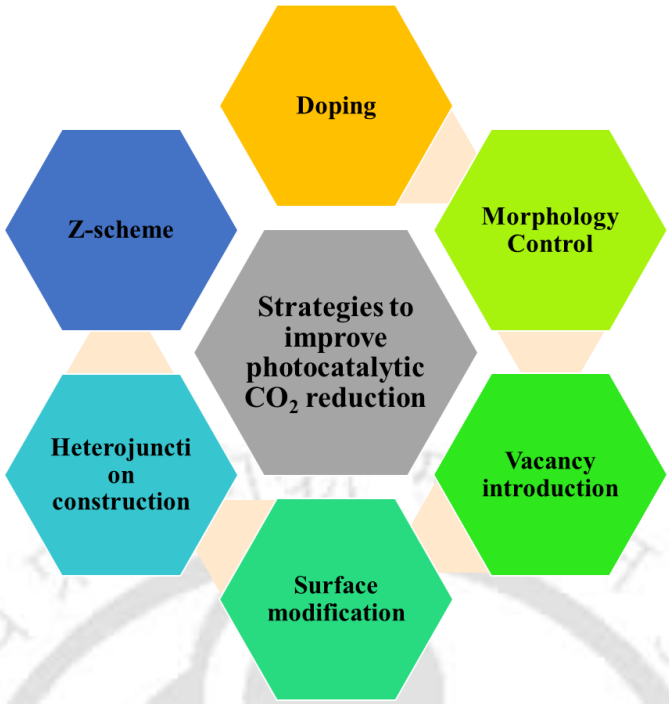

Figure 1.10. Strategies for improving the photocatalytic reduction of CO_2 over a photocatalyst.

1.5.2.1 Reduction of bandgap

Elemental doping is an effective strategy to significantly modify the electronic and optical properties of photocatalytic materials. The type and concentration of dopants play a crucial role in influencing the photocatalyst's performance [12]. Recent studies on doped photocatalysts for CO_2 reduction are summarized in **Table 1.5**. These findings indicate that elemental doping can tailor the local surface microstructure and electronic structure of photocatalysts, thereby enhancing their efficiency in CO_2 photoreduction.

Table 1.5. Summary of recent studies on the photocatalytic CO_2 reduction by elemental-doped photocatalysts.

Photocatalyst	**Synthetic method**	**Reaction medium**	**Performance (μmol/g·h)**	**Ref.**
O-doped g-C_3N_4	Thermal oxidation exfoliation and curling-condensation method	300 W Xenon lamp, $NaHCO_3$ and H_2SO_4	CH_3OH:0.88	[31]
Ag-doped CdS	Photodeposition	300 W Xenon Lamp, water/TEOA	CO: 260	[32]

In doped TiO_2	Sol-gel Method	500 W Hg flash lamp, H_2O (vapor)	CH_4:1120	[33]
K-doped g-C_3N_4	Thermal condensation method	300 W Xenon lamp, water	CO:87	[34]
Mo-doped g-C_3N_4	Pyrolysis Method	300 W Hg lamp, water as a reductant	CO:887, CH_4:124	[35]
N doped TiO_2 nanotubes	Hydrothermal method	500 W tungsten-halogen lamp, Water as reductant	CH_3OH:94.38, HCHO:76.75 HCOOH:1039	[36]
O and C co-doped g-C_3N_4	In situ soft chemical method	300 W Xenon lamp, H_2O/MeCN/TEOA	CO:4.46	[37]
K and O co-doped on polymeric Carbon nitride	Thermal polymerization process	300 W Xenon lamp, Water as reductant	CO:1.62, CH_4:0.28	[38]

Ref: References; MeCN: Methyl cyanide; TEOA: Triethanolamine

Non-metal atom doping

Non-metal doping is an effective strategy to enhance photocatalytic activity by broadening the light absorption range and promoting efficient charge carrier separation [11]. For instance, oxygen doping into g-C_3N_4 nanotubes can optimize its band structure, resulting in a narrower bandgap, increased CO_2 adsorption capacity, and improved charge separation efficiency [31]. The synthesis process of oxygen-doped g-C_3N_4 (OCN) nanotube is shown in **Figures 1.11a–1.11c**. This hierarchical OCN tube demonstrated significantly enhanced visible-light-driven CO_2 reduction activity, producing CH_3OH at a rate of 0.88 μmol/g·h, approximately five times higher than that of bulk g-C_3N_4 (0.17 μmol/g·h). Similarly, nitrogen doping into TiO_2 helps suppress the recombination of photogenerated e^-/h^+ pairs and extends TiO_2's light absorption into the visible range. N-doped TiO_2 nanotubes exhibited significantly higher production rates of CH_3OH (94.38 μmol/g·h), HCHO (76.75 μmol/g·h), and HCOOH (1039 μmol/g·h), compared to undoped TiO_2 powder [36].

Beyond single-element doping, multi-element co-doping has also been employed to further enhance the photocatalytic activity for CO_2 reduction. For example, the simultaneous doping of carbon and oxygen into g-C_3N_4 effectively reduces its bandgap energy from 2.79 to 2.52 eV, leading to improved visible light absorption and significantly enhanced CO

selectivity, with a production rate of 4.46 μmol/g·h [37]. Co-doping not only tunes the electronic structure but also facilitates faster electron transport and migration, thereby boosting overall photocatalytic efficiency.

Metal atom doping

Doping semiconductor photocatalysts with metal atoms introduces impurity levels within the bandgap, which can act as electron traps under photoexcitation. These traps facilitate charge separation by capturing electrons, thereby reducing recombination with holes [12]. For instance, doping potassium (K) into g-C_3N_4 modifies its band structure and charge distribution, enhancing visible light absorption and acting as an effective electron trap. This leads to a significant improvement in photocatalytic activity for CO_2 reduction, yielding CO at a rate of 8.7 μmol/g·h, approximately 25 times higher than that of undoped g-C_3N_4 [34]. Similarly, in Ag-doped CdS composites, the incorporation of silver enhances CO_2 photoreduction performance. Ag-doped CdS achieves a CO rate of 260 μmol/g·h, which is three times higher than that of pure CdS. In this system, Ag serves both as an electron trap and as an active site, further promoting the photocatalytic reduction of CO_2 [32].

Metal and non-metal co-doping is a promising strategy to enhance the photocatalytic performance for CO_2 reduction. For example, polymeric carbon nitride co-doped with potassium and oxygen demonstrated a narrowed bandgap, leading to improved visible light absorption and enhanced separation efficiency of photogenerated charge carriers (**Figures 1.12a–1.12d**). These modifications significantly improve the photocatalytic activity, achieving CO and CH_4 production rates of 1.62 and 0.28 μmol/g·h, respectively, substantially higher than those of bulk carbon nitride [38]. This highlights that elemental co-doping is an effective method for tuning the optical and electronic properties of photocatalyst band structures, thereby improving their efficiency in CO_2 reduction.

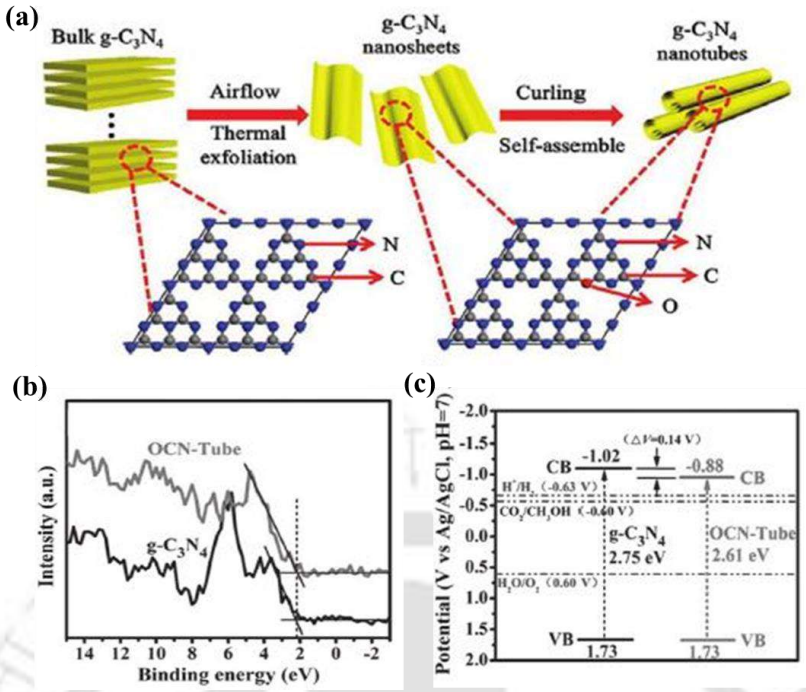

Figure 1.11. (a) Schematic of the synthesis of hierarchical O-doped g-C_3N_4 nanotubes (OCN-Tube), (b) XPS VB spectra, and (c) Band alignments of bulk g-C_3N_4 and OCN-Tube (vs. Ag/AgCl, pH 7) (Reproduced with permission from [31], Copyright 2017, Wiley).

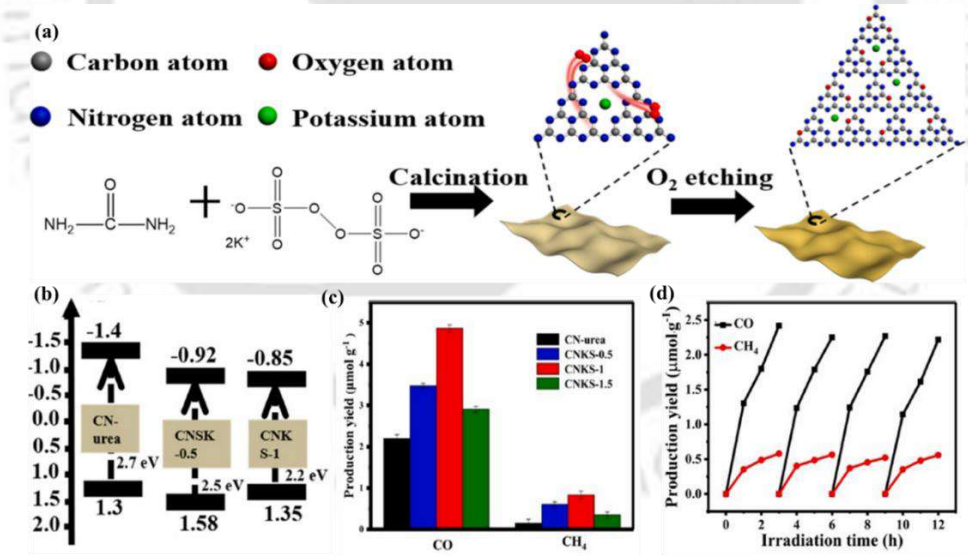

Figure 1.12. (a) Illustration of formation process of K and O co-doped CN (C, N, O, and K atoms are respectively represented by gray, blue, red, and green spheres in the atomic model.), (b) Band alignments of pristine CN and CNKS-x, (c) photocatalytic reduction of CO_2 performance of CN-urea and CNKS-x after 3 h irradiation, and (d) stability test for four runs (Reproduced with permission from [38], Copyright 2021, Elsevier).

1.5.2.2 Vacancy introduction

Introducing vacancies is an effective strategy for tuning the electronic structure of photocatalysts. Surface vacancies can enhance visible light absorption, improve charge carrier separation and transport, and serve as active sites for CO_2 adsorption and activation. Various types of vacancies, such as nitrogen, oxygen, and carbon vacancies, have been extensively studied to boost the photocatalytic CO_2 reduction [39]. Recent advancements and examples of vacancy-engineered photocatalysts for CO_2 reduction are summarized in **Table 1.6**.

Carbon vacancy-engineered g-C_3N_4 was synthesized via a thermal annealing process in an NH_3 atmosphere. The resulting material, enriched with carbon vacancies, exhibited more than twice the CO rate for photocatalytic CO_2 reduction compared to bulk g-C_3N_4. This enhancement is attributed to improved CO_2 adsorption and activation, an upward shift in the conduction band, and increased concentration and lifetime of photogenerated e^-/h^+ pairs. Additionally, the introduction of carbon vacancies reduces exciton binding effects and enhances charge carrier generation (**Figure 1.13a**) [40]. Similarly, oxygen vacancy-rich In_2O_3 was synthesized and evaluated for photocatalytic CO_2 reduction. The presence of oxygen vacancies significantly improves CO_2 adsorption, optimizes the band structure, and prolongs the lifetime of photogenerated charge carriers (**Figures 1.13b–1.13e**). As a result, the modified In_2O_3 achieves a CO rate of 63.3 μmol/g·h, nearly three times higher than that of pristine In_2O_3 (21.7 μmol/g·h). These improvements collectively contributed to the enhanced photocatalytic performance of the material [41].

Beyond introducing traditional surface vacancies such as oxygen, carbon, and nitrogen, the incorporation of novel functional groups or species on the photocatalyst surface can further enhance its photocatalytic performance. These modifications help optimize visible light absorption, accelerate charge carrier separation and transport, and improve CO_2 reduction activity [11]. For instance, introducing surface defects such as cyano and carboxyl groups into g-C_3N_4 significantly enhances visible light absorption, promotes surface charge accumulation, improves charge separation, and extends the lifetime of photogenerated carriers (**Figures 1.13f–1.13h**). As a result, this defect-rich g-C_3N_4 exhibits superior photocatalytic activity for CO_2 reduction to CH_4, achieving a rate of 12.07 μmol/g·h and a high selectivity of 91.5%, surpassing many previously reported g-C_3N_4-based photocatalysts [42].

Table 1.6. Summary of recent studies on the photocatalytic CO_2 reduction by a photocatalyst with a vacancy.

Photocatalyst (vacancies)	**Synthetic method**	**Reaction medium**	**Performance (µmol/g·h)**	**Ref.**
g-C_3N_4 (carbon)	Thermal reaction method	300 W Xenon Lamp, water vapor as reductant	CO:4.18	[39]
In_2O_3 (oxygen)	-	300 W Xenon Lamp, MeCN/H_2O (3:2), TEOA	CO:63.3	[41]
TiO_2 (oxygen)	Ti-OH bond breakage approach	300 W Xenon Lamp, Water vapor	CH_4:2.6, CO:1.56	[43]
g-C_3N_4 (surface defect)	Solvothermal-calcination method	300 W Xenon Lamp, Water vapor, H_2SO_4, and $NaHCO_3$	CH_4:12.07, selectivity: 91.5%	[42]
ZnO (oxygen)	Thermal decomposition technique	150 W Hg lamp 0.5 M aqueous solution of ($NaHCO_3$)	CH_3OH:28.4 CH_3CHO:3	[44]
g-C_3N_4 (nitrogen)	Thermal treating-hydrogenate method	300 W Xenon lamp, water as a reductant	CO:124.2	[45]

Ref: References; MeCN: Methyl cyanide; TEOA: Triethanolamine

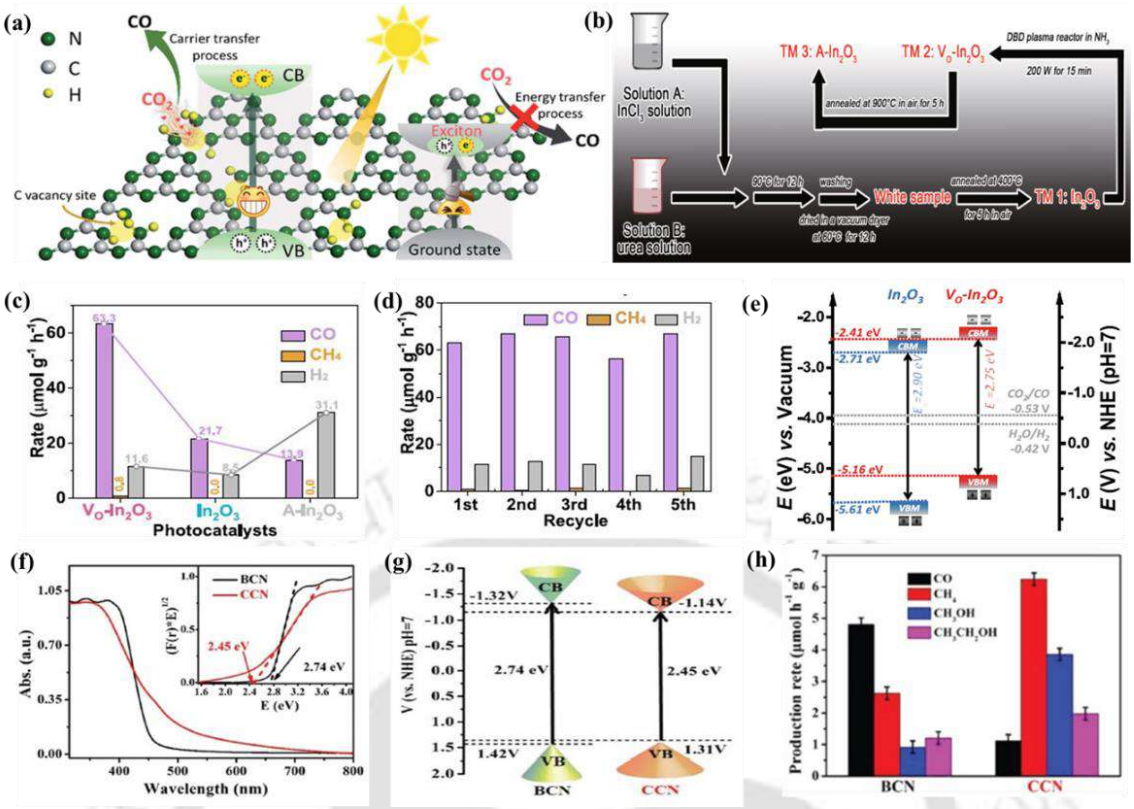

Figure 1.13. (a) Schematic illustration of the promoted CO_2 photoreduction activity on carbon-vacancy modified GCN (Reproduced with permission from [40], Copyright 2019, Royal Society of Chemistry), (b) Schematic illustration for preparing In_2O_3-based model photocatalysts, (c) Production rates of CO and H_2 of V_O-In_2O_3, In_2O_3, and A-In_2O_3 for the photocatalytic CO_2 reduction carried out under visible light irradiation, (d) Stability test of VO-In_2O_3 for the photocatalytic CO_2 reduction, (e) Schematic band structure of In_2O_3 and V_O-In_2O_3 (Reproduced with permission from [41], Copyright 2021, Elsevier), f) UV–vis diffuse reflectance spectra (DRS), (g) band structure alignment of BCN and CCN, and (h) Photocatalytic CO_2-reduction property of CCN and BCN (Reproduced with permission from [42], Copyright 2019, Wiley).

1.5.2.3 Morphology control

The morphology of semiconductor materials plays a critical role in determining their photocatalytic performance. By controlling factors such as particle size, shape, geometric structure, and surface texture, it is possible to enhance charge carrier transport and migration, as well as increase surface reactivity. These improvements can significantly boost the efficiency of photocatalytic CO_2 reduction. Various photocatalysts with tailored morphologies

have been synthesized and studied for this purpose [11]. Recent research on photocatalysts with diverse morphological structures for CO_2 photoreduction is summarized in **Table 1.7**.

Porous, nitrogen-rich g-C_3N_4 nanotubes were synthesized using a supramolecular self-assembly strategy. These nanotubes demonstrate excellent efficiency and stability as visible-light-driven photocatalysts for CO_2 reduction. CO was the primary product, with a rate of 103.6 μmol/g·h, approximately 17 and 15 times higher than that of bulk g-C_3N_4 and P25-TiO_2, respectively. The superior performance is attributed to the unique porous nanotube architecture and the nitrogen-rich nature of TCN (NH_3), which provides abundant Lewis basic sites and a large surface area. These features enhance CO_2 adsorption and facilitate charge transfer, as illustrated in **Figures 1.14a–1.14d**, ultimately boosting the photocatalytic activity for CO_2 reduction [46].

Similarly, CdS hierarchical multi-cavity hollow particles (HMCHPs) were synthesized using a sequential solution growth, sulfidation, and cation exchange approach (**Figures 1.14e–1.14h**). The unique architecture of these HMCHPs offers superior light-harvesting ability, a high density of catalytic active sites, and efficient mass-transfer channels, collectively accelerating the photocatalytic reaction. As a result, they could achieve a remarkable CO rate of 1337 μmol/g·h, significantly outperforming bulk CdS and conventional hollow CdS structures [47]. In another study, three-dimensional spherical β-SiC with a hollow morphology was prepared via a simple sol-gel method. This photocatalyst features a unique electronic structure and a high surface area, both of which facilitate the efficient photocatalytic reduction of CO_2 into CH_4 and other hydrocarbon products [48].

Table 1.7. Summary of recent studies on photocatalytic CO_2 reduction by photocatalysts of various morphologies.

Photocatalyst (morphology)	**Synthetic method**	**Reaction medium**	**Performance (μmol/g·h)**	**Ref.**
SiC (hollow sphere)	Sol-gel method	300 W Xenon lamp, water as a reductant	CH_4: 16.8	[48]
Porous nitrogen-rich g-C_3N_4 nanotubes	Supramolecular self-assembly	300 W Xenon lamp, water vapor as reductant	CO:103.6	[46]

CdS-HMCHPs	Cation exchange strategy	300 W Xenon lamp, MeCN/H_2O, TEOA	CO:1337	[47]
N-doped mesoporous CeO_2	Urea-assisted Method	300 W Xenon lamp, H_2O	CO:0.15, CH_4:0.1041	[49]
CdS/ZIF-8 composites (core-shell structure)	In situ heterogeneous deposition	300 W Xenon lamp, MeCN/H_2O, TEOA	CO:803.3	[50]

Ref: References; MeCN: Methyl cyanide; TEOA: Triethanolamine; HMCHPs: hierarchical multi-cavity hollow particles; ZIF: Zeolitic imidazolate framework

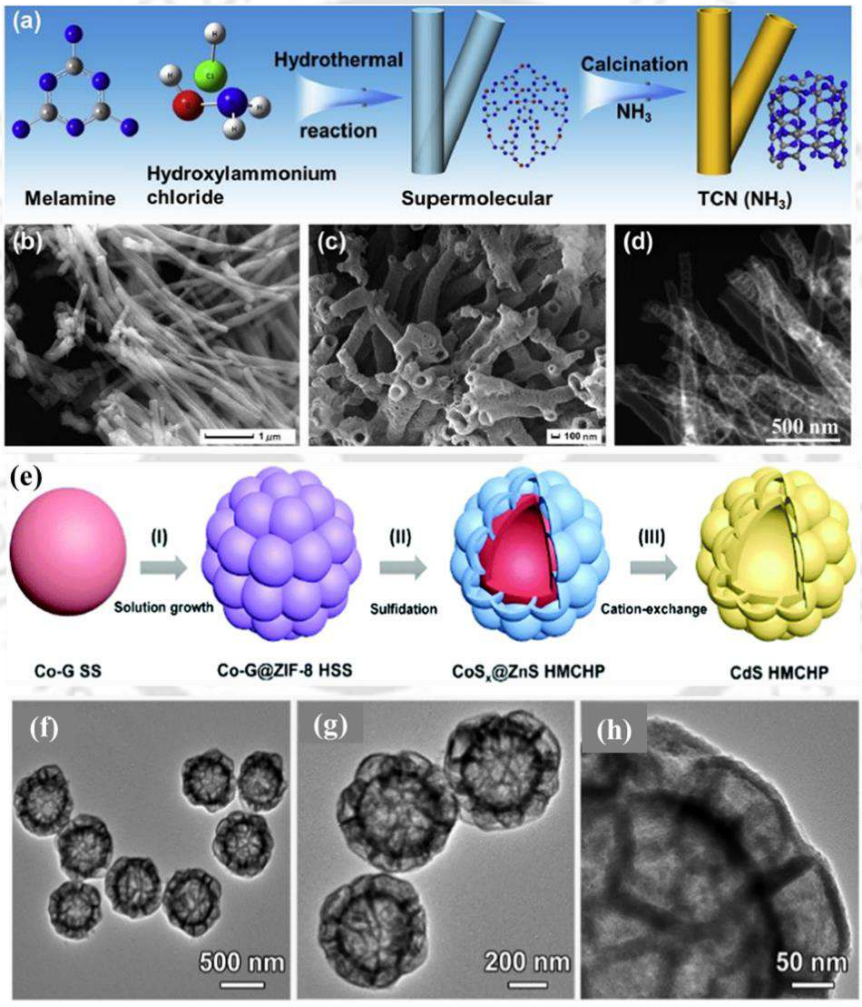

Figure 1.14. (a) Schematic of synthesis of TCN (NH_3), (b) & (c) Scanning electron microscopy (SEM), (d) Transmission electron microscopy (TEM) (Reproduced with permission from [46], Copyright 2019, Elsevier), (e) Schematic illustration of the formation process of CdS HMCHPs, and (f-h) TEM images of CoSx@ZnS HMCHPs (Reproduced with permission from [47], Copyright 2019, Royal Society of Chemistry).

1.5.2.4 Surface modification

Surface functional group

Surface modification of photocatalysts with functional groups is an effective strategy to enhance both reaction activity and product selectivity. For instance, amine groups can increase CO_2 adsorption capacity due to the Lewis acid–base interaction, as CO_2 is a Lewis acid [11]. Tian et al. demonstrated that amine-functionalized g-C_3N_4 could significantly boost CH_4 production, achieving a rate of 0.34 μmol/g·h [51]. Additionally, co-modification with elements and basic functional groups can further improve CO_2 reduction performance. For example, g-C_3N_4 modified with phosphorus and cyano groups exhibits a 1.57-fold increase in CO_2 reduction efficiency compared to pristine g-C_3N_4. This improvement is attributed to the modified visible light absorption and optimized bandgap structure induced by these functional groups [52].

Cocatalysts

Loading appropriate cocatalysts onto semiconductor photocatalysts is also an effective strategy to enhance photocatalytic CO_2 reduction performance. Cocatalysts can activate surface reactive sites, lower the activation energy, improve product selectivity, and increase photostability of the system [11]. Various types of cocatalysts have been employed to boost the efficiency of semiconductor materials, including noble metals (e.g., Au, Pd, Pt), non-noble metals and their oxides (e.g., Co, Cu, Bi, Mg, Ni, MnOx, CuOx, NiO), metal alloys, and non-metallic materials such as carbon quantum dots and graphene. Recent advancements in cocatalyst-modified semiconductors for CO_2 photoreduction are summarized in **Table 1.8**.

Non-metallic materials such as carbon quantum dots (CQDs) and graphene have demonstrated significant potential in enhancing CO_2 conversion. In one study, nonpolar CQD-modified g-C_3N_4 was synthesized via thermal polymerization followed by a hydrothermal treatment. The incorporation of CQDs reduces the surface polarity of the photocatalyst, thereby improving the adsorption of nonpolar CO_2 molecules and enhancing reaction kinetics. Additionally, CQDs contribute to increased visible light absorption and improve charge carrier separation efficiency, owing to their photosensitization effect and strong electron-withdrawing capability (**Figures 1.15a–1.15b**). As a result, the modified photocatalyst exhibits a CO rate of 118 μmol/g·h, approximately six times higher than that of pristine g-C_3N_4 [53].

Co(II)-dispersed CdS was synthesized via the controlled decomposition of Co-EDTA precursors (**Figure 1.15c**). Co(II) species, particularly in a tetra-coordinated configuration, act as active sites and facilitate efficient charge transfer, significantly enhancing the photocatalytic

CO_2 reduction performance. CO was the primary product, with a rate of 392 µmol/g·h [54]. In another study, a CdS/A-GO (aspartic acid-modified graphene oxide with –COOH groups) photocatalyst was prepared using an ultrasonication method. The A-GO offers improved electrical conductivity and hydrophilicity, promoting effective charge separation, faster electron transport, and enhanced CO_2 adsorption. These properties collectively lead to a significant boost in CO_2 reduction efficiency. CH_3OH was the main product observed, with a rate of 662.5 µmol/g·h, substantially higher than that of pristine CdS or unmodified GO [55].

g-C_3N_4/FeTCPP heterogeneous catalyst was synthesized using a simple assembly technique (**Figure 1.15d**). In this system, g-C_3N_4 functions as the light-harvesting material, while FeTCPP (iron tetrakis(4-carboxyphenyl) porphyrin) serves as the molecular catalytic center. Upon light irradiation, photoexcited electrons generated in the g-C_3N_4 nanosheets are efficiently transferred to FeTCPP, facilitating the CO_2 reduction reaction. CO was the primary product, with a high rate of 1086.66 µmol/g·h and excellent selectivity of up to 98%, demonstrating the strong synergistic effect between the light absorber and the molecular catalyst [56].

Table 1.8. Summary of recent studies on photocatalytic CO_2 reduction by a photocatalyst along with a cocatalyst.

Photocatalyst (cocatalyst)	**Synthetic method**	**Reaction medium**	**Performance (µmol/g·h)**	**Ref.**
g-C_3N_4 (carbon quantum dots)	Thermal polymerization and hydrothermal method	300 W halogen lamp	CO:118	[53]
CdS (Co(II))	Chemical anchoring method	300 W Xenon lamp, 0.3M Na_2CO_3 0.06 M Na_2SO_3	CO:392 TOF:7.94 %	[54]
TiO_2 nanowires (AuNPs)	Hydrothermal and chemical reduction method	HID 30 W Xenon lamp, H_2 as reductant	CO: 1237 CH_3OH: 13	[57]
Cu_2O (rGO)	Simple solution chemical method	300 W Xenon lamp, water	CH_3OH:17.76	[58]

CdS (A-GO)	Ultrasonication	350 W Xenon lamp, H_2O/TEOA	CH_3OH:662.5	[55]
SiC nanosheets (PtNPs)	facile acid-base mediated alcohol reduction method	300 W Xenon lamp, H_2O	CH_4:13.6, selectivity: 88.3%	[59]
g-C_3N_4 (FeTCPP)	Thermal polymerization and mechanical mix method	300 W Xenon lamp, water	CO:1086.66	[56]
CdS (Co-bpy)	-	300 W Xenon lamp, MeCN/TEOA	CO:844	[60]
TiO_2 (Cr_2O_3)	Solvothermal and photodeposition Method	300 W Xenon lamp, H_2O	CO:3.96 CH4:1.54	[61]
CdS (Co-ZIF-9)	-	300 W Xenon lamp, MeCN/H_2O/TEOA	CO:1625 AQY:1.93%	[62]

Ref: References; MeCN: Methyl cyanide; TEOA: Triethanolamine; HMCHPs: hierarchical multi-cavity hollow particles; TOF: Turnover frequency; AQY: Apparent quantum yield; ZIF: Zeolitic imidazolate framework; bpy: bipyridine; FeTCPP: Fe tetra(4-carboxyphenyl) porphyrin.

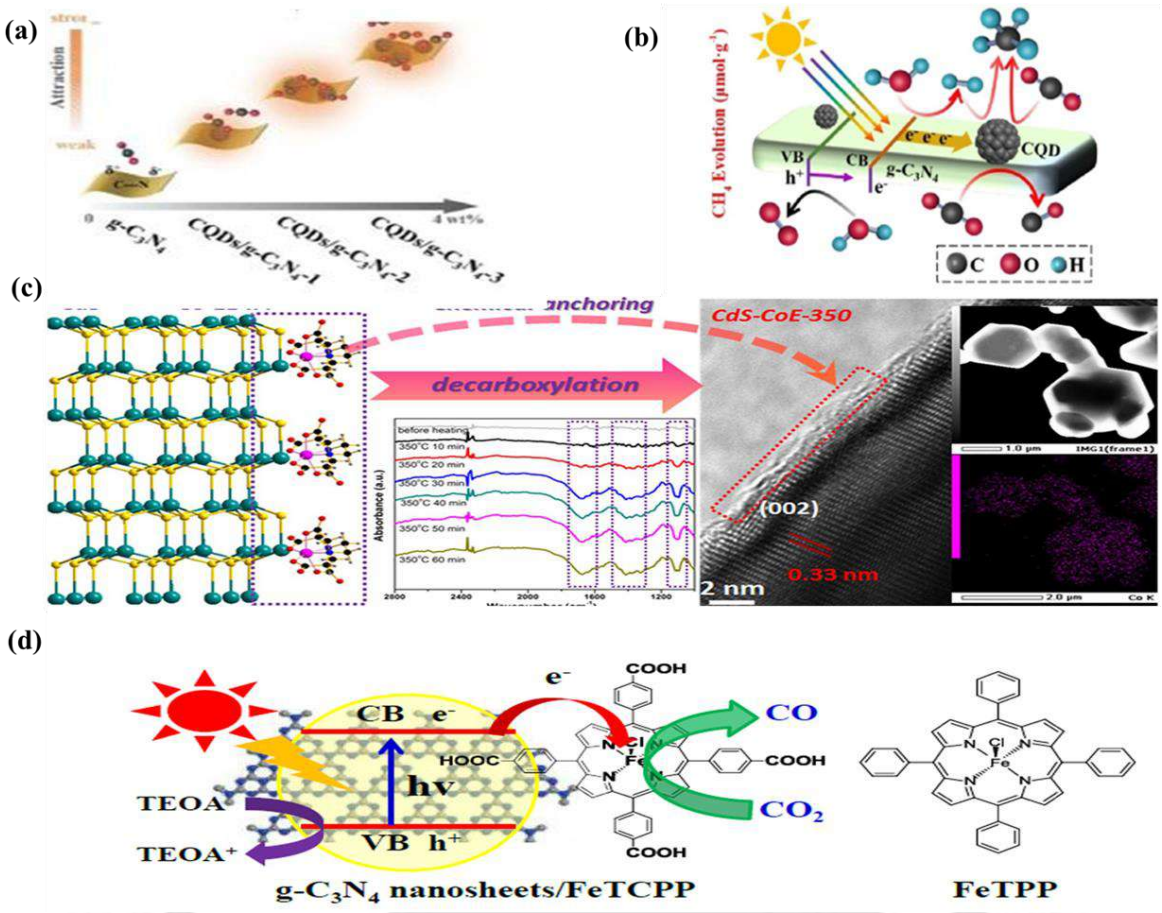

Figure 1.15. (a) Schematic depicting enhanced surface adsorption of nonpolar CO_2 molecules, (b) Illustration of photoreduction process for CO_2 on the surface of the CQDs/g- C_3N_4 composite (Reproduced with permission from [53], Copyright 2018, Wiley), (c) Schematic illustration for the chemical anchoring of the Co species on the CdS surface through the controlled decomposition of Co-EDTA precursor (Reproduced with permission from [54], Copyright 2018, Elsevier), and (d) Structure of g-C_3N_4/FeTCPP and FeTPP (Reproduced with permission from [56], Copyright 2018, Elsevier).

1.5.2.5 Heterojunction construction

Coupling a selective semiconductor with another to form a heterojunction is an effective strategy to enhance charge-carrier transfer and separation, which is achieved via the interface between semiconductors with well-aligned band potentials [16]. Based on the relative band positions of the two semiconductors, heterojunctions can be classified into three types, as illustrated in **Figure 1.16**. Among various configurations, type-II heterostructures are especially advantageous for photocatalytic CO_2 reduction. By spatially directing photogenerated electrons and holes to different semiconductors, they promote efficient charge

separation, suppress recombination, and thereby enhance photocatalytic activity. Owing to these benefits, type-II heterostructures have attracted considerable interest in CO_2 photoreduction studies. Recent studies on semiconductor-based heterojunctions for CO_2 reduction are summarized in **Table 1.9**.

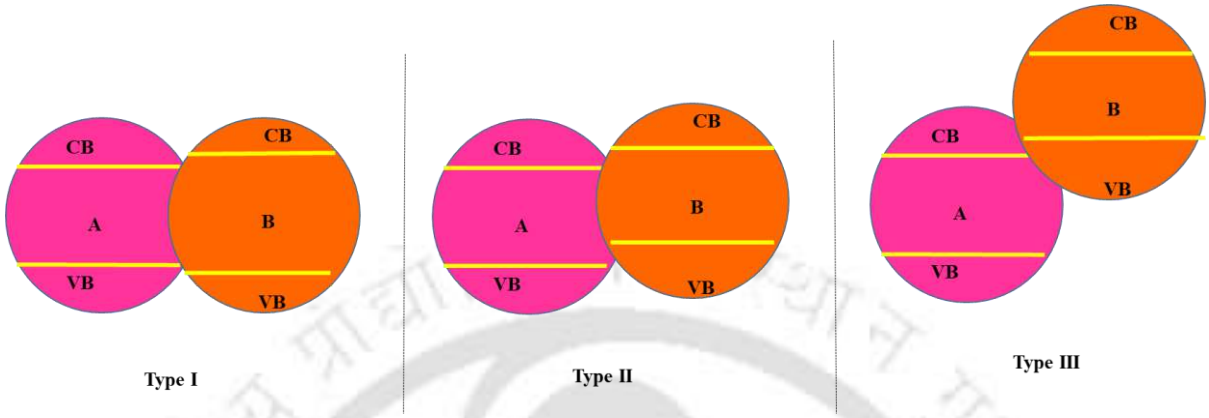

Figure 1.16. Different types of semiconductor heterojunctions.

The hierarchical branch-like ZnS-DETA/CdS heterostructure, composed of ultrathin nanowires (**Figures 1.17a–1.17b)**, was synthesized via a cation-exchange method. This architecture exhibits a porous structure with a high surface area, providing numerous active sites for CO_2 reduction. Additionally, the heterostructure efficiently harvests visible light and significantly improves charge carrier separation. As a result, it could achieve a maximum CO production yield of 8325 µmol/g·h [63].

CdS/Bi_2S_3 heterostructure was synthesized via an ion-exchange method and employed as a photosensitizer in combination with the FeTCPP molecular catalyst. This heterostructure effectively reduces sulfur vacancies in CdS, thereby enhancing charge separation and utilization. Moreover, integration with the FeTCPP catalyst alters the direction of electron transfer, as illustrated in **Figure 1.17c**. The resulting photocatalytic CO_2 reduction to CO achieves a rate of 1930 µmol/g·h, which is 8.2 times higher than that of the CdS/FeTCPP hybrid catalyst [56].

Similarly, the CdS/ZnO heterostructure enables visible-light-driven photocatalytic CO_2 reduction by utilizing CdS as the primary light absorber. Electron migration from CdS to ZnO (**Figure 1.17d**) enhances charge separation, while ZnO facilitates improved CO_2 adsorption and activation. CO and CH_4 were identified as the main products, with rates of 35.2 and 5.9 µmol/g·h, respectively, demonstrating a 13-fold increase in activity compared to pristine CdS [64].

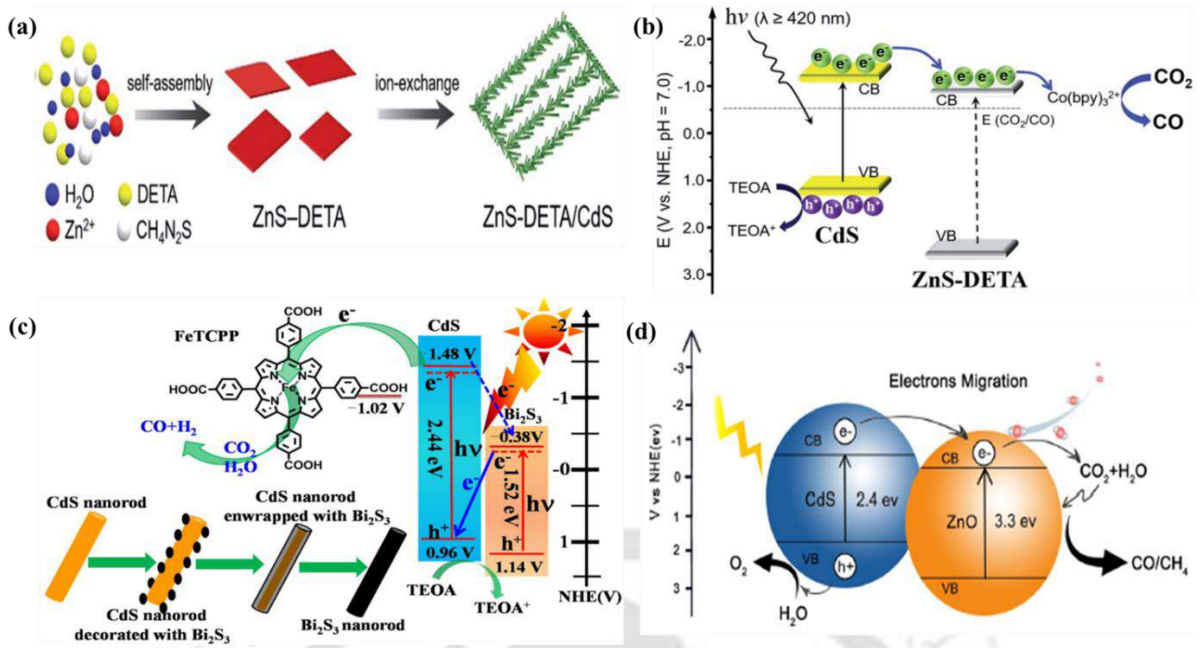

Figure 1.17. (a) Schematic illustration of the synthetic process of branch-like ZnS–DETA/CdS hierarchical heterostructures, (b) Possible reaction mechanism of photocatalytic CO_2 reduction over the ZnS–EDTA/CdS heterostructure (Reproduced with permission from [63], Copyright 2019, Royal Society of Chemistry), (c) Formation of CdS/Bi_2S_3 heterostructure and proposed charge transfer mechanism in CO_2 photoreduction over CdS/Bi_2S_3/FeTCPP hybrid catalysts under visible-light illumination (Reproduced with permission from [65], Copyright 2018, Elsevier), and (d) Proposed mechanism of photocatalytic reduction CO_2 over CdS/ZnO (Reproduced with permission from [64], Copyright 2020, American Chemical Society).

Table 1.9. Summary of recent studies on photocatalytic CO_2 reduction by using heterostructure photocatalysts.

Photocatalyst	**Synthetic method**	**Reaction medium**	**Performance (μmol/g·h)**	**Ref.**
g-C_3N_4/Cu-TiO_2	Solid state synthesis	500 W Xen arch lamp, Water	CH_3OH: 321.75, HCOOH:633.62	[66]
CdS/Bi_2S_3/FeTCPP	Ion exchange reaction	300 W Xenon lamp, MeCN/H_2O/TEOA	CO:1930	[56]
CdS/g-C_3N_4	Polycondensation and hydrothermal method	250 W Lamp, CH_3OH	$HCOOCH_3$:135 2.07	[67]

CdS/ZnO	Solvothermal method	500 W Hg Lamp, H_2O	CO:35.2, CH_4:5.9	[64]
$LaPO_4$/CdS	Self-assembly approach	300 W Xenon lamp, H_2O/TEOA/MeCN	CO:960	[68]
ZnS-DETA/CdS	Ion exchange strategy	300 W Xenon lamp, 2'2-bipyridine (bpy) MeCN/H_2O/TEOA	CO:8325	[63]

Ref: References; MeCN: Methyl cyanide; TEOA: Triethanolamine; DETA: Diethylenetriamine; bpy: bipyridine; FeTCPP: Fe tetra(4-carboxyphenyl) porphyrin.

1.5.2.6 Z-scheme construction

Artificial Z-scheme architectures markedly improve photocatalytic performance by providing an extended light-absorption range, efficient separation of e^-/h^+ pairs, strong redox potential, and unique charge-transfer pathways [12]. Z-scheme photocatalysts are generally classified into two main categories, as illustrated in **Figure 1.18**.

In direct Z-scheme photocatalysts (**Figure 1.18a**), the intimate contact between two semiconductors facilitates the formation of an internal electric field, which accelerates charge carrier transfer. In contrast, all-solid-state Z-scheme photocatalysts (**Figure 1.18b**) utilize an electron mediator (e.g., Ag, Au) to promote efficient charge transport between semiconductors. Both configurations have attracted growing interest for photocatalytic CO_2 reduction using a variety of semiconductor materials [16]. Recent advancements in CO_2 reduction using Z-scheme photocatalysts are summarized in **Table 1.10**.

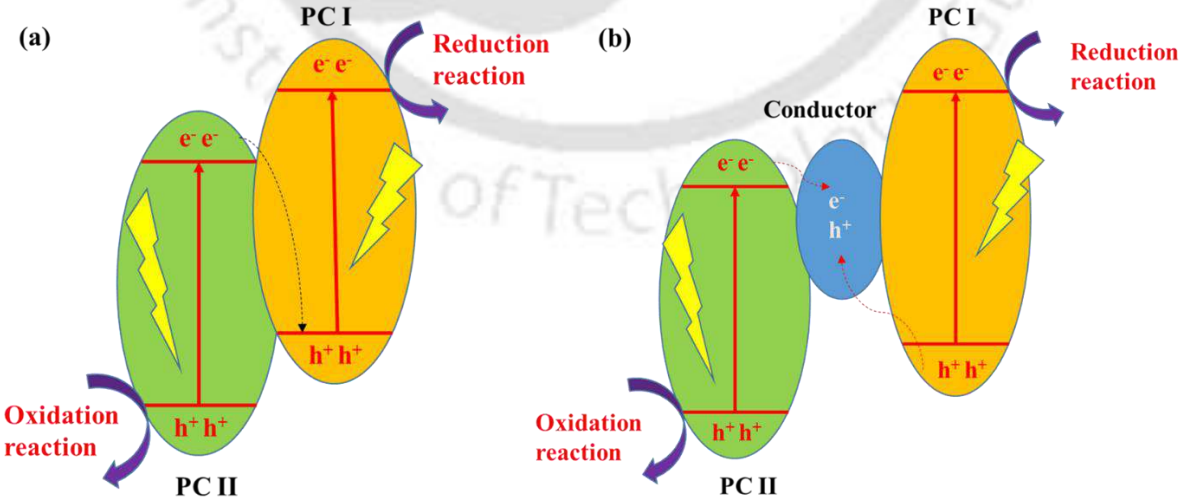

Figure 1.18. Z-scheme photocatalytic mechanism: (a) Direct Z-scheme and (b) All-solid-state Z-scheme.

Au-TiO_2/g-C_3N_4 Z-scheme core–shell structure was synthesized using a precise method, as illustrated in **Figure 1.19a**. In this configuration, Au nanoparticles serve as electron mediators, facilitating electron transfer from TiO_2 nanoparticles to the ultrathin g-C_3N_4 layer (**Figure 1.19b**). g-C_3N_4 nanosheets, wrapped around the structure, not only trap electrons but also enhance CO_2 adsorption through their surface π-bond interactions. Under visible light irradiation with water as the electron donor, the photocatalyst exhibited outstanding CO_2 photoreduction performance, producing CO and CH_4 at rates of 21.7 and 37.4 μmol/g·h, respectively, 36 and 41 times higher than those of commercial P25 TiO_2 [69].

Nb-TiO_2/g-C_3N_4 direct Z-scheme system was synthesized via a solid-state method and investigated for photocatalytic CO_2 reduction with water under visible light irradiation. Nb doping in TiO_2 effectively narrows the bandgap, enabling visible-light-driven photocatalytic activity. The Z-scheme configuration not only suppresses the rapid recombination of photogenerated e^-/h^+ pairs but also enhances the redox potential of the Nb-TiO_2/g-C_3N_4 system. In this mechanism, photoexcited electrons in the conduction band (CB) of Nb-TiO_2 recombine with holes in the valence band (VB) of g-C_3N_4, preserving the electrons in the CB of g-C_3N_4 and holes in the VB of Nb-TiO_2 (**Figure 1.19c**). The main products detected were CH_4, CO, and HCOOH, with respective rates of 562, 420, and 698 μmol/g·h [70].

SiC/MoS_2 Z-scheme nanoflower heterostructure was synthesized via a self-assembly method, as shown in **Figure 1.19d**. This Z-scheme configuration enables efficient charge transfer by facilitating the recombination of electrons in MoS_2 with holes in SiC, thereby preserving the photogenerated electrons in the conduction band of SiC for effective photocatalysis (**Figure 1.19e**). As a result, the photocatalyst achieved a maximum CH_4 production rate of 323 μmol/g·h [71].

Table 1.10. Summary of recent studies on the photocatalytic CO_2 reduction by Z-scheme photocatalyst.

Photocatalyst	**Synthetic method**	**Reaction medium**	**Performance (μmol/g·h)**	**Ref.**
Nb-TiO_2/g-C_3N_4	Solid-state synthesis	30 W white bulbs, water	CH_4:562,CO:420 ,HCOOH:698	[70]
Au-TiO_2/g-C_3N_4	Deft Method	300 W Xenon lamp, water	CH_4:37.4,CO:21.7	[69]

CdS/WO_3	Precipitation Method	300 W Xenon arc lamp, Water	CH_4:1.02	[72]
SiC/MoS_2	Self-assembly method	300 W Xenon lamp,	CH_4:323, AQY:1.75%	[71]
Au-CdS/IO-TiO_2	GBMR/P	300 W Xenon lamp, H_2O	CH_4:41.6	[73]

GBMR/P: Gas bubbling-assisted membrane reduction precipitation

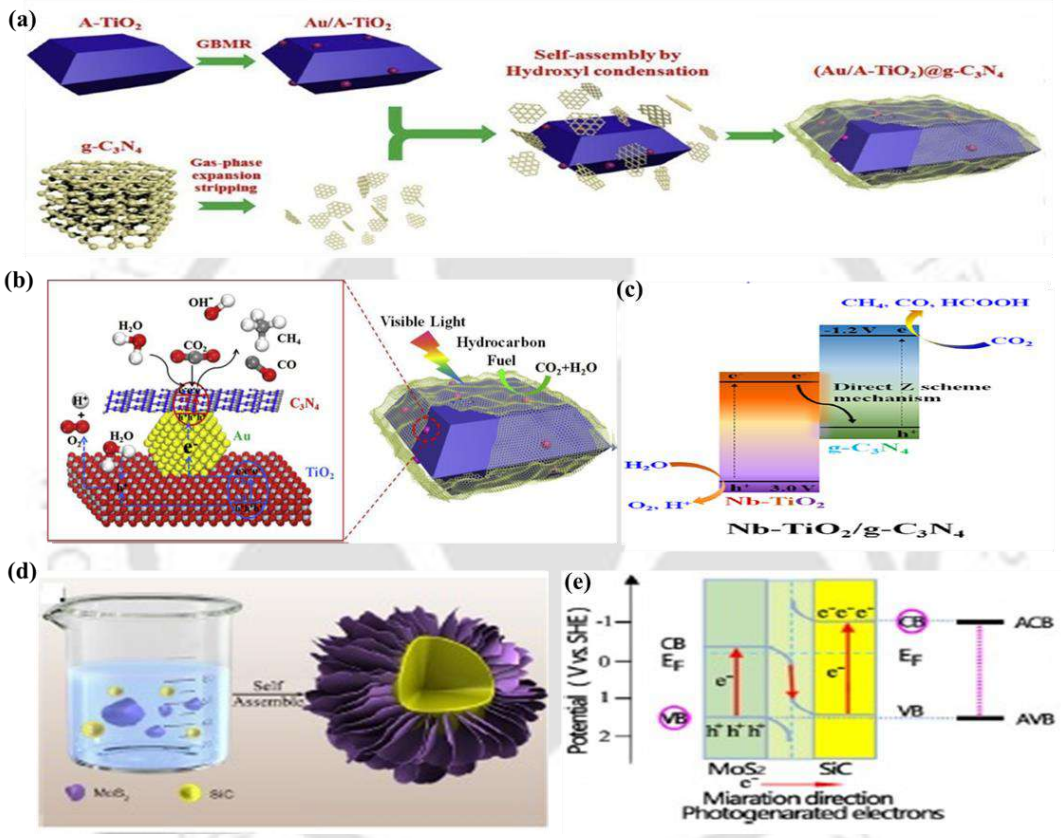

Figure 1.19. (a) Schematic of preparation processes of Au-TiO_2/ g-C_3N_4, (b) Schematic of the mechanism for CO_2 photoreduction with H_2O to CH_4 over (Au/TiO_2)@g-C_3N_4 catalysts (Reproduced with permission from [69], Copyright 2020, Elsevier), (c) Direct Z-scheme mechanism of Nb-TiO_2/g-C_3N_4 for reduction of CO_2 (Reproduced with permission from [70], Copyright 2019, Elsevier), (d) Schematically synthetic process of SiC@MoS_2 nanoflower, and (e) Z-scheme model of SiC@MoS_2 photocatalyst and its charge transfer process under light irradiation (Reproduced with permission from [71], Copyright 2018, American Chemical Society).

1.5.3 Challenges and scale-up considerations in photocatalytic CO_2 reduction

Despite the significant progress achieved in laboratory-scale photocatalytic CO_2 reduction, several technical challenges must be addressed before the developed bioinspired photocatalysts can be translated to industrial-scale applications. One of the major concerns is the long-term stability of photocatalysts under prolonged light irradiation, particularly for sulfide- and oxide-based systems that are prone to photocorrosion and structural degradation [25,26]. In addition, the scalability and reproducibility of bio-based synthesis routes remain challenging due to variations in biological precursors and difficulties in maintaining uniform physicochemical properties at large-scale production [27]. Practical implementation is further constrained by limited light penetration in dense reaction media, complex reactor designs, and inefficient photon utilization at scaled-up conditions [11]. Mass transfer limitations, including restricted CO_2 diffusion to active sites and sluggish desorption of reaction products, can significantly reduce overall conversion efficiency [28]. Furthermore, catalyst recovery, recyclability, and associated cost considerations play a critical role in determining the economic feasibility of photocatalytic CO_2 reduction processes [16]. Addressing these challenges is essential to bridge the gap between laboratory performance and real-world industrial deployment, thereby guiding the rational design of robust, scalable, and cost-effective photocatalytic systems.

1.6 Knowledge gap and objectives of the doctoral work

Various semiconductor materials have been explored as photocatalysts for CO_2 reduction. However, they often suffer from critical limitations-such as rapid e^-/h^+ pairs recombination, low charge transfer efficiency, poor stability, and susceptibility to photocorrosion, which hinder their overall performance. To overcome these drawbacks, several catalyst modification strategies have been employed, including metal and non-metal doping, morphology tuning, defect/vacancy engineering, co-catalyst integration, and the construction of heterojunctions or Z-scheme systems. These approaches are proven to be effective in improving photocatalytic activity. These photocatalysts have traditionally been synthesized through chemical methods. However, these approaches often involve significant drawbacks, including high cost, energy consumption, extended processing time, and the use of hazardous, environmentally aggressive chemicals. To date, no studies have explored a bioinspired strategy for synthesizing modified nanoparticles specifically for PCO_2RR. Green synthesis approaches

using natural resources, such as plant-based analytes, offer a sustainable and eco-friendly alternative.

This work aims to develop modified nanoparticles through environmentally benign methods for the photocatalytic conversion of CO_2 into valuable chemical products. The source of bio-extract was selected based on availability, richness in reducing compounds, economic value, and favourable growth characteristics. Northeastern states of India, known for their rich biodiversity and abundance of tropical plants, serve as a promising reservoir of natural resources. These plants offer an effective and eco-friendly source of reducing and capping agents, making them ideal for the green synthesis of nanoparticles (NPs).

A short exposure of microwave irradiation in concurrence with the bioinspired process could accelerate the rate of NPs formation by several folds, along with relatively low cost, rapid synthesis, energy saving, high efficiency, small particle size, narrow particle size distribution, etc. [74]. Herein, a microwave-assisted bioinspired process is employed to synthesize NPs for PCO_2RR photocatalytic CO_2 reduction. In this study, *Aegle marmelos* has been selected as a plant source based on its natural phytochemicals contents, namely, phenol, flavonoids, alkaloids, tannins, saponins, steroids, proteins, and amino acids [75]. These bioactive compounds are known to be effectively for the reduction of metal ions into their nanoparticles, making *Aegle marmelos* a suitable candidate for the green synthesis of nanoparticles for photocatalytic CO_2 reduction reaction [27,76].

Cadmium sulfide (CdS) has been selected as the semiconductor material due to its advantageous properties, including an appropriate bandgap (Eg = 2.4 eV), efficient solar energy conversion, a suitable conduction band potential (–0.95 V vs. NHE at pH 7), and earth abundance [25,30]. However, CdS also faces significant limitations for photocatalytic CO_2 reduction, such as rapid e^-/h^+ pairs recombination and oxidative corrosion. To address these issues, the synthesized CdS nanoparticles are further modified to enhance stability and reduce charge carrier recombination. The coupling of CdS with carbon quantum dots (CQDs) is carried out in a bioinspired route to enhance the separation and transport of charge carriers and CO_2 adsorption, minimizing e^-/h^+ recombination and photo corrosion [77]. The construction of CdS/In_2O_3, CdS/CuO, and CdS/SnO_2 heterostructured materials is also performed using a bio-based route to improve its charge separation efficiency, minimize the recombination of e^-/h^+ pairs, and suppress the oxidative corrosion to a greater extent [64,78,79]. Furthermore, theoretical studies have been conducted to gain a fundamental understanding of the semiconducting properties of the synthesized photocatalysts for CO_2 reduction. The specific

merits for the selection of these photocatalysts are provided in the respective chapters of the thesis.

Based on the above knowledge gaps, the following objectives are taken into consideration.

- To synthesis CQDs/CdS nanocomposites in a vegetal route for photocatalytic reduction of CO_2 to methanol under visible light (**Chapter 3**)
- To investigate plant-based phytochemicals for the synthesis of Z-scheme In_2O_3/CdS heterostructures and its DFT analysis for photocatalytic CO_2 reduction to HCOOH and CO (**Chapter 4**)
- To perform experimental and theoretical studies on photocatalytic CO_2 reduction to HCOOH by biomass-derived carbon dots embedded phytochemical-based CdS quantum dots (**Chapter 5**)
- To synthesize Z-scheme SnO_2/CdS heterostructure and its DFT study for photocatalytic CO_2 reduction to methanol and hydrogen (**Chapter 6**)
- To construct phytochemical-based synthesis of p-n Junction CuO/CdS heterostructures for photocatalytic carbon dioxide reduction to ethanol and carbon monoxide (**Chapter 7**)

1.7 Organization of the Thesis

The thesis is organized into seven chapters, which are outlined below.

CHAPTER 1: Introduction and Literature Review

This chapter presents a general introduction to CO_2 emission and its global and Indian scenario, the fundamentals of CO_2 photoreduction, various technologies for CO_2 reduction to value-added chemicals, a review of the state-of-the-art literature on photocatalysts and its modifications for photocatalytic CO_2 reduction, and a knowledge gap and the research objectives are composed.

CHAPTER 2: Materials and Methodology

This chapter describes the experimental methods, chemicals used, and equipment employed for the characterization of catalysts and analysis of the products. It also includes a discussion of the Density Functional Theory (DFT) calculations conducted in this study.

CHAPTER 3: Vegetal Route for Synthesis of CQDs/CdS Nanocomposites for Photocatalytic Reduction of CO_2 to Methanol under Visible Light

This chapter discusses on the synthesis of CQDs/CdS nanorod composites via a bio-based route, utilizing natural precursors such as *orange peels* and phytochemicals from *Aegle marmelos* plant extract. The catalysts were comprehensively characterized using X-ray diffraction, microscopic, spectroscopic, and electrochemical techniques. The photocatalytic activity of CQDs/CdS(bio) composites was evaluated for CO_2 reduction to methanol under visible light irradiation.

CHAPTER 4: Phytochemicals-based Synthesis of Z-Scheme In_2O_3/CdS Heterostructures: DFT Analysis and Photocatalytic CO_2 Reduction to HCOOH and CO

In this chapter, a Z-scheme In_2O_3/CdS heterostructure was developed through a bioinspired approach using phytochemicals from *Aegle marmelos*, employing a short-duration microwave irradiation. Density Functional Theory (DFT) calculations were carried out on the synthesized catalysts, including optimized geometry, band structure, and density of states (DOS) analysis. Detailed characterization of the catalysts was performed using various techniques. The photocatalytic performance of In_2O_3CdS(bio) composite was evaluated for CO_2 reduction to formic acid and carbon monoxide under visible light illumination.

CHAPTER 5: Experimental and Theoretical Studies on Photocatalytic CO_2 Reduction to HCOOH using Plant-based CDs/CdS Quantum Dots composites

This study presents bioinspired synthesis of CdS quantum dots (QDs) using phytochemicals found in *Agle mamelos* and carbon dots (CDs) using *orange peels*. CDs were homogeneously incorporated into CdS QDs(bio) via a simple deposition method, forming CDs/CdS QDs(bio) nanocomposites. The photocatalytic activity of the CDs/CdS QDs(bio) composite was studied for CO_2 reduction to HCOOH under visible light irradiation. Both experimental investigations and theoretical insights into the CO_2 reduction mechanism to HCOOH are also presented in this study.

CHAPTER 6: Green Synthesis of Z-Scheme SnO_2/CdS Heterostructures: DFT Calculation and Photocatalytic CO_2 Reduction to Methanol and Hydrogen

This chapter discusses on the synthesis of Z-scheme SnO_2/CdS QDs heterostructures in a bio-based route using bio-analytes found in *Aegle Marmelos* via microwave irradiation. DFT calculations were performed on the synthesized catalysts, including geometry optimization,

band structure, and DOS analysis. The catalysts were thoroughly characterized using a various of analytical techniques. The photocatalytic performance of SnO_2/CdS QDs(bio) heterostructures was evaluated for CO_2 reduction to methanol and hydrogen under visible light irradiation.

CHAPTER 7: Phytochemicals for Synthesis of p-n Junction CuO/CdS Heterostructures for Photocatalytic Carbon Dioxide Reduction to Ethanol and Carbon Monoxide

This chapter focuses on the bioinspired synthesis of zero-dimensional (0D) p-n junction CuO/CdS QDs heterostructures using bio-analytes from *Aegle marmelos* via microwave irradiation method. The catalysts were characterized using various analytical techniques. The photocatalytic test of CuO/CdS QDs(bio) heterostructure was carried out for CO_2 reduction to ethanol (C_2 hydrocarbon) and carbon monoxide under visible light illumination. Additionally, DFT calculations were conducted to investigate the optimized geometry, band structure, and DOS of the synthesized catalysts.

CHAPTER 8: Conclusions and Scopes for Future Studies

This chapter outlines the key findings of the overall work. It also presents suggestions and recommendations for future research based on the shortcomings in the present study.

References

[1] M. Filonchyk, M.P. Peterson, L. Zhang, V. Hurynovich, Y. He, Greenhouse gases emissions and global climate change: Examining the influence of CO_2, CH_4, and N_2O, Sci. Total Environ. 935 (2024) 173359. https://doi.org/https://doi.org/10.1016/j.scitotenv.2024.173359.

[2] L.J.R. Nunes, The Rising Threat of Atmospheric CO_2: A Review on the Causes, Impacts, and Mitigation Strategies, Environments. 10 (2023) 66. https://doi.org/10.3390/environments10040066.

[3] M.N. Rahman, M.A. Wahid, Renewable-based zero-carbon fuels for the use of power generation: A case study in Malaysia supported by updated developments worldwide, Energy Reports. 7 (2021) 1986–2020. https://doi.org/https://doi.org/10.1016/j.egyr.2021.04.005.

[4] C. Zou, Q. Zhao, G. Zhang, B. Xiong, Energy revolution: From a fossil energy era to a new energy era, Nat. Gas Ind. B. 3 (2016) 1–11. https://doi.org/https://doi.org/10.1016/j.ngib.2016.02.001.

[5] P.J. Megía, A.J. Vizcaíno, J.A. Calles, A. Carrero, Hydrogen Production Technologies:

From Fossil Fuels toward Renewable Sources. A Mini Review, Energy & Fuels. 35 (2021) 16403–16415. https://doi.org/10.1021/acs.energyfuels.1c02501.

[6] M. Muratori, H. Kheshgi, B. Mignone, L. Clarke, H. McJeon, J. Edmonds, Carbon capture and storage across fuels and sectors in energy system transformation pathways, Int. J. Greenh. Gas Control. 57 (2017) 34–41. https://doi.org/10.1016/j.ijggc.2016.11.026.

[7] J. Gao, C. Jia, B. Liu, Direct and selective hydrogenation of CO_2 to ethylene and propene by bifunctional catalysts, Catal. Sci. Technol. 7 (2017) 5602–5607. https://doi.org/10.1039/c7cy01549f.

[8] R. Daiyan, X. Lu, Y.H. Ng, R. Amal, Liquid Hydrocarbon Production from CO_2: Recent Development in Metal-Based Electrocatalysis, ChemSusChem. 10 (2017) 4342–4358. https://doi.org/10.1002/cssc.201701631.

[9] R. Snoeckx, A. Bogaerts, Plasma technology-a novel solution for CO_2 conversion?, Chem. Soc. Rev. 46 (2017) 5805–5863. https://doi.org/10.1039/c6cs00066e.

[10] P.M. Gawal, J. Ishrat, K. Bhattacharyya, A.K. Golder, Experimental and Theoretical Studies on Photocatalytic CO_2 Reduction to HCOOH by Biomass-Derived Carbon Dots Embedded Phytochemical-Based CdS Quantum Dots, Langmuir. 41 (2025) 11161–11172. https://doi.org/10.1021/acs.langmuir.5c01002.

[11] H. Shen, T. Peppel, J. Strunk, Z. Sun, Photocatalytic Reduction of CO_2 by Metal-Free-Based Materials: Recent Advances and Future Perspective, Sol. RRL. 4 (2020) 1900546. https://doi.org/10.1002/solr.201900546.

[12] K. Yang, Z. Yang, C. Zhang, Y. Gu, J. Wei, Z. Li, C. Ma, X. Yang, K. Song, Y. Li, Q. Fang, J. Zhou, Recent advances in CdS-based photocatalysts for CO_2 photocatalytic conversion, Chem. Eng. J. 418 (2021) 129344. https://doi.org/10.1016/j.cej.2021.129344.

[13] P. Chen, Y. Zhang, Y. Zhou, F. Dong, Photoelectrocatalytic carbon dioxide reduction: Fundamental, advances and challenges, Nano Mater. Sci. 3 (2021) 344–367. https://doi.org/10.1016/j.nanoms.2021.05.003.

[14] J. Mao, K. Li, T. Peng, Recent advances in the photocatalytic CO_2 reduction over semiconductors, Catal. Sci. Technol. 3 (2013) 2481–2498. https://doi.org/10.1039/c3cy00345k.

[15] W. Leitner, The coordination chemistry of carbon dioxide and its relevance for catalysis: A critical survey, Coord. Chem. Rev. 153 (1996) 257–284. https://doi.org/10.1016/0010-8545(95)01226-5.

[16] X. Li, J. Yu, M. Jaroniec, X. Chen, Cocatalysts for selective photoreduction of CO_2 into solar fuels, Chem. Rev. 119 (2019) 3962–4179. https://doi.org/10.1021/acs.chemrev.8b00400.

[17] K. Li, B. Peng, T. Peng, Recent Advances in Heterogeneous Photocatalytic CO_2 Conversion to Solar Fuels, ACS Catal. 6 (2016) 7485–7527. https://doi.org/10.1021/acscatal.6b02089.

[18] X. Chang, T. Wang, J. Gong, CO_2 photo-reduction: insights into CO_2 activation and reaction on surfaces of photocatalysts, Energy Environ. Sci. 9 (2016) 2177–2196. https://doi.org/10.1039/C6EE00383D.

[19] W.J. Ong, L.K. Putri, A.R. Mohamed, Rational Design of Carbon-Based 2D Nanostructures for Enhanced Photocatalytic CO_2 Reduction: A Dimensionality Perspective, Chem. - A Eur. J. 26 (2020) 9710–9748. https://doi.org/10.1002/chem.202000708.

[20] Q. Lu, K. Eid, W. Li, A.M. Abdullah, G. Xu, R.S. Varma, Engineering graphitic carbon nitride (g-C_3N_4) for catalytic reduction of $CO_2$to fuels and chemicals: Strategy and mechanism, Green Chem. 23 (2021) 5394–5428. https://doi.org/10.1039/d1gc01303c.

[21] N. Shehzad, M. Tahir, K. Johari, T. Murugesan, M. Hussain, A critical review on TiO_2 based photocatalytic CO_2 reduction system: Strategies to improve efficiency, J. CO2 Util. 26 (2018) 98–122. https://doi.org/https://doi.org/10.1016/j.jcou.2018.04.026.

[22] Z. Xiong, Z. Lei, Y. Li, L. Dong, Y. Zhao, J. Zhang, A review on modification of facet-engineered TiO_2 for photocatalytic CO_2 reduction, J. Photochem. Photobiol. C Photochem. Rev. 36 (2018) 24–47. https://doi.org/https://doi.org/10.1016/j.jphotochemrev.2018.07.002.

[23] C. Xin, M. Hu, K. Wang, X. Wang, Significant Enhancement of Photocatalytic Reduction of CO_2 with H_2O over ZnO by the Formation of Basic Zinc Carbonate, Langmuir. 33 (2017) 6667–6676. https://doi.org/10.1021/acs.langmuir.7b00620.

[24] Y. Pu, Y. Luo, X. Wei, J. Sun, L. Li, W. Zou, L. Dong, Synergistic effects of Cu_2O-decorated CeO_2 on photocatalytic CO_2 reduction: Surface Lewis acid/base and oxygen defect, Appl. Catal. B Environ. 254 (2019) 580–586. https://doi.org/10.1016/j.apcatb.2019.04.093.

[25] K. Yang, Z. Yang, C. Zhang, Y. Gu, J. Wei, Z. Li, C. Ma, X. Yang, K. Song, Y. Li, Q. Fang, J. Zhou, Recent advances in CdS-based photocatalysts for CO_2 photocatalytic conversion, Chem. Eng. J. 418 (2021) 129344. https://doi.org/10.1016/j.cej.2021.129344.

[26] Z. Zhao, H. Wang, Q. Yu, S. Roy, X. Yu, Photo-/electrocatalytic approaches to CO_2 conversion on Cu_2O-based catalysts, Appl. Catal. A Gen. 667 (2023) 119445. https://doi.org/10.1016/j.apcata.2023.119445.

[27] H. Dabhane, S. Ghotekar, P. Tambade, S. Pansambal, H.C.A. Murthy, R. Oza, V. Medhane, A review on environmentally benevolent synthesis of CdS nanoparticle and their applications, Environ. Chem. Ecotoxicol. 3 (2021) 209–219.

https://doi.org/10.1016/j.enceco.2021.06.002.

[28] H.N. Wang, Y.H. Zou, H.X. Sun, Y. Chen, S.L. Li, Y.Q. Lan, Recent progress and perspectives in heterogeneous photocatalytic CO_2 reduction through a solid–gas mode, Coord. Chem. Rev. 438 (2021). https://doi.org/10.1016/j.ccr.2021.213906.

[29] Q. Lu, K. Eid, W. Li, A.M. Abdullah, G. Xu, R.S. Varma, Engineering graphitic carbon nitride (g-C_3N_4) for catalytic reduction of CO_2 to fuels and chemicals: Strategy and mechanism, Green Chem. 23 (2021) 5394–5428. https://doi.org/10.1039/d1gc01303c.

[30] L. Cheng, Q. Xiang, Y. Liao, H. Zhang, CdS-Based photocatalysts, Energy Environ. Sci. 11 (2018) 1362–1391. https://doi.org/10.1039/c7ee03640j.

[31] J. Fu, B. Zhu, C. Jiang, B. Cheng, W. You, J. Yu, Hierarchical Porous O-Doped g-C_3N_4 with Enhanced Photocatalytic CO_2 Reduction Activity, Small. 13 (2017) 1–9. https://doi.org/10.1002/smll.201603938.

[32] Z. Zhu, J. Qin, M. Jiang, Z. Ding, Y. Hou, Enhanced selective photocatalytic CO_2 reduction into CO over Ag/CdS nanocomposites under visible light, Appl. Surf. Sci. 391 (2017) 572–579. https://doi.org/10.1016/j.apsusc.2016.06.148.

[33] M. Tahir, N.S. Amin, Indium-doped TiO_2 nanoparticles for photocatalytic CO_2 reduction with H_2O vapors to CH_2, Appl. Catal. B Environ. 162 (2015) 98–109. https://doi.org/10.1016/j.apcatb.2014.06.037.

[34] S. Wang, J. Zhan, K. Chen, A. Ali, L. Zeng, H. Zhao, W. Hu, L. Zhu, X. Xu, Potassium-Doped g-C_3N_4 Achieving Efficient Visible-Light-Driven CO_2 Reduction, ACS Sustain. Chem. Eng. 8 (2020) 8214–8222. https://doi.org/10.1021/acssuschemeng.0c01151.

[35] Y. Wang, Y. Xu, Y. Wang, H. Qin, X. Li, Y. Zuo, S. Kang, L. Cui, Synthesis of Mo-doped graphitic carbon nitride catalysts and their photocatalytic activity in the reduction of CO_2 with H_2O, Catal. Commun. 74 (2016) 75–79. https://doi.org/10.1016/j.catcom.2015.10.029.

[36] Z. Zhao, J. Fan, J. Wang, R. Li, Effect of heating temperature on photocatalytic reduction of CO_2 by N-TiO_2 nanotube catalyst, Catal. Commun. 21 (2012) 32–37. https://doi.org/10.1016/j.catcom.2012.01.022.

[37] S. Wan, M. Ou, X. Wang, Y. Wang, Y. Zeng, J. Ding, S. Zhang, Q. Zhong, Facile fabrication of oxygen and carbon co-doped carbon nitride nanosheets for efficient visible light photocatalytic H_2 evolution and CO_2 reduction, Dalt. Trans. 48 (2019) 12070–12079. https://doi.org/10.1039/c9dt02507c.

[38] Y. Hou, H. Guan, J. Yu, S. Cao, Potassium/oxygen co-doped polymeric carbon nitride for enhanced photocatalytic CO_2 reduction, Appl. Surf. Sci. 563 (2021) 150310. https://doi.org/10.1016/j.apsusc.2021.150310.

[39] M. Shen, L. Zhang, M. Wang, J. Tian, X. Jin, Carbon-vacancy modified graphitic carbon nitride: enhanced CO_2 photocatalytic reduction performance and mechanism probing, J.

Mater. Chem. A. 7 (2019) 1556–1563. https://doi.org/10.1039/c8ta09302d.

[40] M. Shen, L. Zhang, M. Wang, J. Tian, X. Jin, L. Guo, L. Wang, J. Shi, Carbon-vacancy modified graphitic carbon nitride: Enhanced CO_2 photocatalytic reduction performance and mechanism probing, J. Mater. Chem. A. 7 (2019) 1556–1563. https://doi.org/10.1039/c8ta09302d.

[41] X. Zhu, J. Yang, X. Zhu, J. Yuan, M. Zhou, X. She, Q. Yu, Y. Song, Y. She, Y. Hua, H. Li, H. Xu, Exploring deep effects of atomic vacancies on activating CO_2 photoreduction via rationally designing indium oxide photocatalysts, Chem. Eng. J. 422 (2021) 129888. https://doi.org/10.1016/j.cej.2021.129888.

[42] P. Xia, M. Antonietti, B. Zhu, T. Heil, J. Yu, S. Cao, Designing Defective Crystalline Carbon Nitride to Enable Selective CO_2 Photoreduction in the Gas Phase, Adv. Funct. Mater. 29 (2019) 1–9. https://doi.org/10.1002/adfm.201900093.

[43] M. Shen, M. Wang, Q. Wang, J. Tian, L. Zhang, L. Wang, J. Shi, A Ti-OH bond breaking route for creating oxygen vacancy in titania towards efficient CO_2 photoreduction, Chem. Eng. J. 425 (2021) 131513. https://doi.org/10.1016/j.cej.2021.131513.

[44] I.M. Hegazy, R.A. Geioushy, S.M. El-Sheikh, A. Shawky, S. El-Sherbiny, A.H.T. Kandil, Influence of oxygen vacancies on the performance of ZnO nanoparticles towards CO_2 photoreduction in different aqueous solutions, J. Environ. Chem. Eng. 8 (2020). https://doi.org/10.1016/j.jece.2020.103887.

[45] W. Tu, Y. Xu, J. Wang, B. Zhang, T. Zhou, S. Yin, S. Wu, C. Li, Y. Huang, Y. Zhou, Z. Zou, J. Robertson, M. Kraft, R. Xu, Investigating the Role of Tunable Nitrogen Vacancies in Graphitic Carbon Nitride Nanosheets for Efficient Visible-Light-Driven H_2 Evolution and CO_2 Reduction, ACS Sustain. Chem. Eng. 5 (2017) 7260–7268. https://doi.org/10.1021/acssuschemeng.7b01477.

[46] Z. Mo, X. Zhu, Z. Jiang, Y. Song, D. Liu, H. Li, X. Yang, Y. She, Y. Lei, S. Yuan, H. Li, L. Song, Q. Yan, H. Xu, Porous nitrogen-rich g-C_3N_4 nanotubes for efficient photocatalytic CO_2 reduction, Appl. Catal. B Environ. 256 (2019). https://doi.org/10.1016/j.apcatb.2019.117854.

[47] P. Zhang, S. Wang, B.Y. Guan, X.W.D. Lou, Fabrication of CdS hierarchical multi-cavity hollow particles for efficient visible light CO_2 reduction, Energy Environ. Sci. 12 (2019) 164–168. https://doi.org/10.1039/C8EE02538J.

[48] Y. Wang, L. Zhang, X. Zhang, Z. Zhang, Y. Tong, F. Li, J.C.S. Wu, X. Wang, Openmouthed B-SiC hollow-sphere with highly photocatalytic activity for reduction of CO_2 with H_2O, Appl. Catal. B Environ. 206 (2017) 158–167. https://doi.org/10.1016/j.apcatb.2017.01.028.

[49] Z. Shen, Q. Xia, Y. Li, C. Yin, Z. Ge, X. Li, Y. Wang, Adsorption-enhanced nitrogen-

doped mesoporous CeO_2 as an efficient visible-light-driven catalyst for CO_2 photoreduction, J. CO2 Util. 39 (2020) 2–7. https://doi.org/10.1016/j.jcou.2020.101176.

[50] L. Wang, Z. Zhang, Q. Han, Y. Liu, J. Zhong, J. Chen, J. Huang, H. She, Q. Wang, Preparation of CdS-P25/ZIF-67 composite material and its photocatalytic CO_2 reduction performance, Appl. Surf. Sci. 584 (2022) 152645. https://doi.org/10.1016/j.apsusc.2022.152645.

[51] N. Tian, H. Huang, X. Du, F. Dong, Y. Zhang, Rational nanostructure design of graphitic carbon nitride for photocatalytic applications, J. Mater. Chem. A. 7 (2019) 11584–11612. https://doi.org/10.1039/c9ta01819k.

[52] X. Liu, P. Wang, H. Zhai, Q. Zhang, B. Huang, Z. Wang, Y. Liu, Y. Dai, X. Qin, X. Zhang, Synthesis of synergetic phosphorus and cyano groups (–C[tbnd]N) modified g-C_3N_4 for enhanced photocatalytic H_2 production and CO_2 reduction under visible light irradiation, Appl. Catal. B Environ. 232 (2018) 521–530. https://doi.org/10.1016/j.apcatb.2018.03.094.

[53] H. Feng, Q. Guo, Y. Xu, T. Chen, Y. Zhou, Y. Wang, M. Wang, D. Shen, Surface Nonpolarization of g-C_3N_4 by Decoration with Sensitized Quantum Dots for Improved CO_2 Photoreduction, ChemSusChem. 11 (2018) 4256–4261. https://doi.org/10.1002/cssc.201802065.

[54] G. Zhao, W. Zhou, Y. Sun, X. Wang, H. Liu, X. Meng, K. Chang, J. Ye, Efficient photocatalytic CO_2 reduction over Co(II) species modified CdS in aqueous solution, Appl. Catal. B Environ. 226 (2018) 252–257. https://doi.org/10.1016/j.apcatb.2017.12.054.

[55] L. Zhu, Y. Liu, X. Peng, Y. Li, Y.-L. Men, P. Liu, Y.-X. Pan, Noble-metal-free CdS nanoparticle-coated graphene oxide nanosheets favoring electron transfer for efficient photoreduction of CO_2, ACS Appl. Mater. Interfaces. 12 (2020) 12892–12900. https://doi.org/10.1021/acsami.0c00163.

[56] L. Lin, C. Hou, X. Zhang, Y. Wang, Y. Chen, T. He, Highly efficient visible-light driven photocatalytic reduction of CO_2 over g-C_3N_4 nanosheets/tetra(4-carboxyphenyl)porphyrin iron(III) chloride heterogeneous catalysts, Appl. Catal. B Environ. 221 (2018) 312–319. https://doi.org/10.1016/j.apcatb.2017.09.033.

[57] M. Tahir, B. Tahir, N.A.S. Amin, Gold-nanoparticle-modified TiO_2 nanowires for plasmon-enhanced photocatalytic CO_2 reduction with H_2 under visible light irradiation, Appl. Surf. Sci. 356 (2015) 1289–1299. https://doi.org/10.1016/j.apsusc.2015.08.231.

[58] S.H. Liu, J.S. Lu, Y.C. Pu, H.C. Fan, Enhanced photoreduction of CO_2 into methanol by facet-dependent Cu_2O/reduce graphene oxide, J. CO2 Util. 33 (2019) 171–178. https://doi.org/10.1016/j.jcou.2019.05.020.

[59] C. Han, B. Wang, N. Wu, S. Shen, Y. Wang, Deep and selective photoreduction of CO_2

to CH_4 over ultrafine Pt nanoparticles-decorated SiC nanosheets, Appl. Surf. Sci. 515 (2020) 145952. https://doi.org/10.1016/j.apsusc.2020.145952.

[60] Z. Chai, Q. Li, D. Xu, Photocatalytic reduction of CO_2 to CO utilizing a stable and efficient hetero-homogeneous hybrid system, RSC Adv. 4 (2014) 44991–44995. https://doi.org/10.1039/c4ra08848d.

[61] J. Dong, Z. Wang, H. Cao, J. Xue, C. Liu, S. Sun, C. Gao, X. Zhu, J. Bao, Independent Cr_2O_3 functions as efficient cocatalyst on the crystal facets engineered TiO_2 for photocatalytic CO_2 reduction, Appl. Surf. Sci. 554 (2021) 149634. https://doi.org/10.1016/j.apsusc.2021.149634.

[62] S. Wang, X. Wang, Photocatalytic CO_2 reduction by CdS promoted with a zeolitic imidazolate framework, Appl. Catal. B Environ. 162 (2015) 494–500. https://doi.org/10.1016/j.apcatb.2014.07.026.

[63] B. Su, L. Huang, Z. Xiong, Y. Yang, Y. Hou, Z. Ding, S. Wang, Branch-like ZnS–DETA/CdS hierarchical heterostructures as an efficient photocatalyst for visible light CO_2 reduction, J. Mater. Chem. A. 7 (2019) 26877–26883. https://doi.org/10.1039/C9TA10470D.

[64] L. Zhang, L. Zhang, Y. Chen, Y. Zheng, J. Guo, S. Wan, S. Wang, C.K. Ngaw, J. Lin, Y. Wang, CdS/ZnO: A Multipronged Approach for Efficient Reduction of Carbon Dioxide under Visible Light Irradiation, ACS Sustain. Chem. Eng. 8 (2020) 5270–5277. https://doi.org/10.1021/acssuschemeng.0c00190.

[65] P. Li, X. Zhang, C. Hou, Y. Chen, T. He, Highly efficient visible-light driven solar-fuel production over tetra(4-carboxyphenyl)porphyrin iron(III) chloride using CdS/Bi_2S_3 heterostructure as photosensitizer, Appl. Catal. B Environ. 238 (2018) 656–663. https://doi.org/10.1016/j.apcatb.2018.07.066.

[66] D.O. Adekoya, M. Tahir, N.A.S. Amin, g-C_3N_4/(Cu/TiO_2) nanocomposite for enhanced photoreduction of CO_2 to CH_3OH and HCOOH under UV/visible light, J. CO2 Util. 18 (2017) 261–274. https://doi.org/10.1016/j.jcou.2017.02.004.

[67] X. Yang, W. Xin, X. Yin, X. Shao, Enhancement of photocatalytic activity in reducing CO_2 over CdS/g-C_3N_4 composite catalysts under UV light irradiation, Chem. Phys. Lett. 651 (2016) 127–132. https://doi.org/10.1016/j.cplett.2016.03.027.

[68] B. Pan, J. Qin, X. Wang, W. Su, Efficient self-assembly synthesis of $LaPO_4$/CdS hierarchical heterostructure with enhanced visible-light photocatalytic CO_2 reduction, Appl. Surf. Sci. 504 (2020) 144379. https://doi.org/10.1016/j.apsusc.2019.144379.

[69] C. Wang, Y. Zhao, H. Xu, Y. Li, Y. Wei, J. Liu, Z. Zhao, Efficient Z-scheme photocatalysts of ultrathin g-C_3N_4-wrapped Au/TiO_2-nanocrystals for enhanced visible-light-driven conversion of CO_2 with H_2O, Appl. Catal. B Environ. 263 (2020) 118314. https://doi.org/10.1016/j.apcatb.2019.118314.

[70] N.T. Thanh Truc, L. Giang Bach, N. Thi Hanh, T.D. Pham, N. Thi Phuong Le Chi, D.T. Tran, M.V. Nguyen, V.N. Nguyen, The superior photocatalytic activity of Nb doped TiO_2 /g-C_3N_4 direct Z-scheme system for efficient conversion of CO_2 into valuable fuels, J. Colloid Interface Sci. 540 (2019) 1–8. https://doi.org/10.1016/j.jcis.2019.01.005.

[71] Y. Wang, Z. Zhang, L. Zhang, Z. Luo, J. Shen, H. Lin, J. Long, J.C.S. Wu, X. Fu, X. Wang, C. Li, Visible-Light Driven Overall Conversion of CO_2 and H_2O to CH_4 and O_2 on 3D-SiC@2D-MoS_2 Heterostructure, J. Am. Chem. Soc. 140 (2018) 14595–14598. https://doi.org/10.1021/jacs.8b09344.

[72] J. Jin, J. Yu, D. Guo, C. Cui, W. Ho, A Hierarchical Z-Scheme CdS-WO3 Photocatalyst with Enhanced CO2 Reduction Activity, Small. 11 (2015) 5262–5271. https://doi.org/10.1002/smll.201500926.

[73] Y. Wei, J. Jiao, Z. Zhao, J. Liu, J. Li, G. Jiang, Y. Wang, A. Duan, Fabrication of inverse opal TiO_2-supported Au@CdS core-shell nanoparticles for efficient photocatalytic CO_2 conversion, Appl. Catal. B Environ. 179 (2015) 422–432. https://doi.org/10.1016/j.apcatb.2015.05.041.

[74] Y.J. Zhu, F. Chen, Microwave-assisted preparation of inorganic nanostructures in liquid phase, Chem. Rev. 114 (2014) 6462–6555. https://doi.org/10.1021/cr400366s.

[75] F. Mujeeb, P. Bajpai, N. Pathak, Phytochemical Evaluation, Antimicrobial Activity, and Determination of Bioactive Components from Leaves of Aegle marmelos, Biomed Res. Int. 2014 (2014) 1–11. https://doi.org/10.1155/2014/497606.

[76] A.K. Jha, K. Prasad, Biosynthesis of gold nanoparticles using bael (Aegle marmelos) leaf: mythology meets technology, Int. J. Green Nanotechnol. 3 (2011) 92–97. https://doi.org/10.1080/19430892.2011.574560.

[77] C. Zhu, C. Liu, Y. Zhou, Y. Fu, S. Guo, H. Li, S. Zhao, H. Huang, Y. Liu, Z. Kang, Carbon dots enhance the stability of CdS for visible-light-driven overall water splitting, Appl. Catal. B Environ. 216 (2017) 114–121. https://doi.org/10.1016/j.apcatb.2017.05.049.

[78] M.-Y. Qi, Q. Lin, Z.-R. Tang, Y.-J. Xu, Photoredox coupling of benzyl alcohol oxidation with CO_2 reduction over CdS/TiO_2 heterostructure under visible light irradiation, Appl. Catal. B Environ. Energy. 307 (2022) 121158.

[79] Y. Bai, M. Li, X. Liu, J. Han, X. Zhu, Q. Ge, H. Wang, Ti^{3+}Defective TiO_2/CdS Z-Scheme Photocatalyst for Enhancing Photocatalytic CO_2 Reduction to C1-C3 Products, Ind. Eng. Chem. Res. 61 (2022) 8724–8737. https://doi.org/10.1021/acs.iecr.2c01113.

CHAPTER 2

Materials and Methodology

This chapter outlines the experimental procedures, chemicals, and equipment used for catalyst characterization and product analysis. It also details the Density Functional Theory (DFT) calculations performed in this study. Any deviations or modifications from the methods described here are specified in the relevant chapters.

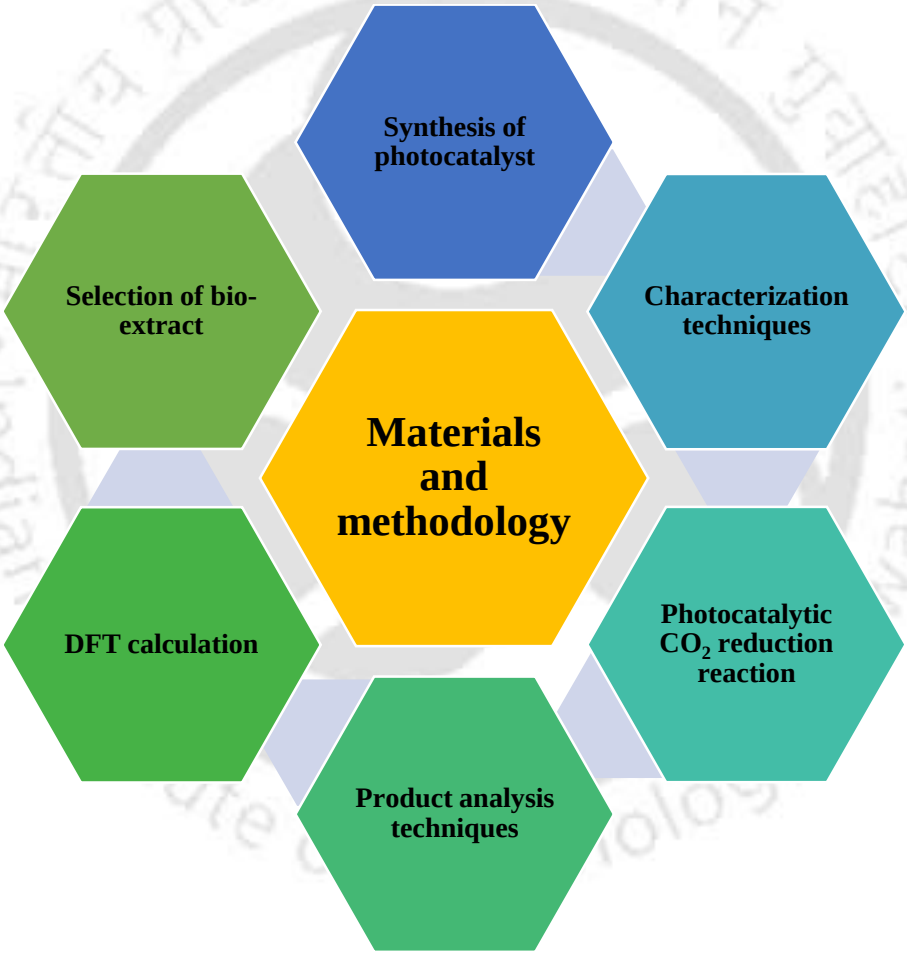

2.1 Chemicals and Reagents

Chemicals, reagents, and materials listed in **Table 2.1** were used as received without further purification unless otherwise specified. All the solutions were prepared using deionized water (DI) (resistivity: 18.2 MΩ.cm) obtained from the water purifier (Millipore, USA).

Table 2.1. List of chemicals, reagents, and materials used in this doctoral work.

Reagents/Chemicals	**Purity (%)**	**Grade**	**CAS/Catalogue no.**	**Make**
Cadmium chloride monohydrate ($CdCl_2.H_2O$)	99.99	AR	35658-65-2	Himedia, India
Sodium sulfide (Na_2S)	60	-	27610-45-3	Merck, India
Ethanol (C_2H_5OH)	99.99	ACS	64-17-5	
Dimethyl sulfoxide ($(CH_3)_2SO$)	99.9	ACS	67-68-5	
Thiourea (H_2NCSNH_2)	99.9	ACS	62-56-6	
Copper (II) sulfate pentahydrate ($CuSO_4.5H_2O$)	99	ACS	6046-93-1	
Tin (II) chloride dehydrate ($SnCl_2.2H_2O$)	98	ACS	10025-69-1	
Formic acid (HCOOH)	98-100	ACS	64-18-6	
Sodium sulfate anhydrous (Na_2SO_4)	99	ACS	7757-82-6	SRL, India
Cadmium acetate dehydrate ($Cd(CH_3COO)_2 \cdot 2H_2O$)	99.50	AR	5743-04-4	
Methanol (CH_3OH)	99.8	ACS	67-65-1	Sigma Aldrich, Germany
Indium (III) nitrate hydrate ($In(NO_3)_3 \cdot xH_2O$)	99.9	-	207398-97-8	

Deuterium oxide (D_2O)	99.9 atom% D	-	7789-20-0	Sigma Aldrich, USA
Nafion® D-521 dispersion	5%(w/w) in water and 1-propanol	-	31175-20-9	Alfa Aesar, USA
Triethanolamine ($C_6H_{15}NO_3$)	99.9	AR	102-71-6	Loba Chemie, India
Carbon dioxide (CO_2)	99.9	-	-	Assam Air Product Pvt. Ltd., India
Nitrogen (N_2)	99.9	-	-	
Carbon monoxide (CO)	99.9	-	-	
Hydrogen (H_2)	99.9	-	-	

2.2 Biomass and bio-extract

2.2.1 Selection of *Aegle Marmelos* leaves extract

The fresh *Aegle Marmelos* leaves were collected from the plants naturally grown at the Indian Institute of Technology Guwahati campus, Assam, India. The local name of *Aegle Marmelos* is 'Bael,' and it is abundantly present in India, Pakistan, Bangladesh, Sri Lanka, Nepal, Malaysia, Myanmar, Thailand, and most of the East Asian countries. The abundance of active phytochemicals in *Aegle marmelos* from various geographical locations—identified through mass spectrometry as flavonoids, alkaloids, tannins, phenols, saponins, etc., along with their concentrations, is summarized in **Table 2.2** [1]. It has been reported that the parts of the plant contain natural phytochemicals such as phenol, flavonoids, alkaloids, tannins, saponins, steroids, proteins, amino acids, etc, which have been used to reduce the metal ions to their corresponding nanoparticles [2]. There are recent reports for the synthesis of Ag and Au nanoparticles (NPs) using plant-based phytochemicals extracted from *Aegle marmelos* [3,4]. These studies also served as the foundation for selection of *Aegle marmelos* for the synthesis of CdS nanorods (CdS(bio) NRs), CdS NPs(CdS(bio) NPs), CdS quantum dots (CdS QDs(bio)), CuO quantum dots (CuO QDs(bio)), In_2O_3 NPs (In_2O_3(bio) NPs), and SnO_2 NPs (SnO_2(bio) NPs) for photocatalytic CO_2 reduction reaction (PCO_2RR) in the present study.

Table 2.2. Active phytochemical constituents of *Aegle marmelos* plants and plant organs.

Plants	**Alkaloids (mg/g)**	**Flavonoids (mg/g)**	**Phenols (mg/g)**	**Saponins (mg/g)**	**Tannins (mg/g)**	**Proteins (mg/g)**
Aegle Marmelos	16.08	63.9	29.4	11.98	8.38	-

2.2.2 Preparation of *Aegle Marmelos* leaves extract

Fresh *Aegle marmelos* leaves (10 g) were collected and washed thoroughly under running water for 10 min to eliminate dust particles, followed by a final wash with distilled water. The leaves were cut into small pieces and placed in a beaker with 100 mL of 50% ethanol (EtOH), then stirred at 70°C until the solution acquired a dark green color [5]. After cooling, the extract was filtered through a nylon filter and stored for further use. The quantitative assay of phytochemical contents in *Aegle marmelos* was performed following previously reported methods [1,6]. The results are presented in **Table 2.3**. Phytochemical concentrations are expressed as mg of standard equivalents per g of dry leaves. For example, rutin was used as the standard for flavonoid quantification. The analytes identified in *Aegle marmelos* by HRMS (**Figure 2.1**) are summarized in **Table 2.4**. A flavonoid fraction of 3,5-dihydroxy-6-methyl-2H-pyran-4(3H)-one was rich in the bio-extract, and it could act as a reducing and capping agent for catalysts synthesis. The calibration graph of the rutin standard is shown in **Figure 2.2**. The flavonoid fraction concentration in bio-extract was measured in different seasons, with a concentration of 27-28 mg/g, and it was uniformly maintained across the different batches of experiments.

Table 2.3. Quantitative analysis of phytochemicals (mg/g) present in bio-extract.

Aegle marmelos (bael) type	**Alkaloids**	**Tannins**	**Flavonoids**	**Phenol**	**Saponins**
Rutaceae	9.28	5.62	27.00	14.44	11.23

Table 2.4. Active analytes /compounds present in *Aegle marmelos* identified using mass spectroscopic analysis.

Compounds	Chemical structure	m/z (HRMS)	m/z (structure proposed)	Mass error (mol/g)
4H-Pyran-4- one, 2,3-dihydro-3,5-dihydroxy-6-methyl-($C_6H_8O_4$) [Flavonoids fraction]	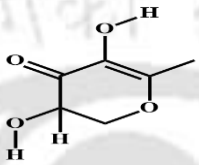	144.04	144.10	0.06
((2R,3S,4S,5R,6S)-3,4,5-trihydroxy-6-((5-hydroxy-2-(4-hydroxyphenyl)-4-oxo-4H-chromen-7-yl)oxy)tetrahydro-2H-pyran-2-yl)methyl acetate ($C_{23}H_{22}O_{11}$)	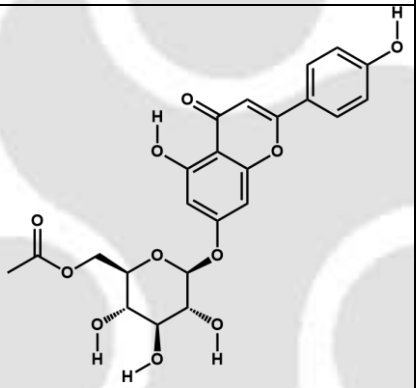	475.3260	475.12	0.2
1,8,15,22,29,36-hexaazacyclodotetracontane-2,7,16,21,30,35-hexone($C_{36}H_{66}N_6O_6$)	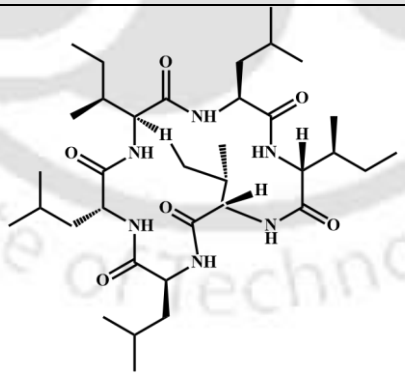	701.4939	701.49	0
Auraptene($C_{19}H_{22}O_3$)	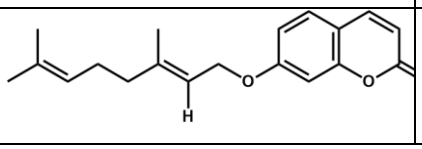	299.1102	299.11	0

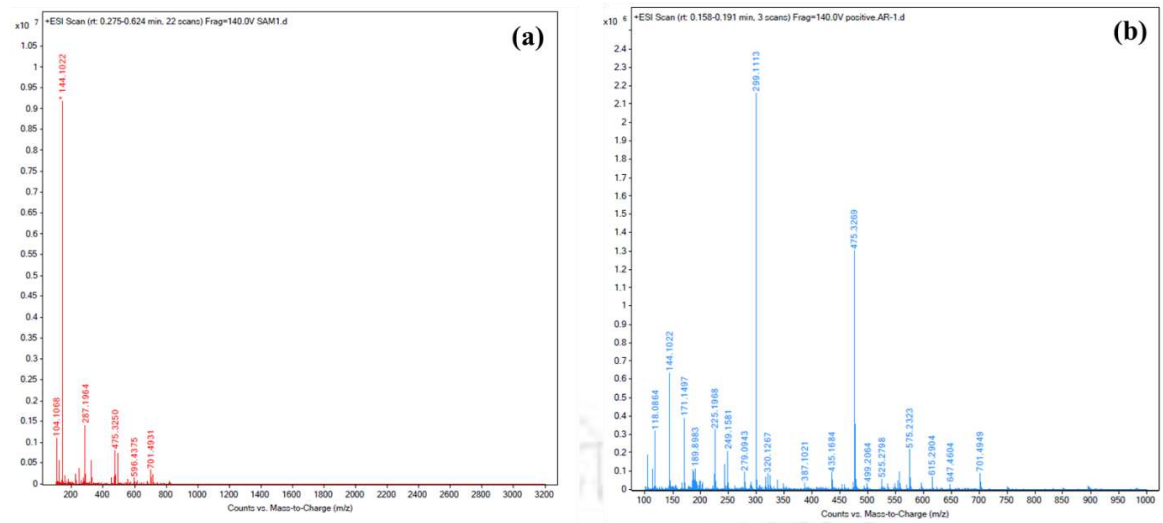

Figure 2.1. HRMS spectra of *Aegle marmelos* extract (a) Before reaction and (b) After reaction showing different bio-constituents present in the extract.

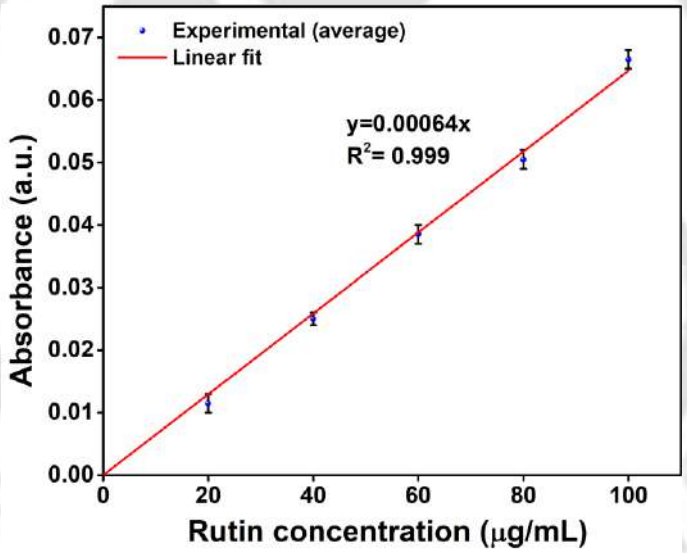

Figure 2.2. Calibration graph of rutin standard.

2.3 Methodologies of photocatalyst synthesis

2.3.1 Bioinspired synthesis of CQDs/CdS nanocomposite

2.3.1.1 Synthesis of CdS(bio) nanorods using bio-extract

A 0.1 M solution of $CdCl_2$ was placed in a beaker, followed by the dropwise addition of a 0.1 M Na_2S solution and 20% (v/v) bio-extract under continuous stirring [7]. The resulting solution was transferred into a microwave reactor (Discover System, CEM Matthews NC, USA) and irradiated for 5 min at 100°C. The precipitate was centrifuged (5000 rpm, 5 min)

and washed numerous times using distilled water and 50% (v/v) ethanol. The obtained yellow residue was oven-dried for 12 h at 65°C to recover CdS(bio) nanorods. The control synthesis of CdS(con) was done at the experimental condition (optimized using bio-extract), using distilled water instead of bio-extract. The schematic of CdS(bio) nanorod synthesis is given in **Figure 2.3**.

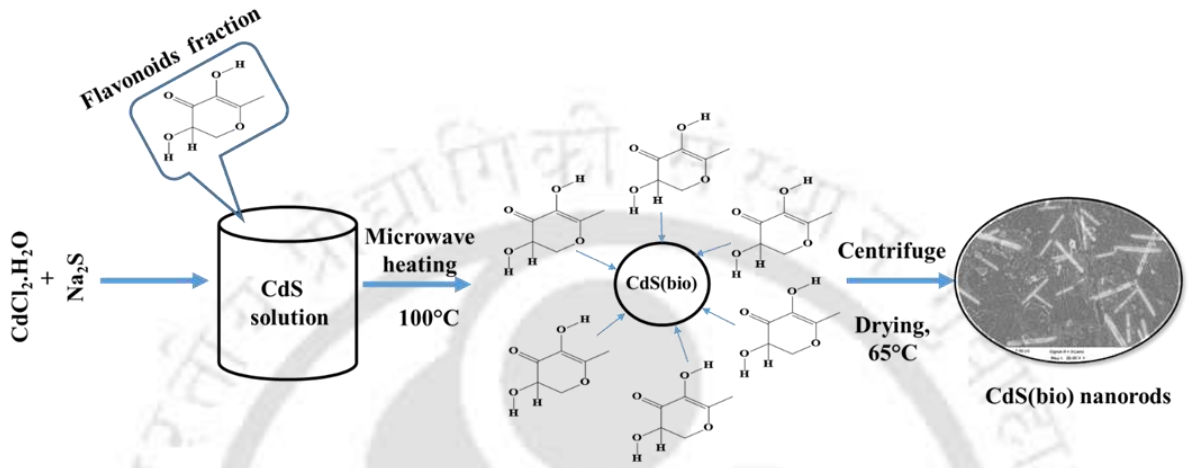

Figure 2.3. Possible schematic synthesis mechanism of CdS(bio) nanorods using flavonoid fraction of 4H-Pyran-4- one, 2,3-dihydro-3,5-dihydroxy-6-methyl- present in *Aegle marmelos*.

2.3.1.2 Synthesis of CQDs(bio) using waste orange peels

Orange peels were purchased from the fruit market located at IIT Guwahati. Firstly, orange peels were thoroughly washed in tap water, dried in sunlight, and then ground into powder (20-40 μm, **Figure 2.4**) using a grinder-mixer. A quantity of 1 g of obtained powder was mixed with 40 mL distilled water, and the mixture was stirred for 15 min to obtain a homogeneous suspension. Then, the solution was placed in a Teflon-line hydrothermal reactor and heated at 180°C for 12 h [8]. After reaching room temperature, the solution was centrifuged (5000 rpm, 10 min) to separate residues and then filtered using a 0.2 μm PTFE filter. The CQDs residue (10 mg/mL) was stored for further use. The primary constituents of orange peel powder were determined by CHNSO analysis to be carbon (43%), hydrogen (5%), nitrogen (3%), sulfur (0%), and oxygen (49%). For the synthesis of carbon quantum dots (CQDs), a uniform carbon content of 43 % (w/w) was maintained across different batches of experiments.

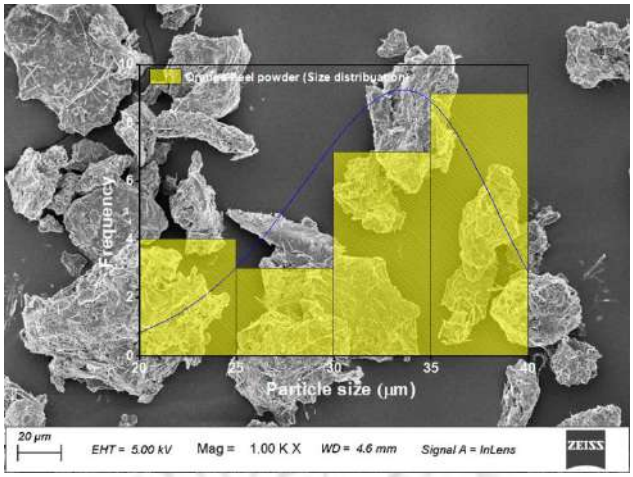

Figure 2.4. FESEM image of orange peel powder.

2.3.1.3 Synthesis of CQDs/CdS(bio) composites

A facile deposition method was used to prepare CQDs/CdS(bio) nanocomposites (**Figure 2.5**). Firstly, a known quantity of CQDs (0.25, 0.50, 0.75, and 1% w/w) was mixed in a 50 mL aliquot using distilled water in a beaker. Then, 100 mg CdS(bio) nanorods were added to this dispersion, and the mixture was stirred at room temperature for 12 h. The solution was then centrifuged and left to dry overnight in an oven [9].

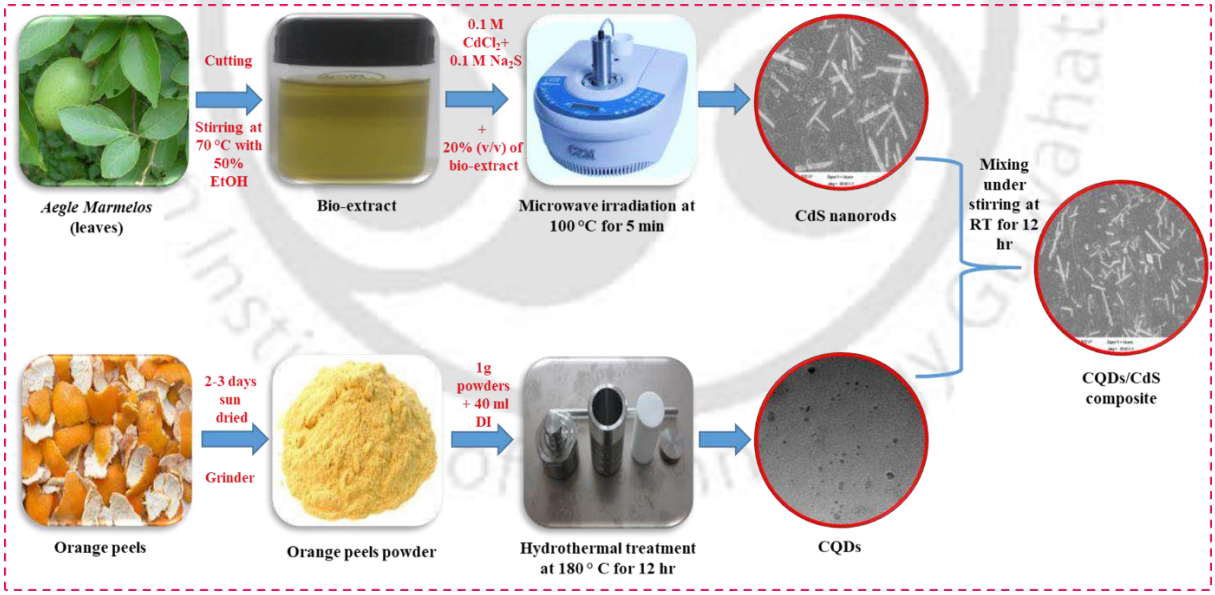

Figure 2.5. Schematic representation of CQDs/CdS(bio) composites synthesis using a simple deposition approach.

2.3.2 Bioinspired synthesis of In_2O_3/CdS heterostructure

2.3.2.1 Synthesis of CdS(bio) NPs

First, 10 mL of thiourea solution (0.1M) was added to an equal volume of cadmium acetate (0.1 M) with constant stirring [10]. Subsequently, 5 mL of bio-extract was gradually added to the above solution. The resulting mixture underwent irradiation in a microwave reactor at 100°C for 5 min. The solution was centrifuged and washed repeatedly with DI water and 50% (v/v) EtOH. The resulting solution was then oven-dried at 65°C for 12 h to obtain CdS(bio) NPs. For a control synthesis of CdS(con), DI water was used instead of bio-extract under optimal experimental conditions.

2.3.2.2 Synthesis of In_2O_3(bio) NPs

A 5 mL *Aegle marmelos* extract was mixed with 5 mL of $In(NO_3)_3 \cdot H_2O$ (0.1 M) solution under constant stirring. Subsequently, the solution was moved to a microwave reactor and irradiated at 120°C for 5 min. Afterward, the solution underwent centrifugation (6000 rpm for 8 min) and repeated washing with DI water. The resulting residue was oven-dried at 80°C overnight, crushed into powder, and subjected to calcination for 2 h at 400°C [11]. A control synthesis of In_2O_3(con) was conducted using DI water instead of the bio-extract under the same optimal experimental conditions.

2.3.2.3 Synthesis of In_2O_3/CdS(bio) NPs heterostructures

A volume of 10 mL of thiourea solution (0.1 M) was added to an equal volume of cadmium acetate solution (0.1 M) with constant stirring. Then, 10 mL of $In(NO_3)_3.H_2O$ (0.1 M) solution was added dropwise to the mixture, followed by 7.5 mL of the bio-extract. The resulting mixture was transferred to a microwave reactor and irradiated at 100°C for 5 min. The solution underwent centrifugation at 8000 rpm for 8 min to eliminate the residue, followed by multiple washes with DI water and 50% (v/v) EtOH. Afterward, the sample was oven-dried overnight at 80°C (**Figure 2.6**). The dried residue was pulverized into powder and subjected to calcination at 150°C for 4 h. The calcination temperature is selected based on the mass loss vs. temperature curve obtained from the thermogravimetric analyzer (TGA) analysis. In_2O_3/CdS heterostructures with various molar ratios of In_2O_3 (0.2, 0.4, 0.6, 0.8, and 1.0) were synthesized using this procedure. The corresponding catalysts are designated as $0.2In_2O_3$/CdS(bio), $0.4In_2O_3$/CdS(bio), $0.6In_2O_3$/CdS(bio) $0.8In_2O_3$/CdS(bio), and $1.0In_2O_3$/CdS(bio).

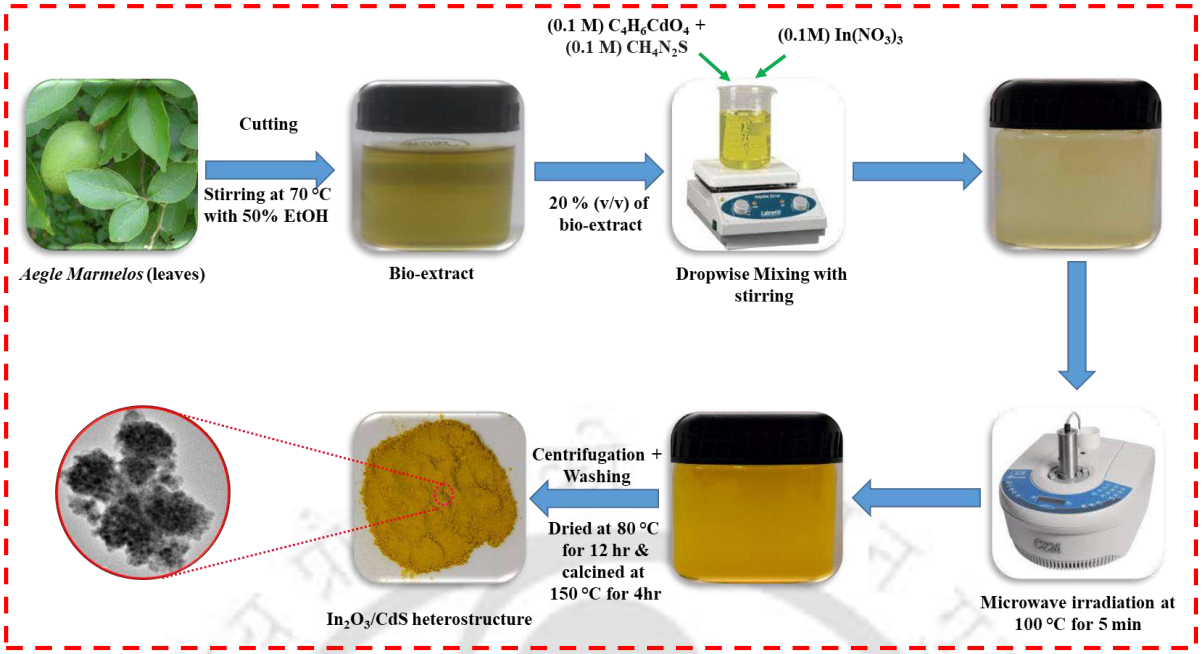

Figure 2.6. Process schematic of In_2O_3/CdS(bio) heterostructures synthesis with a combination of vegetal extract and microwave irradiation process.

2.3.3 Bioinspired synthesis of CDs/CdS QDs composites

2.3.3.1 Synthesis of CdS QDs(bio), CDs(bio), and CDs/CdS QDs(bio)

To synthesize CdS QDs(bio), A 0.1 M solution of $CdCl_2$ was placed in a beaker, followed by the dropwise addition of a 0.1 M Na_2S solution and 20% (v/v) bio-extract under continuous stirring [12]. The resulting mixture underwent microwave irradiation at 100°C for 5 min, followed by centrifugation, washing, and drying at 80°C for 15 h to obtain CdS QDs(bio). For comparison, CdS QDs(con) were synthesized using DI water instead of bio-extract under the same conditions.

A weight of 1 g of the *orange peel* powder (20-40 µm) was mixed with 40 mL of DI water, stirred for 10 min for homogeneity, and subsequently transferred to a PTFE-lined hydrothermal reactor. The mixture was heated at 180°C for 12 h [9]. After cooling, the resulting solution was centrifuged at 5000 rpm for 8 min and filtered through a 0.2 µm Teflon filter to remove residues. The resulting CDs (15 mg/mL) were stored for future use. CHNSO analysis revealed that orange peel powder consists mainly of carbon (53.84%), hydrogen (5.86%), nitrogen (1.54%), sulfur (6.41%), and oxygen (35.35%). Carbon content was maintained consistently at 53.84% (w/w) during the synthesis of CDs(bio) across various experimental batches.

A straightforward deposition technique was employed for CDs/CdS QDs(bio) composites synthesis. First, a dispersion of 1 mg/mL CDs was prepared by mixing the

synthesized carbon dots with water. Then, 200 mg of CdS QDs(bio) was added to a definite volume of CDs dispersion, and the mixture was stirred for 12 h (**Figure 2.7**). Afterward, the resulting solution underwent centrifugation and was dried overnight in an oven at 80°C [8]. Using this approach, CDs/CdS QDs(bio) composites with different mass ratios of CDs (0.2, 0.4, 0.6, 0.8, and 1% w/w) were synthesized, labeled as 0.2CDs/CdS QDs(bio), 0.4CDs/CdS QDs(bio), 0.6CDs/CdS QDs(bio), 0.8CDs/CdS QDs(bio), and 1.0CDs/CdS QDs(bio).

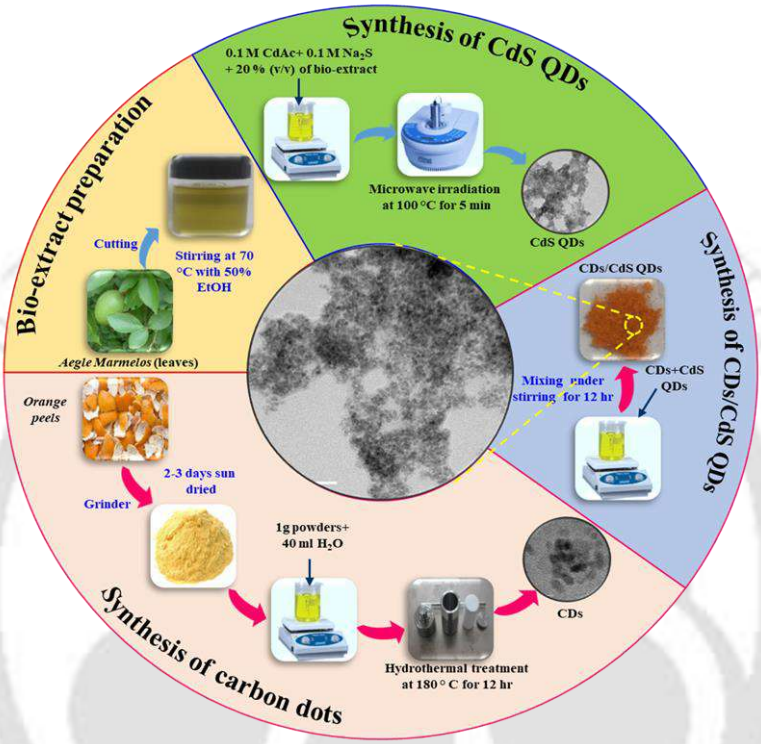

Figure 2.7. Schematic synthesis route of CDs/CdS QDs(bio) composites.

2.3.4 Bioinspired synthesis of SnO_2/CdS heterostructures

2.3.4.1 Synthesis of CdS QDs(bio)

Aegle marmelos vegetal leaves extract was prepared following our previous study [12]. To synthesize CdS QDs(bio), 0.1 M of sodium sulfide (10 mL) solution was added dropwise to 0.1 M solution of cadmium acetate (10 mL) under constant stirring at 300 rpm [10]. Subsequently, 5 mL of the extract was introduced dropwise into the resulting mixture. The solution was transferred to a microwave reactor (MR) (Discover system, CEM Matthews NC, USA) and irradiated at 100°C for 5 min. After centrifugation at 7500 rpm for 10 min thorough washing with DI water and 50% EtOH, the yellow residue was dried at 80°C for 15 h to obtain CdS QDs(bio). For comparison, CdS(con) was also synthesized under identical conditions without the bio-extract.

2.3.4.2 Synthesis of SnO_2 NPs

A 10 mL volume of 0.1 M Tin(II) chloride solution was sonicated (GT-1990QTS, GTSONIC, ultrasonic power 200 W, frequency 33/40 kHz, China) for 15 min before it was mixed with 5 mL of the bio-extract. The resulting mixture was moved to the MR and heated at 100 °C for 10 min. Subsequently, the solution was centrifuged at 10000 rpm for 10 min, repeatedly washed with DI water and 50% EtOH, and dried at 80 °C for 12 h. The dried material was ground into a fine powder with a particle size of 7.6 nm and calcined at 550°C for 2 h in a muffle furnace (NU-126, Navyug®, India). The calcination temperature was selected based on thermogravimetric analysis (TGA). For comparison, SnO_2(con) was synthesized under identical conditions using DI water.

2.3.4.3 Synthesis of SnO_2/CdS QDs(bio) heterostructure

A volume of 10 mL of 0.1 M sodium sulfide solution was added to an equal volume of 0.1 M cadmium acetate solution with constant stirring. Then, a volume of 10 mL sonicated solution of 0.1 M Sn(II) chloride was added dropwise, followed by 7.5 mL of the bio-extract. The mixture was transferred to an MR and irradiated at 100 °C for 5 min. The solution was centrifuged and then washed multiple times with DI water and 50% EtOH. Afterward, the sample was oven-dried overnight at 80 °C, and ground into powder, calcined at 150°C for 4 h (**Figure 2.8**). Using this approach, SnO_2/CdS heterostructures with varying SnO_2 molar ratios (0.25, 0.50, 0.75, and 1.00) were synthesized, labeled as 0.25SnO_2/CdS QDs(bio), 0.50SnO_2/CdS QDs(bio), 0.75SnO_2/CdS QDs(bio), and 1.00SnO_2/CdS QDs(bio), respectively.

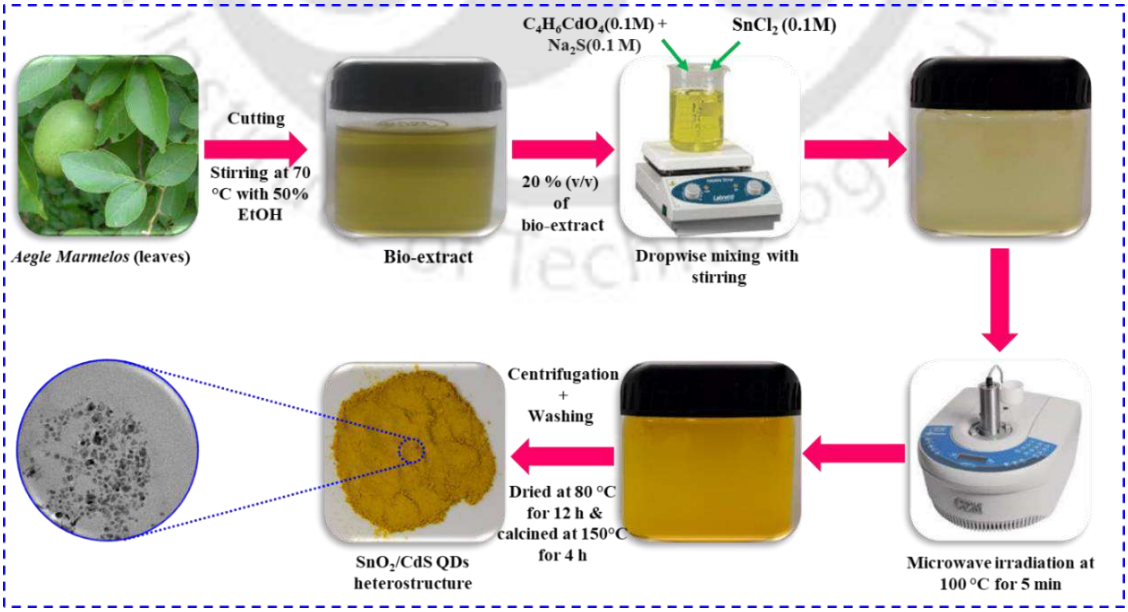

Figure 2.8. Schematic illustration of the bio-based synthesis route of SnO_2/CdS QDs(bio) heterostructures.

2.3.5 Bioinspired synthesis of CuO/CdS heterostructure

2.3.5.1 Synthesis of CdS QDs(bio)

To synthesize CdS QDs(bio) QDs, 0.1 M of sodium sulfide (10 mL) was added dropwise to 0.1 M solution of cadmium acetate (10 mL) under constant stirring [10], followed by the addition of 5 mL of the extract. The resulting mixture was moved to a microwave reactor and irradiated at 100°C for 5 min. After centrifugation and washing with DI water and 50% EtOH, the residue was dried at 80°C for 15 h to obtain CdS(bio) QDs. For comparison, CdS(con) was synthesized using DI water in place of bio-extract under the same conditions.

2.3.5.2 Synthesis of CuO QDs(bio)

A 5 mL volume of bio-extract was added dropwise to 10 mL of (0.1M) copper (II) sulfate solution under stirring. The mixture's pH was adjusted from 3.6 to 12 using a 2 M NaOH solution [13]. The resulting solution was irradiated in a microwave at 100°C for 10 min. After that, the solution was centrifuged at 9000 rpm for 10 min, washed with water and 50% EtOH, dried at 80°C for 15 h, crushed into powder, and calcined at 550°C for 5 h. The calcination temperature is determined based on thermogravimetric analysis (TGA). For comparison, CuO(con) was synthesized using DI water, keeping the conditions the same.

2.3.5.3 Synthesis of CuO/CdS QDs(bio) heterostructure

A volume of 10 mL of sodium sulfide solution (0.1 M) was added to an equal volume of cadmium acetate solution (0.1 M) with constant stirring. Then, 10 mL of copper (II) sulfate solution (0.1 M) was added dropwise to the mixture, followed by 7.5 mL of the bio-extract. The resulting mixture was transferred to a microwave reactor and irradiated at 100°C for 5 min. The solution was centrifuged at 10000 rpm for 12 min to eliminate the residue, followed by multiple washes with DI water and 50% EtOH. Afterward, the sample was oven-dried overnight at 80°C (**Figure 2.9**). Using this approach, CuO/CdS heterostructures with different molar ratios of CuO (0.25, 0.50, 0.75, and 1.00) were synthesized, labeled as 0.25CuO/CdS QDs(bio), 0.50CuO/CdS QDs(bio), 0.75CuO/CdS QDs(bio), and 1.00CuO/CdS QDs(bio).

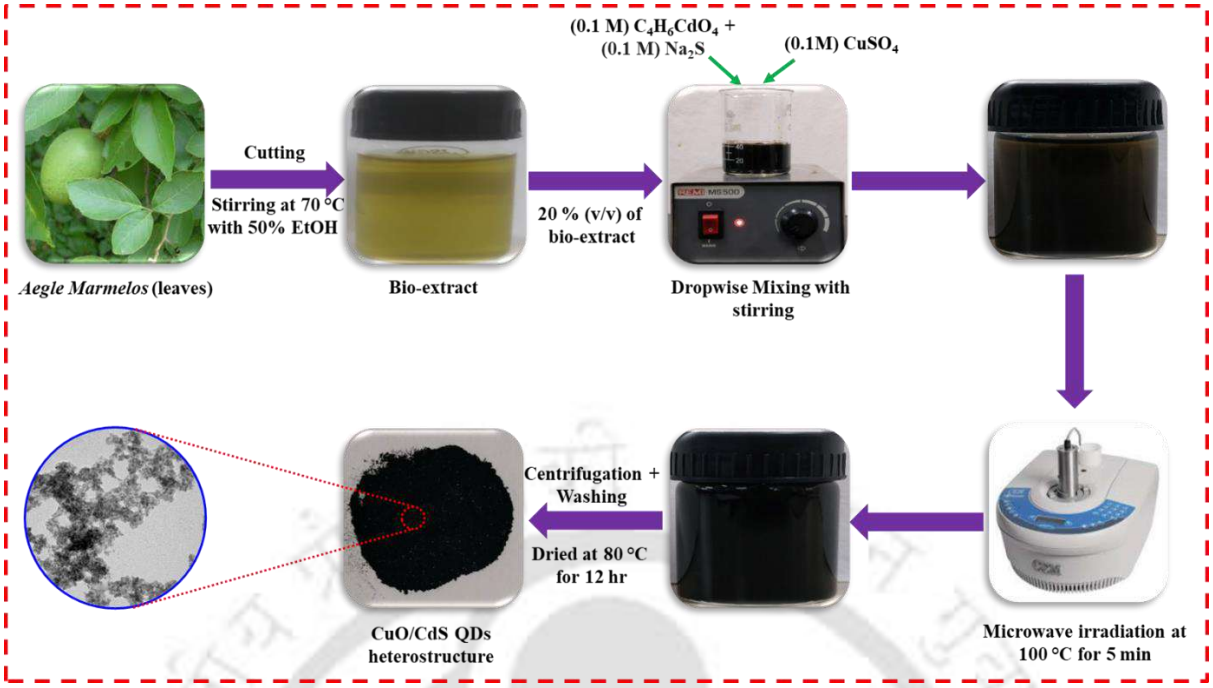

Figure 2.9. Schematic representation of bioinspired synthesis of CuO/CdS QDs(bio) heterostructures.

2.4 Characterizations of photocatalysts

2.4.1 UV-vis spectroscopy

UV-diffuse reflectance spectra (UV-DRS) and absorption spectra were obtained using a spectrophotometer (UV-2600, Shimadzu, Japan) in the range of 200 - 700 nm, with $BaSO_4$ as a reference. For the analysis, a thin and uniform layer of $BaSO_4$ powder was evenly spread over the sample holder, followed by an even layer of the catalyst sample on the top.

2.4.2 High-resolution mass spectroscopy

The mass spectra of *Aegle marmelos* leave extract were obtained using a high-resolution mass spectrometer (HRMS, G1969A, Agilent, USA) in positive ion mode. Bio-extract was first diluted with DI water and filtered through a 0.2 μm membrane filter. After that, the mass spectra of active phytochemicals present in *Aegle marmelos* leaves extract were captured.

2.4.3 X-ray diffraction

The crystallinity and phase structure of synthesized catalysts were characterized using a powder X-ray diffractometer (XRD, Smart lab, Rigaku, Japan) with Cu Kα radiation

(λ=1.540 Å) in 2θ range of 5 - 80° at a scan rate of 20° min^{-1}. About 20 mg of catalyst powder was placed in the sample holder, and the XRD pattern was recorded.

2.4.4 Field emission scanning electron microscopy

The morphological characteristics of catalyst particles, including particle sizes and shapes, were imaged using a field emission scanning electron microscope (FESEM, Sigma 300, Zeiss, Germany) equipped with a Fe cathode electron gun and In-lens detector, operated under a system vacuum of 1.2×10^{-5} mbar. For FESEM analysis, an amount of 1 mg of catalyst powder was dispersed on carbon tape, followed by gold coating onto it.

2.4.5 Field emission transmission electron microscopy

The particle size and morphology of the catalyst were also analysed by a field emission transmission electron microscope (FETEM, JEM2100F, JEOL, Japan) with a ZrO/W(100) Schottky electron gun, operated at a background pressure of 5.8×10^{-5} mbar. For sample preparation, 0.5 mg of catalyst was mixed with 2 mL DI water and sonicated for 45 min. An 8 µL aliquot of the resulting suspension was drop-cast onto a TEM grid, which was then dried overnight at 50°C before analysis. FETEM analysis was also employed to get the information on the fringe width (from HRTEM data) and crystallinity (from selected area electron diffraction data) of the catalysts.

2.4.6 Energy-dispersive X-ray spectroscopy

The catalyst's surface elemental composition was analyzed by energy-dispersive X-ray spectroscopy (EDS, Sigma 300, Zeiss, Germany). Sample preparation followed the same procedure as described for the FESEM analysis.

2.4.7 BET surface area analysis

The surface area of synthesized catalysts was determined using a BET analyzer (Micromeritics, Tristar-II 3020, USA) by N_2 sorption isotherm technique. A quantity of 70-80 mg of catalyst powder was degassed at 150°C for 5 h before analysis. The parameters, such as pore volume and pore size, were obtained from the BET Analysis.

2.4.8 X-ray photoelectron spectroscopic analysis

The elemental composition, valence state, and valence band position of catalysts were analyzed by using X-ray photoelectron spectroscopy (XPS, PHI 5000 Versa Probe III,

ULVAC-PHI, USA) with the Al Kα (1486.6 eV) as an X-ray source (1486.6 eV). XPS spectra were generated using XPSPEAK41 software.

2.4.9 Thermogravimetric analysis

The thermal stability of synthesized catalysts was analyzed by thermogravimetric analysis (TGA 209 F1, Netzch, Germany). For this analysis, a sample quantity of 8-10 mg was used and heated in the temperature range of 25 to 1000°C with a N_2 flow rate of 20 mL/min and a heating rate of 10°C/min.

2.4.10 Photoluminescence spectroscopy

Photoluminescence (PL) spectra were analyzed by a fluorescence spectrophotometer (Fluromax-4, Horiba Jobin Yvon, Japan) to explore e^-/h^+ carriers dynamics and its trapping efficiency. A catalyst mass of 2 mg was dispersed in DI water and sonicated for 30 min. After sonication, the PL spectra were recorded at the excitation wavelength specific to a catalyst as mentioned in the respective chapter.

2.4.11 Time-resolved photoluminescence spectroscopy

The time-resolved photoluminescence (TRPL) (FLS 1000, Eddinburg Instrument, UK) spectra were recorded to comprehend e^-/h^+ carrier behaviour with 1000 counts. TRPL spectra were recorded based on the excitation and emission wavelengths specific to a catalyst, as mentioned in the respective chapter. TRPL curve fitting was done with an exponential decay function to calculate the average e^-/h^+ carrier lifetime.

2.4.12 Zeta potential and particle size measurement

The hydrodynamic diameter and zeta potential of catalyst particles were obtained using dynamic light scattering technique (DLS, Litesizer TM 500, Anton Paar, USA). For this analysis, 2 mg catalyst powder was dispersed in 10 mL DI water (pH 7.5), and then the mixture was sonicated for 30 min. After that, particle size and zeta potential values were recorded.

2.4.13 High-pressure gas sorption analyzer

CO_2 adsorption capacity was studied using a high-pressure gas sorption analyzer (SorbHP1-XKRLSPN100, Quantachrome Instrument, Austria) at a pressure range of 0.1 to 1 bar.

2.5 Photocatalytic CO_2 reduction reaction experiment

PCO_2RRs experiments were conducted in a quartz reactor cell (50 mL) with a sealed headspace under visible light illumination under constant stirring (**Figure 2.10**). A 250 W metal halide (MH) lamp (λ >420 nm, Halonix Technologies, India) provided a light intensity of 3.51W/m^2 and a photon flux of 8.12 ×10^{18} photons/m^2. s. The MH lamp emitted primarily visible light (96.8%), with some infrared (3.2%) IR and no ultraviolet radiation [12]. The solution temperature (30°C) was maintained by a water circulation system. For each experiment, 20 mg of catalyst was mixed into 20 mL aqueous solution and sonicated for 15 min to prevent particle aggregation. The mixture was degassed with N_2 gas at a rate of 20 mL/min for 15 min, followed by CO_2 purging at 10 mL/min under constant stirring until saturation. The concentration of CO_2 was monitored using an Ion-selective electrode (PS-3517, Thermo Scientific, USA). Samples were periodically collected during irradiation and analyzed via HPLC, GC, and NMR spectroscopy to identify PCO_2RR products. Three control experiments were carried out to determine the carbon source involved in the formation of products: one with a catalyst, DI water, and light without CO_2; another with a catalyst, DI water, and CO_2 but with the lamp off; and a third with DI water, CO_2, and light but excluding the catalyst. To investigate the impact of carbonaceous material present on catalysts in PCO_2RR [12,14], a control experiment was conducted under optimal conditions for 10 h. Instead of CO_2, a 30-min N_2 purge at a flow rate of 10 mL/min was carried out in the dark conditions. Subsequently, the experiment was irradiated with light under continuous N_2 flow for 10 h, with samples collected at 5 h intervals.

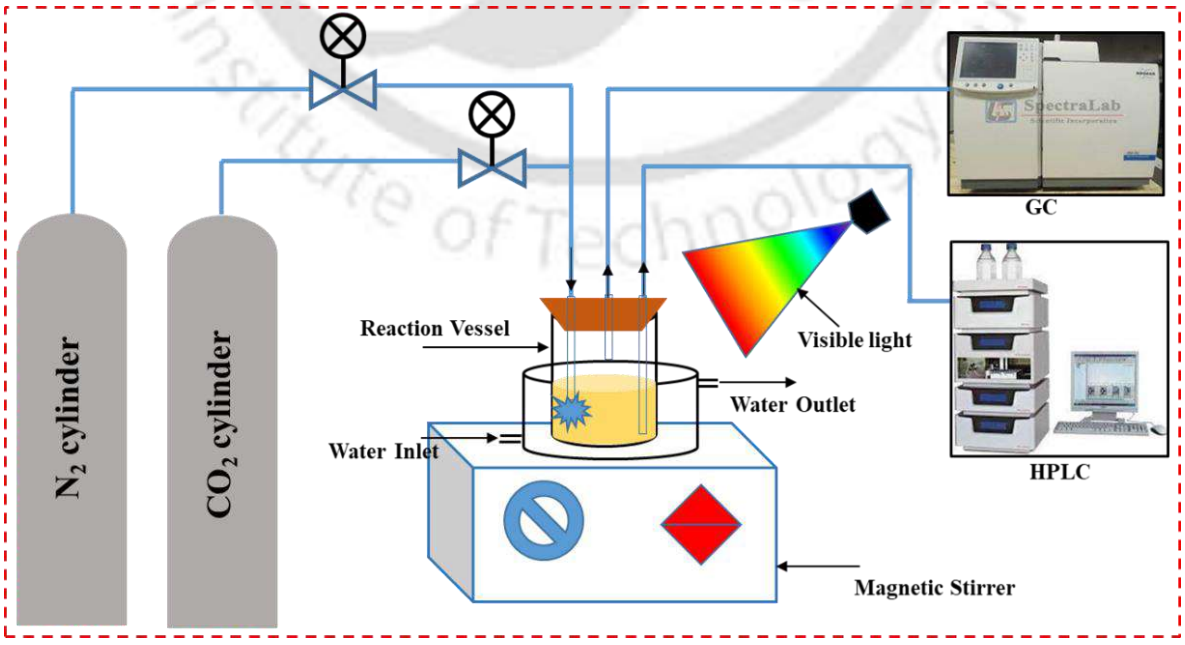

Figure 2.10. Schematic experimental setup of PCO_2R employed in this study.

2.6 PCO_2RR product analysis techniques

2.6.1 Gas chromatography (GC)

The gas sample was analyzed by Gas chromatography (450GC, Bruker, USA) equipped with a 60/80 Carboxen 1000 (15ft× 1/8in × 2.1mm) column and TCD detector. The oven temperature was initially held at 35°C for 6 min and then raised to 220°C at a rate of 20°C/ min. The temperature of the detector and injector were maintained at 200°C and 100°C, respectively. Nitrogen served as the carrier gas at a flow rate of 30 mL/min.

2.6.2 High-performance liquid chromatography (HPLC)

The liquid product was tested using High-performance liquid chromatography (HPLC, SPD-M30A, RID-20A, SHIMADZU, USA) equipped with a RID detector and Aminex HPX-87H column. A mobile phase of 5 mM H_2SO_4 flowed at 0.6 mL/min.

2.6.3 Nuclear Magnetic Resonance (NMR) spectroscopy

The liquid product was analyzed using 600 MHz ^1H NMR spectroscopy (ASCEND 600, Bruker, Germany). NMR identification and quantification of liquid product was carried out as follows. A volume of 1 mL of solution was collected from the photocatalytic reactor after 60 min of reaction. It was mixed with 100 µL internal standard 5 mM dimethyl sulfoxide (99.99%). 250 µL of this mixture was mixed with 250 µL D_2O (99.9%, Sigma Aldrich) and transferred into an NMR tube [15]. ^1H NMR spectroscopy of the prepared sample was performed in a 600 MHz spectrometer. The concentration of the liquid product was calculated using the standard curve made using the internal standard mentioned previously. The methanol standard was used to develop the calibration (2-10 mM) to measure its concentration. A linear calibration fit was obtained with an R^2 of 0.999. The H^1 NMR graph of methanol is presented in **Figure 2.11**.

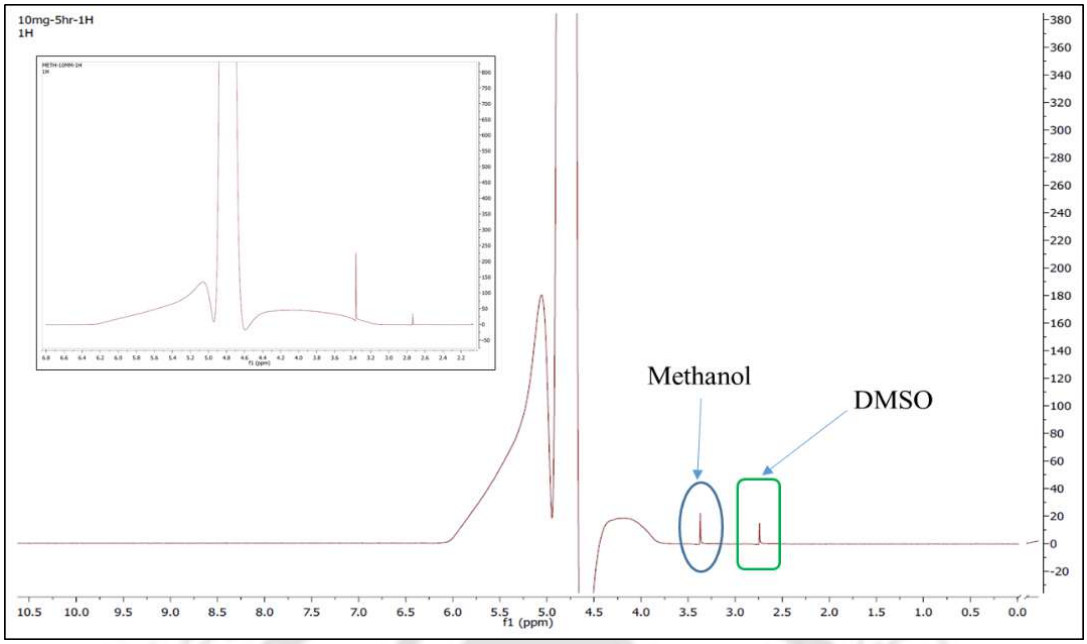

Figure 2.11. NMR spectra of solution after 300 s of CO_2 reduction, and (inset) 10 mM methanol standard solution.

2.7 Photoelectrochemical measurement

The PEC characteristics of the photocatalysts were examined by a three-electrode system on a potentiostat (AUTOLAB 302N, Metrohm Autolab, Netherlands). The working electrode was a catalyst-coated FTO glass with a platinum wire counter and an Ag/AgCl reference electrode. The electrolyte was a 0.5 M Na_2SO_4 solution [10]. To prepare the working electrode, the catalyst (10 mg) was mixed with 200 µL Nafion and EtOH solution (1:3 v/v), sonicated for 30 min, and then spin-coated onto the FTO glass at 2500 rpm for 20s with a projected area of (2×1) cm^2, followed by overnight drying at 60°C. The chronoamperometric test evaluated photocurrent density in both dark and light conditions, while electrochemical impedance spectroscopy (EIS) analyzed the resistance of the working electrode and charge transfer efficiency.

2.8 Density functional theory (DFT) studies

2.8.1 In_2O_3/CdS heterostructures

DFT calculations were executed using the Quantum Espresso software package with BURAI software as a graphical user interface (GUI)[16]. An ultrasoft pseudopotential describes the interaction between electrons and ions[16]. The Perdew-Burke-Ernzerhof (PBE) generalized gradient approximation (GGA) considered exchange-correlation interactions[17]. However, the PBE functional's bandgap estimation was lower than the experimental values.

To improve the accuracy, GGA+U was applied in the DFT calculation, introducing the Hubbard-U parameter to Cd-d and S-p orbitals for CdS and In-d for In_2O_3 [18,19]. The CdS lattice parameters are 5.88 Å (JCPDF database:00-001-0783), while those for In_2O_3 are 10.17 Å (JCPDF database: 00-001-0929). To minimize lattice mismatch between CdS and In_2O_3 surfaces, a 1.73 ×1 supercell for CdS with lattice parameters of 10.17 Å, matching with In_2O_3 surface lattice, was utilized by using VESTA software[20]. In both CdS and In_2O_2 structures, slabs with two thicknesses are separated by a 12 Å vacuum. The generated crystal structure of the heterostructures XYZ file was exported to BURAI for geometric optimization, band structure, and density of state (DOS) calculation. The Brillouin zone utilized a 420 Ry plane wave cut-off energy and a 12×12×1 k-point grid with an energy threshold of 1×10^{-6} eV. The structures were relaxed until the maximum force on each atom was below 0.001 eV/Å.

2.8.2 CDs/CdS QDs composite

All DFT calculations were performed using the Vienna ab initio simulation package (VASP) [21–23]. The Perdew-Burke-Ernzerhof (PBE) exchange-correlation functional within the generalized gradient approximation and the projected augmented wave (PAW) was applied using a plane wave basis set throughout the calculations [24]. To model the CdS QDs (111)-zero-dimensional CDs surface, first, we have built the 2×2×2 supercell with 15 Å of vacuum space along the C-axis. After generations of CdS QDs (111) surface, non-periodic CDs terminated by hydrogen atoms were deposited along the C-axis to make the final composite catalyst structures. We used a 3×3×1 Monkhorst-Pack mesh to perform the computational calculations with k-point sampling of the Brillouin zone. The energy cutoff, maximum force, and convergence criteria for energy are set to 500 eV, -0.02 eV $Å^{-1}$, and 10^{-5} eV, respectively. The Van der Waals (vdW) interaction was included using the DFT-D3 approach [25]. The free energy changes of reaction intermediates were calculated according to the computational hydrogen electrode (CHE)[26] model using the following Eq 2.1:

$$\Delta G\ [A^* + (e^- + H^+) \longrightarrow AH^*] = \mu(AH^*) - \mu(A^*) + \mu(H^+) + \mu(e^-) \qquad (2.1)$$

In the CHE model, it is considered that the chemical potential of the (electron (e^-)/proton (H^+)) couple is half of the chemical potential of the hydrogen molecule in the gas phase. The total chemical potential of the e^-/H^+couple can thus be computed as a function of the applied potential U, as seen in Eq. 2.2:

$$\mu(e^-) + \mu(H^+) = 1/2\mu(H_2(g)) - eU \qquad (2.2)$$

In our calculations, we are considering U=0 and pH=0, respectively.

2.8.3 SnO_2/CdS QDs heterostructures

DFT calculations were performed using Quantum Espresso, with BURAI software serving as the GUI [9,14]. The electron-ion interaction was modeled using an ultrasoft pseudopotential [15], and exchange-correlation interactions were treated with the PBE GGA [16]. However, the bandgap estimation using the PBE functional was lower than the experimental values. To enhance accuracy, GGA+U was employed in the DFT calculation, incorporating the Hubbard-U parameter to Cd-d and S-p orbitals in CdS and Sn-d and O-p orbitals in SnO_2 [12,27]. The lattice parameters of SnO_2 are 4.72 Å and 4.72 Å (JCPDF: 00-001-0657), while those for CdS QDs are 5.88 Å and 5.88 Å (JCPDF: 00-002-0454). To reduce the lattice mismatch between the SnO_2 and CdS QDs, a 1.25×1 supercell of SnO_2 with lattice parameters of 5.9 Å and 5.9 Å was designed to align with the CdS QDs lattice using VESTA software. For both the SnO_2 and CdS QDs models, the slabs with two thicknesses were separated by a 15 Å vacuum layer. The generated crystal structure of the heterostructure was exported in XYZ format to BURAI for geometric optimization, band structure analysis, and DOS calculations. The Brillouin zone was sampled using a 6×6×6 Monkhorst-pack k-point grid, with a plane wave cut-off energy of 575 Ry and an energy convergence threshold of 1×10^{-6} eV. Structural relaxation was performed until the maximum force on each atom was reduced to below 0.001 eV/Å.

2.8.4 CuO/CdS QDs heterostructures

DFT calculations were performed using the Quantum Espresso with BURAI software as a GUI [12,16]. Electron-ion interaction was described by an ultrasoft pseudopotential [28], and the PBE GGA was applied for exchange-correlation interactions [29]. However, the bandgap estimation using the PBE functional was lower than the experimental values. To enhance accuracy, GGA+U was employed in the DFT calculation, incorporating the Hubbard-U parameter to Cd-d and S-p orbitals in CdS and Cu-d in CuO [12,18]. First, the CdS QDs(111) and CuO QDs (111) surfaces were created using VESTA software [20]. The lattice parameters of CdS QDs (111) are 7.20 Å and 4.16 Å, while those of CuO QDs (111) are 6.01 Å and 2.93 Å. To minimize the lattice mismatch between CdS QDs (111) and CuO QDs (111), a 2.1×2.1 supercell for the CdS QDs (111) surface with lattice parameters of 15.13 Å and 8.74 Å was constructed. Similarly, a 2.5×2.5 supercell for the CuO QDs (111) surface with lattice parameters of 15.04 Å and 8.81 Å was generated, which matched well with the CdS QDs (111) surface. For both the CdS QDs (111) and CuO QDs (111) models, the slabs with two thicknesses were separated by a 15 Å vacuum layer. The generated crystal structure of the

heterostructure was exported in XYZ format to BURAI for geometric optimization, band structure analysis, and DOS calculations. The Brillouin zone was sampled using a 8×8×1 Monkhorst-pack k-point grid, with a plane wave cut-off energy of 638 Ry and an energy convergence threshold of 1×10^{-6} eV. Structural relaxation was performed until the maximum force on each atom was reduced to below 0.001 eV/Å.

References

[1] F. Mujeeb, P. Bajpai, N. Pathak, Phytochemical Evaluation, Antimicrobial Activity, and Determination of Bioactive Components from Leaves of Aegle marmelos, Biomed Res. Int. 2014 (2014) 1–11. https://doi.org/10.1155/2014/497606.

[2] H. Dabhane, S. Ghotekar, P. Tambade, S. Pansambal, H.C.A. Murthy, R. Oza, V. Medhane, A review on environmentally benevolent synthesis of CdS nanoparticle and their applications, Environ. Chem. Ecotoxicol. 3 (2021) 209–219. https://doi.org/10.1016/j.enceco.2021.06.002.

[3] A.K. Jha, K. Prasad, Biosynthesis of gold nanoparticles using bael (Aegle marmelos) leaf: mythology meets technology, Int. J. Green Nanotechnol. 3 (2011) 92–97. https://doi.org/10.1080/19430892.2011.574560.

[4] N.D.A. Krupa, V. Raghavan, Biosynthesis of silver nanoparticles using aegle marmelos (Bael) fruit extract and its application to prevent adhesion of bacteria: A strategy to control microfouling, Bioinorg. Chem. Appl. 2014 (2014). https://doi.org/10.1155/2014/949538.

[5] A.K. Jha, K. Prasad, Biosynthesis of gold nanoparticles using bael (Aegle marmelos) leaf: Mythology meets technology, Int. J. Green Nanotechnol. Biomed. 3 (2011) 92–97. https://doi.org/10.1080/19430892.2011.574560.

[6] Z. Naheed, Z. Cheng, C. Wu, Y. Wen, H. Ding, Total polyphenols, total flavonoids, allicin and antioxidant capacities in garlic scape cultivars during controlled atmosphere storage, Postharvest Biol. Technol. 131 (2017) 39–45. https://doi.org/10.1016/j.postharvbio.2017.05.002.

[7] S. Raziya, B. Durga, and N.A. Rajamahanti Santhoshi Ganesh, Boddeti Govind, Synthesis and characterization of novel antibacterial agents enclosing, RJPBCS. 4 (2017) 1452–1459.

[8] D. Gogoi, R. Koyani, A.K. Golder, N.R. Peela, Enhanced photocatalytic hydrogen evolution using green carbon quantum dots modified 1-D CdS nanowires under visible light irradiation, Sol. Energy. 208 (2020) 966–977. https://doi.org/10.1016/j.solener.2020.08.061.

[9] Y. Wang, J. Chen, L. Liu, X. Xi, Y. Li, Z. Geng, G. Jiang, Z. Zhao, Novel metal doped

carbon quantum dots/CdS composites for efficient photocatalytic hydrogen evolution, Nanoscale. 11 (2019) 1618–1625. https://doi.org/10.1039/C8NR05807E.

[10] P.M. Gawal, A.K. Golder, Vegetal route for synthesis of CQDs/CdS nanocomposites for photocatalytic reduction of CO_2 to methanol under visible light, Colloids Surfaces A Physicochem. Eng. Asp. 683 (2024) 133068. https://doi.org/10.1016/j.colsurfa.2023.133068.

[11] S. Phokha, S. Seraphin, S. Maensiri, P. Laokul, J. Klinkaewnarong, S. Phokha, S. Seraphin, Indium oxide (In_2O_3) nanoparticles using Aloe vera plant extract: Synthesis and optical properties Indium oxide (In_2O_3) nanoparticles using Aloe vera plant extract: Synthesis and optical properties, Optoelectron. Adv. Mater. Commun. 2 (2008) 161–165. https://www.researchgate.net/publication/237548361.

[12] P.M. Gawal, A.K. Golder, Plant-Based Phytochemicals for Synthesis of Z-Scheme In_2O_3/CdS Heterostructures: DFT Analysis and Photocatalytic CO_2 Reduction to HCOOH and CO, Langmuir. 40 (2024) 13538–13549. https://doi.org/10.1021/acs.langmuir.4c01015.

[13] A. Chowdhury, N.R. Peela, A.K. Golder, Synthesis of Cu_2O NPs using bioanalytes present in Sechium edule: Mechanistic insights and application in electrocatalytic CO_2 reduction to formate, J. CO2 Util. 51 (2021) 2–13. https://doi.org/10.1016/j.jcou.2021.101622.

[14] D. Laishram, S. Zeng, K.M. Alam, A.P. Kalra, K. Cui, P. Kumar, R.K. Sharma, K. Shankar, Air- and water-stable halide perovskite nanocrystals protected with nearly-monolayer carbon nitride for CO_2 photoreduction and water splitting, Appl. Surf. Sci. 592 (2022) 153276. https://doi.org/10.1016/j.apsusc.2022.153276.

[15] D. Ren, Y. Deng, A.D. Handoko, C.S. Chen, S. Malkhandi, B.S. Yeo, Selective Electrochemical Reduction of Carbon Dioxide to Ethylene and Ethanol on Copper(I) oxide catalysts, ACS Catal. 5 (2015) 2814–2821. https://doi.org/10.1021/cs502128q.

[16] A. Halal, K.S. Rahman, S.F. Abdullah, K. Sopian, N. Amin, An investigation on CdS1-xTex interface compound in CdS/CdTe hetero-junction solar cells by density functional theory (DFT), Superlattices Microstruct. 151 (2021) 106805. https://doi.org/10.1016/j.spmi.2021.106805.

[17] T. Tian, X. Jin, N. Guo, H. Li, Y. Han, Y. Yuan, CdS/ethylenediamine nanowires 3D photocatalyst with rich sulfur vacancies for efficient syngas production from CO_2 photoreduction, Appl. Catal. B Environ. 308 (2022) 121227. https://doi.org/10.1016/j.apcatb.2022.121227.

[18] A. Biswas, S.R. Meher, D.K. Kaushik, Electronic and Band Structure calculation of Wurtzite CdS Using GGA and GGA+U functionals, J. Phys. Conf. Ser. 2267 (2022) 012155. https://doi.org/10.1088/1742-6596/2267/1/012155.

[19] H. A. Rahnamaye Aliabad, The effect of Hubbard potential on effective mass of carriers in doped Indium oxide, Int. J. Phys. Sci. 7 (2012) 696–708. https://doi.org/10.5897/IJPS11.1319.

[20] K. Momma, F. Izumi, VESTA 3 for three-dimensional visualization of crystal, volumetric and morphology data, J. Appl. Crystallogr. 44 (2011) 1272–1276. https://doi.org/10.1107/S0021889811038970.

[21] G. Kresse, J. Furthmüller, Efficient iterative schemes for ab initio total-energy calculations using a plane-wave basis set, Phys. Rev. B. 54 (1996) 11169–11186. https://doi.org/10.1103/PhysRevB.54.11169.

[22] G. Kresse, J. Furthmüller, Efficiency of ab-initio total energy calculations for metals and semiconductors using a plane-wave basis set, Comput. Mater. Sci. 6 (1996) 15–50. https://doi.org/10.1016/0927-0256(96)00008-0.

[23] G. Kresse, D. Joubert, From ultrasoft pseudopotentials to the projector augmented-wave method, Phys. Rev. B. 59 (1999) 1758–1775. https://doi.org/10.1103/PhysRevB.59.1758.

[24] J.P. Perdew, K. Burke, M. Ernzerhof, Generalized Gradient Approximation Made Simple, Phys. Rev. Lett. 77 (1996) 3865–3868. https://doi.org/10.1103/PhysRevLett.77.3865.

[25] S. Grimme, J. Antony, S. Ehrlich, H. Krieg, A consistent and accurate ab initio parametrization of density functional dispersion correction (DFT-D) for the 94 elements H-Pu, J. Chem. Phys. 132 (2010). https://doi.org/10.1063/1.3382344.

[26] J.K. Nørskov, J. Rossmeisl, A. Logadottir, L. Lindqvist, J.R. Kitchin, T. Bligaard, H. Jónsson, Origin of the Overpotential for Oxygen Reduction at a Fuel-Cell Cathode, J. Phys. Chem. B. 108 (2004) 17886–17892. https://doi.org/10.1021/jp047349j.

[27] M. Baral, P. Patnaik, D.K. Das, S.K. Nayak, SnO_2 DOPED WITH Sc, Ti, V, Cr, AND Mn: AN INSIGHT INTO THE STRUCTURAL, ELECTRICAL, MAGNETIC AND OPTICAL PROPERTIES, USING THE GGA+U SCHEME, Rasayan J. Chem. 18 (2025) 158–166. https://doi.org/10.31788/RJC.2025.1819044.

[28] K. Ghosh, P.K. Giri, Experimental and theoretical study on the role of 2D Ti_3C_2Tx MXenes on superior charge transport and ultra-broadband photodetection in MXene/Bi_2S_3 nanorod composite through local Schottky junctions, Carbon N. Y. 216 (2024) 118515. https://doi.org/10.1016/j.carbon.2023.118515.

[29] D. Nayak, R. Thangavel, Strain Modulated Electronic and Photocatalytic Properties of MoS_2/WS_2 Heterostructure: A DFT Study, ACS Appl. Electron. Mater. 5 (2023) 302–316. https://doi.org/10.1021/acsaelm.2c01344.

CHAPTER 3

Vegetal Route for Synthesis of CQDs/CdS Nanocomposites for Photocatalytic Reduction of CO_2 to Methanol under Visible Light

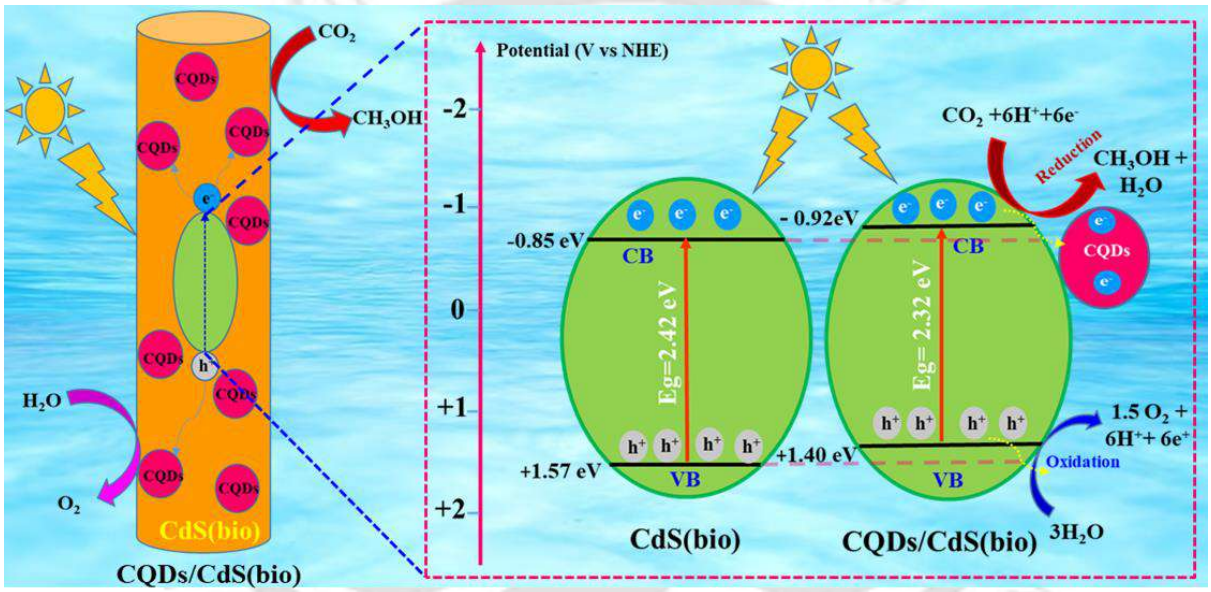

Chapter highlights

- CdS(bio) nanorods synthesized using phytochemicals present in *Aegle Marmelos*
- Bio-based CQDs synthesized using *orange peels*
- Tuneable CQDs/CdS(bio) composites fabricated by a simple deposition method
- Photostability of CdS(bio) improved notably with CQDs incorporation
- High methanol production of 1060.52 µmol/g·h using CQDs/CdS(bio) photocatalyst

3.1 Introduction

The world is dependent on the burning of non-renewable fossil fuels to meet the bulk of its energy demand (~80%) even in the 21st century[1]. Consequently, excessive carbon dioxide (CO_2) emission causes the grievous greenhouse gas effect [2,3]. Currently, CO_2 emission stands at over 40 gigatons per year with an atmospheric concentration of 421 ppm (International Energy Agency). In fact, global energy consumption has been estimated to rise by 28% in the next 17 years [4,5] because of the industrial boom and improved living standards of humans. Factually, the world needs sustainable technologies to fulfill the mammoth energy demand alongside CO_2 mitigation to control the greenhouse gas effect.

The photoreduction of CO_2 has been considered one of the most efficient techniques for CO_2 utilization because abundant solar energy and H_2O are used in this process to convert CO2 into valuable chemicals such as ethanol (C_2H_5OH), methanol (CH_3OH), formic acid (HCOOH), methane (CH_4), carbon monoxide (CO), etc. [2,3,6–9]. This process could mimic natural photosynthesis in the plant [10,11]. Therefore, photocatalytic reduction of CO_2 could meet the energy demand with a plausible solution to CO_2 emission [5,12].

CO_2 is a very stable linearly symmetric molecule with excellent thermodynamic stability. The double bond (C=O) energy of CO_2 is 750 kJ/mol compared to the single bond energy of 336 (C-C), 327 (C-O), and 411 kJ/mol (C-H) [13,14]. Due to the large negative potential of CO_2 (-1.9 V vs. NHE, pH 7), the direct one-electron reduction of CO_2 is challenging [15]. To date, no photocatalyst has been invented for a single electron for CO_2 reduction. In contrast, the multi-electron/proton-assisted reduction is an alternative and more beneficial approach because of the lower CO_2 reduction potential [16,17]. Therefore, designing an active, robust, and cost-effective multifunctional photocatalyst is essential to achieve efficient CO_2 reduction to useful chemicals for practical applications.

For photocatalytic CO_2 reduction reaction, several nanocatalysts have been tested, namely, TiO_2 [18], ZnO[19], ZnS [20], SiC [21], g-C_3N_4 [22], CdS [13], In_2O_3 [23], WO_3 [24], Bi_2S_3 [25], Cu_2O [26], and MOFs[27]. Among these, CdS has been intensively studied for CO_2 reduction owing to a suitable bandgap (2.4 eV) and conduction band potential (-0.95 V vs. NHE, pH 7) and high solar energy conversion [12,13]. However, CdS suffers from oxidative corrosion and quick recombination of electron (e^-)/hole (h^+) pairs [13]. As a remedial action, various modification techniques have been developed, namely, doping with metal and non-metal [28], morphological control [12], co-catalysis [6], and formation of heterojunction [29] and Z-scheme heterojunction [30].

The chemical synthesis methods of photocatalysts involve costly and environmentally aggressive chemicals. However, the bio-based approach for synthesizing semiconductor nanoparticles (NPs) has advantages over chemical-based methods, such as its eco-friendly nature, cost-effectiveness, one-pot synthesis process, and abundant sources of biomaterials [31,32]. Developing green pathways for NP_S synthesis and their application in CO_2 photoreduction to value-added chemicals could be a potential technique for controlling industrial CO_2 emissions. The Northeastern states of India are the hub of several tropical and subtropical plants. These plants could be employed as potential capping and reducing analytes for the quick and effective synthesis of semiconductor nanomaterials [33]. A short exposure of microwave irradiation in concurrence with the bio-based process could also accelerate the rate of NPs formation by several folds.

The carbon quantum dots (CQDs) have gained tremendous research interest owing to diverse applications in the last two decades. CQDs own unique characteristics, such as low toxicity, luminescence, and high thermal stability with zero-dimensionality (<10 nm size) [34,35]. In addition, due to their superior charge transfer and electron donor/acceptor properties, CQDs have been considered promising candidates for developing effective and stable composite photocatalysts [36,37]. Different techniques have been used to synthesize CQDs using several carbon sources such as urea, thiourea, citric acid, ethylene glycol, etc. The renewable and abundant biomass reserves are also potential carbon precursors for CQD_S synthesis. The biomass sources, such as leaves, flowers, or roots of the plant [38,39], fruits and their peels [35], human derivatives [40], and animal derivatives [41], are carbonized for the low-cost and environmentally friendly synthesis of CQDs.

The first study of this doctoral work focused on the synthesis of microwave-assisted bio-based CdS(bio) nanorods using plant-based phytochemicals present in *Aegle marmelos*. It contains a variety of strong reducing and capping analytes, including alkaloids, flavonoids, phenols, tannins, and saponins, which could control the nucleation, growth, morphology, and surface stabilization of CdS(bio) nanorods [33,42,43]. CdS(bio) nanorods were modified to minimize their oxidative corrosion and high e^-/h^+ recombination during photocatalytic CO_2 reduction reaction (PCO_2RR). Further, bio-based CQDs were synthesized from waste orange peels and incorporated into CdS(bio) by a simple deposition method. Orange peels provide a carbon-rich source for CQDs, whose excellent electron donor/acceptor properties could enhance charge transfer, suppress recombination, and improve CO_2 reduction in CQDs/CdS(bio) composites [44,45]. The modified catalysts (CQDs/CdS(bio) composites)

were tested for PCO_2RR to methanol formation in batch mode under visible-light irradiation. The maximum methanol production rate of 1062.68 μmol/g·h was achieved using CQDs/CdS(bio) composites with a CQDs loading of 0.50% (w/w). The reusability of CQDs/CdS(bio) composites has also been examined. Factually, this is the first study on the bio-based synthesis of composite nano-structures for PCO_2RR to methanol formation.

3.2 Results and discussion

3.2.1 Photocatalyst characterizations

3.2.1.1 Structural and composition analyses

X-ray diffraction: Figure 3.1 depicts the XRD patterns of CdS(bio) and CQDs/CdS(bio) composites. For CdS(bio), the diffraction peaks observed at 2θ values of 26.31, 43.64, and 51.68° correspond to the crystal plane with Miller indices of (111), (220), and (311), respectively. It confirms the cubic CdS phase (JCPDF database, 01-083-5247). The peak intensity and its position agreed well with the earlier study [46]. The peak position of CQDs/CdS(bio) composites is in accordance with CdS(bio). It implies that the incorporation of CQDs(bio) during the formation of CQDs/CdS(bio) composites didn't change its crystal structure or phase. The XRD peak of CQDs was absent in the composite structure because of its tiny mass loading (<1% w/w), well dispersity, and amorphous nature [36]. The crystallinity index of catalysts was computed using the equation (Eq. 3.1) shown below [47].

$$\text{Crystallinity index (\%)} = \frac{A_c}{A_t} \times 100 \qquad (3.1)$$

Where A_c is the area of prominent crystalline peaks [(111), (220), (311)], and A_t is the total area under the peaks. The crystallinity index of CdS(bio) and 0.50% (w/w) CQDs/CdS(bio) was found to be 70.20 % and 69.9%, respectively.

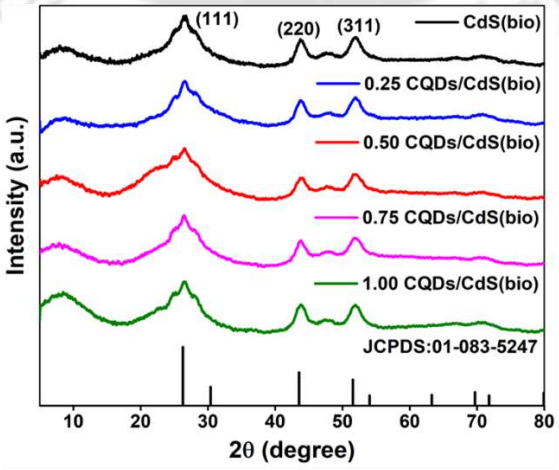

Figure 3.1. XRD patterns of CdS(bio) and CQDs/CdS(bio) composites.

XPS analysis: **Figure 3.2a** depicts the survey and high-resolution (HR) spectra of CdS(bio) and CQDs/CdS(bio) composites. **Figure 3.2b** shows HR Cd 3d spectra of CdS(bio) with two distinct peaks at 409.26 and 402.5 eV, ascribing to the Cd $3d_{3/2}$ and Cd $3d_{5/2}$ spin-orbits, respectively, owing to Cd^{2+} in CdS(bio) nanorods [10]. The S 2p spectra (**Figure 3.2c**) of CdS(bio) showed two peaks at 160.1 and 158.88 eV. It is attributed to the S $2p_{1/2}$ and S $2p_{3/2}$ with a splitting energy of 1.2 eV, which indicates the S^{2-} valence state in CdS(bio) nanorods [48]. The HR S 2p and Cd 3d spectra of 0.50% (w/w) CQDs/CdS(bio) composites also showed a similar trend. The S 2p and Cd 3d peak positions were shifted towards higher binding energy. A reduction in the electron density of CdS(bio) is suggested by the positive shift in the binding energy peak of S 2p and Cd 3d. It implies that CdS and CQDs have a strong chemical interaction that facilitates the transport of electrons from CdS to CQDs [36]. The HR of C 1s spectra (**Figure 3.2d)** of 0.50% (w/w) CQDs/CdS(bio) composites (binding energy peak at 284.8 eV) corresponds to the C-C/C=C of the graphitic or aliphatic structure of CQDs on the surface of CdS. The 288.07 and 286.3 eV peaks correspond to C=O and C-O, respectively [49]. The HR O 1s spectra of 0.50% (w/w) CQDs/CdS(bio) composites exhibited three major deconvoluted peaks at 533.3, 532.7, and 531.4 eV (**Figure 3.2e**) corresponding to the C-OH/C-O-Cs, C=O/$Cd(OH)_2$/Cd-O, and C-O/OH^- respectively [36,37]. Due to the hydroxide group's structural compatibility with sulfur, it may easily interact with the CdS lattice, forming CdO or $Cd(OH)_2$ [28,37].

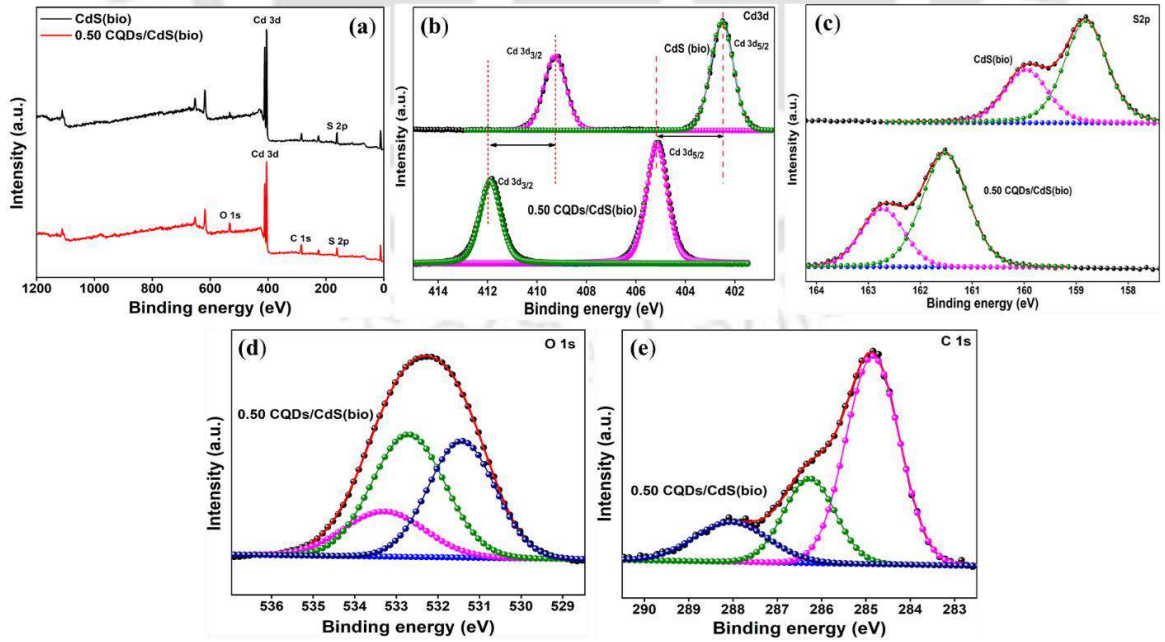

Figure 3.2. (a) XPS survey spectra; High-resolution spectra of (b) Cd 3d and (c) S 2p of CdS(bio) and 0.50% (w/w) CQDs/CdS(bio) composite, and (d) C 1s and (e) O 1s of 0.50% (w/w) CQDs/CdS(bio) composite.

3.2.1.2 Spectroscopic analyses

UV-vis spectra: The UV-Vis spectra of CdS(bio), CQDs(bio), and CQDs/CdS(bio) composites are shown in **Figure 3.3a.** CdS(bio) showed a significant absorption threshold at 520 nm. The absorption edge of CQDs/CdS(bio) composites shifted towards longer wavelengths, resulting in a redshift. The absorption spectra of CQDs (**Figure 3.4**) revealed two peaks at 280 nm and 220 nm corresponding to n-π* (C=O) and π-π* (C=C) transitions, respectively. The delocalized large π bonds were present, which could improve the light absorption intensity [50,51]. The bandgap was computed by using Tauc's relation (Eq. 3.2) [52].

$$\alpha = \frac{(h\nu - E_g)^n}{h\nu} \qquad (3.2)$$

Where α=F(R) denotes the absorption coefficient, hν is the photon energy, E_g is the optical bandgap energy, n is a constant, and its value of ½ represents the direct allowed transition [51]. **Figure 3.3b** displays the plot of $(\alpha h\nu)^{1/2}$ vs. hν. CdS(bio) and 0.50% (w/w) CQDs/CdS(bio) bandgap were determined to be 2.42 and 2.32 eV, respectively. The results agree with the values reported earlier [36]. The bandgap of 0.50% (w/w) CQDs/CdS(bio) composites is slightly reduced compared to CdS(bio) due to the quantum confinement effect of CQDs [53]. A similar reduction of bandgap was observed with g-C_3N_4 (2.7 to 2.62 eV) [54] and Cu_2O (2.0 to 1.91 eV) [55] with the incorporation of CQDs.

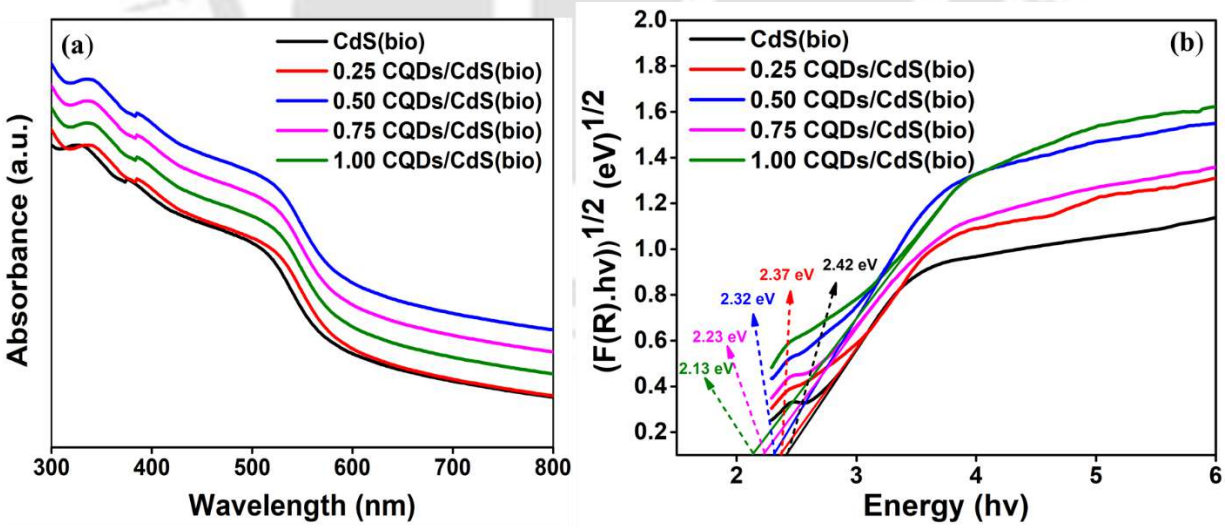

Figure 3.3 (a) Transient photocurrent and (b) EIS Nyquist plots in the dark and with illumination.

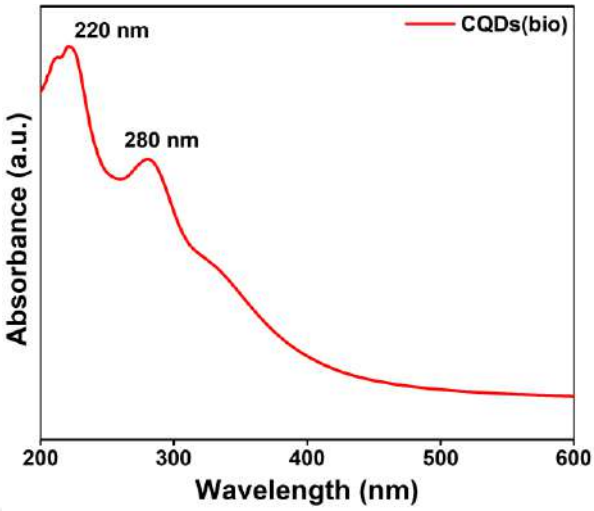

Figure 3.4. UV-Vis absorption spectra of CQDs(bio).

Ultraviolet photoelectron spectroscopy (UPS) spectra: The conduction band position of photocatalyst specimens is a significant aspect in determining the ability of CO_2 reduction. The valence band maximum (VBM) of the synthesized catalyst was characterized using UPS, and the outcomes are shown in **Figure 3.5a**. The linear extrapolation approach is used to calculate the VBM of each sample, which is determined to be 1.57 and 1.40 eV for CdS(bio) and 0.50% (w/w) CQDs/CdS(bio) composites, respectively. Based on the results of UPS spectra and UV- vis DRS spectra (bandgap), the conduction band maximum (CBM) was calculated using the relation $E_{CB} = E_{VB} - E_g$ [3]. CBM of CdS(bio) and 0.50% (w/w) CQDs/CdS(bio) are found to be -0.85 and -0.92 eV, respectively [3,28,36]. **Figure 3.5b** depicts the band diagram of CdS(bio) and 0.50%(w/w) CQDs/CdS(bio) composites. It is clear that the CQDs/CdS(bio) composites exhibit a favorable CBM potential for an increased methanol production rate.

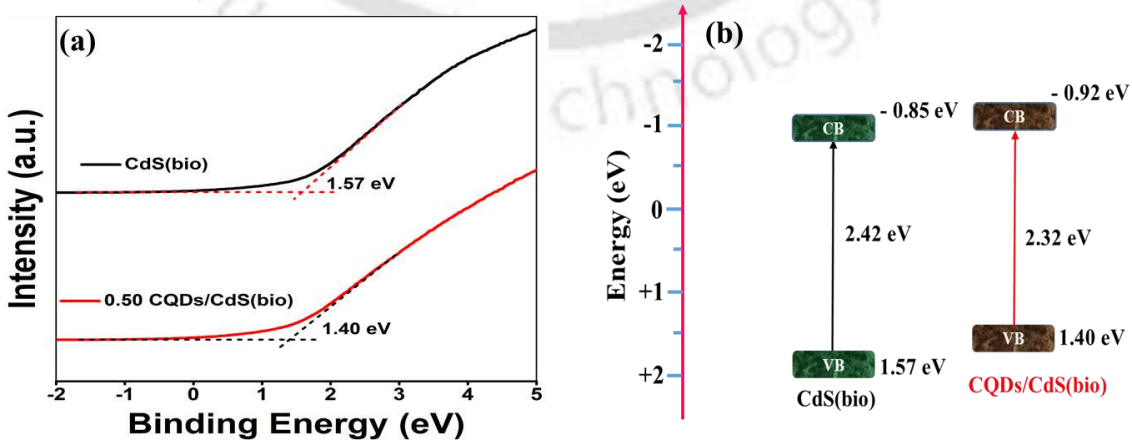

Figure 3.5. (a) UPS spectra and (b) Band position of CdS(bio) and 0.50% (w/w) CQDs/CdS(bio) composite.

Photoluminescence (PL) spectra: The PL spectra were collected at a wavelength of excitation to understand the charge carrier dynamics and its trapping efficiency of synthesized materials (**Figure 3.6**). The prominent peak observed at 450 nm suggests fast recombination of e^-/h^+ pairs. CQDs/CdS(bio) composites exhibited substantially lower PL intensities than that of CdS(bio) (**Figure 3.6a**) due to the presence of a delocalized π-conjugated structure in CQDs, which has an excellent electron-conducting characteristic [56]. It indicates a better separation of photoexcited charge carriers and reduced recombination of e^-/h^+ pairs, allowing a rapid transfer of electrons from the conduction band (CB) of CdS to CQDs [28,36,57]. Hence, more electrons could be available for the CO_2 reduction reactions. A similar observation was reported for CQDs/g-C_3N_4 [51] and CQDs/Cu_2O composites. Furthermore, CQDs exhibited a prominent peak at 443 nm with 360 nm excitation wavelength with a blue emission spectrum (**Figure 3.6b**), suggesting a typical fluorescent nature of CQDs [34]. The strong electron binding is due to the combined effect of the quantum (blue fluorescent) phenomenon and the conjugation effect arising from CQDs' delocalized π bond [50]. The CQDs(bio) showed a dark yellow and blue fluorescent when exposed to visible light and ultraviolet (UV) light, respectively (inset of **Figure 3.6b**).

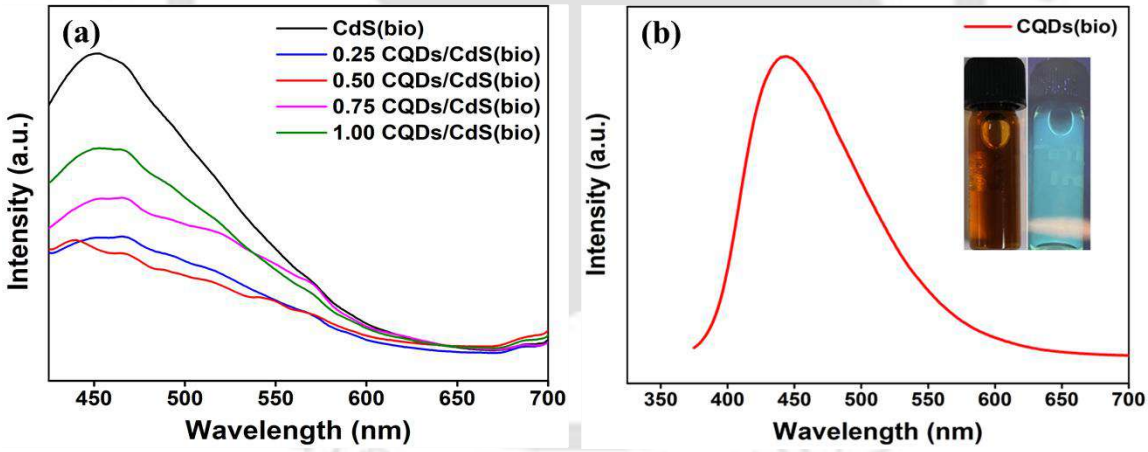

Figure 3.6. PL spectra of (a) CdS(bio) and CQDs/CdS(bio) composite, and (b) CQDs(bio).

Time-resolved photoluminescence (TRPL): TRPL spectra (**Figure 3.7**) of CdS(bio) and CQDs/CdS(bio) composites were recorded with 1000 counts at 405 nm and 450 nm of excitation and emission wavelengths, respectively, to understand the charge transfer behavior. The fitted parameter is shown in **Table 3.1.** A bi-exponential decay function was used to fit the TRPL decay curves. The average lifetime (τ_{avg}) was estimated using (Eq. 3.3) [54].

$$\tau_{average} = \frac{A_1 \times \tau_1^2 + A_2 \times \tau_2^2}{A_1 \times \tau_1 + A_2 \times \tau_2} \quad (3.3)$$

Where A_1, A_2 represents amplitudes, and τ_1, τ_2 represents the lifetime. The average lifetime of CdS(bio) and 0.50% (w/w) CQDs/CdS(bio) composites were determined to be 1.59 ns and 3.74 ns, respectively. This indicates that the 0.50% (w/w) CQDs/CdS(bio) exhibited better e^-/h^+ pairs separation efficiency compared to the CdS(bio). Incorporating CQDs onto CdS serves as a reservoir for capturing excited electrons, facilitated by the surface junction formed between CdS and CQDs. Consequently, this enhanced the separation of e^-/h^+ pairs and reduced their recombination [58,59].

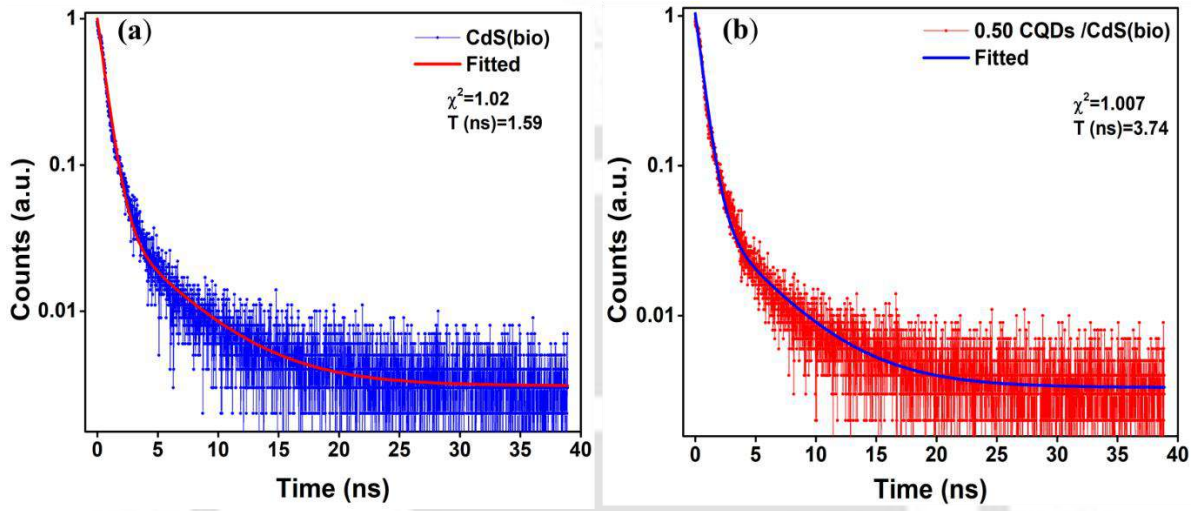

Figure 3.7. TRPL spectra of (a) CdS(bio) and (b) 0.50% (w/w) CQDs/CdS(bio) composite.

Table 3.1. TRPL data of CdS(bio) and 0.50%(w/w) CQDs/CdS(bio) composite.

Catalyst	A_1 (%)	τ_1 (ns)	A_2 (%)	τ_2 (ns)	τ_{ave}(ns)
CdS(bio)	42.5	0.412	57.5	1.797	1.59
0.50% (w/w) CQDs/CdS(bio) composites	62.75	0.639	37.24	4.48	3.74

Electrochemical attributes of CQDs/CdS(bio) composites: The charge separation efficiency of CdS(bio) and 0.50% (w/w) CQDs/CdS(bio) composites was examined using the transient photocurrent measurement and electrochemical impedance spectra (EIS). The chronoamperometry test **(Figure 3.8a)** was carried out with an interval of 25 s of the light on/off cycle. The average photocurrent density of 0.50% (w/w) CQDs/CdS(bio) composites is 0.38 $\mu A/cm^2$, which is nearly four times greater than CdS(bio) (0.095 $\mu A/cm^2$). It indicates that

photogenerated e^-/h^+ pairs are separated efficiently with CQDs incorporation onto CdS(bio) nanorods [6].

EIS spectra of CdS(bio) nanorods and 0.50% (w/w) CQDs/CdS(bio) composites nanorods under both dark conditions and light irradiation are presented in **Figure 3.8b**. Under visible light, the arc radius of 0.5 (w/w) CQDs/CdS(bio) composites was reduced, indicating a higher charge separation and transfer efficiency. It implies that CQDs incorporation could change the distribution of charges and facilitate charge transfer of CdS(bio) nanorods [36]. Furthermore, increased capacitance indicates improved CQDs storing characteristics on the photoanode/electrolyte [28,60]. A similar observation was reported for CQDs/Cu_2O composites and CQDs/g-C_3N_4 [54,61].

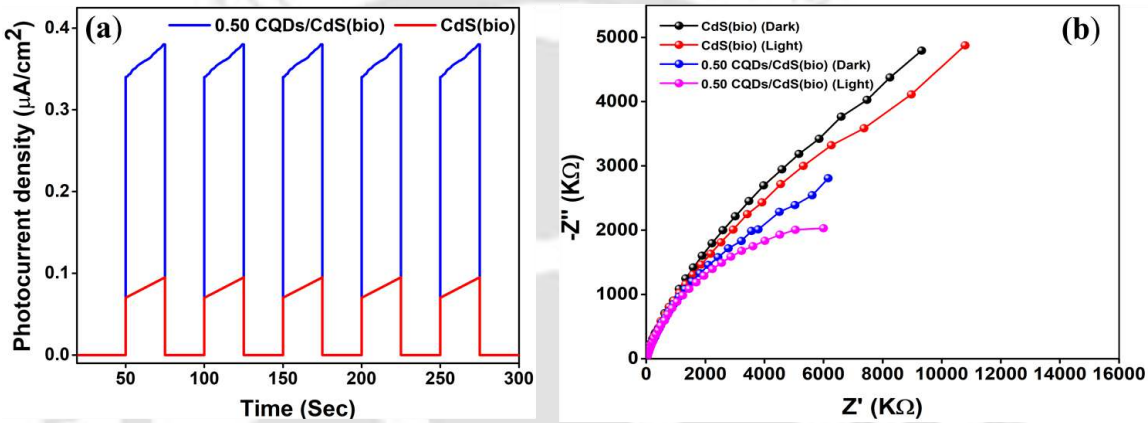

Figure 3.8. (a) Transient photocurrent and (b) EIS Nyquist plots in the dark and with illumination.

Fourier transformed infrared (FTIR) spectra: FTIR spectra of CdS(bio), CQDs(bio), and CQDs/CdS(bio) composites are shown in **Figure 3.9**. The strong broadband peak at around 3290 cm^{-1} corresponds to the stretching vibration of O-H bonds in water molecules[62]. The peak at 1572 cm^{-1} is attributed to the stretching vibration of C=C cyclic alkene, and at 1405 cm^{-1} to the bending vibration C-C in aromatic compounds. The weak absorption band at 1030 cm^{-1} is ascribed to the stretching vibration of C-O bonds, and 616 cm^{-1} corresponds to the Cd-S stretch vibration. An additional peak corresponds to the CdS in CQDs/CdS(bio) composites due to the induction of CQDs into CdS [28]. A weak absorption band at about 2930 cm^{-1} in both CdS(bio) and CQDs/CdS(bio) composites, corresponding to the Cd-O stretching vibration [37], was also confirmed by XPS analysis. A broad absorption band at 3441 cm^{-1} indicates the stretching vibration of O-H bonds. The peak at 1640 cm^{-1} corresponds to the stretching vibration of the C=O bond. The 1405 and 1070 cm^{-1} peaks correspond to the bending vibration

of COO^- and C-O/C-O-C bonds, respectively [63]. The presence of the –OH group on CQDs indicates that it can donate electrons in PCO_2RR [64].

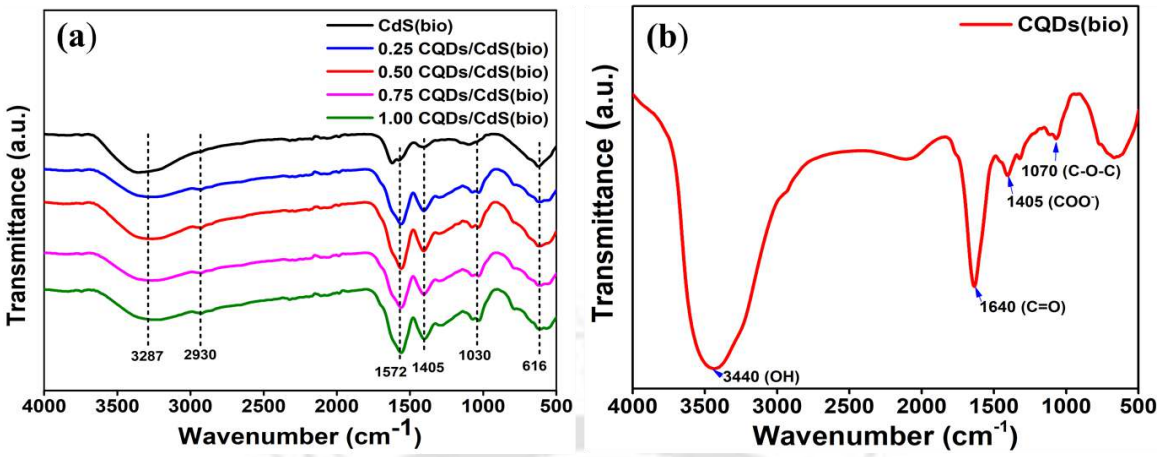

Figure 3.9. FTIR spectra of (a) CdS(bio) and CQDs/CdS(bio) composites, and (b) CQDs(bio).

Zeta potential: The zeta potential of a sample (catalyst + DI water) was measured at different pH (2-12) using the dynamic light scattering method. The variation of zeta potential (mV) against pH is shown in **Figure 3.10** of the Supplementary Information. The pH at the zero-point charge (pHzpc) is found to be 5.61, which is close to the CO_2 saturation point in the aqueous media.

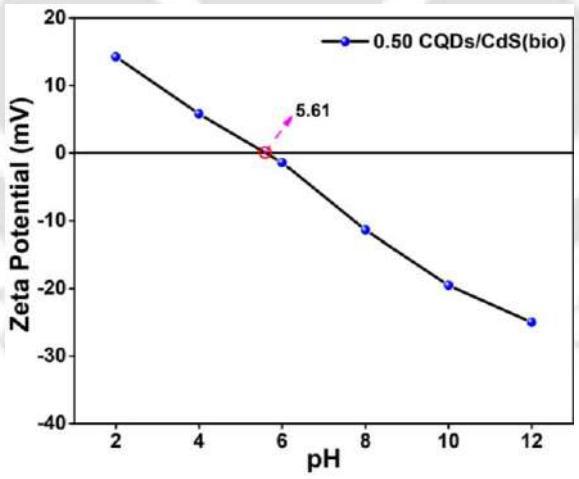

Figure 3.10. Variation of zeta-potential with pH in 0.50% (w/w) CQDs/CdS(bio) composite/water system.

3.2.1.3 Morphology

FESEM and FETEM analyses: Figure 3.11 shows the FESEM images of CdS(bio), CdS(con), and 0.50% (w/w) CQDs/CdS(bio) composites. CdS(bio) nanorods with a defined shape were successfully formed in the proposed bio-based route (**Figure 3.11a**). Whereas no

defined structural formation of CdS nanoparticles was noted for CdS(con) (**Figure 3.11b**). It is evident that CQDs incorporation (CQDs/CdS(bio)) didn't cause any morphological alteration (**Figure 3.11c**). The average length and diameter of both CdS(bio) and 0.50% (w/w) CQDs/CdS(bio) nanorods were 822 and 73 nm [65,66].

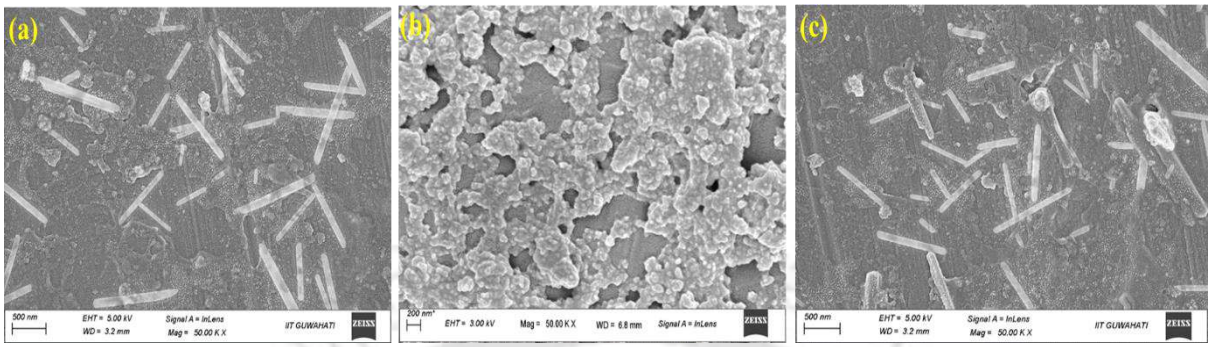

Figure 3.11. (a) FESEM images of CdS(bio), (b) CdS(con), and 0.50% (w/w) CQDs/CdS(bio) composite.

Figure 3.12 shows the FETEM of CdS(bio), CQDs(bio), and CQDs/CdS(bio) composites. The average diameter of nanorods was 822 nm, which is consistent with FESEM analyses (**Figures 3.12a** and **3.12b**). The average CQDs size was 7 nm (**Figure 3.12c**). **Figure 12d** shows the HRTEM images of 0.50% (w/w) CQDs/CdS(bio) composites. The interplanar spacing of CdS(bio) lattice fringes is 0.34 nm, corresponding to the (111) plane [67]. It was 0.32 nm for (002) graphitic lattice planes of CQDs [38]. The SAED patterns of 0.50% (w/w) CQDs/CdS(bio) composites (**Figure 3.12d**(insect)**)** exhibited the amorphous nature of CQDs compared to CdS(bio), which has a monocrystalline structure with one-dimensional morphology. The well-crystalline phase of CdS nanorods was indicated by SAED patterns of CdS(bio) nanorods (**Figure 3.13**) [68], but the amorphous nature of CQDs resulted in a fuzzy ring structure in the SAED patterns of CQDs [39]. The SAED pattern of 0.50% (w/w) CQDs/CdS(bio) composites showed a slight SAED pattern deviation. It could be attributed to the CQDs incorporation onto CdS(bio) nanorods. EDX analysis of 0.50% (w/w) CQDs/CdS(bio) composites (**Figure 3.12e**) showed C, S, and Cd contents of 20.14, 16.29, and 63.57%, respectively. **Figure 3.12f** shows the elemental mapping of the elements present in the composites.

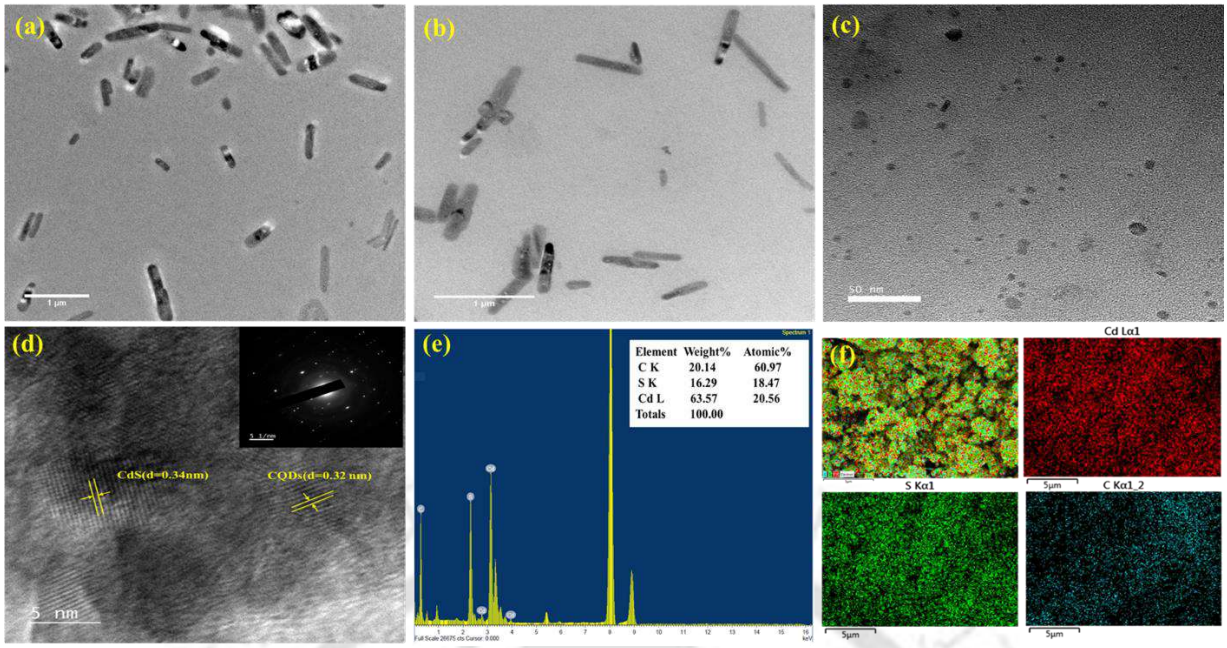

Figure 3.12. FETEM image of (a) CdS(bio), (b) 0.50% (w/w) CQDs/CdS(bio) composite, and (c) CQDs(bio), (d) HRTEM image (insect SAED patterns), (e) EDX spectra, and (f) Elemental mapping of Cd, S, and C of 0.50% (w/w) CQDs/CdS(bio) composite.

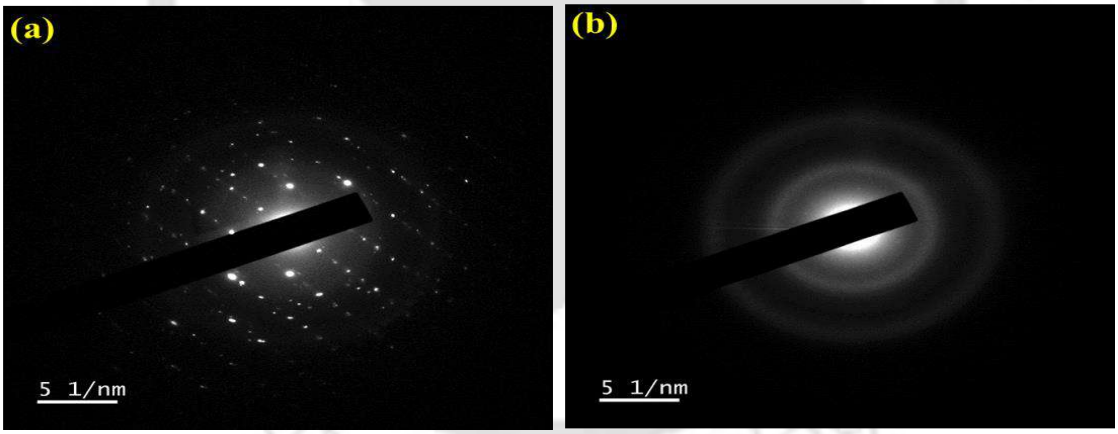

Figure 3.13. SAED patterns of (a) CdS(bio) and (b) CQDs(bio).

BET surface area analysis: The surface area and pore structure of CdS(bio) and 0.50% (w/w) CQDs/CdS(bio) were determined using N_2 adsorption-desorption, and the results are summarized in **Table 3.2**. **Figure 3.14** illustrates the N_2 adsorption-desorption isotherms and the corresponding pore size distribution curve (inset of **Figure 3.14**). Both CdS(bio) and 0.50% (w/w) CQDs/CdS(bio) composites exhibited type IV isotherms with mesoporous nature, with an average pore size was 7.58 and 6.48 nm, respectively. Hence, CQDs/CdS(bio) composites could provide effective transport pathways for reactant and product molecules [69,70]. Almost

no variation was noted in surface area and adsorption isotherm with CQDs incorporation onto CdS(bio). As seen from **Table 3.2**, 0.50% (w/w) CQDs/CdS(bio) composites exhibit a higher CO_2 adsorption capacity (0.292 mmol/g) than that of CdS(bio) (0.075 mmol/g) tested at 1 bar. The π–π-conjugate structure of CQDs enhances CO_2 adsorption. CO_2 molecules have delocalized π-conjugate binding π_3 and π-π combination interaction between CO_2 and CQDs for enhanced CO_2 adsorption onto CQDs/CdS(bio) composites [6,60].

Table 3.2. Physical characteristic parameters of synthesized catalysts.

Photocatalysts	Bandgap (eV)	Surface area, m^2/g	Average pore diameter, nm	Total pore volume, cm^3/g	CO_2 adsorption (mmol/g)
CdS(bio)	2.42	88.88	7.58	0.14	0.075
0.50% (w/w) CQDs/CdS(bio) composite	2.32	82.25	6.41	0.085	0.292

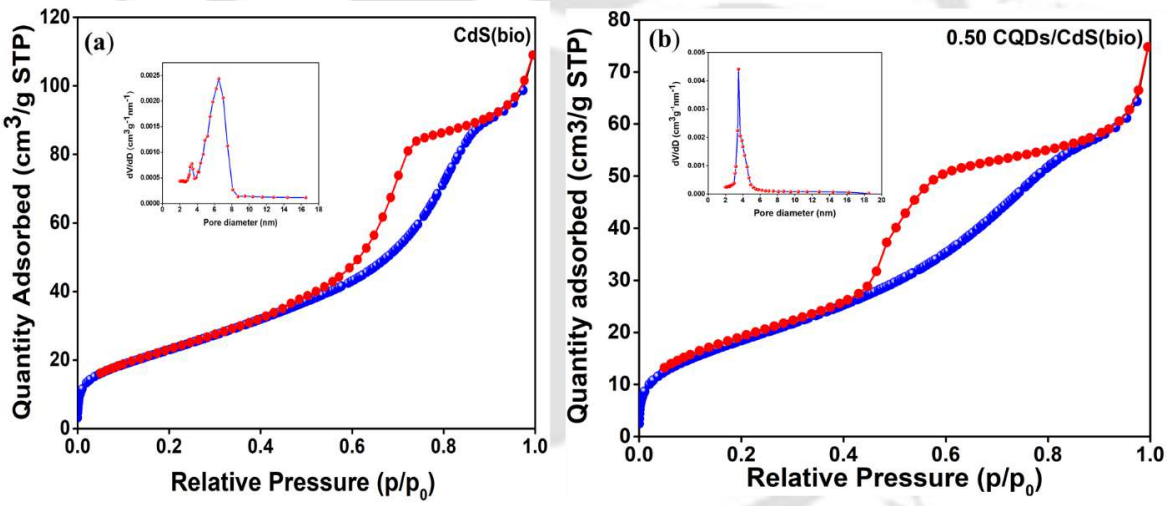

Figure 3.14. N_2 adsorption-desorption isotherm and (inset) Barrett-Joyner-Halenda (BJH) pore size distribution plot of (a) CdS(bio) and (b) 0.50% (w/w) CQDs/CdS(bio) composites.

3.2.2 Testing of catalytic activity for PCO_2RR

The production of methanol using synthesized catalysts was tested under visible light illumination. The methanol standard calibration graph is given in **Figure 3.15.** There was no noticeable methanol production in the absence of either catalyst or light irradiation. The control experiment was performed using composite and water without CO_2 purging under visible light

irradiation. The NMR spectra, depicted in **Figure 3.16**, confirm that methanol is produced from the CO_2 feedstock in the system.

Figure 3.17a shows the methanol production rate using CdS(bio) and CQDs/CdS(bio) composites (0.25, 0.50, 0.75, and 1% w/w). In fact, methanol production was negligible using CdS(bio) due to its photo-corrosion (**Figures 3.19c & 3.20a**) and quick recombination of e^-/h^+ pairs. It implies that bare CdS is not a suitable catalyst for reducing CO_2 to methanol [6,71]. For CQDs, there is no product formation (**Figure 3.18**) due to a lack of effective catalytic sites [36]. In the case of CQDs/CdS(bio) composites, the rate of methanol formation exhibited an increasing trend with a loading percentage of CQDs and reached its maximum at 0.50% (w/w) loading of CQDs with a rate of 773.38 μmol/g·h. The rate of methanol formation was then decreased drastically with an increase in the percentage (w/w) of CQDs. An excess CQDs loading results in excessive surface coverage of CdS(bio), promoting CQDs-CQDs interactions, screening surface charges, and reducing electrostatic stabilization [44,45]. This causes particle aggregation, blocks the active sites of CdS(bio), decreases the effective surface area, and hinders both charge transfer and light absorption [28,36,37]. The hydrodynamic diameter of the catalysts was determined by DLS, and the corresponding result can be found in **Table 3.3**. The particle size was increased significantly with the increase in CQDs loading onto CdS(bio) beyond 0.50% (w/w). It indicates that an excess CQDs loading would lead to particle agglomeration. Therefore, 0.50% (w/w) CQDs loading was considered the optimal CQDs loading.

The methanol production rate with different photocatalyst concentrations (0, 0.25, 0.50, 0.75, 1 g/L) of 0.50% (w/w) CQDs/CdS(bio) composites is presented in **Figure 3.17b**. A concentration of 0.50 g/L photocatalyst exhibited the highest methanol production, yielding 1062.68 μmol/g·h and an apparent quantum yield (AQY) of 7% (calculation of AQY provided in **Table A1**). The solution becomes turbid, preventing light irradiation at increasing concentrations of photocatalysts [37]. The methanol production rate achieved in this study was compared with values reported in the literature **(Table 3.4),** implying a clear superiority of bio-based CQDs/CdS(bio) composites.

The time-dependent PCO_2RR to methanol production over 0.50% (w/w) CQDs/CdS(bio) composites was tested with five repeated cycles to investigate the functional stability of the synthesized catalyst **(Figure 3.17c)**. After a 25 h reaction, the composites maintained a consistent photocatalytic activity with a 1.28% decline in their performance in the 5th cycle due to the inevitable loss of photocatalyst during the multistep recovery processes. The

excellent stability of the composites suggests that the incorporation of CQDs on the surface of CdS(bio) reduced its photocorrosion and suppressed e^-/h^+ pairs recombination [28,36,37].

The impact of common inorganic ions on the photocatalytic CO_2 reduction to methanol in an aqueous media under visible light was investigated by mimicking the real environmental conditions. We selected the average ion concentration as reported in the literature[72]. The results are summarized in **Table 3.5**. Ca^{2+} and Mg^{2+} cations exhibited a slight increase in CO2 reduction due to improved CO2 adsorption. While the influence of Na^+ and K^+ was minimal. For anions, Cl^- addition showed a negligible impact, but SO_4^{2-} hindered CO_2 reduction. However, CO_3^{2-} could facilitate the CO_2 conversion reaction by serving as a carbon source for methanol formation.

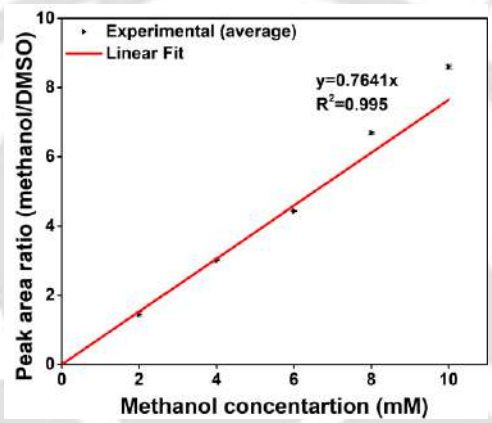

Figure 3.15. Calibration curve of methanol standard.

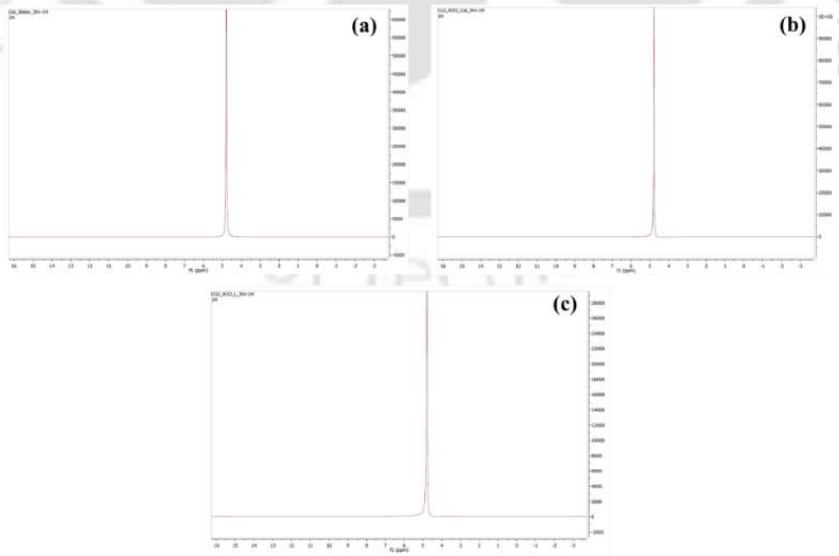

Figure 3.16. NMR spectra of 300 s of CO_2 reduction (a) 0.50% (w/w) CQDs/CdS(bio) composite + DI water + light irradiation, (b) 0.50% (w/w) CQDs/CdS(bio) composite + DI water + CO_2 purge, and (c) DI water + CO_2 purge + light irradiation.

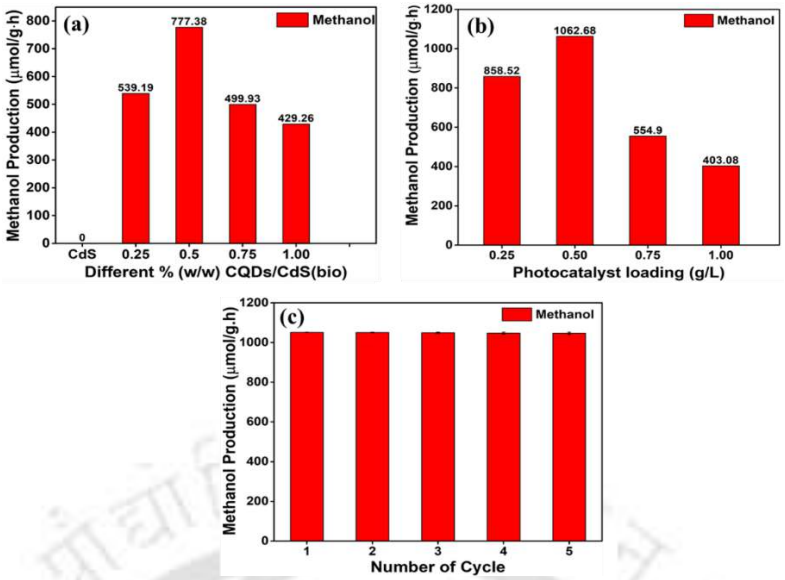

Figure 3.17. (a) Effect of CQDs(bio) loading onto CdS(bio) for methanol formation, (b) Effect of loading (g/L) of 0.50% (w/w) CQDs/CdS(bio) composites on methanol formation, and (c) Stability of CQDs/CdS(bio) composite under visible light irradiation (μmol/g·h) on methanol production rate.

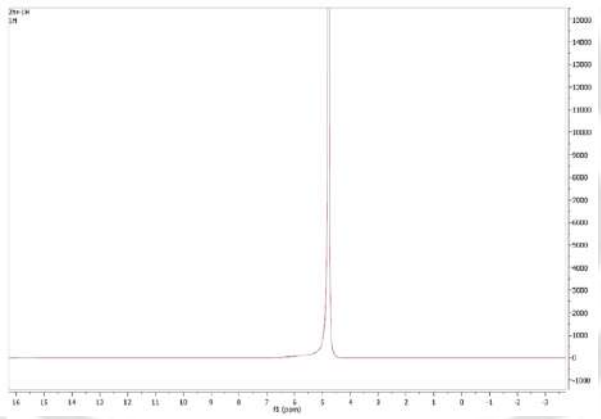

Figure 3.18. NMR spectrum captured after 120 s of CO_2 reduction using CQDs under visible light irradiation.

Table 3.3. Hydrodynamic diameter of CdS(bio) and CQDs/CdS(bio) composites.

Catalysts	Hydrodynamic diameter (nm)
CdS(bio)	613.4
0.25% (w/w) CQDs/CdS(bio)	514.1
0.50% (w/w) CQDs/CdS(bio)	648.6
0.75% (w/w) CQDs/CdS(bio)	1630.7
1.00% (w/w) CQDs/CdS(bio)	1835.9

Table 3.4. Comparison of the methanol production rate with earlier reports.

Photocatalyst	Synthesis method	Reaction solvent	Light source	Products (µmol/g·h)	Sources
CQDs/CdS(bio) composite	Simple deposition method	Water	250 W Mercury vapor lamp, λ> 420 nm	1062.66	**Present Work**
CdS/TiO_2	Direct precipitation reaction	0.1 NaOH/ 0.1 M Na_2SO_3 /H_2O	500 W Xenon lamp, λ>400 nm	31.9	[73]
CdS/A-GO	Ultrasonication	TEOA/H_2O	350W Xenon lamp, λ>420 nm	662.5	[6]
CdS/PAA	SILAR	Water vapour	10 W LED lamp	114.5	[74]
CdS/TiO_2/SBA-15		0.4 M NaOH	Uv-vis 300W Xe lamp	1022	[71]
Bi_2S_3/CdS	Hydrothermal	0.1M NaOH, 0.1M Na_2SO_3, H_2O	500 W Xenon lamp, λ=400-700 nm	122.6	[75]
CdS@CeO_2 core/shell composite	Two-step chemical	Milli-Q water	300W Xenon lamp, λ>420 nm	138	[76]
RGO/CdS/PAA	SILAR	Water vapour	Sunlight	157.3	[77]
CdS@CeO_2 heterojunction	Electrostatic interaction	DMF/H_2O/TEA (2:2:1)	300 W Xenon lamp, λ>420 nm	153.4	[78]

TEOA: Triethanolamine; PAA: Porous anodic alumina; SBA: Santa barbara amorphous; TEA: trimethylamine; DMF: N, N-dimethylformamide; SILAR: Successive ionic layer adsorption and reaction

Table 3.5. Influence of common inorganic ions on photocatalytic CO_2 reduction to methanol formation using CQDs/CdS(bio).

Sr. No	Salt	Ions	Ion concentration (mg/L)	Changes in CH_3OH formation
1	$CaCl_2$	Ca^{2+}	98.8	↑
2	$MgCl_2$	Mg^{2+}	28.0	↑
3	$NaClO_4$	Na^+	13.7	–
4	KCl	K^+	30.2	–
5	Na_2SO_4	SO_4^{2-}	134.0	↓
6	NaCl	Cl^-	92.5	–
7	$NaHCO_3$	HCO_3^-	164.7	↑

Figure 3.19 illustrates the XPS analysis of CdS(bio/used) and 0.50% (w/w) of CQDs/CdS(bio/used) composites. The survey spectrum (**Figure 3.19a**) validates the existence of Cd, S, In, and O in the heterostructure. Only Cd is present in the CdS(bio/used) specimen as expected. The high-resolution spectra of 0.50% (w/w) CQDs/CdS(bio) (**Figures 3.19b-3.19e**) confirm consistent peak intensities before and after PCO_2RR. However, in the case of CdS(bio/used) (**Figures 3.19b-3.19c**), the S 2p peak intensity is shifted to 168.64 eV, indicating sulfur oxidation (photocorrosion) and formation of SO_4^{2-} [79].

Figure 3.20 shows the FESEM images of CdS(bio/used) and 0.50% (w/w) of CQDs/CdS(bio/used) composites after PCO_2RR. CdS(bio) nanorods underwent significant morphological changes due to potential photocorrosion. However, no changes were noted for the composites [80]. The XRD spectra after PCO_2RR of CdS(bio/used) and 0.50% (w/w) CQDs/CdS(bio/used) composites are shown in **Figure 3.21**. The morphological and structural characteristic parameters of CdS(bio/used) and 0.50%(w/w) CQDs/CdS(bio/used) before and after the PCO_2RR are mentioned in **Table 3.6.** A reduction in the crystallinity index of 15% was observed for CdS(bio) against 47.74% and 39.83 % reductions in its length and diameter. In comparison, it was only 0.057% and 0.80% for CQDs/CdS(bio/used) composites, respectively.

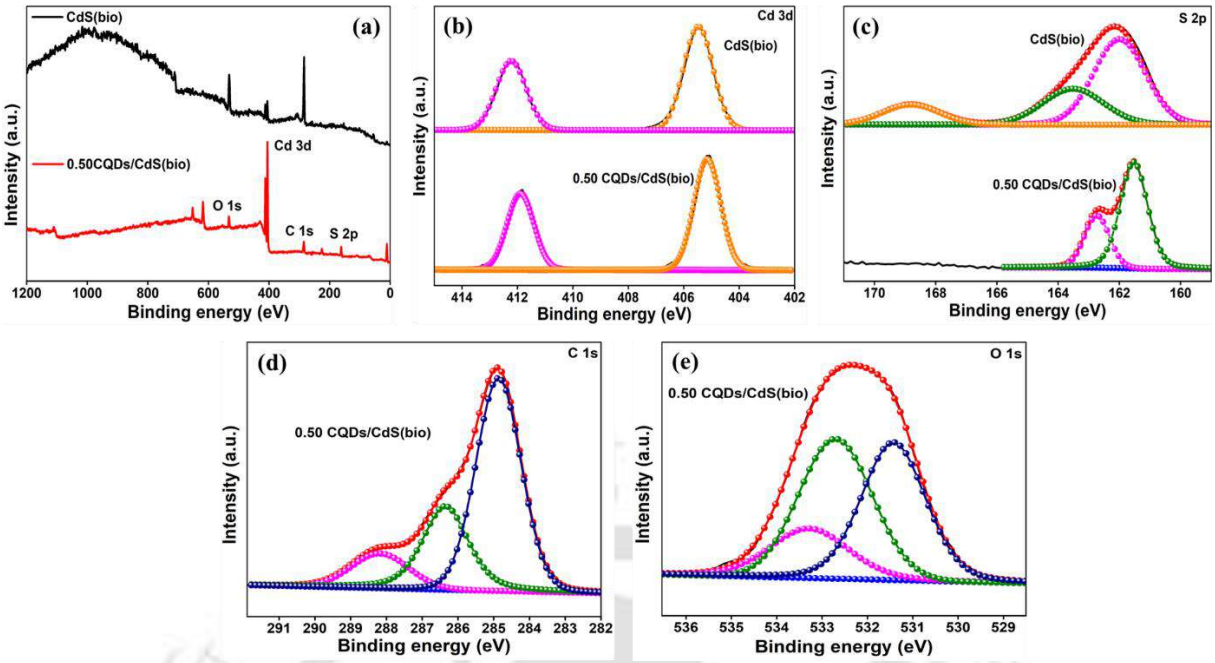

Figure 3.19. (a) XPS survey spectra and high-resolution spectra of (b) Cd 3d and (c) S 2p of CdS(bio/used) and 0.50% (w/w) CQDs/CdS(bio/used) composite, and (d) C 1s and (e) O 1s of 0.50% (w/w) CQDs/CdS(bio/used) composite.

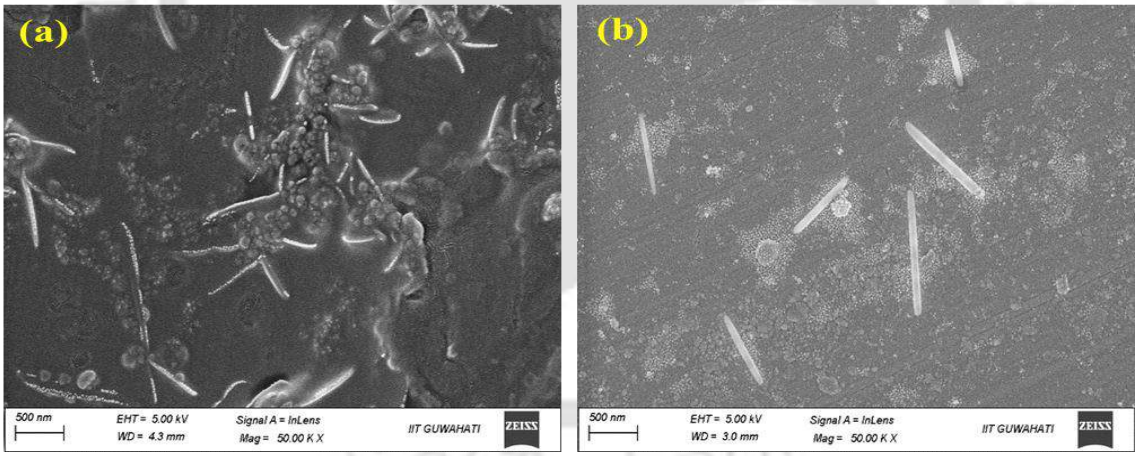

Figure 3.20. FESEM images of used (a) CdS(bio) and (b) CdS/CQDs(bio) composite after PCO_2RR.

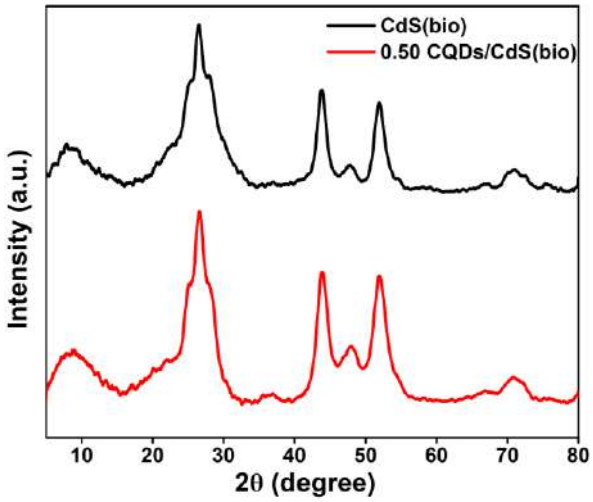

Figure 3.21. XRD diffraction pattern after the PCO_2RR of CdS(bio) and 0.50% (w/w) CQDs/CdS(bio) composite.

Table 3.6. Morphological and structural characteristic parameters of CdS(bio) and 0.50%(w/w) CQDs/CdS(bio) composite before and after the PCO_2RR.

Catalyst	Before the reaction			After the reaction		
	Diameter (nm)	Length (nm)	Crystallinity (%)	Diameter (nm)	Length (nm)	Crystallinity (%)
CdS(bio)	73	822	70.20	43.92	429.5	59.61
0.50% (w/w) CQDs/CdS(bio)	73	822	69.93	72.41	821.53	66.93

3.3 Major findings

This study was successful in synthesizing CQDs/CdS nanorods composites in a bio-based route (diameter 73 nm, length 822 nm, surface area 82.25 m^2/g, bandgap 2.32 eV) by using natural precursors, namely, orange peels and phytochemicals present in *Aegle marmelos* vegetal extract. The photocatalytic activity of CQDs/CdS(bio) composites was evaluated for CO_2 reduction to methanol under 250 W visible light ($\lambda > 420$ nm, 4.2719×10^{18} photons/m^2.s). The bandgap of CdS(bio) was reduced from 2.42 to 2.32 eV with the incorporation of CQDs (0.50 % w/w) onto CdS(bio). The decay lifetime (3.74 ns) of CQDs/CdS(bio) composites was 2.35-fold higher than CdS(bio). CQDs/CdS(bio) composites showed a strong affinity for CO_2 adsorption (0.292 mmol/g at 1 bar) over CdS(bio) (0.075 mmol/g). The photocurrent density of 0.50% (w/w) CQDs/CdS(bio) was 4 times higher than CdS(bio) nanorods. A remarkable

methanol production rate of 1060.52 μmol/g·h (AQY 7%) was achieved using 0.50 % (w/w) CQDs/CdS(bio) composites without using any sacrificial agent over 5 h of irradiation. CQDs/CdS(bio) composites exhibited robust stability (tested for 25 h), with minimal morphological (0.11% size variation) and structural (4.2% crystallinity index variation) changes and resistant to photo and oxidative corrosion, whereas CdS(bio) underwent quick morphological and structural changes. In a nutshell, the present work would provide new insights for developing bio-based CdS-based composites for efficient PCO_2RR to useful chemicals. *However, CQDs/CdS nanorods exhibited low surface area and limited product selectivity. Therefore, the second objective focused on the formation of Z-scheme In_2O_3/CdS heterostructures, which could improve surface area, band alignment, and product selectivity. DFT study further could reveal the mechanism of improved charge transfer and its impact on photocatalytic performance.*

References

[1] P.M. Gawal, S. Subudhi, Advances and challenges in bio-based 2,3-BD downstream purification: A comprehensive review, Bioresour. Technol. Reports. 24 (2023) 101638. https://doi.org/10.1016/j.biteb.2023.101638.

[2] Y.-X. Feng, H.-J. Wang, J.-W. Wang, W. Zhang, M. Zhang, T.-B. Lu, Stand-alone CdS nanocrystals for photocatalytic CO_2 reduction with high efficiency and selectivity, ACS Appl. Mater. Interfaces. 13 (2021) 26573–26580. https://doi.org/10.1021/acsami.1c03606.

[3] T. Tian, X. Jin, N. Guo, H. Li, Y. Han, Y. Yuan, CdS/ethylenediamine nanowires 3D photocatalyst with rich sulfur vacancies for efficient syngas production from CO_2 photoreduction, Appl. Catal. B Environ. 308 (2022) 121227. https://doi.org/10.1016/j.apcatb.2022.121227.

[4] Y. Liu, Y. Wang, C. Shi, W. Zhang, W. Luo, J. Wang, K. Li, N. Yeung, S. Kite, Assessing the CO2 reduction target gap and sustainability for bridges in China by 2040, Renew. Sustain. Energy Rev. 154 (2022) 111811. https://doi.org/10.1016/j.rser.2021.111811.

[5] H. Shen, T. Peppel, J. Strunk, Z. Sun, Photocatalytic Reduction of CO_2 by Metal-Free-Based Materials: Recent Advances and Future Perspective, Sol. RRL. 4 (2020) 1900546. https://doi.org/10.1002/solr.201900546.

[6] L. Zhu, Y. Liu, X. Peng, Y. Li, Y.-L. Men, P. Liu, Y.-X. Pan, Noble-metal-free CdS

nanoparticle-coated graphene oxide nanosheets favoring electron transfer for efficient photoreduction of CO_2, ACS Appl. Mater. Interfaces. 12 (2020) 12892–12900. https://doi.org/10.1021/acsami.0c00163.

[7] L. Zhang, L. Zhang, Y. Chen, Y. Zheng, J. Guo, S. Wan, S. Wang, C.K. Ngaw, J. Lin, Y. Wang, CdS/ZnO: A Multipronged Approach for Efficient Reduction of Carbon Dioxide under Visible Light Irradiation, ACS Sustain. Chem. Eng. 8 (2020) 5270–5277. https://doi.org/10.1021/acssuschemeng.0c00190.

[8] L. Li, C. Guo, J. Ning, Y. Zhong, D. Chen, Y. Hu, Oxygen-vacancy-assisted construction of FeOOH/CdS heterostructure as an efficient bifunctional photocatalyst for CO_2 conversion and water oxidation, Appl. Catal. B Environ. 293 (2021) 120203. https://doi.org/10.1016/j.apcatb.2021.120203.

[9] L. Wang, Z. Zhang, Q. Han, Y. Liu, J. Zhong, J. Chen, J. Huang, H. She, Q. Wang, Preparation of CdS-P25/ZIF-67 composite material and its photocatalytic CO_2 reduction performance, Appl. Surf. Sci. 584 (2022) 152645. https://doi.org/10.1016/j.apsusc.2022.152645.

[10] H.Y. Wang, R. Hu, Y.J. Lei, Z.Y. Jia, G.L. Hu, C.B. Li, Q. Gu, Highly efficient and selective photocatalytic CO_2 reduction based on water-soluble CdS QDs modified by the mixed ligands in one pot, Catal. Sci. Technol. 10 (2020) 2821–2829. https://doi.org/10.1039/d0cy00308e.

[11] S. Wu, H. Pang, W. Zhou, B. Yang, X. Meng, X. Qiu, G. Chen, L. Zhang, S. Wang, X. Liu, R. Ma, J. Ye, N. Zhang, Stabilizing $CuGaS_2$ by crystalline CdS through an interfacial Z-scheme charge transfer for enhanced photocatalytic CO_2 reduction under visible light, Nanoscale. 12 (2020) 8693–8700. https://doi.org/10.1039/D0NR00483A.

[12] P. Zhang, S. Wang, B.Y. Guan, X.W.D. Lou, Fabrication of CdS hierarchical multi-cavity hollow particles for efficient visible light CO_2 reduction, Energy Environ. Sci. 12 (2019) 164–168. https://doi.org/10.1039/C8EE02538J.

[13] K. Yang, Z. Yang, C. Zhang, Y. Gu, J. Wei, Z. Li, C. Ma, X. Yang, K. Song, Y. Li, Q. Fang, J. Zhou, Recent advances in CdS-based photocatalysts for CO_2 photocatalytic conversion, Chem. Eng. J. 418 (2021) 129344. https://doi.org/10.1016/j.cej.2021.129344.

[14] Y. Zhang, Y. Wu, L. Wan, H. Ding, H. Li, X. Wang, W. Zhang, Hollow core–shell Co_9S_8@$ZnIn_2S_4$/CdS nanoreactor for efficient photothermal effect and CO2 photoreduction, Appl. Catal. B Environ. 311 (2022) 121255. https://doi.org/10.1016/j.apcatb.2022.121255.

[15] W.A. Thompson, E. Sanchez Fernandez, M.M. Maroto-Valer, Review and analysis of CO_2 photoreduction kinetics, ACS Sustain. Chem. Eng. 8 (2020) 4677–4692. https://doi.org/10.1021/acssuschemeng.9b06170.

[16] X. Li, J. Yu, M. Jaroniec, X. Chen, Cocatalysts for selective photoreduction of CO_2 into solar fuels, Chem. Rev. 119 (2019) 3962–4179. https://doi.org/10.1021/acs.chemrev.8b00400.

[17] Ž. Kovačič, B. Likozar, M. Huš, Photocatalytic CO_2 reduction: A review of Ab initio mechanism, kinetics, and multiscale modeling simulations, ACS Catal. 10 (2020) 14984–15007. https://doi.org/10.1021/acscatal.0c02557.

[18] H.-N. Wang, Y.-H. Zou, H.-X. Sun, Y. Chen, S.-L. Li, Y.-Q. Lan, Recent progress and perspectives in heterogeneous photocatalytic CO_2 reduction through a solid–gas mode, Coord. Chem. Rev. 438 (2021) 213906. https://doi.org/10.1016/j.ccr.2021.213906.

[19] H. Mahdizadeh, A. Nasiri, M.A. Gharaghani, G. Yazdanpanah, Hybrid UV/COP advanced oxidation process using ZnO as a catalyst immobilized on a stone surface for degradation of acid red 18 dye, MethodsX. 7 (2020) 101118. https://doi.org/10.1016/j.mex.2020.101118.

[20] Y. Meng, G. Liu, G. Zuo, X. Meng, T. Wang, J. Ye, A review on ZnS-based photocatalysts for CO_2 reduction in all-inorganic aqueous medium, Nanoscale. 14 (2022) 14455–14465. https://doi.org/10.1039/D2NR03703C.

[21] Y. Wang, L. Zhang, X. Zhang, Z. Zhang, Y. Tong, F. Li, J.C.S. Wu, X. Wang, Openmouthed B-SiC hollow-sphere with highly photocatalytic activity for reduction of CO_2 with H_2O, Appl. Catal. B Environ. 206 (2017) 158–167. https://doi.org/10.1016/j.apcatb.2017.01.028.

[22] F. Tian, X. Wu, J. Chen, X. Sun, X. Yan, G. Liao, One-step photodeposition of spatially separated CuOx and MnOx dual cocatalysts on g-C_3N_4 for enhanced CO_2 photoreduction, Dalt. Trans. 52 (2023) 11934–11940. https://doi.org/10.1039/D3DT01522J.

[23] Y.X. Pan, Y. You, S. Xin, Y. Li, G. Fu, Z. Cui, Y.L. Men, F.F. Cao, S.H. Yu, J.B. Goodenough, Photocatalytic CO2 Reduction by Carbon-Coated Indium-Oxide Nanobelts, J. Am. Chem. Soc. 139 (2017) 4123–4129. https://doi.org/10.1021/jacs.7b00266.

[24] J.C. Murillo-Sierra, A. Hernández-Ramírez, D.A. Pino-Sandoval, E. Ruiz-Ruiz, A. Martínez-Hernández, Promoting multielectron CO_2 reduction using a direct Z-scheme WO_3/ZnS photocatalyst, J. CO2 Util. 63 (2022) 102122.

https://doi.org/10.1016/j.jcou.2022.102122.

[25] L. Lin, C. Hou, X. Zhang, Y. Wang, Y. Chen, T. He, Highly efficient visible-light driven photocatalytic reduction of CO_2 over g-C_3N_4 nanosheets/tetra(4-carboxyphenyl)porphyrin iron(III) chloride heterogeneous catalysts, Appl. Catal. B Environ. 221 (2018) 312–319. https://doi.org/10.1016/j.apcatb.2017.09.033.

[26] Z. Tang, W. He, Y. Wang, Y. Wei, X. Yu, J. Xiong, X. Wang, X. Zhang, Z. Zhao, J. Liu, Ternary heterojunction in rGO-coated Ag/Cu_2O catalysts for boosting selective photocatalytic CO_2 reduction into CH_4, Appl. Catal. B Environ. 311 (2022) 121371. https://doi.org/10.1016/j.apcatb.2022.121371.

[27] C. Li, G. Ding, X. Liu, P. Huo, Y. Yan, Y. Yan, G. Liao, Photocatalysis over NH_2-UiO-66/$CoFe_2O_4$/CdIn2S4 double p-n junction: Significantly promoting photocatalytic performance by double internal electric fields, Chem. Eng. J. 435 (2022) 134740. https://doi.org/10.1016/j.cej.2022.134740.

[28] C. Zhu, C. Liu, Y. Zhou, Y. Fu, S. Guo, H. Li, S. Zhao, H. Huang, Y. Liu, Z. Kang, Carbon dots enhance the stability of CdS for visible-light-driven overall water splitting, Appl. Catal. B Environ. 216 (2017) 114–121. https://doi.org/10.1016/j.apcatb.2017.05.049.

[29] G. Liao, Y. Gong, L. Zhang, H. Gao, G.-J. Yang, B. Fang, Semiconductor polymeric graphitic carbon nitride photocatalysts: the “holy grail” for the photocatalytic hydrogen evolution reaction under visible light, Energy Environ. Sci. 12 (2019) 2080–2147. https://doi.org/10.1039/C9EE00717B.

[30] G. Liao, C. Li, S.Y. Liu, B. Fang, H. Yang, Z-scheme systems: From fundamental principles to characterization, synthesis, and photocatalytic fuel-conversion applications, Phys. Rep. 983 (2022) 1–41. https://doi.org/10.1016/j.physrep.2022.07.003.

[31] C. Bhan, A. Kumar Golder, Bio-based hierarchical vertically aligned 2D ZnO nanostructures for ultra selective electrochemical sensing of p-Chloroaniline, Chem. Eng. J. 475 (2023) 146122. https://doi.org/10.1016/j.cej.2023.146122.

[32] M. Malakootian, A. Nasiri, A. Asadipour, M. Faraji, E. Kargar, A facile and green method for synthesis of ZnFe2O4@CMC as a new magnetic nanophotocatalyst for ciprofloxacin removal from aqueous media, MethodsX. 6 (2019) 1575–1580. https://doi.org/10.1016/j.mex.2019.06.018.

[33] H. Dabhane, S. Ghotekar, P. Tambade, S. Pansambal, H.C.A. Murthy, R. Oza, V. Medhane, A review on environmentally benevolent synthesis of CdS nanoparticle and

their applications, Environ. Chem. Ecotoxicol. 3 (2021) 209–219. https://doi.org/10.1016/j.enceco.2021.06.002.

[34] S. Chahal, J.R. Macairan, N. Yousefi, N. Tufenkji, R. Naccache, Green synthesis of carbon dots and their applications, RSC Adv. 11 (2021) 25354–25363. https://doi.org/10.1039/d1ra04718c.

[35] M. Kurian, A. Paul, Recent trends in the use of green sources for carbon dot synthesis–A short review, Carbon Trends. 3 (2021). https://doi.org/10.1016/j.cartre.2021.100032.

[36] Y. Wang, J. Chen, L. Liu, X. Xi, Y. Li, Z. Geng, G. Jiang, Z. Zhao, Novel metal doped carbon quantum dots/CdS composites for efficient photocatalytic hydrogen evolution, Nanoscale. 11 (2019) 1618–1625. https://doi.org/10.1039/C8NR05807E.

[37] D. Gogoi, R. Koyani, A.K. Golder, N.R. Peela, Enhanced photocatalytic hydrogen evolution using green carbon quantum dots modified 1-D CdS nanowires under visible light irradiation, Sol. Energy. 208 (2020) 966–977. https://doi.org/10.1016/j.solener.2020.08.061.

[38] D. Bano, V. Kumar, V.K. Singh, S.H. Hasan, Green synthesis of fluorescent carbon quantum dots for the detection of mercury(ii) and glutathione, New J. Chem. 42 (2018) 5814–5821. https://doi.org/10.1039/c8nj00432c.

[39] P.K. Yadav, V.K. Singh, S. Chandra, D. Bano, V. Kumar, M. Talat, S.H. Hasan, Green synthesis of fluorescent carbon quantum dots from Azadirachta indica leaves and their peroxidase-mimetic activity for the detection of H_2O_2 and ascorbic acid in common fresh fruits, ACS Biomater. Sci. Eng. 5 (2019) 623–632. https://doi.org/10.1021/acsbiomaterials.8b01528.

[40] P.K. Yadav, S. Chandra, V. Kumar, D. Kumar, S.H. Hasan, Carbon Quantum Dots: Synthesis, Structure, Properties, and Catalytic Applications for Organic Synthesis, Catalysts. 13 (2023). https://doi.org/10.3390/catal13020422.

[41] H. Feng, Q. Guo, Y. Xu, T. Chen, Y. Zhou, Y. Wang, M. Wang, D. Shen, Surface Nonpolarization of g-C_3N_4 by Decoration with Sensitized Quantum Dots for Improved CO_2 Photoreduction, ChemSusChem. 11 (2018) 4256–4261. https://doi.org/10.1002/cssc.201802065.

[42] F. Mujeeb, P. Bajpai, N. Pathak, Phytochemical Evaluation, Antimicrobial Activity, and Determination of Bioactive Components from Leaves of Aegle marmelos, Biomed Res. Int. 2014 (2014) 1–11. https://doi.org/10.1155/2014/497606.

[43] G. Angajala, P. Pavan, R. Subashini, One-step biofabrication of copper nanoparticles from Aegle marmelos correa aqueous leaf extract and evaluation of its anti-

inflammatory and mosquito larvicidal efficacy, RSC Adv. 4 (2014) 51459–51470. https://doi.org/10.1039/C4RA10003D.

[44] H. K, A review on carbon quantum dot/semiconductor-based nanocomposites as hydrogen production photocatalysts, RSC Adv. 14 (2024) 23404–23422. https://doi.org/10.1039/D4RA04149F.

[45] Y. Yao, H. Zhang, K. Hu, G. Nie, Y. Yang, Y. Wang, X. Duan, S. Wang, Carbon dots based photocatalysis for environmental applications, J. Environ. Chem. Eng. 10 (2022) 107336. https://doi.org/10.1016/j.jece.2022.107336.

[46] A. Sankhla, R. Sharma, R.S. Yadav, D. Kashyap, S.L. Kothari, S. Kachhwaha, Biosynthesis and characterization of cadmium sulfide nanoparticles - An emphasis of zeta potential behavior due to capping, Mater. Chem. Phys. 170 (2016) 44–51. https://doi.org/10.1016/j.matchemphys.2015.12.017.

[47] A. Chowdhury, C. Bhan, N.R. Peela, A.K. Golder, A tunable bioinspired process of SnO_2 NPs synthesis for electrochemical CO_2-into-formate conversion, J. CO2 Util. 66 (2022) 102263. https://doi.org/10.1016/j.jcou.2022.102263.

[48] Y. Chai, J. Lu, L. Li, D. Li, M. Li, J. Liang, TEOA-induced in situ formation of wurtzite and zinc-blende CdS heterostructures as a highly active and long-lasting photocatalyst for converting CO_2 into solar fuel, Catal. Sci. Technol. 8 (2018) 2697–2706. https://doi.org/10.1039/C8CY00274F.

[49] Z. Zhu, J. Qin, M. Jiang, Z. Ding, Y. Hou, Enhanced selective photocatalytic CO_2 reduction into CO over Ag/CdS nanocomposites under visible light, Appl. Surf. Sci. 391 (2017) 572–579. https://doi.org/10.1016/j.apsusc.2016.06.148.

[50] J. Li, B. Zhang, J. Lu, Z. Guo, M. Zhang, D. Li, Z. Zhao, S. Song, Y. Liu, L. Qin, A CQD/CdS/g-C_3N_4 photocatalyst for dye and antibiotic degradation: Dual carrier driving force and tunable electron transfer pathway, Sep. Purif. Technol. 305 (2023) 122333. https://doi.org/10.1016/j.seppur.2022.122333.

[51] Z. Zhang, S. Lin, X. Li, H. Li, W. Cui, Metal free and efficient photoelectrocatalytic removal of organic contaminants over g-C_3N_4 nanosheet films decorated with carbon quantum dots, RSC Adv. 7 (2017) 56335–56343. https://doi.org/10.1039/c7ra11205j.

[52] P. George, P. Chowdhury, Complex dielectric transformation of UV-vis diffuse reflectance spectra for estimating optical band-gap energies and materials classification, Analyst. 144 (2019) 3005–3012. https://doi.org/10.1039/c8an02257g.

[53] C. Wang, K. Yang, X. Wei, S. Ding, F. Tian, F. Li, One-pot solvothermal synthesis of carbon dots/Ag nanoparticles/TiO_2 nanocomposites with enhanced photocatalytic

performance, Ceram. Int. 44 (2018) 22481–22488. https://doi.org/10.1016/j.ceramint.2018.09.017.

[54] C. Zhao, Z. Liao, W. Liu, F. Liu, J. Ye, J. Liang, Y. Li, Carbon quantum dots modified tubular g-C3N4 with enhanced photocatalytic activity for carbamazepine elimination: Mechanisms, degradation pathway and DFT calculation, J. Hazard. Mater. 381 (2020) 120957. https://doi.org/10.1016/j.jhazmat.2019.120957.

[55] T. Kulandaivalu, S. Abdul Rashid, N. Sabli, T.L. Tan, Visible light assisted photocatalytic reduction of CO_2 to ethane using CQDs/Cu_2 O nanocomposite photocatalyst, Diam. Relat. Mater. 91 (2019) 64–73. https://doi.org/10.1016/j.diamond.2018.11.002.

[56] Y. Wang, X. Liu, X. Han, R. Godin, J. Chen, W. Zhou, C. Jiang, J.F. Thompson, K.B. Mustafa, S.A. Shevlin, J.R. Durrant, Z. Guo, J. Tang, Unique hole-accepting carbon-dots promoting selective carbon dioxide reduction nearly 100% to methanol by pure water, Nat. Commun. 11 (2020) 1–9. https://doi.org/10.1038/s41467-020-16227-3.

[57] M. Moniruzzaman, J. Kim, Shape-engineered carbon quantum dots embedded on CdS-nanorods for enhanced visible light harvesting towards photocatalytic application, Appl. Surf. Sci. 552 (2021). https://doi.org/10.1016/j.apsusc.2021.149372.

[58] A.P. Singh, S. Kumar, M. Thirumal, Efficient Charge Transfer in Heterostructures of CdS/$NaTaO_3$ with Improved Visible-Light-Driven Photocatalytic Activity, ACS Omega. 4 (2019) 12175–12185. https://doi.org/10.1021/acsomega.9b01133.

[59] D. Gogoi, A.K. Shah, P. Rambabu, M. Qureshi, A.K. Golder, N.R. Peela, Step-Scheme Heterojunction between CdS Nanowires and Facet-Selective Assembly of MnOx - $BiVO_4$ for an Efficient Visible-Light-Driven Overall Water Splitting, ACS Appl. Mater. Interfaces. 13 (2021) 45475–45487. https://doi.org/10.1021/acsami.1c11740.

[60] J. Yu, J. Jin, B. Cheng, M. Jaroniec, A noble metal-free reduced graphene oxide–CdS nanorod composite for the enhanced visible-light photocatalytic reduction of CO_2 to solar fuel, J. Mater. Chem. A. 2 (2014) 3407. https://doi.org/10.1039/c3ta14493c.

[61] H. Li, X. Zhang, D.R. MacFarlane, Carbon quantum dots/Cu2O heterostructures for solar-light-driven conversion of CO2 to methanol, Adv. Energy Mater. 5 (2015) 1–6. https://doi.org/10.1002/aenm.201401077.

[62] M. Pourshaban-Mazandarani, M. Ahmadian, A. Nasiri, A. Poormohammadi, $CuCoFe_2O_4$@AC magnetic nanocomposite as a novel heterogeneous Fenton-like nanocatalyst for Ciprofloxacin degradation from aqueous solutions, Appl. Water Sci. 13 (2023) 1–18. https://doi.org/10.1007/s13201-023-02002-4.

[63] S. Pandiyan, L. Arumugam, S.P. Srirengan, R. Pitchan, P. Sevugan, K. Kannan, G. Pitchan, T.A. Hegde, V. Gandhirajan, Biocompatible carbon quantum dots derived from sugarcane industrial wastes for effective nonlinear optical behavior and antimicrobial activity applications, ACS Omega. 5 (2020) 30363–30372. https://doi.org/10.1021/acsomega.0c03290.

[64] S. Manchala, A. Gandamalla, N.R. Vempuluru, S. Muthukonda Venkatakrishnan, V. Shanker, High potential and robust ternary $LaFeO_3$/CdS/carbon quantum dots nanocomposite for photocatalytic H_2 evolution under sunlight illumination, J. Colloid Interface Sci. 583 (2021) 255–266. https://doi.org/10.1016/j.jcis.2020.08.125.

[65] C.G. Cho, Y.G. You, H.Y. Jang, J.K. Woo, S.K. An, Synthesis of poly(styrene-b-styrenesulfonic acid) and its blend with PPO for proton exchange membrane, J. Nanosci. Nanotechnol. 6 (2006) 3665–3669. https://doi.org/10.1166/jnn.2006.078.

[66] N.S. Nirmala Jothi, P. Dennis Christy, A.R. Baby Suganthi, G. Ramalingam, P. Sagayaraj, Development of CdS nanorods of high aspect ratio under hydrothermal conditions with PEG template, J. Cryst. Growth. 316 (2011) 126–131. https://doi.org/10.1016/j.jcrysgro.2010.12.055.

[67] P. Fatahi, A. Roy, M. Bahrami, S.J. Hoseini, Visible-light-driven efficient hydrogen production from CdS nanorods anchored with Co-catalysts based on transition metal alloy nanosheets of NiPd, NiZn, and NiPdZn, ACS Appl. Energy Mater. 1 (2018) 5318–5327. https://doi.org/10.1021/acsaem.8b00900.

[68] R.K. Chava, N. Son, Y.S. Kim, M. Kang, Controlled Growth and Bandstructure Properties of One Dimensional Cadmium Sulfide Nanorods for Visible Photocatalytic Hydrogen Evolution Reaction, Nanomaterials. 10 (2020) 619. https://doi.org/10.3390/nano10040619.

[69] S.M. Chaudhari, P.M. Gawal, P.K. Sane, S.M. Sontakke, P.R. Nemade, Solar light-assisted photocatalytic degradation of methylene blue with Mo/TiO_2: a comparison with Cr- and Ni-doped TiO_2, Res. Chem. Intermed. 44 (2018) 3115–3134. https://doi.org/10.1007/s11164-018-3296-1.

[70] C. Wei, L. Tan, Y. Zhang, S. Xiong, J. Feng, Metal-organic frameworks and their derivatives in stable Zn metal anodes for aqueous Zn-ion batteries, ChemPhysMater. 1 (2022) 252–263. https://doi.org/10.1016/j.chphma.2021.09.003.

[71] R. Chen, X. Cheng, X. Zhu, Q. Liao, L. An, D. Ye, X. He, Z. Wang, High-performance optofluidic membrane microreactor with a mesoporous CdS/TiO_2 /SBA-15@carbon paper composite membrane for the CO_2 photoreduction, Chem. Eng. J. 316 (2017) 911–

918. https://doi.org/10.1016/j.cej.2017.02.044.

[72] J. Lin, Y. Li, The influence of inorganic anions on photocatalytic CO2 reduction, Catal. Sci. Technol. 10 (2020) 959–966. https://doi.org/10.1039/c9cy02180a.

[73] X. Li, H. Liu, D. Luo, J. Li, Y. Huang, H. Li, Y. Fang, Y. Xu, L. Zhu, Adsorption of CO_2 on heterostructure $CdS(Bi_2S_3)/TiO_2$ nanotube photocatalysts and their photocatalytic activities in the reduction of CO_2 to methanol under visible light irradiation, Chem. Eng. J. 180 (2012) 151–158. https://doi.org/10.1016/j.cej.2011.11.029.

[74] M.M. Kandy, V.G. Gaikar, Photocatalytic reduction of CO_2 using CdS nanorods on porous anodic alumina support, Mater. Res. Bull. 102 (2018) 440–449. https://doi.org/10.1016/j.materresbull.2018.02.054.

[75] X. Li, J. Chen, H. Li, J. Li, Y. Xu, Y. Liu, J. Zhou, Photoreduction of CO_2 to methanol over Bi_2S_3/CdS photocatalyst under visible light irradiation, J. Nat. Gas Chem. 20 (2011) 413–417. https://doi.org/10.1016/S1003-9953(10)60212-5.

[76] S. Ijaz, M.F. Ehsan, M.N. Ashiq, N. Karamat, T. He, Preparation of $CdS@CeO_2$ core/shell composite for photocatalytic reduction of CO_2 under visible-light irradiation, Appl. Surf. Sci. 390 (2016) 550–559. https://doi.org/10.1016/j.apsusc.2016.08.098.

[77] M.M. Kandy, V.G. Gaikar, Continuous photocatalytic reduction of CO_2 using nanoporous reduced graphene oxide (RGO)/cadmium sulfide (CdS) as catalyst on porous anodic alumina (PAA)/aluminum support, J. Nanosci. Nanotechnol. 19 (2019) 5323–5331. https://doi.org/10.1166/jnn.2019.16817.

[78] Q. Mou, Z. Guo, Y. Chai, B. Liu, C. Liu, Visible light assisted production of methanol from CO_2 using $CdS@CeO_2$ heterojunction, J. Photochem. Photobiol. B Biol. 219 (2021) 112205. https://doi.org/10.1016/j.jphotobiol.2021.112205.

[79] D. Meissner, C. Benndorf, R. Memming, Photocorrosion of cadmium sulfide: Analysis by photoelectron spectroscopy, Appl. Surf. Sci. 27 (1987) 423–436. https://doi.org/10.1016/0169-4332(87)90152-8.

[80] C. Yang, Y. Zhang, F. Xiong, Y. Sun, Photocorrosion of CdS nanorod arrays and fabrication of $CdS@TiO_2$ core@shell nanorod arrays by atomic layer deposition for improved photostability, Opt. Mater. X. 9 (2021) 100070. https://doi.org/10.1016/j.omx.2021.100070.

CHAPTER 4

Phytochemicals-based Synthesis of Z-Scheme In_2O_3/CdS Heterostructures: DFT Analysis and Photocatalytic CO_2 Reduction to HCOOH and CO

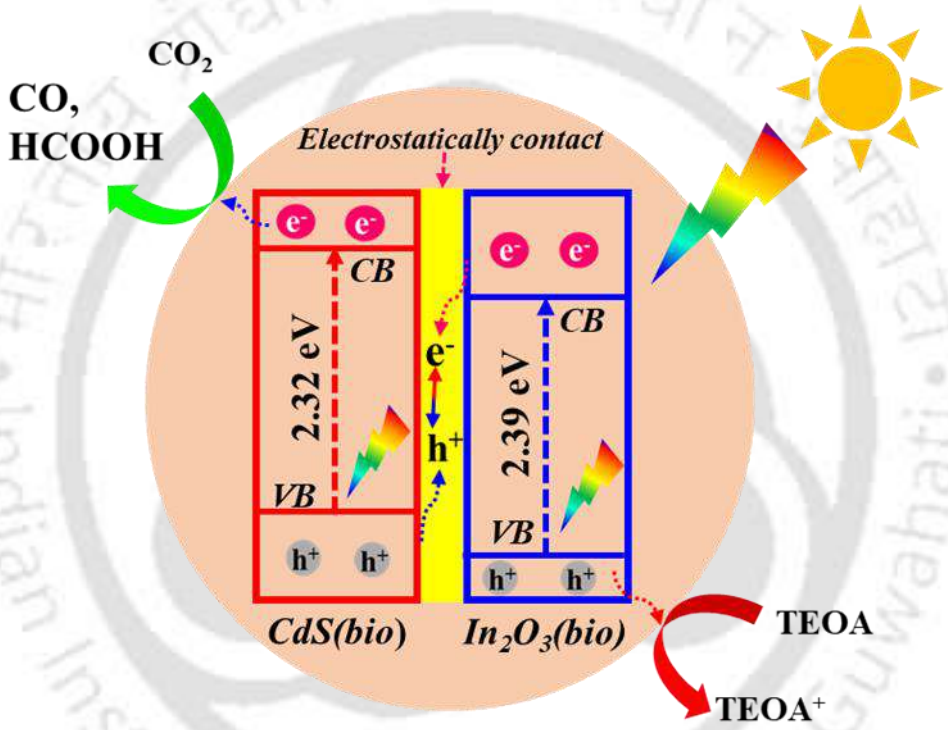

Chapter highlights

- CdS(bio) and In_2O_3(bio) NPs synthesized using plant-based phytochemicals
- Photocorrosion of CdS(bio) forming SO_4^{2-} inhibited in In_2O_3/CdS(bio) heterostructures
- Band overlapping of In_2O_3/CdS heterostructure near Fermi level reducing its bandgap
- In_2O_3(bio) incorporation in heterostructure is conducive to CO_2 adsorption by fivefold
- HCOOH/CO production of 514.4/162 μmol/g·h (AQY 4.44/2.45%) over In_2O_3/CdS(bio)

4.1 Introduction

The growing energy demands have a significant impact on the health of the environment due to greenhouse gas emissions. Therefore, there is a need for technologies that could alleviate the consequences arising from greenhouse gas emissions [1,2]. Photocatalytic CO_2 reduction reaction (PCO_2RR) has emerged as an attractive technique for utilizing CO_2 by harnessing abundant solar energy and water to produce valuable fuels such as ethanol, methanol, formic acid, carbon dioxide, and methane [3,4]. This approach meets energy requirements while mitigating greenhouse gas impact. Semiconductor materials with tuneable bandgaps and broad wavelength responses are ideal for PCO_2RR, and research in this field has gained significant interest since the pioneering work on p-type gallium phosphide in 1982 [5]. Subsequently, various semiconductors have been developed for effective CO_2 conversion into fuels [4,6–11].

CdS has gained significant attention for PCO_2RR owing to its favorable properties such as high solar energy conversion, favorable bandgap (2.42 eV), strong conduction band position (-0.92 eV), strong chemical and thermal stability, excellent transport characteristics, tunable size and shape [12–15]. However, CdS faces challenges such as photocorrosion and rapid charge carrier recombination, limiting its further development and application [16,17]. Therefore, various modification techniques have been explored to address these limitations and enhance CdS catalytic performance in PCO_2RR. Modifications such as morphology control, heterostructures, Z-scheme systems, and co-catalyst integration have been explored to boost the catalytic efficiency of CdS for PCO_2RR by improving charge separation by reducing its recombination [18–20].

Constructing heterojunctions is crucial in facilitating charge separation and mitigating photocorrosion issues in CdS-based semiconductors. Two common heterostructures used in CdS-based catalysts are Type-II and Z-scheme. The type II and Z scheme heterostructures exhibit an identical structure except for the difference in the charge migration pathways. In the Z-scheme heterostructure, the conduction band (CB) of one semiconductor is higher than the CB of the other, while the valence band (VB) of the second semiconductor is higher than the VB of the first, enabling an efficient electron transfer and minimizing interlayer recombination. In the Z-scheme, the electron and the holes with a small redox potential in either semiconductor combine, retaining the electron and holes with superior redox potentials [21–23]. In Type-II heterostructure, the photogenerated electron and holes accumulate in the CB and VB of the semiconductor with a lesser reduction and oxidation efficiency, respectively. Hence,

significant band offsets between the CB and VB levels of the two semiconductors are essential for efficient charge separation and photocatalytic activity, often facilitated by built-in electric field gradients at the interface [24–26]. In comparison to a Type II heterostructure, Z-scheme has a better charge separation efficiency and a stronger negative reduction potential, effectively addressing the issue of photocorrosion of CdS [4].

In_2O_3 is gaining prominence as a photocatalyst due to its notable properties, such as multiple oxidation states, higher electron production, trapping, mobility, and relatively cheap [27]. In_2O_3 has a 2.8 eV bandgap, with CB and VB positions of -0.6 and 2.2 eV, respectively [28]. CdS and In_2O_3 are both n-type semiconductors with well-aligned Fermi energy levels, enabling band bending and facilitating the creation of an efficient Z-scheme heterostructure [4,8]. In this configuration, the photogenerated electrons (e^-) in the CdS CB and holes (h^+) in the In_2O_3 VB with strong redox abilities are retained. While the photogenerated e^- in the In_2O_3 CB and h^+ in the CdS VB with lower redox power are recombined. As a result, the Z-scheme structure exhibits high redox capabilities while efficiently preventing photocorrosion triggered by holes of CdS at VB [4,29]. To achieve this, it is essential to ensure that semiconductor materials' band structure and Fermi levels are well-matched with CdS.

Bio-based synthesis methods of nanoparticles (NPs) offer benefits over chemical approaches, including eco-friendliness, economic efficiency, simplicity, and availability of plentiful bio-sources [1,30]. The Northeastern parts of India are well known for their resource reservation and the indigenous bio-analytes that exist in various plants that could efficiently serve as capping and reducing agents for the green synthesis of semiconductor NPs [31]. The rate of formation of NPs in a bio-based process can be further accelerated by several folds with short microwave irradiation.

In this Chapter, bio-based In_2O_3/CdS(bio)(oxide/sulfide) heterostructures are synthesized with vegetal phytochemicals found in *Aegle marmelos* in combination with microwave irradiation. The local name of *Aegle Marmelos* is 'Bael,' and it is abundantly present in India, Pakistan, Bangladesh, Sri Lanka, Nepal, Malaysia, Myanmar, Thailand, and most of the East Asian countries. The *Aegle marmelos* constituents, including flavonoids, alkaloids, tannins, phenols, and saponins, served as effective reducing and capping agents [1]. DFT was used for geometry optimization, band structure, and DOS analysis of synthesized catalysts. The synthesized catalyst was evaluated for PCO_2RR under visible light, producing HCOOH and CO. Moreover, the stability and reusability of these heterostructures were tested. This study introduces a novel bio-based synthesis of heterostructures for efficient PCO_2RR, specifically targeting HCOOH and CO production.

4.2 Results and discussion

4.2.1 Characterizations of photocatalyst

UV-Spectra: Figure 4.1a displays the absorption spectra of synthesized catalysts. The absorption threshold of CdS(bio) and In_2O_3(bio) nanoparticles was observed at 530 nm and 440 nm, respectively, which is consistent with earlier reports [14,32]. In_2O_3(bio) has a limited visible light range than CdS(bio). The absorption edge of In_2O_3/CdS(bio) heterostructures displayed a redshift, enhancing its light absorption in the visible range. Hence, the broadening light absorption ranges could enhance the generation of e^-/h^+ pairs [1]. The bandgap was calculated by the Tauc equation (Eq. 4.1)[1].

$$\alpha = \frac{(h\nu - E_g)^n}{h\nu} \quad (4.1)$$

Where hν, α, and E_g represent the incident photon energy, absorption coefficient, and bandgap energy, respectively, while n denotes a constant (½ the direct allowed transition). **Figure 4.1b** illustrates the plot of $(\alpha h\nu)^{1/2}$ vs. photon energy. The calculated bandgap for CdS(bio), In_2O_3(bio), and 0.4In_2O_3/CdS(bio) heterostructures is 2.32, 2.39, and 2.22 eV, respectively, aligning with earlier reported values [14,32]. The reduced heterostructures bandgap compared to the CdS(bio) and In_2O_3(bio) is attributed to decreased nanoparticle size, confining electrons to a smaller space and leading to a decreased bandgap [33].

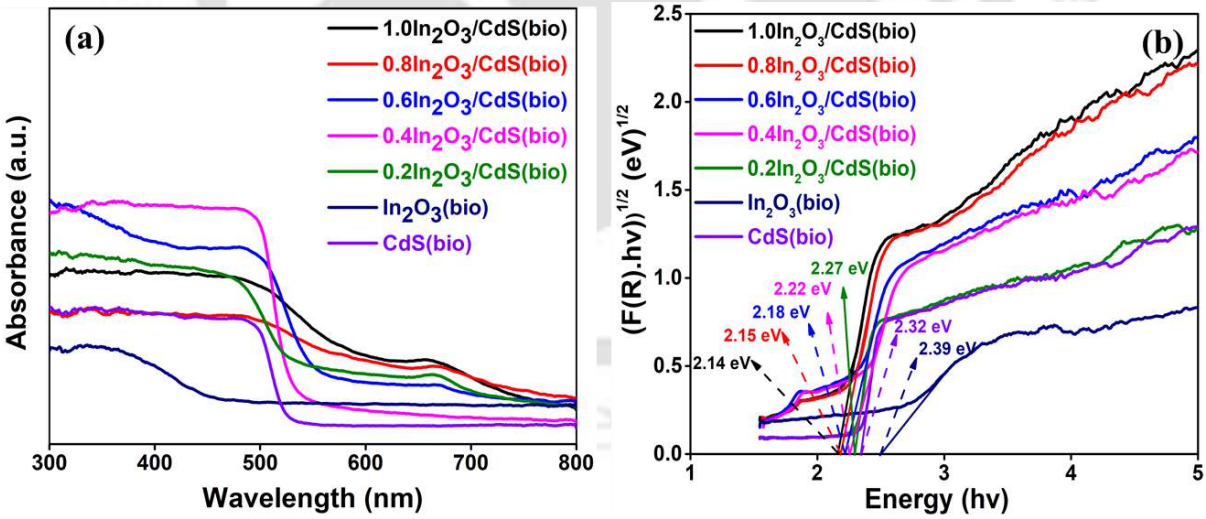

Figure 4.1. (a) UV-Vis absorption spectra and (b) Tauc plot of CdS(bio), In_2O_3(bio), and In_2O_3/CdS(bio) heterostructures.

Ultraviolet photoelectron spectroscopy (UPS) valence band (VB) spectra: The position of the CB of photocatalyst samples is vital for evaluating PCO_2RR potential. Using UPS, the minimal VB of the photocatalysts was determined and is illustrated in **Figure 4.2a**.

The minimal VB of each sample is calculated using linear extrapolation, resulting in values of 1.53 eV for CdS(bio), 2.1eV for In_2O_3(bio), and 1.37 eV for 0.4In_2O_3/CdS(bio) heterostructures. Using UPS and bandgap, the maximal of CB was determined via the equation $Eg=E_{VB}- E_{CB}$ [1]. The maximal CB values of -0.79 eV for CdS(bio), -0.29 eV for In_2O_3(bio), and -0.85 eV for 0.4In_2O_3/CdS(bio) were determined [8,15]. **Figure 4.2b** shows the energy level diagram of In_2O_3(bio), CdS(bio), and 0.4In_2O_3/CdS(bio) heterostructures, indicating a promising maximal CB position for enhanced formic acid and carbon monoxide production rates.

The work function (φ) is calculated using Eq. 4.2[16]. The Fermi level (E_F) is obtained from the work function using Eq. 4.3.

$$\Phi = h\nu - E_{cutoff} \quad (4.2)$$

$$E_F = -\varphi \quad (4.3)$$

Here, hν = 21.22 eV represents the energy of the monochromatic ionizing light, while E_{cutoff} is determined by the intersection of the secondary electron cut-off at a high binding energy. The UPS VB spectra for secondary electron onset are presented in **Figure 4.3**. For CdS(bio), the measured value of secondary electron cut-off energy is 16.46 eV, with a calculated work function of 4.76 eV. In the case of In_2O_3(bio), E_{cutoff} energy is 15.58 eV, corresponding to a work function value of 5.64 eV. Similarly, for 0.4In_2O_3/CdS(bio) heterostructure, the cut-off energy is 16.40 eV, giving the work function value of 4.82 eV. The Fermi level of CdS(bio), In_2O_3(bio), and 0.4In_2O_3/CdS(bio) heterostructure is calculated as -4.76, -5.64, and -4.82 eV, respectively [34,35].

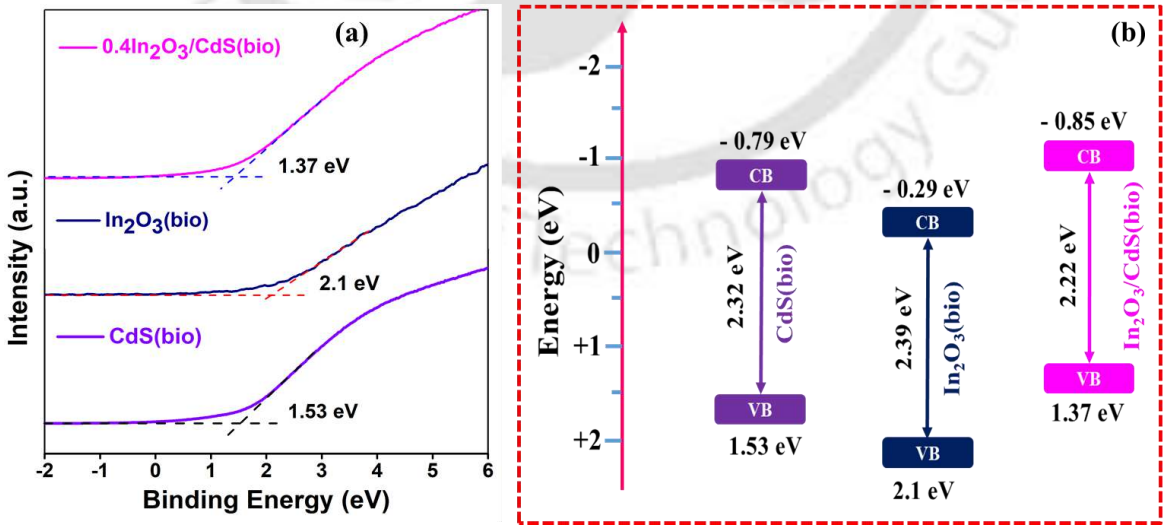

Figure 4.2. (a) UPS VB spectra and (b) Energy level diagram of CdS(bio), In_2O_3(bio), and In_2O_3/CdS(bio) heterostructures.

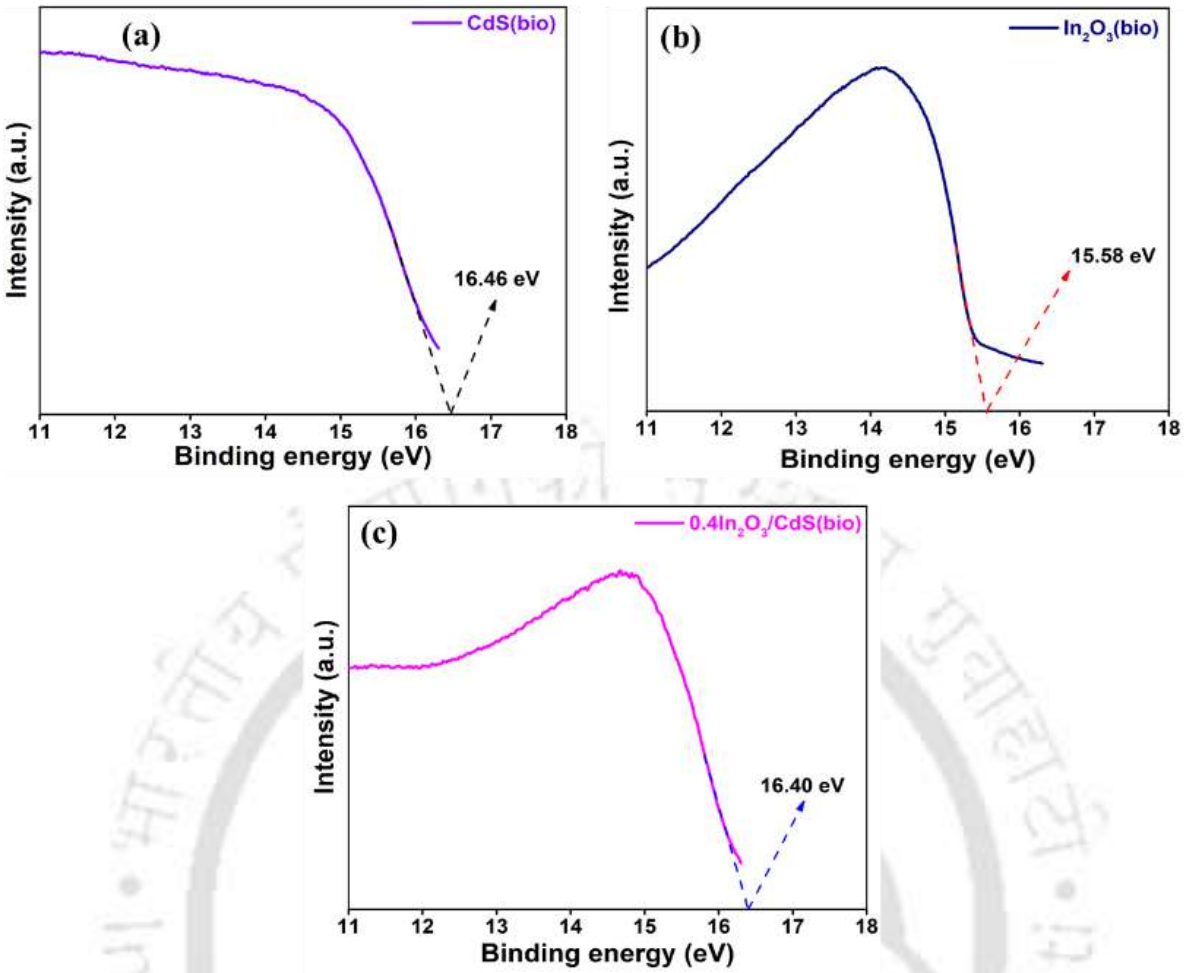

Figure 4.3. UPS VB spectra for secondary electron onset.

XRD analysis: Figure 4.4 displays the XRD diffraction pattern of synthesized catalysts. For CdS(bio), the peaks position at 2θ= 25.06(100), 26.67(002), 28.40(101), 36.96(102),, 43.92(110), 48.10(103), and 52.23°(112) cubic structure of CdS (JCPDF database: 00-001-0783). For In_2O_3(bio) specimen, the peaks position at 2θ= 30.70(222), 35.60(400), 51.28(440), and 60.90°(622) correspond to its cubic crystal structure (JCPDF database: 00-001-0929). The peak position perfectly matches the reported literature [36,37]. In In_2O_3/CdS(bio) heterostructures, In_2O_3 peaks are absent due to its low content (<1% molar ratio), its uniform distribution, and small particle size, falling below the XRD detection limit, while CdS(bio) peak positions remain consistent across all heterostructures. The crystal size was determined using Debye-Scherrer's equation (Eq. 4.4) [38].

$$D = \frac{K\,\lambda}{\beta\,Cos\theta} \qquad (4.4)$$

Where λ represents the X-ray radiation wavelength (Cu Kα=0.1540 nm), D represents the average crystal size, K denotes a dimensionless factor (0.89), β stands for FWHM, and θ

denotes the diffraction angle. The crystal size of CdS(bio), In_2O_3(bio), and In_2O_3/CdS(bio) heterostructures was determined to be 7.76, 8.73, and 17.76 nm, respectively.

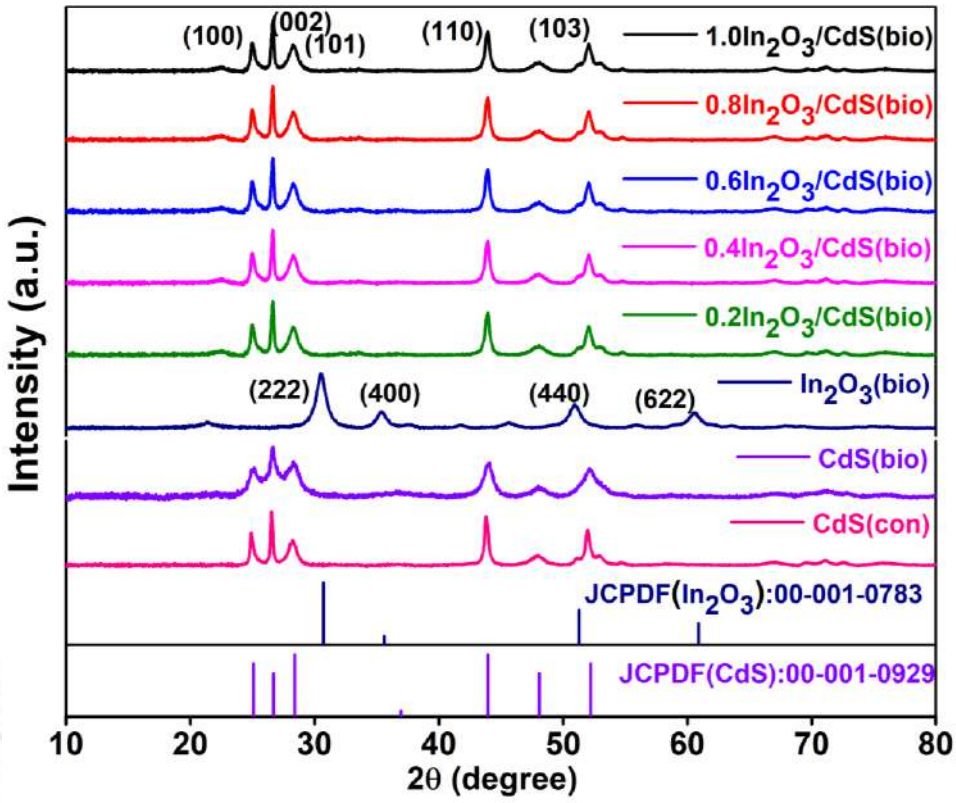

Figure 4.4. X-ray diffraction patterns of CdS(bio), In_2O_3(bio), and In_2O_3/CdS(bio) heterostructures.

XPS analysis: XPS survey spectra in **Figure 4.5a** confirm the presence of In, Cd, O, and S in In_2O_3/CdS(bio) heterostructures. The high resolution of Cd 3d of CdS(bio) (**Figure 4.5b**) shows peaks at 405.3 and 412.2 eV, corresponding to the Cd $3d_{5/2}$ and Cd $3d_{3/2}$ peaks of Cd^{2+}, respectively [32]. The S 2p spectrum of CdS(bio) (**Figure 4.5c**) displays peaks at 161.87 and 163.16 eV, attributed to the S $2p_{3/2}$ and S $2p_{1/2}$ peaks of S^{2-} [39]. In 3d of In_2O_3(bio) (**Figure 4.5d**) exhibited two peaks 444.2 and 451.8 eV, corresponding to the $In3d_{5/2}$ and $In3d_{3/2}$ of In^{3+}, respectively [40]. The O1s spectrum of In_2O_3(bio) (**Figure 4.5e**) exhibits two characteristic peaks at 529.6 eV and 531.4 eV, indicating lattice oxygen and surface hydroxyl oxygen, respectively [41]. The In 3d, O 1s, Cd 3d, and S 2p spectra of In_2O_3/CdS(bio) heterostructures showed a similar trend. The negative shift in the binding energy peak of In 3d and Cd 3d and the positive shift of S 2p suggest a strong interaction at the interfacial zone between CdS and In_2O_3, indicative of the formation of heterostructures. The In, O, Cd, and S binding energies closely match with earlier reported studies, confirming the formation of the In_2O_3/CdS(bio) heterostructures [32,39].

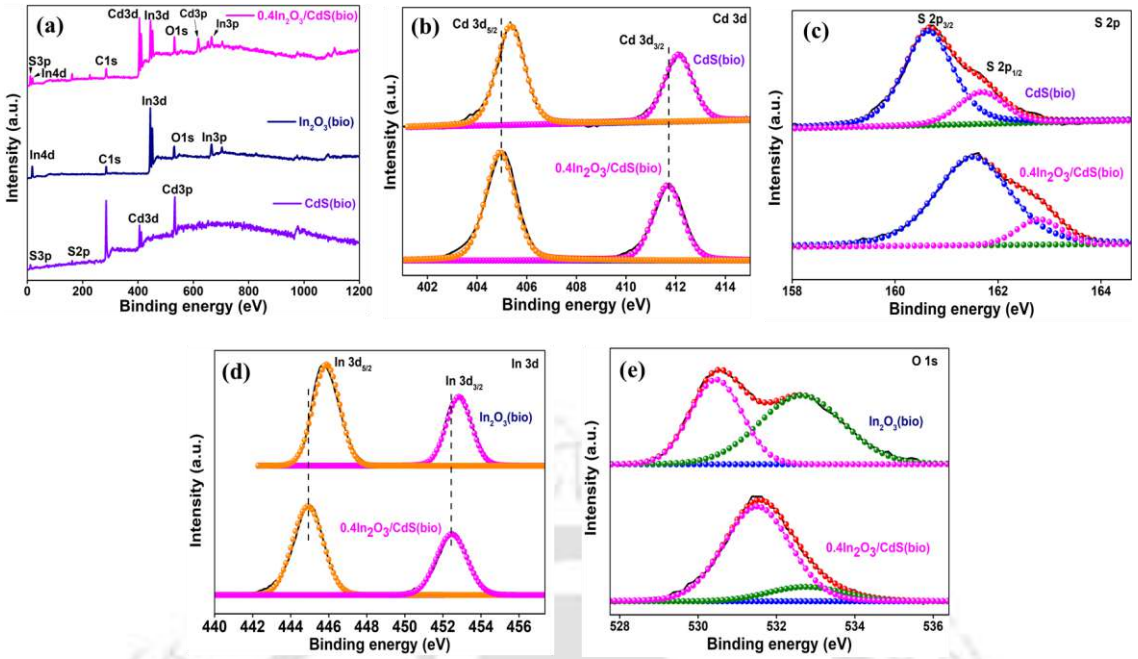

Figure 4.5. (a) XPS survey spectra, (b & c) high-resolution spectra for Cd 3d and S 2p of CdS(bio) and 0.4In_2O_3/CdS(bio) heterostructure, and (d & e) In 3d and O 1s of In_2O_3(bio) and 0.4In_2O_3/CdS(bio) heterostructure.

FESEM and FETEM analysis: FESEM images of synthesized catalysts are shown in **Figures 4.6a-4.6c.** CdS(bio), In_2O_3(bio), and In_2O_3/CdS(bio) NPs with defined shapes were successfully synthesized using the proposed bio-based approach. No specific structural development of In_2O_3 and CdS NPs was observed for In_2O_3(con), CdS(con), and In_2O_3/CdS(bio) heterostructures (con) (**Figures 4.6d-4.6f**). The average size of In_2O_3(bio), CdS(bio), and In_2O_3/CdS(bio) heterostructures were 75, 250, and 25 nm, respectively[42,43]. The positive charge of CdS(bio) nanoparticles, as confirmed by zeta potential (**Table 4.1**), allows them to electrostatically adsorb negatively charged In^{3+} ions. Subsequently, these ions react with oxygen sources to form In_2O_3. After In_2O_3 growth, the resulting In_2O_3/CdS(bio) heterostructures undergo noticeable morphological changes [32].

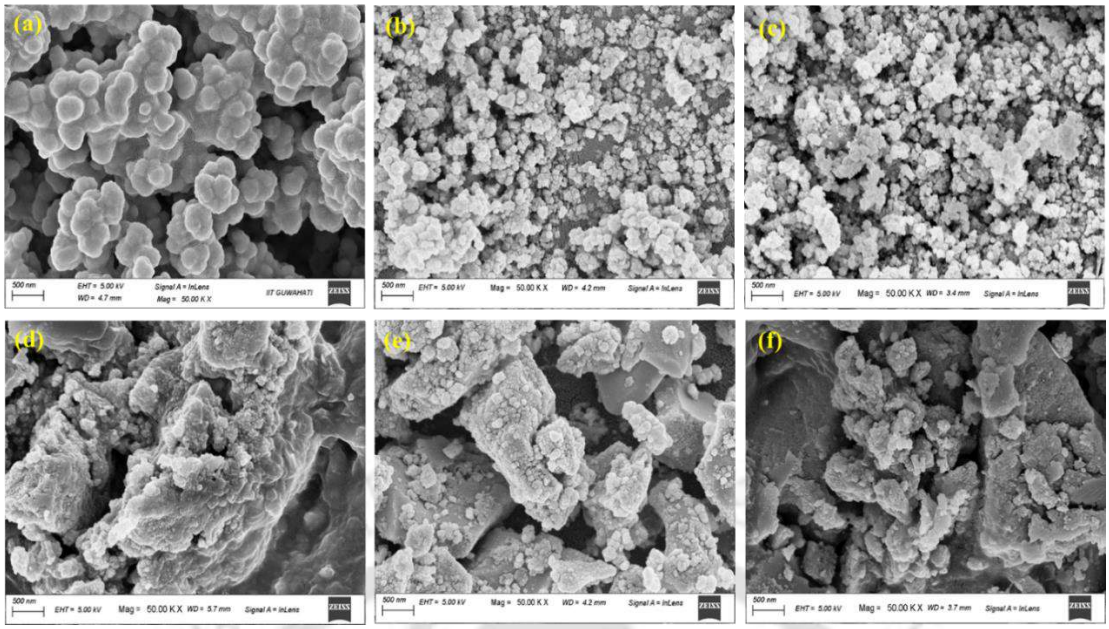

Figure 4.6. FESEM images of (a) CdS(bio), (b) In_2O_3(bio), (c) 0.4In_2O_3/CdS(bio) heterostructure, (d) CdS(con), (e) In_2O_3(con), and (f) 0.4In_2O_3/CdS(con) heterostructure.

Table 4.1. Hydrodynamic diameter of CdS(bio), In_2O_3(bio), and In_2O_3/CdS(bio) heterostructures.

Catalysts	Hydrodynamic diameter (nm)	Zeta potential (mV)
CdS(bio)	312.3	20.6
In_2O_3(bio)	289.2	-42.23
0.2In_2O_3/CdS(bio)	189.3	-12.6
0.4In_2O_3/CdS(bio)	219.2	-13.9
0.6In_2O_3/CdS(bio)	245.6	-22.23
0.8In_2O_3/CdS(bio)	286.3	-25.67
1.0In_2O_3/CdS(bio)	314.5	-30.32

Figures 4.7a-4.7c show the FETEM of CdS(bio), In_2O_3(bio), and In_2O_3/CdS(bio) heterostructures, with average sizes of 250.2, 74.8, and 25.1 nm, respectively, are consistent with FESEM studies. In the heterostructures, the In_2O_3(bio) NPs seem to be more uniformly distributed. This suggests that CdS(bio) NPs could provide excellent support for the uniform growth of In_2O_3(bio) NPs, which occur without the surfactants. This could be beneficial for enhancing surface area and exposing more active sites compared with CdS(bio) and In_2O_3(bio) nanoparticles. To confirm the combination of CdS(bio) and In_2O_3(bio), HRTEM micrograph of 0.4In_2O_3/CdS(bio) heterostructures was recorded (**Figure 4.7d)**. The d-spacings of

In_2O_3(bio) and CdS(bio) are 0.28 and 0.35 nm, corresponding to the(222) and (100) planes, respectively, indicating the formation of In_2O_3/CdS(bio) heterostructures [44,45]. Additionally, the SAED patterns of 0.4In_2O_3/CdS(bio) heterostructures (**Figure 4.7d**(inset)) exhibited a polycrystalline nature, supporting the formation of In_2O_3/CdS(bio) heterostructures. The polycrystalline nature of In_2O_3(bio) and CdS(bio) nanoparticles was indicated by SAED patterns (**Figure 4.8**). Furthermore, EDX analysis of 0.4In_2O_3/CdS(bio) heterostructures (**Figure 4.7e** & **Figure 4.9**) shows the contents of Cd, S, In, and O to be 48.05, 21.7, 15.6, and 14.3%, respectively. The mapping of the elements found in the heterostructures is displayed in **Figure 4.7f**.

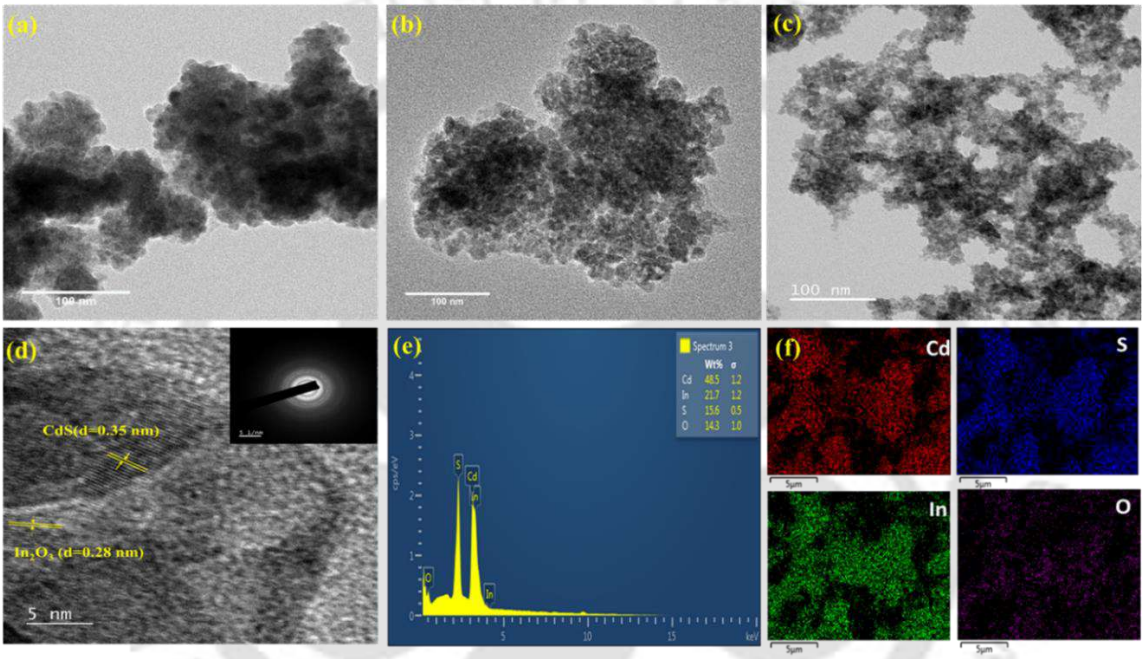

Figure 4.7. FETEM images (a) CdS(bio), (b) In_2O_3(bio), and (c) 0.4In_2O_3/CdS(bio) heterostructure, (d) HRTEM image (inset SAED pattern), (e) EDX spectrum, and (f) Mapping of In, O, Cd, S of 0.4In_2O_3/CdS(bio) heterostructure.

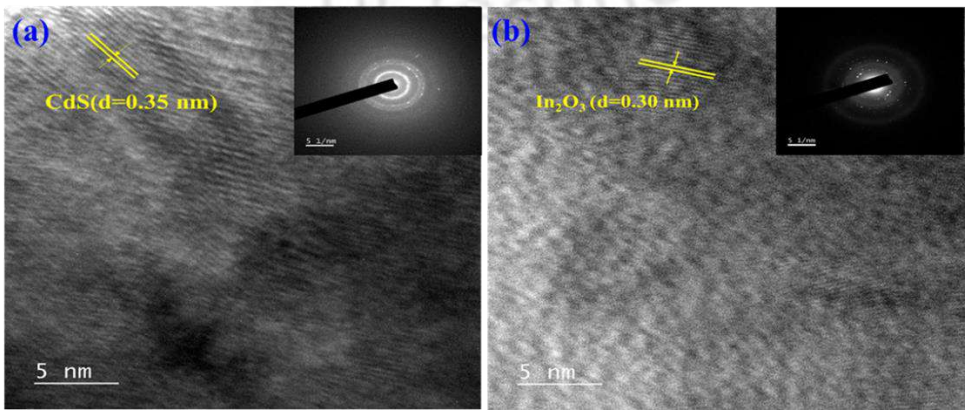

Figure 4.8. HRTEM images and (inset) SAED patterns of (a) CdS(bio) and (b) In_2O_3 (bio).

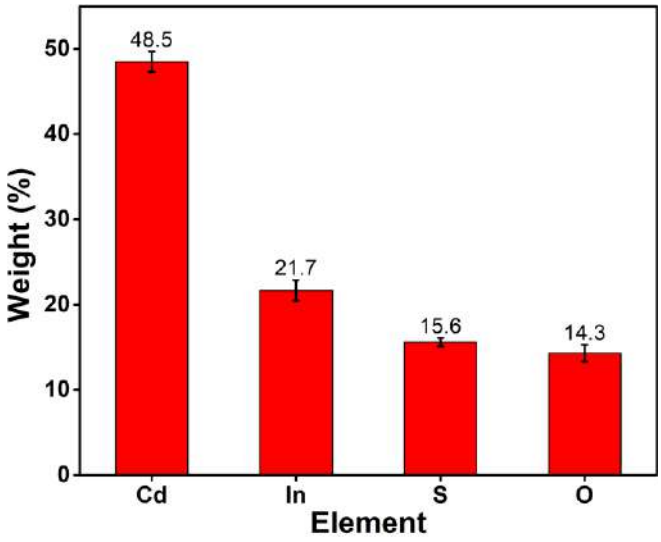

Figure 4.9. Elemental composition from EDX analysis of 0.4In_2O_3/CdS(bio) heterostructure.

PL and TRPL spectra: To investigate the dynamics of e^-/h^+ pairs and its trapping efficiency in the catalysts, PL spectra of CdS(bio) and heterostructures were obtained at the excitation wavelength of 360 nm, while In_2O_3(bio) was obtained at 325nm (**Figure 4.10a**). The In_2O_3(bio), CdS(bio), and In_2O_3/CdS(bio) heterostructures exhibited prominent emission peaks at approximately 450, 460, and 465 nm, respectively. When In_2O_3(bio) is combined with CdS(bio), there is a noticeable reduction in PL intensity, indicating a lower charge carriers recombination rate. In other words, the heterojunction formation accelerates the separation of e^-/h^+ pairs [39]. A comparable finding was documented for CdS/$BiVO_4$ and CdS/WO_3 [21,46].

TRPL spectra (**Figure 4.10b)** of synthesized catalysts were acquired at 450 nm emission and 405 nm excitation wavelengths with 1000 counts to understand the nature of charge carrier lifetime. The TRPL data were fitted using a bi-exponential decay function, and the fitted parameters are presented in **Table 4.2**. The average charge carrier lifetime(τ_{avg}) was determined by Eq. 4.5 [1].

$$\tau_{average} = \frac{A_1 \times \tau_1^2 + A_2 \times \tau_2^2}{A_1 \times \tau_1 + A_2 \times \tau_2} \quad (4.5)$$

Where, τ_1, τ_2 denotes the charge carriers' lifetime and A_1, A_2 represents amplitudes. The average charge carriers lifetime in In_2O_3(bio), CdS(bio), and 0.4In_2O_3/CdS(bio) heterostructures were found to be 2.02, 2.76, and 4.38 ns, respectively. The heterostructures have a higher lifetime of charge carriers than the CdS(bio) and In_2O_3(bio) NPs, indicating that 0.4In_2O_3/CdS(bio) exhibits better separation efficiency of e^-/h^+ pairs than In_2O_3(bio) and CdS(bio). The incorporation of In_2O_3(bio) into CdS(bio) acts as a reservoir for trapping

excited e^- at the In_2O_3 and CdS interface, leading to improved separation of e^-/h^+ pairs and decreased recombination[32,39].

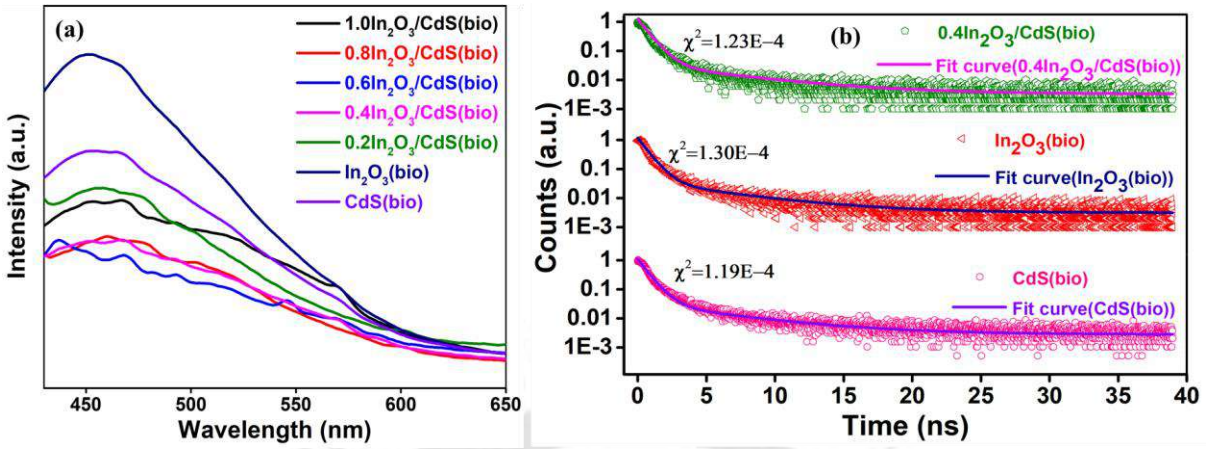

Figure 4.10. (a) Photoluminescence (PL) and (b) Time-resolved photoluminescence (TRPL) spectra of In_2O_3(bio), CdS(bio), and In_2O_3/CdS(bio) heterostructures.

Table 4.2. TRPL data of In_2O_3(bio), CdS(bio), and 0.4In_2O_3/CdS(bio) heterostructure.

Photocatalysts	**A_1 (%)**	**A_2 (%)**	**τ_1 (ns)**	**τ_2 (ns)**	**τ_{ave} (ns)**
In_2O_3(bio)	95.96	4.04	0.7	5.816	2.02
CdS(bio)	6.82	93.18	6.07	0.717	2.76
0.4In_2O_3/CdS(bio)	17.18	82.82	6.4	0.73	4.38

Surface area analysis: Table 4.3 summarizes the results of the N_2 sorption analysis of In_2O_3(bio), CdS(bio), and 0.4In_2O_3/CdS(bio). **Figure 4.11** shows the N_2 sorption isotherms along with the pore size distribution (inset of **Figure 4.11**). The In_2O_3 (bio), CdS(bio), and In_2O_3/CdS(bio) heterostructures exhibited type-II, type-IV, and type-I isotherms, along with type H3, H1, and H2 hysteresis loops. These properties indicate a mesoporous nature with average pore sizes of 11.60, 14.18, and 2.71 nm, respectively. The BET surface area of the In_2O_3/CdS(bio) heterostructures is 217.0 m^2/g, larger than that of CdS(bio) (108.36 m^2/g) and In_2O_3(bio) (37.1 m^2/g). Heterostructures have a substantial surface area and porous properties, offering numerous catalytically active sites for redox reactions [32,47]. Additionally, the CO_2 adsorption ability of 0.4In_2O_3/CdS(bio) heterostructures (0.431 mmol/g) surpasses that of In_2O_3(bio) (0.060 mmol/g) and CdS(bio) (0.087 mmol/g) under 1 bar, as indicated in **Table 4.3**. The residual carbon content (**Table 4.4**) is calculated from the thermogravimetric

calculation between the temperature range of 300-600 °C [42,48]. It was only 1.11 % (w/w) for 0.4In_2O_3/CdS(bio). No carbon presence was observed in In_2O_3(con) (**Figure 4.12).**

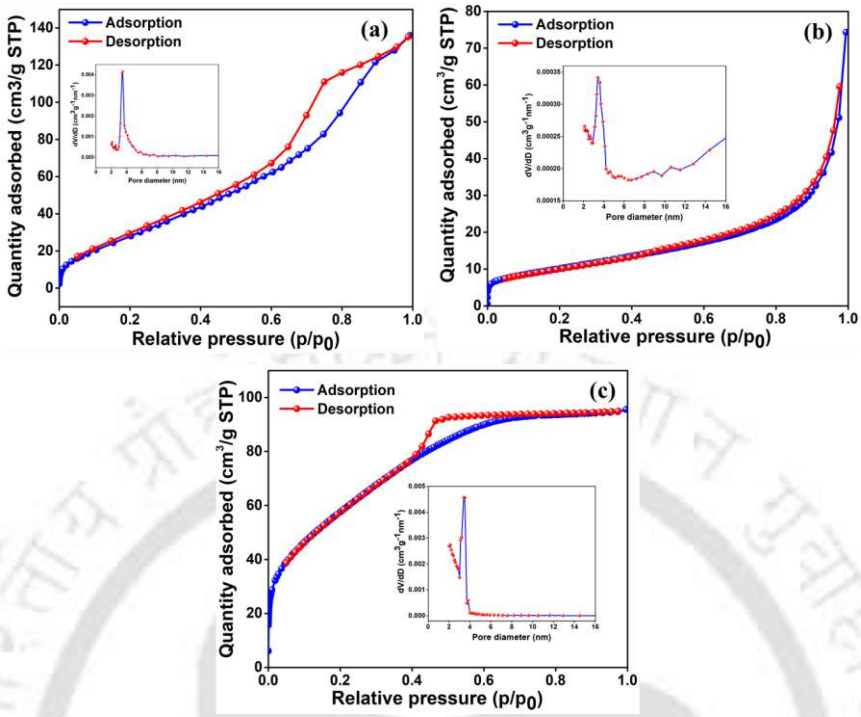

Figure 4.11. N_2 sorption isotherm and (inset) pore size distribution plots of (a) CdS(bio), (b) In_2O_3 (bio), and (b) 0.4In_2O_3/CdS(bio) heterostructure.

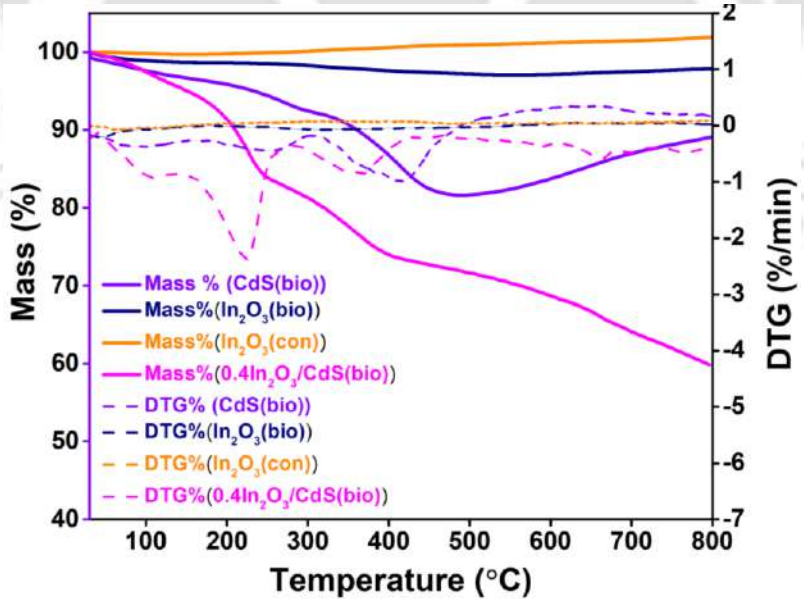

Figure 4.12. (a) TGA, and (b) DTG analysis of CdS(bio), In_2O_3 (bio), In_2O_3(con) and 0.4In_2O_3/CdS(bio) heterostructure.

Table 4.3. Physical properties of photocatalysts.

Photocatalysts	Surface area (m^2/g)	Average pore diameter (nm)	Total pore volume (cm^3/g)	CO_2 adsorption (mmol/g)	Bandgap (eV)
In_2O_3(bio)	37.1	11.60	0.073	0.060	2.39
CdS(bio)	108.4	14.18	0.091	0.087	2.32
0.4In_2O_3/CdS(bio)	217	2.71	0.11	0.43	2.22

Table 4.4. Carbon content calculation in catalysts from TGA plot.

Catalysts	Temperature range of carbon % calculation (°C)	Carbon (%)
CdS(bio)	380 to 600	5.9
In_2O_3(bio)	380 to 600	4.8
0.4In_2O_3/CdS(bio)	300 to 580	1.11

4.2.2 Theoretical calculation

DFT calculations were performed to comprehend the band structure, geometry optimization, and DOS of synthesized catalysts. The optimized structures of CdS, In_2O_3, and In_2O_3/CdS heterostructures are shown in **Figures 4.13a-4.13c**, with lattice parameters detailed in **Table 4.5**. The band structure with Hubbard parameter U_d=4.4, U_p=4.1 for CdS, and U_d=6.2 for In_2O_3, applying GGA+U in DFT (**Figures 4.13d-4.13f**) reveals bandgaps of 2.35, 2.38, and 2.20 eV for CdS, In_2O_3, and In_2O_3/CdS heterostructure, respectively, which are close to the experimental values of 2.32, 2.39, and 2.22 eV. Notably, the band structure of In_2O_3/CdS heterostructure displays overlapping electronic bands near the Fermi level (FL) due to the introduction of In_2O_3, inducing additional electronic states in CdS bandgap, effectively reducing its bandgap, as observed in UV-DRS analysis [49]. DOS for CdS, In_2O_3, and In_2O_3/CdS is depicted in **Figures 4.13g-4.13i**. The DOS of the In_2O_3/CdS heterostructure in the CB is moved closer to the FL compared to CdS and In_2O_3, indicating a larger density of electronic states near the FL [50]. This characteristic favors quicker electron transport than CdS and In_2O_3, suggesting superior photocatalytic performance of In_2O_3/CdS heterostructure over CdS and In_2O_3.

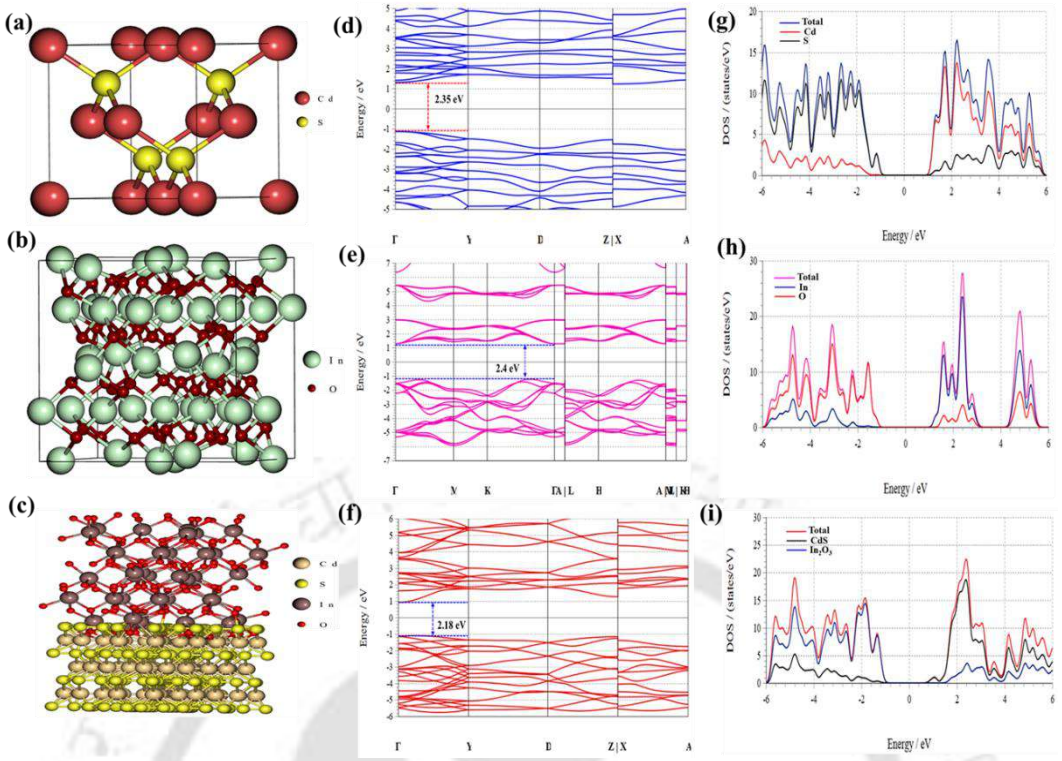

Figure 4.13. DFT calculated (a-c) geometric structure, (d-e) Band structure, and (g-i) Density of state (DOS) of CdS, In_2O_3, and In_2O_3/CdS heterostructure.

Table 4.5. Optimized crystal structure parameters of CdS(bio), In_2O_3(bio), and In_2O_3/CdS(bio) heterostructures considered for DFT calculation.

Catalyst	a (Å)	b (Å)	c (Å)
CdS(bio)	5.88	5.88	5.88
In_2O_3(bio)	10.17	10.17	10.17
In_2O_3/CdS(bio)	10.17	10.17	50.00

4.2.3 Photoelectrochemical (PEC) measurements

Photocurrent measurement and EIS studies were used to examine the charge separation efficiency of In_2O_3(bio), CdS(bio), and 0.4In_2O_3/CdS(bio) heterostructures. The chronoamperometry test was performed at 25 s intervals during the light on/off cycle **(Figure 4.14a)**. The photocurrent density of 0.4In_2O_3/CdS(bio) heterostructures reached 0.82 μA/cm^2, surpassing CdS(bio) (0.10 μA/cm^2) and In_2O_3(bio) (0.082 μA/cm^2) by approximately 8 and 10 times, respectively. This demonstrates the efficient separation of e^-/h^+ pairs by incorporating In_2O_3(bio) into CdS(bio) NPs [12].

Figure 4.14b displays the EIS spectra of synthesized catalysts in both dark and light irradiation circumstances. The EIS data were analyzed and fitted using NOVA software, and the resulting parameters are summarized in **Table 4.6**. Additionally, the equivalent circuit is depicted in **Figure 4.15**. In visible light, the $0.4In_2O_3$/CdS(bio) heterostructures exhibited decreased arc radius, indicating enhanced charge separation and transfer efficiency. Hence, incorporating In_2O_3(bio) could alter the charge and enhance charge transfer in CdS(bio) NPs [51]. Moreover, the increased capacitance signifies an improved charge storage characteristic of heterostructures at the photoanode/electrolyte interfaces [17]. A comparable finding was documented for the CdS/$BiVO_4$ heterostructures and the CdS/WO_3 heterostructures [21,46].

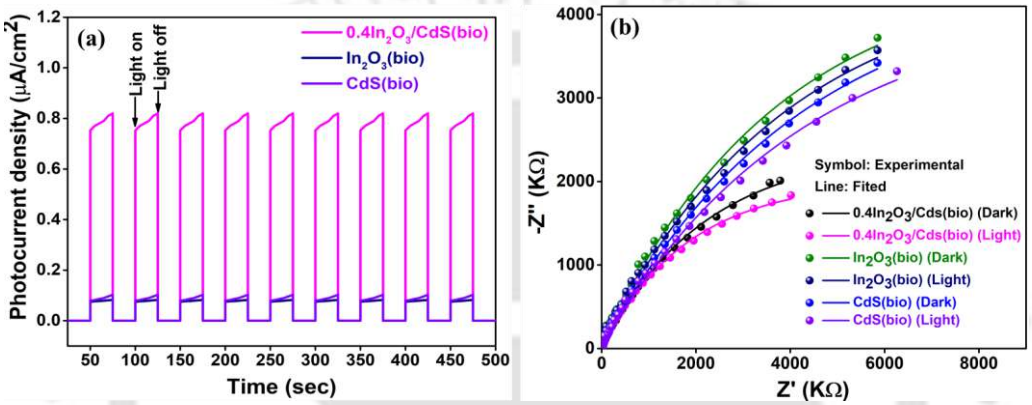

Figure 4.14. (a) Photocurrent response, and (b) EIS Nyquist plots with and without the light of In_2O_3(bio), CdS(bio), and $0.4In_2O_3$/CdS(bio) heterostructure.

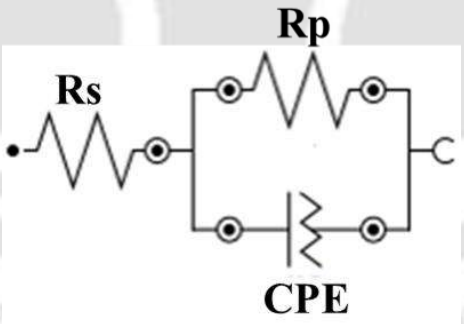

Figure 4.15. Equivalent circuit used for fitting of EIS data [Rs: Electrolytes resistance; Rp: Polarization resistance; CPE: Constant phase element].

Table 4.6. Parameters of the circuit used for fitting of EIS data.

Catalyst	**Rs (KΩ)**	**Rp (MΩ)**	**CPE**
CdS(bio) (Dark)	6.23	14.0	Y_0=188nMho×S^N N=0.566
CdS(bio) (Light)	4.83	13.2	Y_0=221nMho×S^N

			N=0.574
In_2O_3(bio) (Dark)	4.39	15.3	Y_0=220nMho×S^N N=0.569
In_2O_3(bio) (Light)	2.20	6.93	Y_0=273nMho×S^N N=0.579
0.4In_2O_3/CdS(bio) (Dark)	7.94	14.8	Y_0=178nMho×S^N N=0.557
0.4In_2O_3/CdS(bio) (Light)	5.23	12.5	Y_0=202nMho×S^N N=0.557

4.2.4 Photocatalytic testing for CO_2 reduction

The synthesized catalysts were evaluated for HCOOH and CO production under visible light illumination. **Figure 4.16** shows the calibration graphs for HCOOH and CO standards. The chromatograms of both the standards and the resulting products can be found in **Figure 4.17**. It's worth noting that no significant production of HCOOH or CO was found in the absence of catalyst or light illumination. We conducted three separate control experiments to identify the carbon source responsible for the formation of HCOOH and CO. In the first test, the reaction system included CO_2, TEOA, DI water, and photocatalysts with the lamp off. The second test involved CO_2, TEOA, light, and DI water, but no photocatalyst. The third test involved the use of DI water, photocatalysts, light, and TEOA in the reaction, but CO_2 was excluded. Notably, no HCOOH or CO were formed in any of these control tests (**Figure 4.18**). Therefore, it can be concluded that the HCOOH and CO are generated from the CO_2 feedstock in the system, and photoreduction occurs on the photocatalyst. No trace of any CO_2 reduction product was identified in the control experiment, which confirms that the reaction products originated from the photoreduction of CO_2 (**Figure 4.19**).

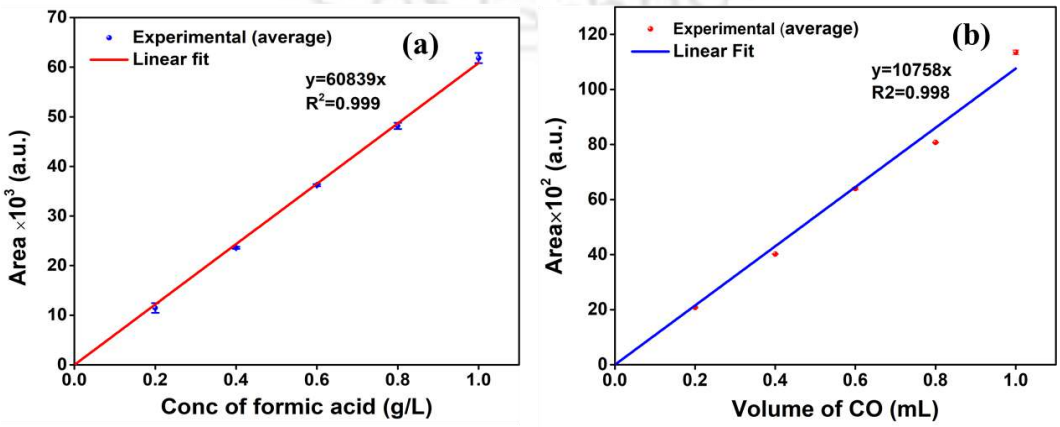

Figure 4.16. Calibration curve of (a) formic acid and (b) carbon monoxide.

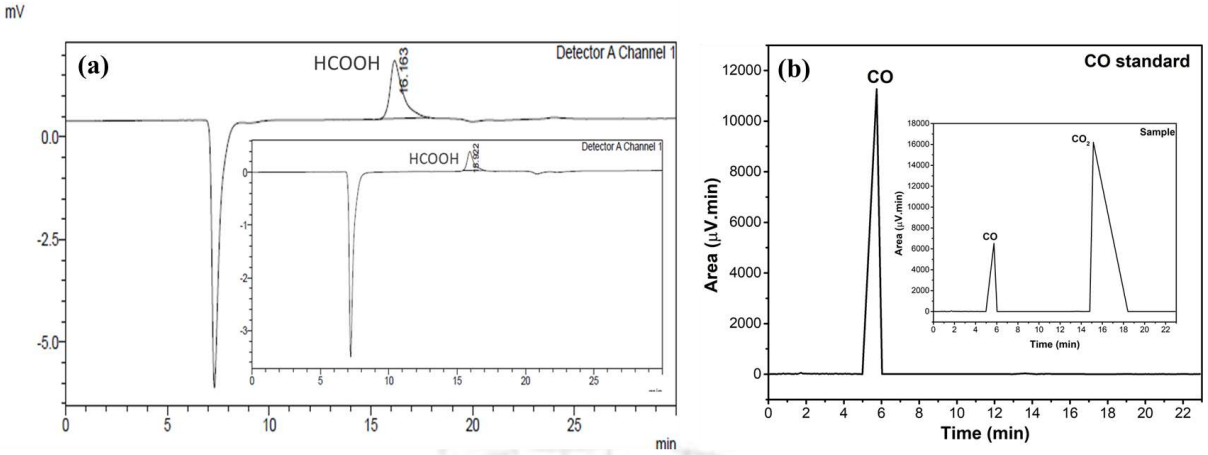

Figure 4.17. (a) HPLC chromatograms of standard 1 g/L HCOOH and (inset) solution after 5h of CO_2 reduction, and (b) GC chromatograms of standard 1 mL CO and (inset) solution after 5h of CO_2 reduction.

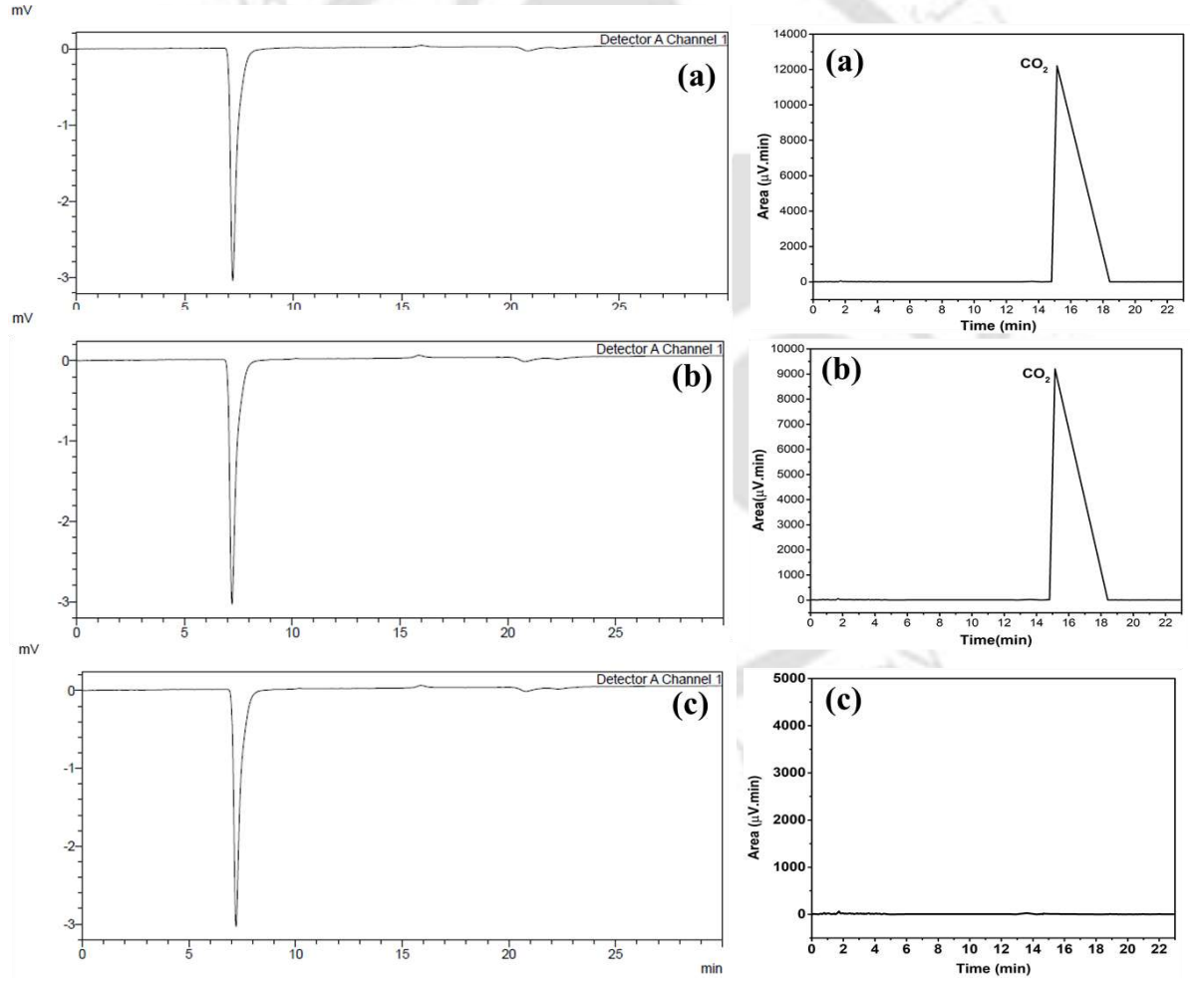

Figure 4.18. HPLC (left side) and GC (right side) chromatograms of 300 s of CO_2 reduction: (a) CO_2+H_2O+TEOA+catalyst, (b) CO_2+H_2O+TEOA+illumination, and (c) H_2O+TEOA+catalyst+illumination.

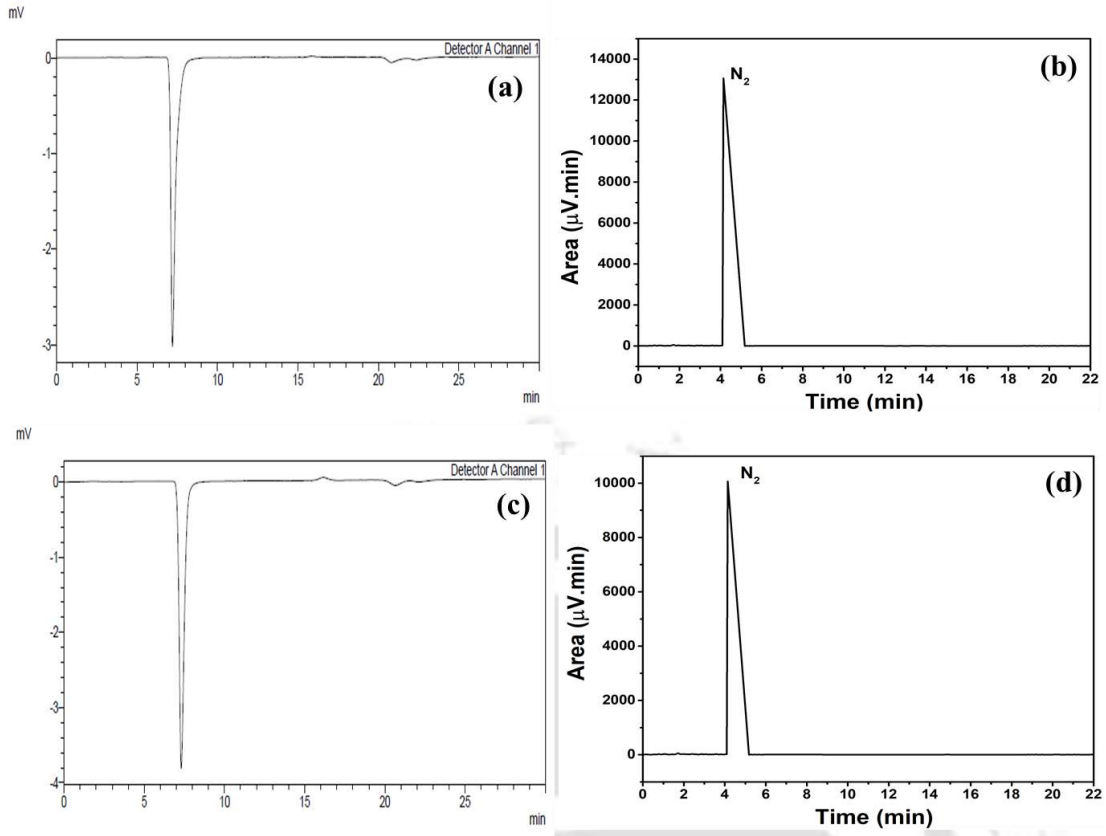

Figure 4.19. (a) HPLC, (b) GC chromatograms after 5 h of the control experiments, (c) HPLC, and (d) GC chromatograms after 10 h of the control experiments using N_2 instead of CO_2.

4.2.4.1 Effect of different photocatalysts

Figure 4.20a shows the rates of HCOOH and CO production for In_2O_3(bio), CdS(bio), and In_2O_3/CdS(bio) heterostructures (0.2, 0.4, 0.6,0.8, and 1 molar ratio). Significantly, CdS(bio) and In_2O_3(bio) nanoparticles didn't produce any products because of the quick recombination of e^-/h^+ pairs (confirmed by PL spectra, **Figure 4.10a).** In addition, CdS suffers from photocorrosion (SO_4^{2-}) (**Figure 4.21c**), while In_2O_3(bio) exhibits weak light absorption (λ_{max}= 440 nm, **Figure 4.1a**), which acts as a limiting factor [4,8]. This indicates that unmodified CdS is not an efficient catalyst for the PCO_2RR to HCOOH and CO. In the case of heterostructures, HCOOH and CO products are formed.

4.2.4.2 Effect of In_2O_3 onto CdS

For In_2O_3/CdS(bio) heterostructures, the HCOOH and CO formation rate displayed an upward trend with increasing In_2O_3 loading percentage, peaking at 0.4 molar In_2O_3 loading, yielding 455.2 and 146.7 µmol/g·h, respectively (**Figure 4.20a**). Subsequently, the rate of product formation exhibited a sharp decline as the In_2O_3 loading percentage increased. This

excessive In_2O_3 loading led to particle aggregation and obstructing active CdS(bio) sites, impeding light absorption [32]. DLS measurements (**Table 4.1**) of the catalysts' hydrodynamic diameter confirmed that particle size notably increased from 219.2 to 314.5 nm when In_2O_3 loading on CdS(bio) exceeded 0.4, indicating potential particle agglomeration. Therefore, $0.4In_2O_3$ loading was determined to be the optimal level.

4.2.4.3 Effect of $0.4In_2O_3$/CdS(bio) concentration

Figure 4.20b illustrates the HCOOH and CO production rate using various concentrations (0, 0.25, 0.50, 0.75, 1, 1.25 g/L) of $0.4In_2O_3$/CdS(bio) heterostructures. The optimal rates for HCOOH and CO production were achieved at a 0.75 g/L photocatalyst concentration, yielding 483.29 and 158.35 μmol/g·h, respectively. However, at higher photocatalyst concentrations, solution turbidity hindered light irradiation [52]. The turbidity was increased by 45.2% upon surpassing the photocatalyst concentration of 0.75g/L (**Table 4.7)**.

4.2.4.4 Effect of sacrificial agent (TEOA) on PCO_2RR

The effect of TEOA (5, 10, 15 % v/v) was carried out on the production rate of HCOOH and CO (**Figure 4.20c**). The production rate of HCOOH and CO was increased by increasing the percentage of TEOA and reached the maximum yield of 514.44 μmol/g·h (AQY 4.44%) and 162 μmol/g·h (AQY 2.45%) of HCOOH and CO, respectively, at 10% (v/v) of TEOA (calculation of AQY provided in **Table A2**). Subsequently, the production rate declined as a high TEOA concentration could restrict electron migration due to increased solution viscosity [53]. Therefore, 10% (v/v) of TEOA was considered optimum for further study. The addition of TEOA in the reaction resulted in a 6.44% rise in HCOOH and a 2.30% increase in CO production rates. TEOA acts as an efficient hole scavenger, rapidly consuming photogenerated holes [3] and thereby suppressing charge recombination in the In_2O_3/CdS(bio) heterostructure. This enhances electron availability at the catalyst surface, facilitating multi-electron CO_2 reduction pathways and increasing the formation rates of HCOOH and CO. Further, we studied the bare CdS(bio) and In_2O_3(bio) with 10% (v/v) of TEOA and water as a reaction mixture (**Figure 4.20d**). The results reveal the formation of 59.49 μmol/g·h HCOOH using CdS(bio) and 25.05 μmol/g·h CO using In_2O_3(bio). A comparison of HCOOH and CO production rates reported in the literature (**Table 4.8**) underlines the superior performance of bio-based In_2O_3/CdS(bio) heterostructures.

4.2.4.5 Reusability and stability of 0.4In_2O_3/CdS(bio) heterostructures

The reusability and stability of the 0.4In_2O_3/CdS(bio)heterostructures photocatalyst were examined by filtering out the catalyst after PCO_2RR and reusing it for several cycles. The performance in producing HCOOH and CO was assessed over five cycles to evaluate the catalyst's functional stability (depicted in **Figure 4.20e**). Even after 25 h of reaction, the heterostructures exhibited a steady photocatalytic efficiency. A 2.5% decrease in performance was noted in 5 cycles due to the loss of photocatalyst particles in the recovery process. This remarkable stability suggests that the incorporation of In_2O_3 onto CdS(bio) curtailed its photo-corrosion while inhibiting the recombination of e^-/h^+ pairs [32,39].

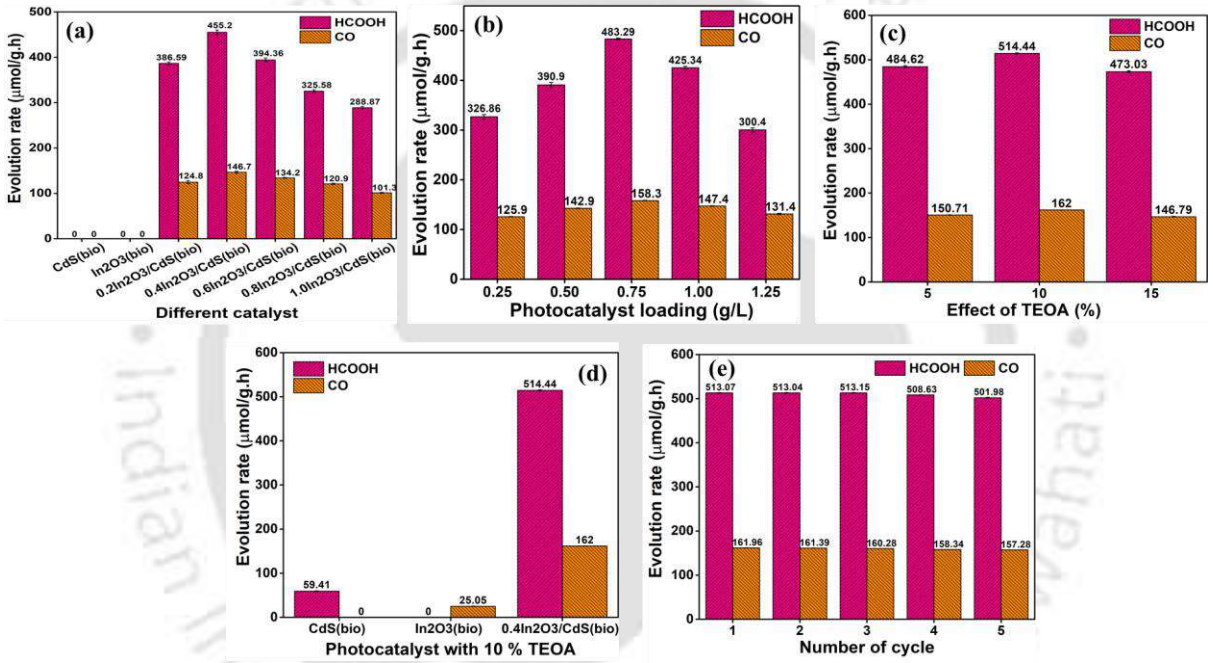

Figure 4.20. (a) Photocatalytic reduction of CO_2 using different bio-based catalysts, (b) Effect of photocatalyst concentration, (c) Effect of sacrificial agent (TEOA), (d) Catalyst with 10% TEOA, and (e) Stability study of 0.4In_2O_3/CdS(bio) heterostructure under visible light irradiation.

Table 4.7. Turbidity of In_2O_3/CdS(bio) heterostructure.

Catalyst concentration (g/L)	Turbidity (NTU)
0.25	147
0.50	183
0.75	208
1.0	247
1.25	302

Table 4.8. Comparison of the formic acid and carbon monoxide rates with the earlier report.

Photocatalysts	Synthesis method	Reaction solvent	Light source	Products (µmol/g·h)		Source
				HCOOH	CO	
In_2O_3/CdS(bio) heterostructure	Microwave irradiation	H_2O/TEOA	250W, Metal halide lamp(λ>420 nm)	514.44	162	**Present work**
CdS/TiO_2	Photodeposition	H_2O (vapor)	300 W Xe arc lamp (λ = 300–800 nm)		3.62	[54]
CdS/ZnO	Solvothermal method	H_2O	500 W Hg lamp (λ > 400 nm)		35.2	[33]
CdS/$CdWO_4$	Chemical deposition	H_2O/TEOA	300 W xenon lamp (λ > 420nm)		1.39	[55]
CdS/Ni_9S_8/Al_2O_3		H_2O/TEOA	300 W Xe lamp (λ > 420 nm)		121	[56]
CdS/MIL-101	Double solvent method	H_2O (vapor)	300 W Xe lamp (λ > 420 nm)		16.35	[57]
CdS/FeTCPP	Hydrothermal	MeCN/H_2O/ TEOA	300 W Xe lamp, λ = 420–780 nm		7.46	[58]
CdS/ethylenediamine	Solvothermal route	MeCN/H_2O/ TEOA	300 W Xe lamp (λ > 420 nm)		115.6	[14]
$CUGAS_2$/CdS	Ultrasonic dispersion	H_2O/K_2SO_3/K HCO_3	300 W Xe lamp		0.75	[59]
CdS/NH_2-UiO-66/Chitosan	Solvent evaporation technique	MeCN/ H_2O/ TEOA	300 W Xe lamp, λ = 400–760 nm		86.98	[53]
(Mo-bi)sx/CdS	Hydrothermal	MeCN/[Bmim] BF_4/TEOA	Visible light (λ = 420–780 nm	208		[60]

TEOA: Triethanolamine; MeCN: Acetonitrile; FeTCPP: 4-carboxyphenyl) porphyrin iron(III) chloride

Figure 4.21 depicts the XPS spectra of CdS(bio)/used and 0.4In_2O_3/CdS(bio)/used heterostructures and the corresponding before reaction sample (inset of **Figure 4.21**). The survey spectra (**Figure 4.21a**) confirm the existence of In, O, Cd, and S in the heterostructures. However, a single Cd is found in CdS(bio)/used. The high-resolution spectrums of 0.4In_2O_3/CdS(bio)/used exhibit consistent peak intensities (**Figures 4.21b-4.21e**) before and after PCO_2RR are evident. The S 2p peak intensity in CdS(bio)/used (**Figure 4.21c**) is shifted from 163.16 to 168.64 eV, suggesting sulfur oxidation, i.e., photocorrosion, and the generation of SO_4^{2-} [1,61].

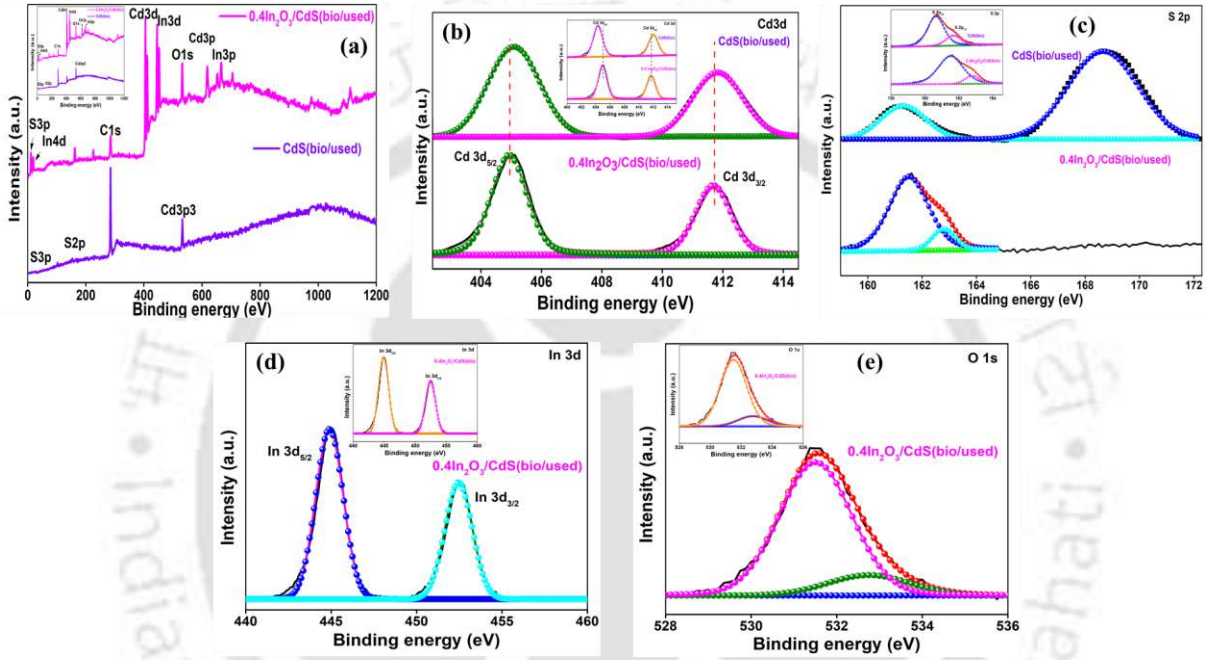

Figure 4.21. (a) XPS survey spectra and high resolution of (b) Cd 3d, (c) S 2p, (d) In 3d, and (e) O 1s of CdS(bio)/used and 0.4In_2O_3/CdS(bio)/used heterostructure. The insets show the XPS spectra of CdS(bio) and 0.4In_2O_3/CdS(bio).

XRD and FETEM analyses were carried out of In_2O_3/CdS(bio) heterostructures, both before and after PCO_2RR, to evaluate its structural and morphological attributes. The XRD spectra of 0.4In_2O_3/CdS(bio) and 0.4In_2O_3/CdS(bio/used) (**Figure 4.22a)** show no significant changes in the lattice structure of 0.4In_2O_3/CdS(bio/used). The crystallite size remained consistent at 17.5 nm in comparison to 17.76 nm for 0.4In_2O_3/CdS(bio). FETEM image of In_2O_3/CdS(bio/used) (**Figure 4.22b**), revealing no noticeable changes in morphology compared to the initial In_2O_3/CdS(bio) (**Figure 4.7c**).

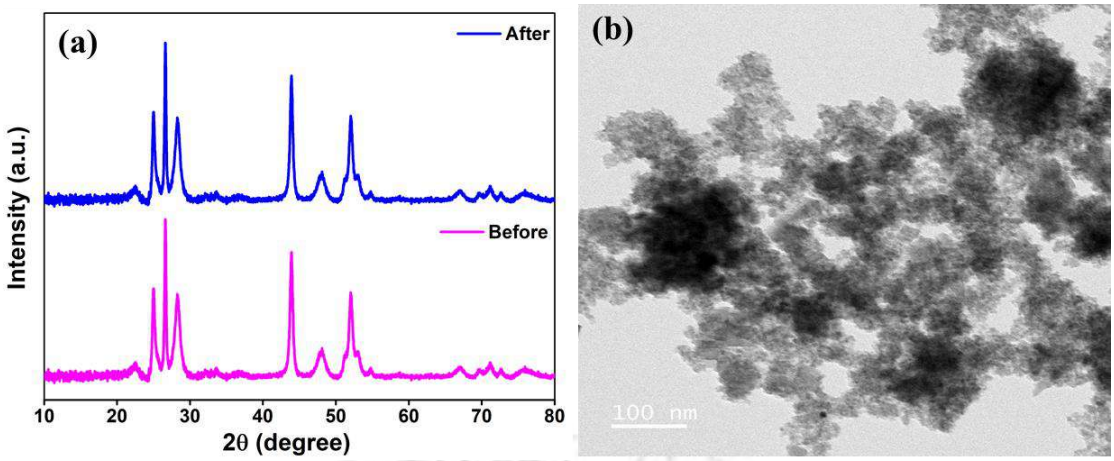

Figure 4.22. (a) XRD patterns of 0.4In_2O_3/CdS(bio) before and after PCO_2RR, and (b) FETEM of 0.4In_2O_3/CdS(bio/used).

4.2.5 Mechanism of PCO_2RR catalysed by In_2O_3/CdS(bio) heterostructure

It is evident from the UPS VB and band position of the catalyst that In_2O_3(bio) has a larger work function and a lower Fermi level, while CdS(bio) has the opposite characteristics. When CdS(bio) and In_2O_3(bio) come in interfacial contact, the electron of CdS(bio) would flow to In_2O_3(bio) spontaneously until the Fermi level reaches equilibrium. Consequently, CdS(bio) experiences an upward energy band bending and positive charge at the interface, while In_2O_3(bio) undergoes a downward band bending and becomes negatively charged at the interface, establishing an internal electric field (IEF) [62–64]. Upon the light illumination, under the influence of the IEF and Coulomb effect, photogenerated electrons of In_2O_3(bio) follow the Z-scheme transfer path to recombine with the photoinduced holes in the VB of CdS (**Figure 4.23**). Meanwhile, the photogenerated holes in the VB of In_2O_3 remain and oxidize the TEOA, and the photoexcited electron in the CB of CdS reacts with CO_2 to produce CO and HCOOH. Thus, a full redox cycle of the photocatalytic system is completed.

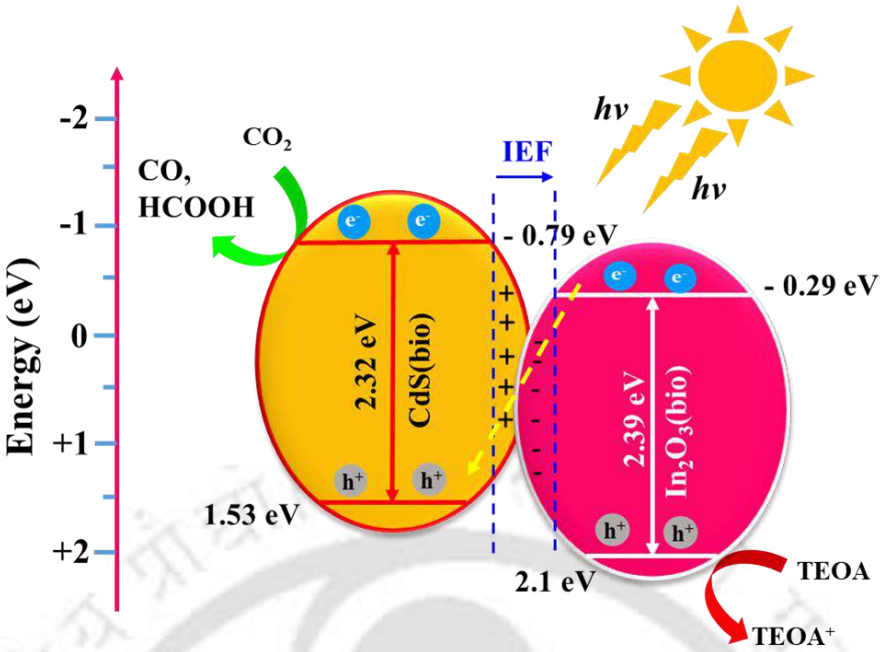

Figure 4.23. Possible reaction mechanism of photocatalytic CO_2 reduction over Z-scheme In_2O_3/CdS(bio) heterostructure.

4.3 Major findings

This study successfully synthesized In_2O_3/CdS heterostructures through bio-based methods with phytochemicals found in *Aegle marmelos* plant extract with microwave irradiation. The DFT yielded bandgaps for CdS, In_2O_3, and In_2O_3/CdS heterostructure, well matched with the experimental values, and the bandgap was reduced from 2.32 to 2.22 eV with In_2O_3 (0.4 molar ratio) incorporation onto CdS(bio). In_2O_3 altered the DOS of CdS due to the introduction of an additional electronic state in the bandgap region, enhancing charge separation at local junctions. In_2O_3/CdS also exhibited longer charge carrier lifetimes (4.38 ns) compared to In_2O_3 and CdS alone. The photocatalytic study of In_2O_3/CdS(bio) was evaluated for PCO_2RR under visible light. CO_2 adsorption capacity and photocurrent density of 0.4In_2O_3/CdS(bio) heterostructures were several folds higher that of CdS(bio) and In_2O_3(bio) nanoparticles. Notably, In_2O_3/CdS(bio) achieved a remarkable HCOOH and CO production rate of 514.44 (AQY 4.44%) and 162 μmol/g·h (AQY 2.54%), outperforming CdS(bio) and In_2O_3(bio) by 9 and 6.5 times. The heterostructures were stable with no noticeable changes in morphology and crystallite size owing to the incorporation of In_2O_3 onto CdS(bio), preventing its photo-corrosion and inhibiting e^-/h^+ pair recombination. *However, the relatively larger particle size limits the quantum confinement effect and restricts precise bandgap tuning. Hence, the third objective aimed in developing CDs/CdS quantum dot (QD) nanocomposites*

to exploit high surface-to-volume ratios and quantum confinement, targeting improved bandgap tuning. The integration of theoretical and experimental studies further optimized charge dynamics and active site engineering.

References

[1] P.M. Gawal, A.K. Golder, Vegetal route for synthesis of CQDs/CdS nanocomposites for photocatalytic reduction of CO_2 to methanol under visible light, Colloids Surfaces A Physicochem. Eng. Asp. 683 (2024) 133068. https://doi.org/10.1016/j.colsurfa.2023.133068.

[2] X. Xu, K. Xie, J. Hu, S. Liu, H. Zhong, H.-R. Wen, The metal-organic frameworks as unique platform for photocatalytic CO_2 conversion to liquid fuels, J. Environ. Chem. Eng. 11 (2023) 110424. https://doi.org/10.1016/j.jece.2023.110424.

[3] X. Li, J. Yu, M. Jaroniec, X. Chen, Cocatalysts for selective photoreduction of CO_2 into solar fuels, Chem. Rev. 119 (2019) 3962–4179. https://doi.org/10.1021/acs.chemrev.8b00400.

[4] K. Yang, Z. Yang, C. Zhang, Y. Gu, J. Wei, Z. Li, C. Ma, X. Yang, K. Song, Y. Li, Q. Fang, J. Zhou, Recent advances in CdS-based photocatalysts for CO_2 photocatalytic conversion, Chem. Eng. J. 418 (2021) 129344. https://doi.org/10.1016/j.cej.2021.129344.

[5] Y. Taniguchi, H. Yoneyama, H. Tamura, Photoelectrochemical Reduction of Carbon Dioxide at p-Type Gallium Phosphide Electrodes in the Presence of Crown Ether, Bull. Chem. Soc. Jpn. 55 (1982) 2034–2039. https://doi.org/10.1246/bcsj.55.2034.

[6] D.P.H. Tran, M.T. Pham, X.T. Bui, Y.F. Wang, S.J. You, CeO_2 as a photocatalytic material for CO_2 conversion: A review, Sol. Energy. 240 (2022) 443–466. https://doi.org/10.1016/j.solener.2022.04.051.

[7] X. Hu, R.T. Guo, X. Chen, Z.X. Bi, J. Wang, W.G. Pan, Bismuth-based Z-scheme structure for photocatalytic CO_2 reduction: A review, J. Environ. Chem. Eng. 10 (2022) 1DUMMY. https://doi.org/10.1016/j.jece.2022.108582.

[8] P. Chang, Y. Wang, Y. Wang, Y. Zhu, Current trends on In_2O_3 based heterojunction photocatalytic systems in photocatalytic application, Chem. Eng. J. 450 (2022) 137804. https://doi.org/10.1016/j.cej.2022.137804.

[9] H. Shen, T. Peppel, J. Strunk, Z. Sun, Photocatalytic Reduction of CO_2 by Metal-Free-Based Materials: Recent Advances and Future Perspective, Sol. RRL. 4 (2020) 1900546. https://doi.org/10.1002/solr.201900546.

[10] K. Guo, I. Hussain, G. Jie, Y. Fu, F. Zhang, W. Zhu, Strategies for improving the photocatalytic performance of metal-organic frameworks for CO_2 reduction: A review, J. Environ. Sci. 125 (2023) 290–308. https://doi.org/10.1016/j.jes.2022.01.005.

[11] H.N. Wang, Y.H. Zou, H.X. Sun, Y. Chen, S.L. Li, Y.Q. Lan, Recent progress and perspectives in heterogeneous photocatalytic CO_2 reduction through a solid–gas mode, Coord. Chem. Rev. 438 (2021). https://doi.org/10.1016/j.ccr.2021.213906.

[12] L. Zhu, Y. Liu, X. Peng, Y. Li, Y.-L. Men, P. Liu, Y.-X. Pan, Noble-metal-free CdS nanoparticle-coated graphene oxide nanosheets favoring electron transfer for efficient photoreduction of CO_2, ACS Appl. Mater. Interfaces. 12 (2020) 12892–12900. https://doi.org/10.1021/acsami.0c00163.

[13] P. Zhang, S. Wang, B.Y. Guan, X.W.D. Lou, Fabrication of CdS hierarchical multi-cavity hollow particles for efficient visible light CO_2 reduction, Energy Environ. Sci. 12 (2019) 164–168. https://doi.org/10.1039/C8EE02538J.

[14] T. Tian, X. Jin, N. Guo, H. Li, Y. Han, Y. Yuan, CdS/ethylenediamine nanowires 3D photocatalyst with rich sulfur vacancies for efficient syngas production from CO_2 photoreduction, Appl. Catal. B Environ. 308 (2022) 121227. https://doi.org/10.1016/j.apcatb.2022.121227.

[15] Y.-X. Feng, H.-J. Wang, J.-W. Wang, W. Zhang, M. Zhang, T.-B. Lu, Stand-alone CdS nanocrystals for photocatalytic CO_2 reduction with high efficiency and selectivity, ACS Appl. Mater. Interfaces. 13 (2021) 26573–26580. https://doi.org/10.1021/acsami.1c03606.

[16] B. Su, L. Huang, Z. Xiong, Y. Yang, Y. Hou, Z. Ding, S. Wang, Branch-like ZnS–DETA/CdS hierarchical heterostructures as an efficient photocatalyst for visible light CO_2 reduction, J. Mater. Chem. A. 7 (2019) 26877–26883. https://doi.org/10.1039/C9TA10470D.

[17] J. Yu, J. Jin, B. Cheng, M. Jaroniec, A noble metal-free reduced graphene oxide–CdS nanorod composite for the enhanced visible-light photocatalytic reduction of CO_2 to solar fuel, J. Mater. Chem. A. 2 (2014) 3407. https://doi.org/10.1039/c3ta14493c.

[18] R. Li, X. Ou, L. Zhang, Z. Qi, X. Wu, C. Lu, J. Fan, K. Lv, Photocatalytic oxidation of NO on reduction type semiconductor photocatalysts: effect of metallic Bi on CdS nanorods, Chem. Commun. 57 (2021) 10067–10070. https://doi.org/10.1039/d1cc03516a.

[19] H. Yang, C. Yang, N. Zhang, K. Mo, Q. Li, K. Lv, J. Fan, L. Wen, Drastic promotion of the photoreactivity of MOF ultrathin nanosheets towards hydrogen production by

deposition with CdS nanorods, Appl. Catal. B Environ. 285 (2021) 119801. https://doi.org/10.1016/j.apcatb.2020.119801.

[20] Z. Qi, J. Chen, Q. Li, N. Wang, S.A.C. Carabineiro, K. Lv, Increasing the Photocatalytic Hydrogen Generation Activity of CdS Nanorods by Introducing Interfacial and Polarization Electric Fields, Small. 19 (2023) 1–9. https://doi.org/10.1002/smll.202303318.

[21] Z.H. Wei, Y.F. Wang, Y.Y. Li, L. Zhang, H.C. Yao, Z.J. Li, Enhanced photocatalytic CO_2 reduction activity of Z-scheme CdS/$BiVO_4$ nanocomposite with thinner $BiVO_4$ nanosheets, J. CO2 Util. 28 (2018) 15–25. https://doi.org/10.1016/j.jcou.2018.09.008.

[22] U. Ghosh, A. Majumdar, A. Pal, Photocatalytic CO_2 reduction over g-C_3N_4 based heterostructures: Recent progress and prospects, J. Environ. Chem. Eng. 9 (2021) 104631. https://doi.org/10.1016/j.jece.2020.104631.

[23] D. Laishram, S. Zeng, K.M. Alam, A.P. Kalra, K. Cui, P. Kumar, R.K. Sharma, K. Shankar, Air- and water-stable halide perovskite nanocrystals protected with nearly-monolayer carbon nitride for CO_2 photoreduction and water splitting, Appl. Surf. Sci. 592 (2022) 153276. https://doi.org/10.1016/j.apsusc.2022.153276.

[24] P. Kumar, S. Mulmi, D. Laishram, K.M. Alam, U.K. Thakur, V. Thangadurai, K. Shankar, Water-splitting photoelectrodes consisting of heterojunctions of carbon nitride with a p-type low bandgap double perovskite oxide, Nanotechnology. 32 (2021). https://doi.org/10.1088/1361-6528/abedec.

[25] P. Kumar, E. Vahidzadeh, K.M. Alam, D. Laishram, K. Cui, K. Shankar, Radial Nano-Heterojunctions Consisting of CdS Nanorods Wrapped by 2D CN:PDI Polymer with Deep HOMO for Photo-Oxidative Water Splitting, Dye Degradation and Alcohol Oxidation, Nanomaterials. 13 (2023). https://doi.org/10.3390/nano13091481.

[26] K.M. Alam, C.E. Jensen, P. Kumar, R.W. Hooper, G.M. Bernard, A. Patidar, A.P. Manuel, N. Amer, A. Palmgren, D.N. Purschke, N. Chaulagain, J. Garcia, P.S. Kirwin, L.C.T. Shoute, K. Cui, S. Gusarov, A.E. Kobryn, V.K. Michaelis, F.A. Hegmann, K. Shankar, Photocatalytic Mechanism Control and Study of Carrier Dynamics in CdS@C_3N_5Core-Shell Nanowires, ACS Appl. Mater. Interfaces. 13 (2021) 47418–47439. https://doi.org/10.1021/acsami.1c08550.

[27] M. Tahir, N.S. Amin, Indium-doped TiO_2 nanoparticles for photocatalytic CO_2 reduction with H_2O vapors to CH_4, Appl. Catal. B Environ. 162 (2015) 98–109. https://doi.org/10.1016/j.apcatb.2014.06.037.

[28] M. Chico-Vecino, J.C. Murillo-Sierra, D.A. Pino-Sandoval, L. Hinojosa-Reyes, M.L.

Maya-Treviño, D. Contreras, A. Hernández-Ramírez, Preparation of WO_3/In_2O_3 heterojunctions and their performance on the CO_2 photocatalytic conversion in a continuous flow reactor, J. Environ. Chem. Eng. 11 (2023) 110372. https://doi.org/10.1016/j.jece.2023.110372.

[29] X. Liu, M. Sayed, C. Bie, B. Cheng, B. Hu, J. Yu, L. Zhang, Hollow CdS-based photocatalysts, J. Mater. 7 (2021) 419–439. https://doi.org/10.1016/j.jmat.2020.10.010.

[30] Y. Monga, P. Kumar, R.K. Sharma, J. Filip, R.S. Varma, R. Zbořil, M.B. Gawande, Sustainable Synthesis of Nanoscale Zerovalent Iron Particles for Environmental Remediation, ChemSusChem. 13 (2020) 3288–3305. https://doi.org/10.1002/cssc.202000290.

[31] H. Dabhane, S. Ghotekar, P. Tambade, S. Pansambal, H.C.A. Murthy, R. Oza, V. Medhane, A review on environmentally benevolent synthesis of CdS nanoparticle and their applications, Environ. Chem. Ecotoxicol. 3 (2021) 209–219. https://doi.org/10.1016/j.enceco.2021.06.002.

[32] J.-T. Ren, K. Yuan, K. Wu, L. Zhou, Y.-W. Zhang, A robust CdS/In_2O_3 hierarchical heterostructure derived from a metal–organic framework for efficient visible-light photocatalytic hydrogen production, Inorg. Chem. Front. 6 (2019) 366–375. https://doi.org/10.1039/C8QI01202D.

[33] L. Zhang, L. Zhang, Y. Chen, Y. Zheng, J. Guo, S. Wan, S. Wang, C.K. Ngaw, J. Lin, Y. Wang, CdS/ZnO: A Multipronged Approach for Efficient Reduction of Carbon Dioxide under Visible Light Irradiation, ACS Sustain. Chem. Eng. 8 (2020) 5270–5277. https://doi.org/10.1021/acssuschemeng.0c00190.

[34] R. Shen, L. Zhang, X. Chen, M. Jaroniec, N. Li, X. Li, Integrating 2D/2D CdS/α-Fe_2O_2 ultrathin bilayer Z-scheme heterojunction with metallic β-NiS nanosheet-based ohmic-junction for efficient photocatalytic H_2 evolution, Appl. Catal. B Environ. 266 (2020) 118619. https://doi.org/10.1016/j.apcatb.2020.118619.

[35] K. Wang, T. Sun, H. Ma, R.J. You, Z.H. He, J.G. Chen, H. Wang, W. Wang, Y. Yang, L. Wang, Z.T. Liu, In-situ construction of S-scheme heterojunction nanoflowers by In_2O_3-regulated the growth of metal Bi and oxygen vacancy on BiOCl surface for boosting photocatalytic CO_2 reduction, Sep. Purif. Technol. 340 (2024) 126786. https://doi.org/10.1016/j.seppur.2024.126786.

[36] T. Rao, B. Kumar B*., Reddy, V. , Rao, Preparation and characterization of CdS nanoparticles by chemical coprecipitation technique, Calcogenide Lett. 8 (2011) 117–128.

[37] H. Ullah, Z.H. Yamani, A. Qurashi, J. Iqbal, K. Safeen, Study of the optical and gas sensing properties of In_2O_3 nanoparticles synthesized by rapid sonochemical method, J. Mater. Sci. Mater. Electron. 31 (2020) 17474–17481. https://doi.org/10.1007/s10854-020-04303-9.

[38] S.M. Chaudhari, P.M. Gawal, P.K. Sane, S.M. Sontakke, P.R. Nemade, Solar light-assisted photocatalytic degradation of methylene blue with Mo/TiO_2: a comparison with Cr- and Ni-doped TiO_2, Res. Chem. Intermed. 44 (2018) 3115–3134. https://doi.org/10.1007/s11164-018-3296-1.

[39] T. Wang, Z. Zeng, J. Yang, Z. Pan, X. Zheng, Y. Guo, T. Huang, Construction of 3D marigold-like direct Z-scheme heterojunction In_2O_3/CdS with boosted photocatalytic degradation of antibiotics under visible light, Colloid Interface Sci. Commun. 51 (2022) 100674. https://doi.org/10.1016/j.colcom.2022.100674.

[40] K. Chen, X. Zhao, X.-J. Zhang, W.-S. Zhang, Z.-F. Wu, H.-Y. Wang, D.-X. Han, L. Niu, Enhanced photocatalytic CO_2 reduction by constructing an In_2O_3 –CuO heterojunction with CuO as a cocatalyst, Catal. Sci. Technol. 11 (2021) 2713–2717. https://doi.org/10.1039/D1CY00318F.

[41] S. Martha, K.H. Reddy, K.M. Parida, Fabrication of In_2O_3 modified Zno for enhancing stability, optical behaviour, electronic properties and photocatalytic activity for hydrogen production under visible light, J. Mater. Chem. A. 2 (2014) 3621–3631. https://doi.org/10.1039/c3ta14285j.

[42] S. Naranthatta, P. Janardhanan, R. Pilankatta, S.S. Nair, Green Synthesis of Engineered CdS Nanoparticles with Reduced Cytotoxicity for Enhanced Bioimaging Application, ACS Omega. 6 (2021) 8646–8655. https://doi.org/10.1021/acsomega.1c00519.

[43] J. Chandradass, D.S. Bae, K.H. Kim, A simple method to prepare indium oxide nanoparticles: Structural, microstructural and magnetic properties, Adv. Powder Technol. 22 (2011) 370–374. https://doi.org/10.1016/j.apt.2010.05.006.

[44] S.W. Cao, X.F. Liu, Y.P. Yuan, Z.Y. Zhang, Y. Sen Liao, J. Fang, S.C.J. Loo, T.C. Sum, C. Xue, Solar-to-fuels conversion over In_2O_3/g-C_3N_4 hybrid photocatalysts, Appl. Catal. B Environ. 147 (2014) 940–946. https://doi.org/10.1016/j.apcatb.2013.10.029.

[45] M. Zhou, S. Wang, P. Yang, C. Huang, X. Wang, Boron Carbon Nitride Semiconductors Decorated with CdS Nanoparticles for Photocatalytic Reduction of CO_2, ACS Catal. 8 (2018) 4928–4936. https://doi.org/10.1021/acscatal.8b00104.

[46] J. Jin, J. Yu, D. Guo, C. Cui, W. Ho, A Hierarchical Z-Scheme CdS-WO3 Photocatalyst with Enhanced CO2 Reduction Activity, Small. 11 (2015) 5262–5271.

https://doi.org/10.1002/smll.201500926.

[47] B. Su, L. Huang, Z. Xiong, Y. Yang, Y. Hou, Z. Ding, S. Wang, Branch-like ZnS-DETA/CdS hierarchical heterostructures as an efficient photocatalyst for visible light CO_2 reduction, J. Mater. Chem. A. 7 (2019) 26877–26883. https://doi.org/10.1039/c9ta10470d.

[48] Y.X. Pan, Y. You, S. Xin, Y. Li, G. Fu, Z. Cui, Y.L. Men, F.F. Cao, S.H. Yu, J.B. Goodenough, Photocatalytic CO_2 Reduction by Carbon-Coated Indium-Oxide Nanobelts, J. Am. Chem. Soc. 139 (2017) 4123–4129. https://doi.org/10.1021/jacs.7b00266.

[49] Y. Zhang, Y. Wu, L. Wan, H. Ding, H. Li, X. Wang, W. Zhang, Hollow core–shell Co_9S_8@$ZnIn_2S_4$/CdS nanoreactor for efficient photothermal effect and CO2 photoreduction, Appl. Catal. B Environ. 311 (2022) 121255. https://doi.org/10.1016/j.apcatb.2022.121255.

[50] L. Li, C. Guo, J. Ning, Y. Zhong, D. Chen, Y. Hu, Oxygen-vacancy-assisted construction of FeOOH/CdS heterostructure as an efficient bifunctional photocatalyst for CO_2 conversion and water oxidation, Appl. Catal. B Environ. 293 (2021) 120203. https://doi.org/10.1016/j.apcatb.2021.120203.

[51] Y. Wang, J. Chen, L. Liu, X. Xi, Y. Li, Z. Geng, G. Jiang, Z. Zhao, Novel metal doped carbon quantum dots/CdS composites for efficient photocatalytic hydrogen evolution, Nanoscale. 11 (2019) 1618–1625. https://doi.org/10.1039/C8NR05807E.

[52] D. Gogoi, A.K. Shah, P. Rambabu, M. Qureshi, A.K. Golder, N.R. Peela, Step-Scheme Heterojunction between CdS Nanowires and Facet-Selective Assembly of MnOx - $BiVO_4$ for an Efficient Visible-Light-Driven Overall Water Splitting, ACS Appl. Mater. Interfaces. 13 (2021) 45475–45487. https://doi.org/10.1021/acsami.1c11740.

[53] H. Zhao, X. Yang, R. Xu, J. Li, S. Gao, R. Cao, CdS/NH_2 -UiO-66 hybrid membrane reactors for the efficient photocatalytic conversion of CO_2, J. Mater. Chem. A. 6 (2018) 20152–20160. https://doi.org/10.1039/C8TA05970E.

[54] X. Pan, Y.-J. Xu, Graphene-Templated Bottom-up Fabrication of Ultralarge Binary CdS–TiO_2 Nanosheets for Photocatalytic Selective Reduction, J. Phys. Chem. C. 119 (2015) 7184–7194. https://doi.org/10.1021/jp512797t.

[55] Y.Y. Li, Z.H. Wei, J. Bin Fan, Z.J. Li, H.C. Yao, Photocatalytic CO_2 reduction activity of Z-scheme CdS/$CdWO_4$ catalysts constructed by surface charge directed selective deposition of CdS, Appl. Surf. Sci. 483 (2019) 442–452. https://doi.org/10.1016/j.apsusc.2019.03.333.

[56] S. Li, Q. Wang, X. Yan, H.Q. Zhuang, C. Yuan, J. Feng, M. Wang, R. Li, W. Li, Y.X. Pan, Al_2O_3 support triggering highly efficient photoreduction of CO_2 with H_2 on noble-metal-free $CdS/Ni_9S_8/Al_2O_3$, Appl. Catal. B Environ. 240 (2019) 174–181. https://doi.org/10.1016/j.apcatb.2018.08.060.

[57] D. Ding, Z. Jiang, J. Jin, J. Li, D. Ji, Y. Zhang, L. Zan, Impregnation of semiconductor CdS NPs in MOFs cavities via double solvent method for effective photocatalytic CO_2 conversion, J. Catal. 375 (2019) 21–31. https://doi.org/10.1016/j.jcat.2019.05.015.

[58] P. Li, C. Hou, X. Zhang, Y. Chen, T. He, Ethylenediamine-functionalized CdS/tetra(4-carboxyphenyl)porphyrin iron(III) chloride hybrid system for enhanced CO_2 photoreduction, Appl. Surf. Sci. 459 (2018) 292–299. https://doi.org/10.1016/j.apsusc.2018.08.002.

[59] S. Wu, H. Pang, W. Zhou, B. Yang, X. Meng, X. Qiu, G. Chen, L. Zhang, S. Wang, X. Liu, R. Ma, J. Ye, N. Zhang, Stabilizing $CuGaS_2$ by crystalline CdS through an interfacial Z-scheme charge transfer for enhanced photocatalytic CO_2 reduction under visible light, Nanoscale. 12 (2020) 8693–8700. https://doi.org/10.1039/D0NR00483A.

[60] B. Zhou, J. Song, C. Xie, C. Chen, Q. Qian, B. Han, Mo–Bi–Cd Ternary Metal Chalcogenides: Highly Efficient Photocatalyst for CO_2 Reduction to Formic Acid Under Visible Light, ACS Sustain. Chem. Eng. 6 (2018) 5754–5759. https://doi.org/10.1021/acssuschemeng.8b00956.

[61] D. Meissner, C. Benndorf, R. Memming, Photocorrosion of cadmium sulfide: Analysis by photoelectron spectroscopy, Appl. Surf. Sci. 27 (1987) 423–436. https://doi.org/10.1016/0169-4332(87)90152-8.

[62] B. Su, H. Huang, Z. Ding, M.B.J. Roeffaers, S. Wang, J. Long, S-scheme $CoTiO_3/Cd_{9.51}Zn_{0.49}S_{10}$ heterostructures for visible-light driven photocatalytic CO_2 reduction, J. Mater. Sci. Technol. 124 (2022) 164–170. https://doi.org/10.1016/j.jmst.2022.01.030.

[63] B. Su, M. Zheng, W. Lin, X.F. Lu, D. Luan, S. Wang, X.W. Lou, S-Scheme Co_9S_8@$Cd0_{0.8}Zn_{0.2}$S-DETA Hierarchical Nanocages Bearing Organic CO_2 Activators for Photocatalytic Syngas Production, Adv. Energy Mater. 13 (2023) 1–9. https://doi.org/10.1002/aenm.202203290.

[64] G. Chen, Z. Zhou, B. Li, X. Lin, C. Yang, Y. Fang, W. Lin, Y. Hou, G. Zhang, S. Wang, S-scheme heterojunction of crystalline carbon nitride nanosheets and ultrafine WO_3 nanoparticles for photocatalytic CO_2 reduction, J. Environ. Sci. (China). 140 (2024) 103–112. https://doi.org/10.1016/j.jes.2023.05.028.

CHAPTER 5

Experimental and Theoretical Studies on Photocatalytic CO_2 Reduction to HCOOH using Plant-based CDs/CdS Quantum Dots Composites

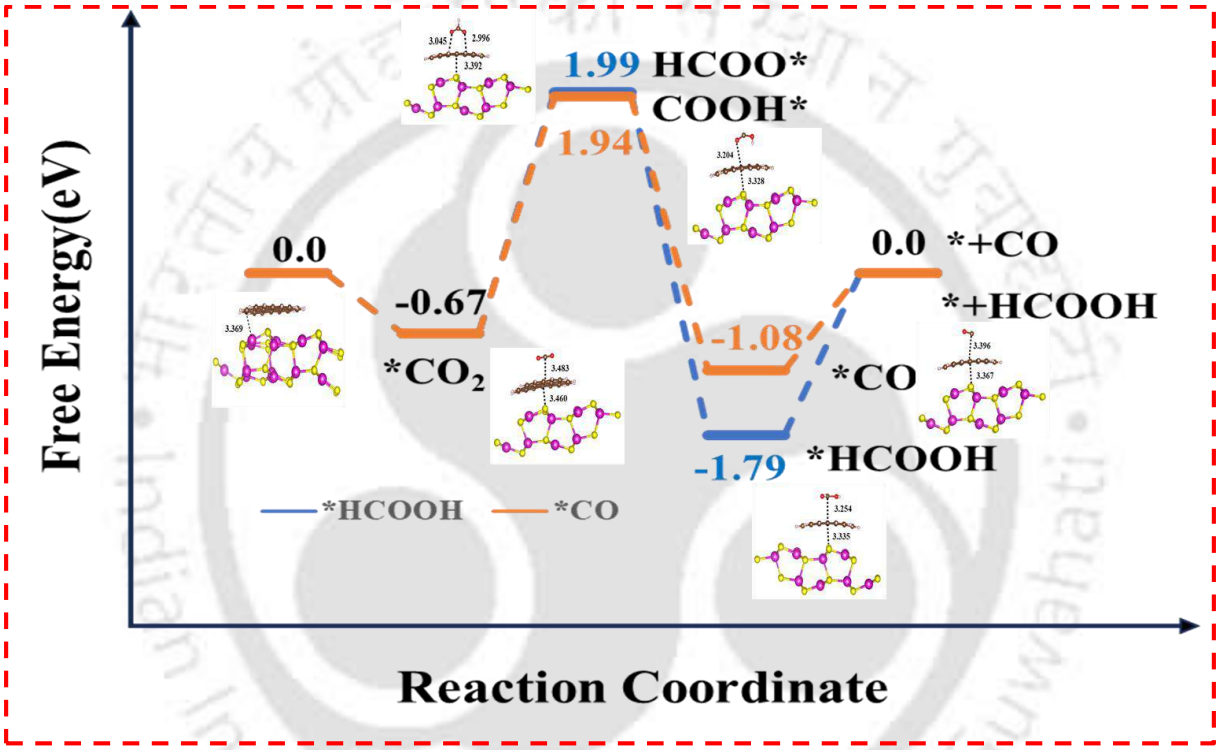

Chapter highlights

- Fabricated bioinspired 0D CDs/CdS QDs(bio) composites with rich sulfur vacancies
- Inhibits sulphur photocorrosion of CdS QDs(bio) with CDs composites formation
- Surface vacancies of CDs/CdS QDs(bio) increase CO_2 adsorption by 3.35 folds
- Formic acid production of 439.51 μmol/g·h using CDs/CdS QDs(bio) photocatalyst
- DFT calculations confirm thermodynamic favourability of HCOOH over CO formation
- HCOO* as a key reaction intermediate for HCOOH formation

5.1 Introduction

Overconsumption of fossil fuels primarily drives the rise in atmospheric CO_2 levels, contributing to global warming and climate change [1,2]. Converting CO_2 into valuable chemicals (e.g., CH_3OH, C_2H_6O, HCOOH, CH_4, and CO) is crucial to address climate change and meet energy needs [3,4]. Among various technologies developed for CO_2 utilization, the photocatalytic CO_2 reduction reaction (PCO_2RR) stands out as an effective method. PCO_2RR harnesses abundant solar energy, uses cost-effective water as a reactant, and operates under ambient conditions, making it sustainable, economical, and environmentally friendly [5,6]. However, the stability of linear CO_2 molecule ($\Delta_fG_{298}^0$ = -394.36 kJ/mol) makes its activation a critical step [7]. Additionally, the fast recombination of photogenerated electrons (e^-) and holes (h^+) pairs in semiconductors during the photocatalytic process significantly hampers PCO_2RR efficiency [8,9].

Various semiconductor nanoparticles (NPs)/quantum dots (QDs) materials have been studied for PCO_2RR, with CdS QDs attracting interest due to their narrow bandgap (2.42 eV), large surface area, efficient solar energy conversion, exceptional charge carrier transport properties, multiexciton generation, and favorable conduction band position (-0.95 eV)[10,11]. However, CdS QDs face challenges such as photocorrosion of sulfur forming SO_4^{2-} and rapid recombination of e^-/h^+ pairs, hindering their advancement and application [12,13]. To address these limitations and enhance CdS QDs efficiency in PCO_2RR, strategies such as morphology control, co-catalyst construction, and heterostructure construction have been explored. These methods aim to enhance charge separation, reduce recombination, and boost the efficacy of CdS QDs in PCO_2RR [6,14].

Bio-based methods for synthesizing NPs/QDs are eco-friendly, cost-effective, and direct, utilizing plentiful biomaterial sources [15,16]. A green approach for synthesizing NPs/QDs and their application in PCO_2RR could help control industrial CO_2 emissions [2,17][18]. Northeastern states of India, abundant in diverse tropical plants, offer potential as sources for capping and reducing agents in efficient NP/QDs synthesis. Additionally, combining microwave irradiation with bioinspired processes can significantly increase NP/QDs formation rates [17].

Carbon dots (CDs) are a novel class of carbon nanostructures known for their uniform dispersion and small size (<10 nm) [19]. They offer several advantages, including high surface area, charge transfer properties, an electron reservoir, and functional surface moieties, making them widely employed in photocatalysis [20]. Additionally, CDs are actively involved in the

development of effective and stable composite photocatalysts [21]. Various methods have been employed to synthesize CDs utilizing carbon sources such as citric acid, urea, ethylene glycol, and thiourea [22]. Moreover, renewable biomass resources such as plant leaves, flowers, roots, fruits, and peels, as well as human and animal derivatives, provide eco-friendly and economical carbon sources for synthesizing CDs [23–26].

Chapter 5 reports on the synthesis of biomass-derived CDs(bio) using waste *orange peels* and CdS QDs(bio) phytochemicals found in *Aegle marmelos*. *Orange peel* is a rich carbon source that serves as a natural precursor [27,28]. *Aegle marmelos* plant-derived compounds, including flavonoids, alkaloids, tannins, phenols, and saponins, acted as powerful reducing and capping agents [2,17]. Further, CDs(bio) were impregnated onto CdS QDs(bio) via a facile deposition method. The synthesized catalysts were tested for PCO_2RR under visible light, producing HCOOH. The optimal 0.4% (w/w) CDs/CdS QDs(bio) composites achieved the highest HCOOH production rates of 439.51 μmol/g·h (apparent quantum yield (AQY) 3.79%) among various CDs(bio) compositions. Additionally, the reusability of the composites was examined. Density functional theory (DFT) analysis was performed to understand the binding energy profile and electronic structures of catalysts, leading to favourable HCOOH formation over CO. This study represents a significant advancement in the bioinspired synthesis of composites for efficient PCO_2RR to produce HCOOH.

5.2 Results and discussion

5.2.1 Photocatalyst characterizations

Morphological analyses: Figures 5.1a-5.1c display TEM images of CdS QDs(bio), CDs(bio), and 0.4CDs/CdS QDs(bio) composites, revealing an average particle size of 4.85, 5, and 5.33 nm, respectively (**Figure 5.2**). HRTEM image of 0.4CDs/CdS QDs(bio) composites (**Figure 5.1d**) displayed CdS QDs(bio) lattice fringes with a d-spacing of 0.33 nm for the (111) plane and 0.22 nm for the (002) graphitic lattice planes of CDs. SAED pattern of 0.4CDs/CdS QDs(bio) composites **(Figure 5.1d**(inset)) is indicative of an amorphous nature of CDs, while CdS QDs exhibit a polycrystalline nature. Additionally, the SAED pattern (**Figure 5.3**) confirmed the polycrystalline nature of CdS QDs(bio) and the amorphous nature of CDs(bio). EDS analysis of 0.4CDs/CdS QDs(bio) composites (**Figure 5.1e**) gave C, S, and Cd contents of 40.4, 12.8, and 46.8%, respectively. The elemental mapping of the composites is displayed in **Figure 5.1f**.

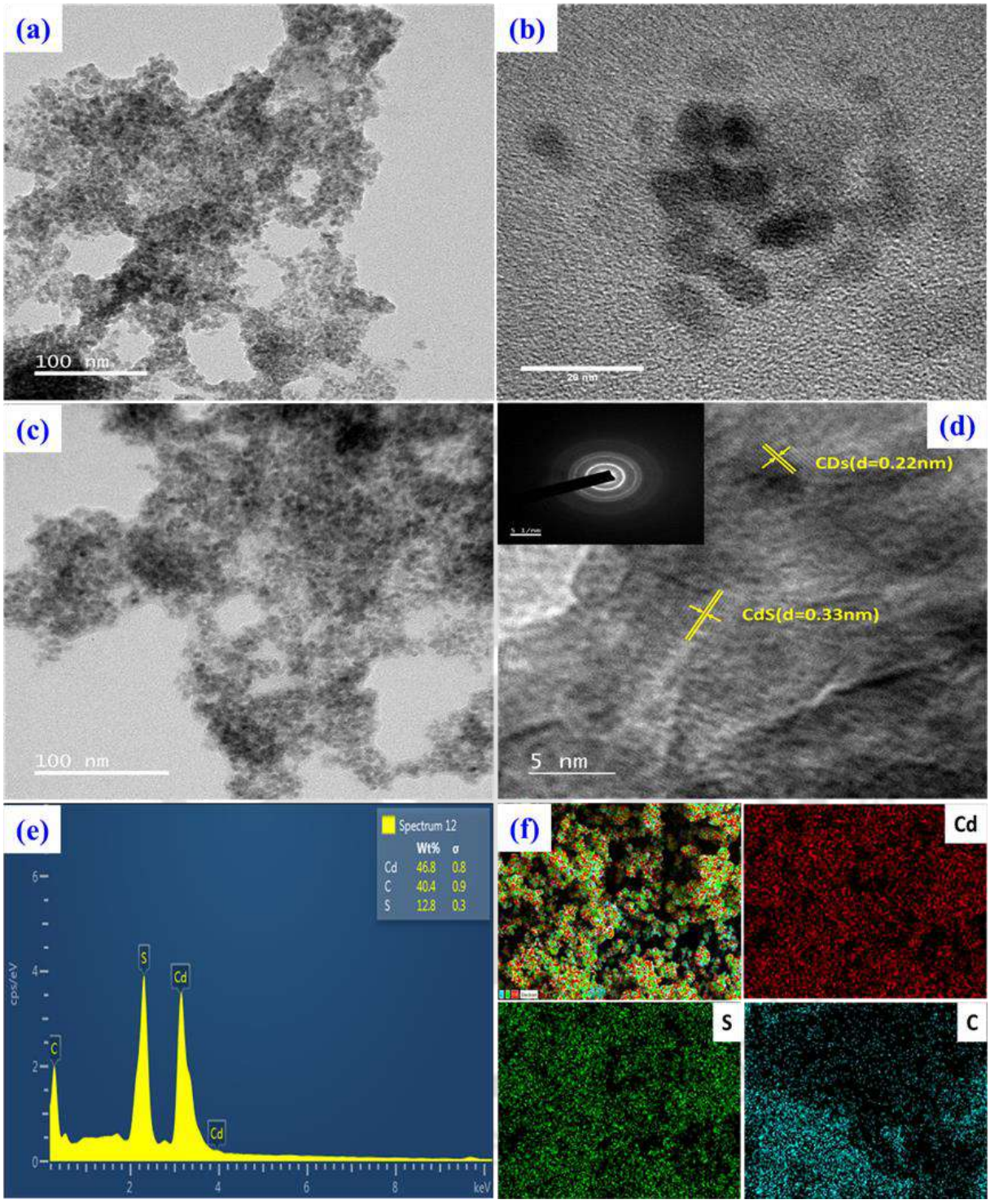

Figure 5.1. TEM images (a) CdS QDs(bio), (b) CDs(bio), and (c) 0.4CDs/CdS QDs(bio) composite, (d) HR-TEM image and (inset) SAED pattern, (e) EDS spectrum, and (f) Elemental mapping with 10 μm scale of 0.4CDs/CdS QDs(bio) composite.

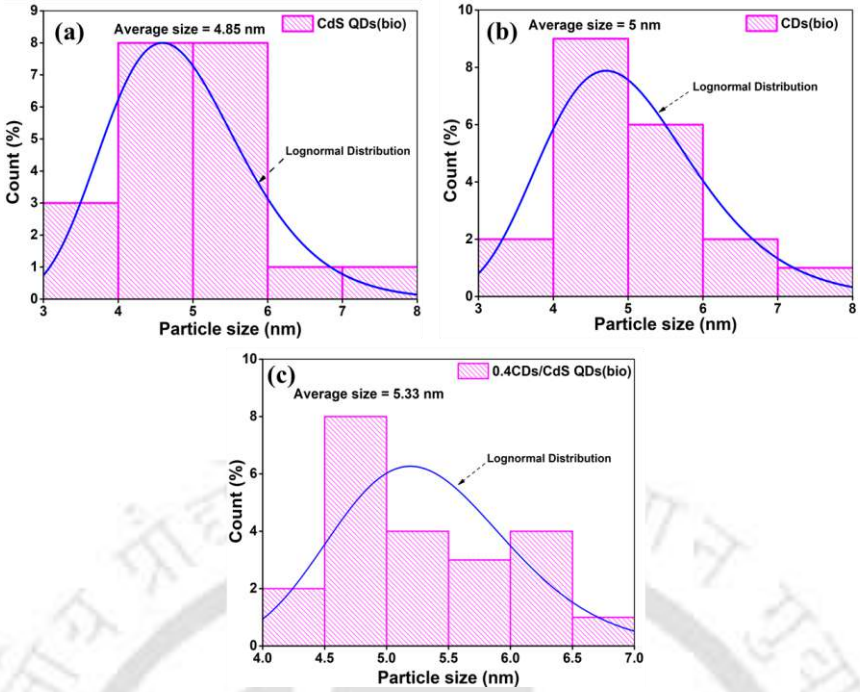

Figure 5.2. TEM particle size distribution of (a) CdS QDs(bio), (b) CDs(bio), and (c) 0.4CDs/CdS QDs(bio) composite.

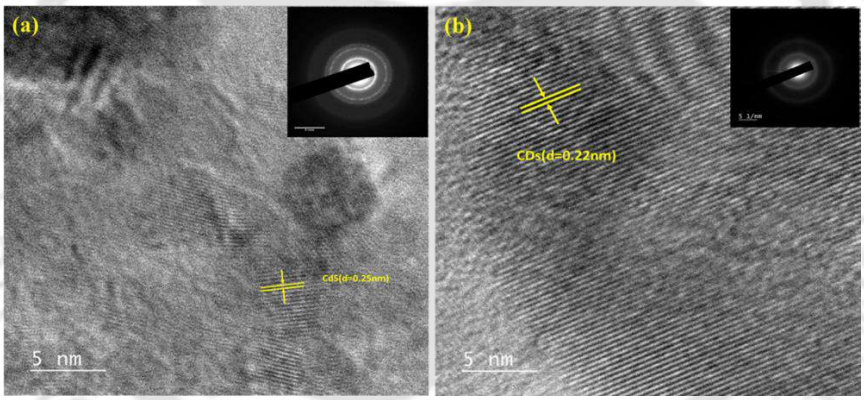

Figure 5.3. HRTEM images and (inset) SAED patterns of (a) CdS QDs(bio) and (b) CDs(bio).

Determination of energy levels: Figure 5.4a depicts the absorption spectra of the synthesized catalysts. CdS QDs(bio) exhibited a notable absorption threshold at 520 nm [17], while CDs exhibited peaks (**Figure 5.4a**(inset)) at 280 nm (n-π* (C=O)) and 220 nm(π-π* (C=C)) [27]. The absorption edge of CDs/CdS QDs(bio) composites displayed a redshift, which is attributed to the existence of delocalized large π bonds, enhancing light absorption intensity [29]. Bandgap energies were determined using Tauc's relation [17], depicted in **Figure 5.4b and Figure 5.4b**(inset). The bandgap of CdS QDs(bio), CDs(bio), and 0.4CDs/CdS QDs(bio) composites were determined to be 2.4, 3, and 2.13 eV, respectively, consistent with reported values [30–32]. The reduction in the bandgap of 0.4CDs/CdS

QDs(bio) composites relative to CdS QDs(bio) is caused by the quantum confinement effect of CDs [26].

Figure 5.4c shows the minimum valence band (VB) energies of CdS QDs(bio) and 0.4CDs/CdS QDs(bio) composites as 1.58 and 1.18 eV, respectively. In **Figure 5.4d**, the energy level diagram of the catalysts gives the calculated maximum conduction band (CB) energies of -0.82 and -0.95 eV for CdS QDs(bio) and 0.4CDs/CdS QDs(bio) composites, respectively. This indicates that the CDs/CdS QDs(bio) composites possess favorable maximum CB energies, suggesting an enhanced rate of HCOOH production [17]. The work function (φ) is determined by the relation $\varphi = hv - E_{cutoff}$ [2], where hv is the energy of the monochromatic ionizing light (21.22 eV), and $E_{cut\text{-}off}$ denotes the threshold energy for the secondary electron obtained from the linear extrapolation of the UPS VB spectrum. The Fermi level (E_F) is determined by the relation $E_F = -\varphi$ [2]. The UPS VB spectra for secondary electrons are presented in **Figure 5.5**. The measured secondary electron cut-off energies for CDs(bio), CdS QDs(bio), and 0.4CDs/CdS QDs(bio) composites are 15.3, 17.41, and 17.0 eV, respectively, with corresponding work function values of 5.92, 3.83, and 4.22 eV. The Fermi level of CDs(bio), CdS QDs(bio), and 0.4CDs/CdS QDs(bio) composites are calculated as -5.92, -3.83, and -4.22 eV, respectively [33,34].

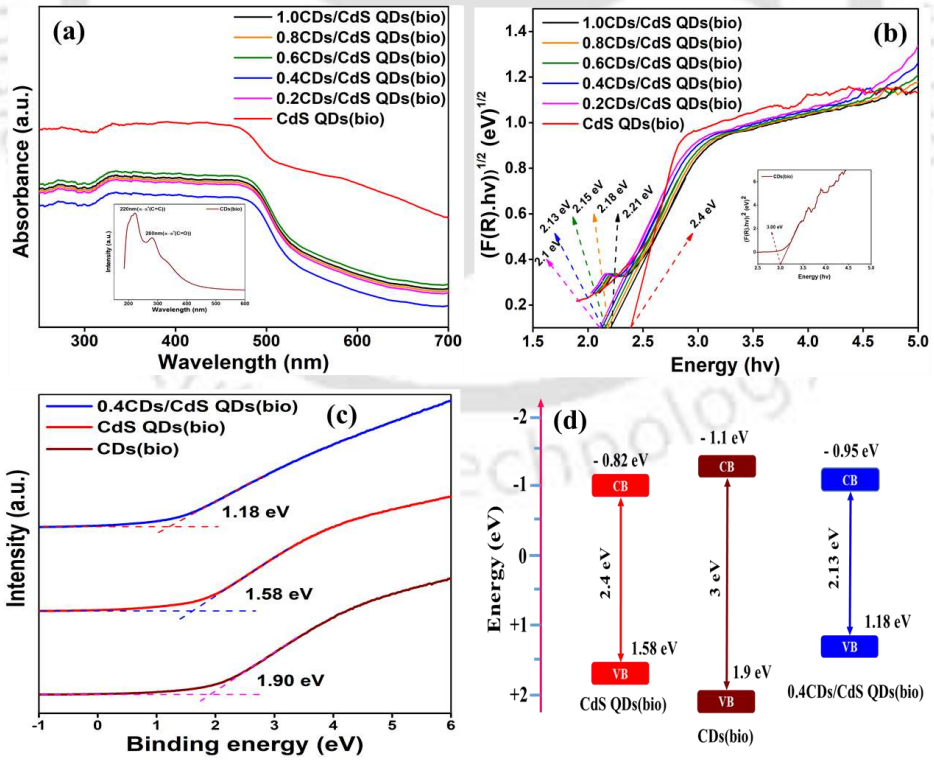

Figure 5.4. (a) Absorption spectra with CDs inset, (b) Bandgap calculation with CDs inset, (c) UPS VB spectra, and (d) Energy band diagram of CdS QDs(bio), CDs(bio), and 0.4CDs/CdS QDs(bio) composites.

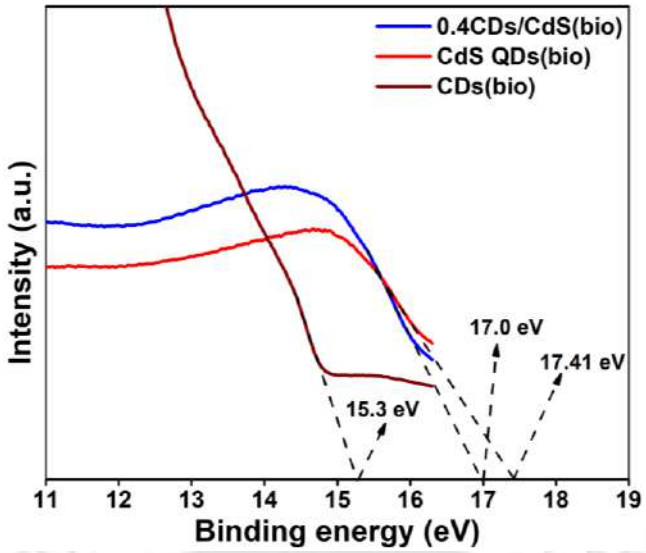

Figure 5.5. UPS VB spectra for secondary electron onset.

XRD analysis: Figure 5.6a displays the XRD patterns of synthesized catalysts. The peaks at 2θ of 51.91°, 43.92°, and 26.51° for CdS QDs (bio) correspond to crystal planes (311), (220), and (111), confirming its cubic structure (JCPDF: 00-001-0647). CDs (**Figure 5.7**) show a peak at a 2θ of 21°, indicating the (002) crystal plane with hexagonal structure (JCPDF: 00-026-1076) of graphitic carbon, consistent with the literature [17,35]. The crystal structure or phase of CdS QDs(bio) remains unchanged with the addition of CDs(bio) in the formation of CDs/CdS QDs(bio) composites. CDs peak is not observed in the composite structure due to its low mass loading (<1% w/w), excellent dispersity, and amorphous characteristics [17]. The crystallite size was calculated using Debey Scherer's equation [36]. The crystallite size of CdS QDs(bio) and CDs/CdS QDs(bio) composites was calculated to be 3.6 and 2.9 nm, respectively.

XPS analysis: XPS spectra (**Figure 5.6b**) of CdS QDs(bio) and CDs/CdS QDs(bio) composites revealed distinct peaks corresponding to Cd, S, and C elements. Cd 3d spectra (**Figure 5.6c**) of CdS QDs(bio) showed peaks at 405.3 eV ($3d_{5/2}$) and 412.1 eV($3d_{3/2}$), representing Cd^{2+} in CdS QDs(bio). S 2p spectra (**Figure 5.6d**) exhibited peaks at 163.1eV($2p_{1/2}$) and 161.88 eV($2p_{3/2}$), indicating the S^{2-} valence state in CdS QDs(bio) [17]. Similar trends were observed in the composites, with S 2p and Cd 3d peak positions shifting to lower binding energies, suggesting a strong chemical interaction between CDs and CdS QDs, facilitating electron transport from CdS QDs to CDs [30]. C 1s spectrum (**Figure 5.6e**) of the composites displayed peaks at 286.1 eV(C-O)and 284.8 eV(C=O) of the graphitic nature of CDs [37]. High-resolution O 1s spectrum (**Figure 5.6f**) shows peaks at 533.2 eV (O-C=O) and 532.7 eV (C=O), suggesting interactions between the carbonyl group and the CdS lattice [38].

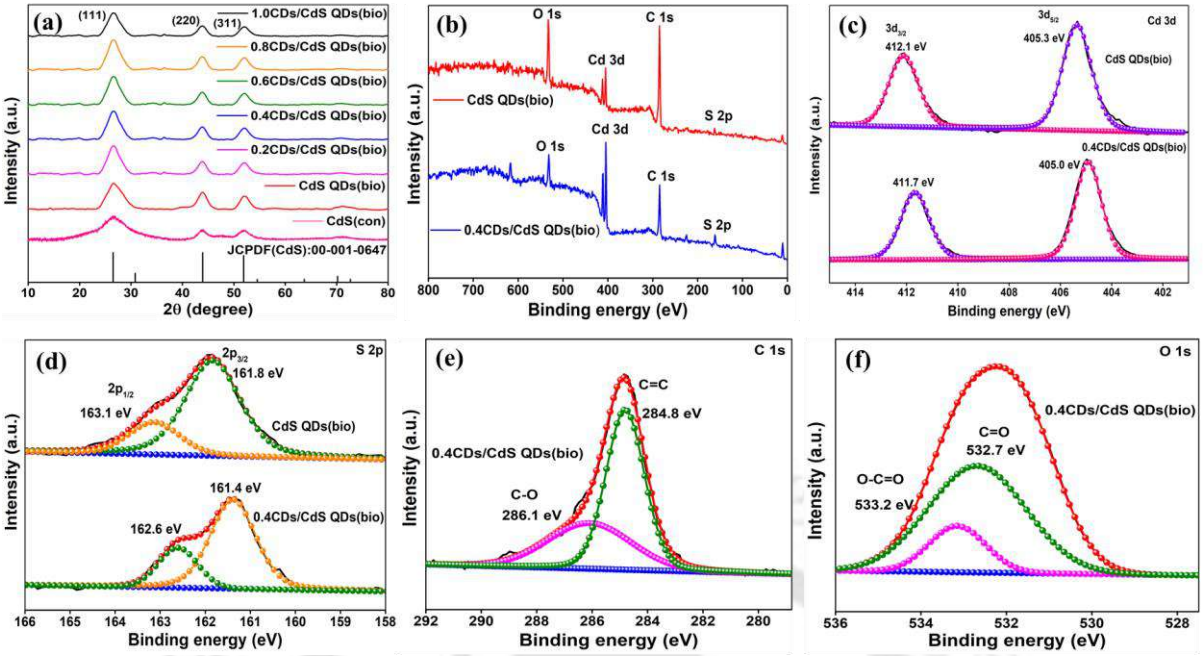

Figure 5.6. (a) XRD diffractograms, (b) XPS survey spectra, (c) Cd 3d and (d) S 2p of CdS QDs(bio) and 0.4CDs/CdS QDs(bio) composites, and (e) C 1s and (f) O 1s of 0.4CDs/CdS QDs(bio) composites.

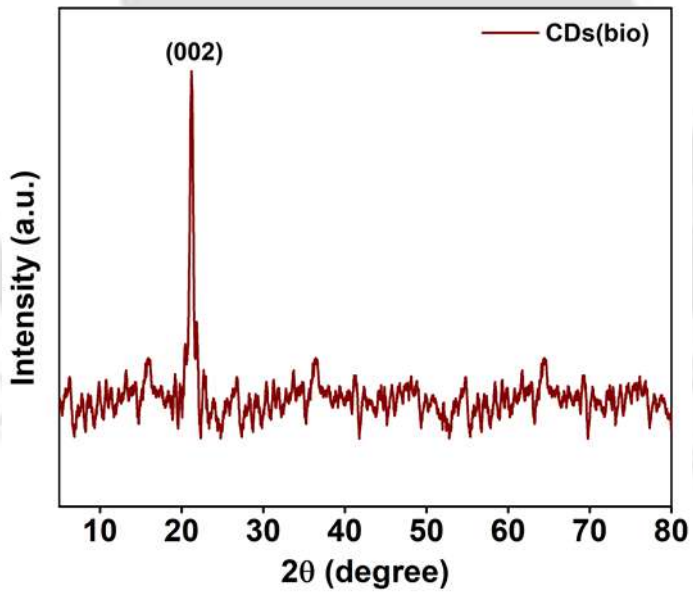

Figure 5.7. XRD pattern of CDs(bio).

Charge trapping and recombination: To examine the charge carrier dynamics and trapping efficiency of the catalysts, PL spectra (**Figure 5.8a**) were obtained with an excitation wavelength of 360 nm. PL intensities of CDs/CdS QDs(bio) composites were notably lower than CdS QDs(bio) because of a delocalized π-conjugated structure of CDs, enhancing electron conduction characteristics. This suggests better separation of photoexcited e^-/h^+ pairs and suppresses recombination [17,26].

TRPL spectra (**Figure 5.8b**) of the synthesized catalyst were recorded with excitation and emission wavelengths of 405 and 450 nm, respectively, to examine charge transfer behavior. The TRPL decay curves were analyzed by fitting them with a bi-exponential decay function. The average lifetimes of charge carriers were determined as 2.7 ns for CdS QDs(bio) and 3.95 ns for 0.4CDs/CdS QDs(bio) composites. The composites exhibit a longer lifetime of charge carriers than the CdS QDs(bio), indicating that 0.4CDs/CdS(bio) demonstrates better efficiency in the separation of e^-/h^+ pairs than CdS(bio). The incorporation of CDs(bio) into CdS(bio) acts as a reservoir for trapping excited e^- at the CDs and CdS interface, resulting in enhanced separation of e^-/h^+ pairs and decreased its recombination [17,26].

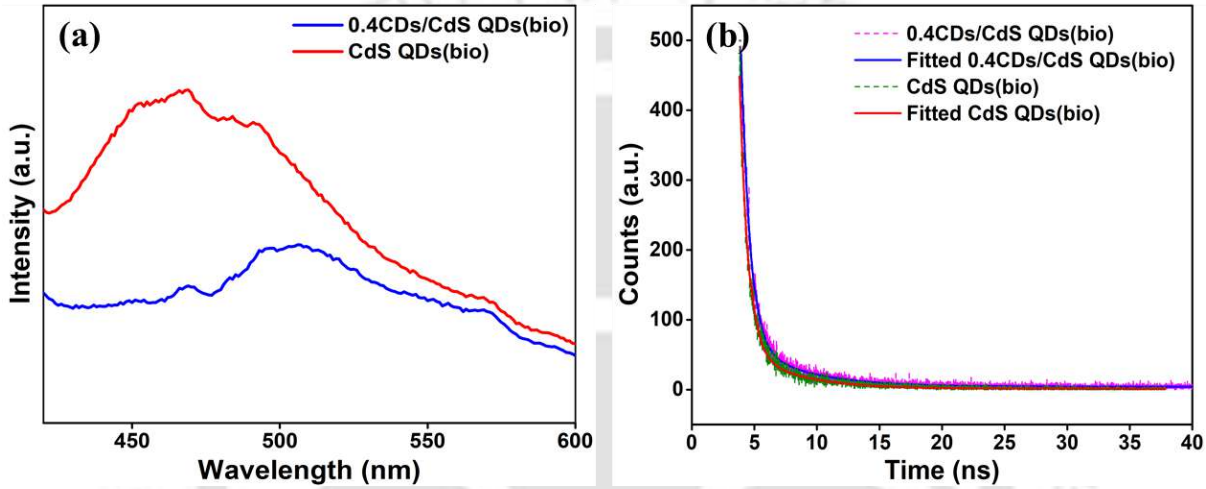

Figure 5.8. (a) PL and (b) TRPL spectra of CdS QDs(bio) and CDs/CdS QDs(bio) composite.

Electron paramagnetic resonance (EPR): The EPR spectra depicted in **Figure 5.9** validate the existence of sulfur vacancies (SVs) in the synthesized catalyst. A faint signal was detected in CdS QDs(bio), while no signal was observed for CDs.The prominent signal at a g value of 2.47 in the 0.4CDs/CdS QDs(bio) composites indicates an abundance of sulfur vacancies, while the faint signal with a g-value of 2.02 may be attributed to the existence of Cd^{2+} [39]. The SVs and Cd^{2+} on the composite surface can effectively trap more photogenerated electrons, thereby extending carrier lifetime. The SVs generate under coordinated metal sites, inducing a bent CO_2 configuration that strengthens adsorption and promotes electron transfer. Additionally, they localize electrons near defect sites, reducing the energy barrier for CO_2 reduction, resulting in enhancing the photocatalytic CO_2 reduction performance [40–42].

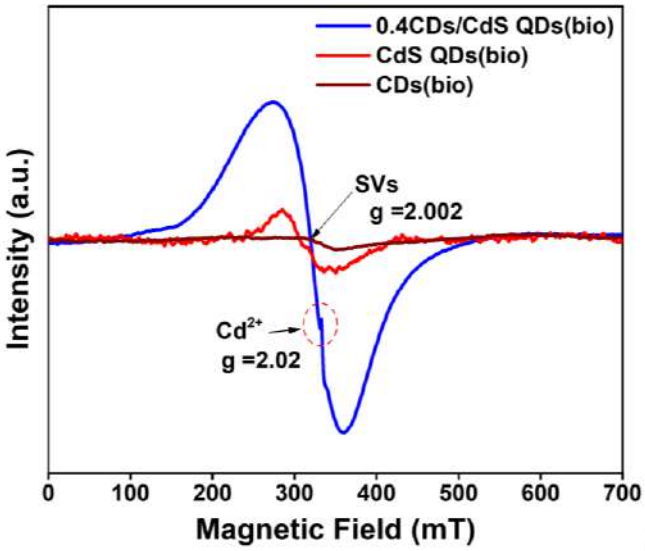

Figure 5.9. EPR spectra of CdS QDs(bio), CDs(bio), and 0.4CD/CdS QDs(bio) composite.

BET surface area analysis: N_2 sorption analysis was conducted to measure the surface area and pore properties of the synthesized catalyst, with results presented in **Table 5.1**. **Figure 5.10a** illustrates the N_2 sorption isotherms, indicating both CdS QDs(bio) and 0.4CDs/CdS QDs(bio) composites display type IV isotherms with an H1 hysteresis loop, indicating a mesoporous characteristic. The surface area and average pore size of CdS QDs(bio) and 0.4CDs/CdS QDs(bio) composites were measured to be 69.52 and 88.8 m^2/g and 6.28 and 7.12 nm, respectively, indicating efficient pathways for molecular transport within the catalysts [18,36]. A minimal variation in surface area was observed with the incorporation of CDs onto CdS QDs(bio). Additionally, the CO_2 adsorption ability of 0.4CDs/CdS QDs(bio) composites (0.342 mmol/g) surpasses that of CdS QDs(bio) (0.102 mmol/g) under 1 bar pressure. The enhancement in CO_2 adsorption is attributed to the π-conjugate structure of CDs, enabling effective binding and interactions between CO_2 and CDs, thereby enhancing adsorption onto CDs/CdS QDs(bio) composites [17]. The TGA analysis is shown in **Figure 5.10b**. The residual carbon content (**Table 5.2**) is determined within the temperature range of 300-500°C [26]. The composite contained 7% (w/w) carbon.

Table 5.1. Physical characteristics of synthesized catalysts.

Catalyst	Bandgap (eV)	Crystallite size (nm)	BET surface area (m^2/g)	Pore volume (cm^3/g)	Average pore (nm)	CO_2 Adsorption (mmol/g)
CdS QDs(bio)	2.4	3.6	69.52	0.11	6.28	0.102

0.4CDs/CdS QDs(bio) composites	2.13	2.9	88.8	0.16	7.12	0.342

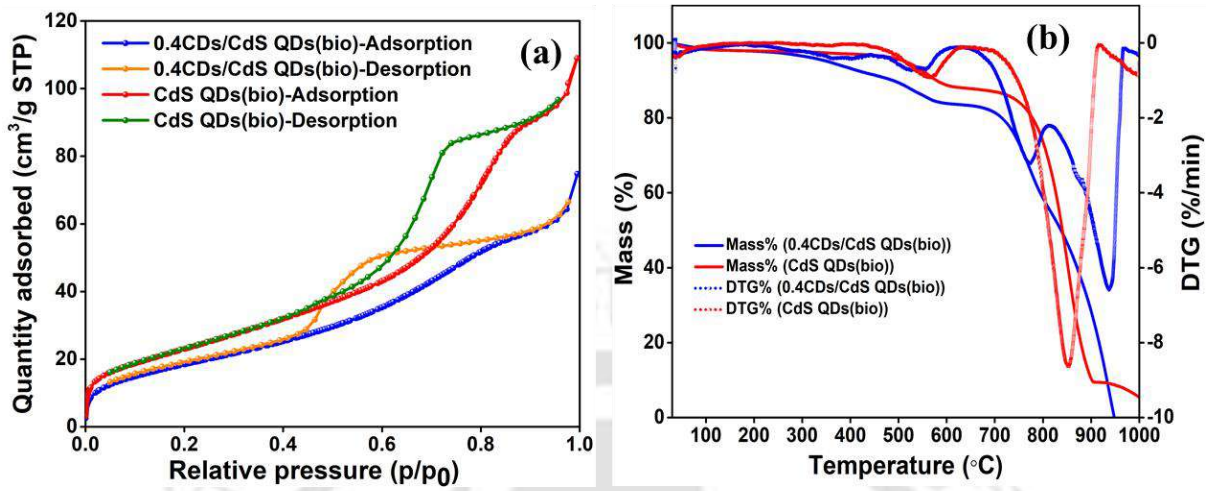

Figure 5.10. (a) N_2 sorption isotherms, and (b) TGA & DTG analysis of CdS QDs(bio) and 0.4CDs/CdS QDs(bio) composite.

Table 5.2. Residual carbon content calculation in catalysts from TGA plot.

Catalysts	**Temperature range of carbon % calculation (°C)**	**Carbon (%)**
CdS QDs(bio)	300 to 500	2.37
0.4CDs/CdS QDs(bio)	300 to 500	7.00

5.2.2 Photoelectrochemical response

The electrochemical characteristics of the synthesized catalyst were investigated through photocurrent measurements and EIS studies. In chronoamperometry (**Figure 5.11a**), the average photocurrent density of 0.4CDs/CdS QDs(bio) composites reached 0.60 μA/cm^2, approximately six-fold higher than that of CdS QDs(bio). This suggests the effective separation of photogenerated e^-/h^+ pairs with the incorporation of CDs(bio) onto CdS QDs(bio) [17].

In the EIS spectra (**Figure 5.11b**) under visible light, a reduced arc radius was observed for 0.4CDs/CdS QDs(bio) composites, indicating enhanced charge separation and transfer efficacy. The EIS-fitted parameters are listed in **Table 5.3**, and the equivalent circuit is depicted in **Figure 5.11b**(inset). Charge transfer resistance (Rp) values for CdS QDs (bio) and 0.4CDs/CdS QDs (bio) under light conditions were 13.2 and 6.93 MΩ, respectively, and under dark conditions, they were 14.8 and 8.17 MΩ, respectively. The smaller arc radius and lower resistance signify enhanced conductivity, faster charge carrier migration, and decreased charge recombination rate [43,44]. This finding indicates improved separation and transfer of charge

carriers in the CDs/CdS QDs(bio) composite, which aligned well with photocurrent and PL analysis results.

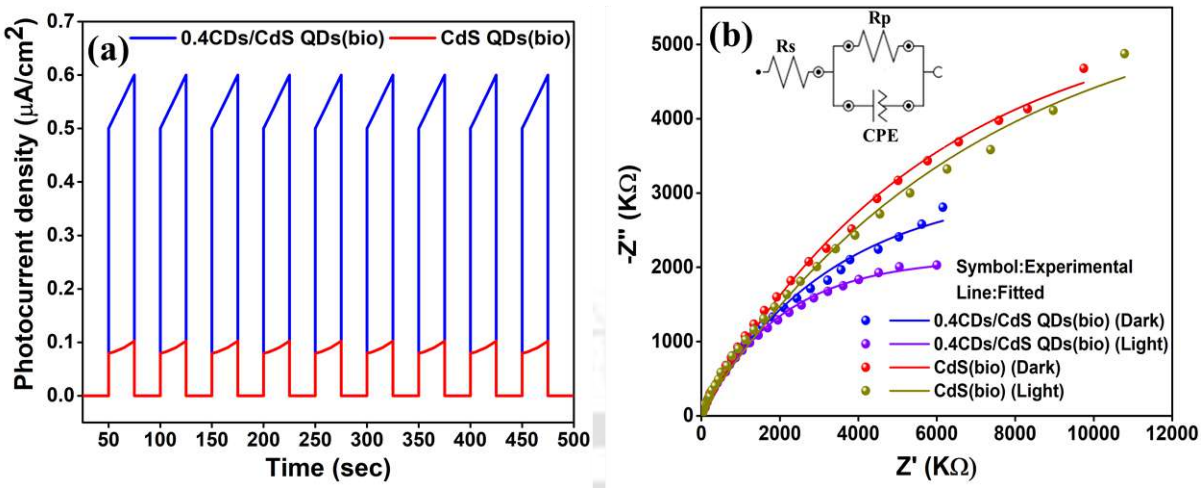

Figure 5.11. (a) Chronamperometry study and (b) Nyquist plots (EIS) under light and dark conditions, and (inset) equivalent circuit used for EIS studies.

Table 5.3. Parameters of circuit used for fitting of EIS data.

Catalyst	Rs (KΩ)	Rp (MΩ)	CPE
CdS QDs(bio) (Dark)	6.23	14.8	Y_0=188nMho×S^N N=0.566
CdS QDs(bio) (Light)	4.83	13.2	Y_0=221nMho×S^N N=0.574
0.4CDs/CdS QDs(bio) (Dark)	2.60	8.17	Y_0=259nMho×S^N N=0.574
0.4CDs/CdS QDs(bio) (Light)	2.20	6.93	Y_0=273nMho×S^N N=0.579

Rs: Electrolytes resistance; Rp: Charge transfer resistance; CPE: Constant phase element

5.2.3 Photocatalytic CO_2 reduction evaluation

The synthesized catalysts were evaluated for HCOOH production under visible light illumination. In this study, HCOOH is the only product formed. The HPLC and GC chromatograms are provided in **Figure 5.12**. **Figure 5.13a** presents the calibration curve of the formic acid standard, and chromatograms of standards and resulting products are shown in **Figure 5.13b**. Negligible HCOOH production was observed without the presence of a catalyst or light illumination. To identify the carbon source involved in HCOOH formation, three control experiments were conducted under optimal conditions, each with one component absent: (i) CO_2, (ii) lamp, and (iii) catalyst. Notably, no HCOOH was generated in any of these

control tests (**Figure 5.14**), indicating that HCOOH originates from the CO_2 feedstock in the system. To verify the PCO_2RR activity and exclude the possibility of organic contaminants photo-degradation, a control experiment using N_2 instead of CO_2 showed no detectable CO_2 reduction products (**Figure 5.15**), confirming the exclusive origin from PCO_2RR.

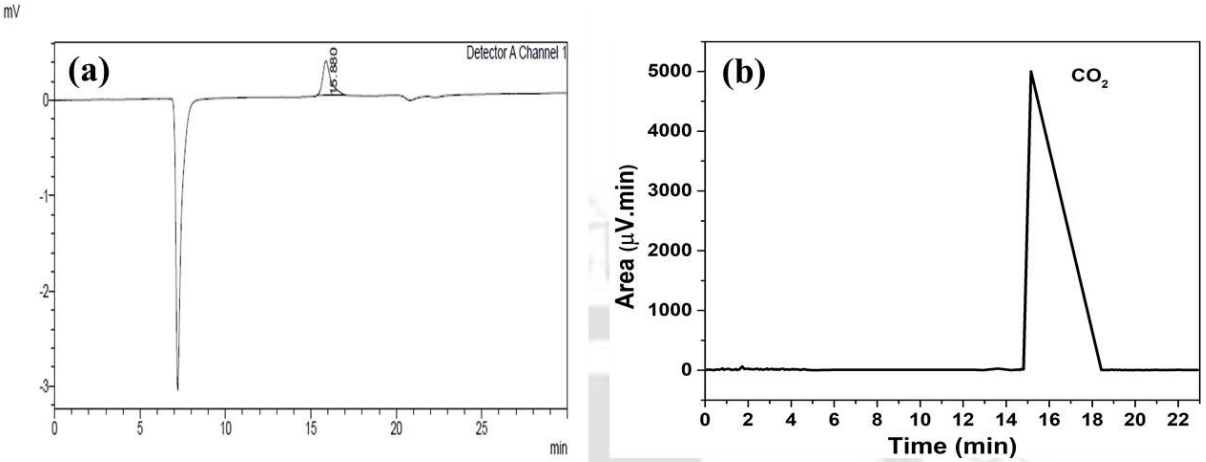

Figure 5.12. Chromatograms of (a) HPLC and (b) GC solution after 5 h of CO_2 reduction.

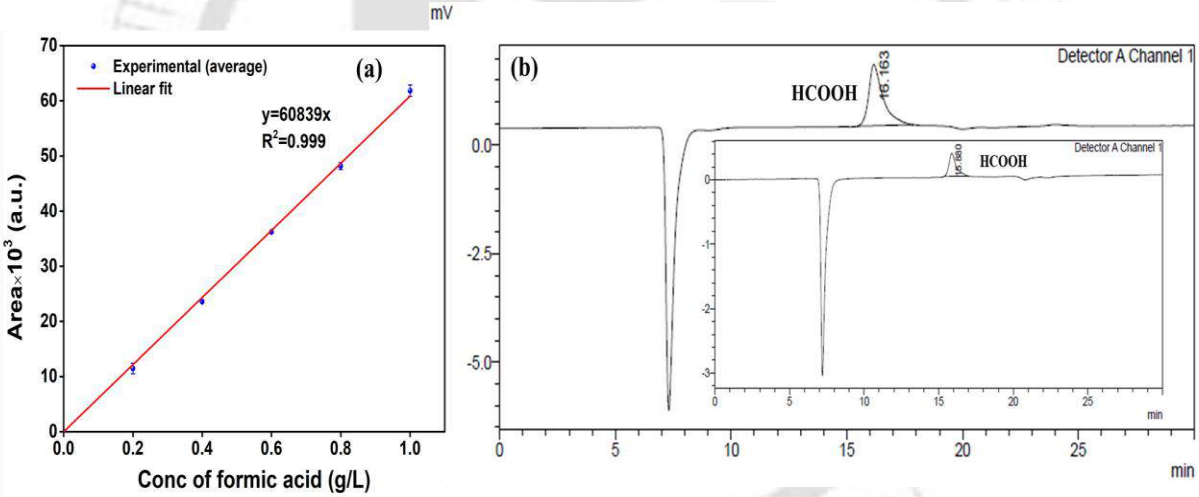

Figure 5.13. (a) Calibration graph of formic acid standard, (b) HPLC chromatograms of standard 1 g/L HCOOH, and (inset) solution after 5 h of CO_2 reduction.

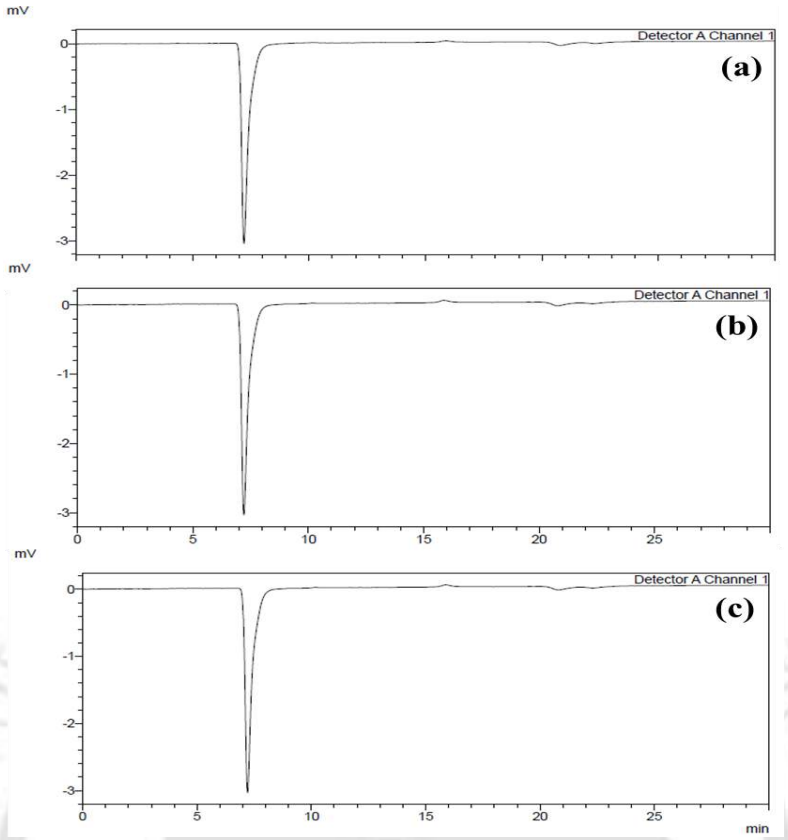

Figure 5.14. HPLC chromatograms of 300 s of CO_2 reduction (a) 0.4CDs/CdS QDs(bio) composite + DI water + light irradiation, (b) 0.4CDs/CdS QDs(bio) composite + DI water + CO_2 purge, and (c) DI water + CO_2 purge + light irradiation.

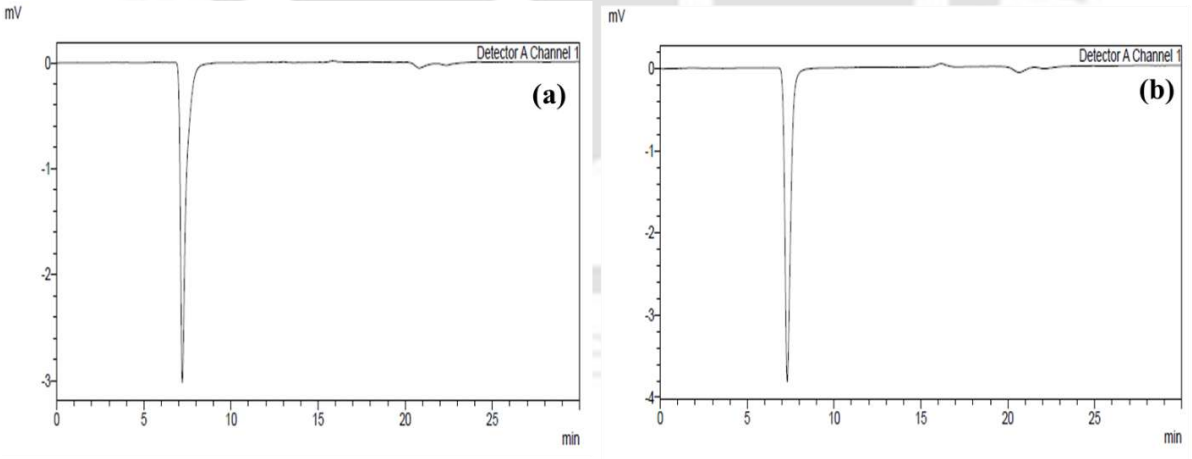

Figure 5.15. HPLC chromatogram of control experiments (a) after 5 h, and (b) after 10 h of the control experiments using N_2 instead of CO_2.

Figure 5.16a shows the rate of HCOOH formation using CdS QDs(bio) and CDs/CdS QDs(bio) composites at varying loading percentages (0.2, 0.40, 0.6, 0.8, and 1% w/w). CdS QDs(bio) exhibited negligible HCOOH production attributed to photo-corrosion and rapid e^-

/h^+ pairs recombination, as evidenced by XPS and PL studies (**Figure 5.17c & Figure 5.8a**), inferring its inefficiency as a catalyst for PCO_2RR to HCOOH [38]. Conversely, CDs(bio) did not generate any product due to the absence of active catalytic sites [17]. HCOOH formation was observed in CDs/CdS QDs(bio) composites, showing an increasing trend in rate up to 0.4% (w/w) CDs loading, peaking at 428.39 μmol/g·h. However, further increases in CDs loading significantly decreased the HCOOH formation rate. This reduction is caused by particle aggregation and blockage of active sites on CdS QDs(bio), which hinder light absorption [26]. Dynamic light scattering (DLS) analysis (**Table 5.4**) indicated particle size increased from 164.5 to 200.2 nm when CDs(bio) loading exceeded 0.4% (w/w), indicating particles agglomeration. Thus, optimal CDs loading for the CDs/CdS QDs(bio) composite catalyst was determined to be 0.4% (w/w).

Figure 5.16b illustrates the HCOOH formation rate using different concentrations of 0.4CDs/CdS QDs(bio) composites (0, 0.25, 0.40, 0.75, 1.0, 1.25 g/L). The highest HCOOH production rate was attained at a 0.75 g/L photocatalyst concentration, yielding 439.51 μmol/g·h with an AQY of 3.79% (AQY calculation provided in **Table A3**). The selectivity is 100% as a single product was formed. However, increased photocatalyst concentrations resulted in turbidity in the solution, impeding efficient light irradiation [17]. Turbidity assessments for various photocatalyst concentrations are outlined in **Table 5.5**, indicating a 23.07% increase in turbidity beyond 0.75 g/L. A comparison of the achieved HCOOH formation rate in this study with reported literature values (**Table 5.6**), the bio-based CDs/CdS QDs(bio) composites demonstrated a clear superiority.

Figure 5.16c illustrates the evaluation of the functional stability of the 0.4CDs/CdS QDs(bio) composites through repeated cycles of time-dependent PCO_2RR to HCOOH production. Over five consecutive cycles, the composites demonstrated consistent photocatalytic activity with only a marginal 2.21% decline in their performance. This minor decrease is attributed to the unavoidable loss of catalysts during the recovery process. This exceptional stability indicates that the integration of CDs(bio) onto CdS QDs(bio) mitigated photocorrosion and inhibited the e^-/h^+ pairs recombination, leading to the improved overall stability of the composites [45,46].

The high HCOOH formation observed in this study is attributed to the synergistic material design of the bio-based CDs/CdS QDs composite. The more negative conduction band position, abundant sulfur vacancies, and enhanced CO_2 adsorption preferentially stabilize the HCOO* intermediate, favoring the two-electron reduction pathway [47,48]. Time-resolved PL and photoelectrochemical studies confirm efficient charge separation and suppressed

recombination, while DFT calculations show HCOO* to be thermodynamically more favorable ($\Delta G = -0.71$ eV) than the COOH* pathway. In addition, improved catalyst stability and reduced photocorrosion enable sustained activity, resulting in higher cumulative HCOOH yields compared to previous reports.

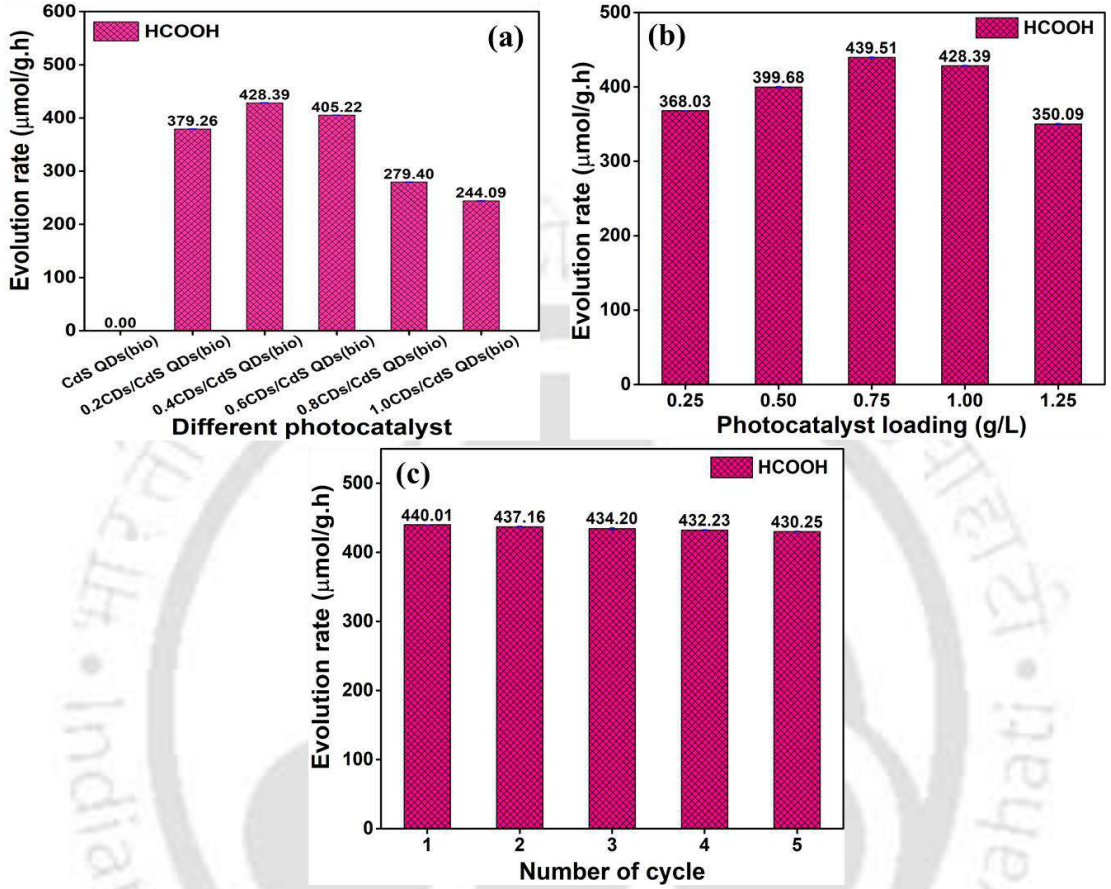

Figure 5.16. (a) Photocatalytic CO_2 reduction using various bio-based photocatalysts, (b) Effect of photocatalyst loading, and (c) Functional stability study of 0.4CDs/CdS QDs(bio) composite under visible light.

Table 5.4. Hydrodynamic diameter of CdS QDs(bio) and CDs/CdS QDs(bio) composites.

Catalysts	Hydrodynamic diameter (nm)
CdS QDs(bio)	180.2
0.2CDs/CdS QDs(bio)	152.6
0.4CDs/CdS QDs(bio)	164.4
0.6CDs/CdS QDs(bio)	178.2
0.8CDs/CdS QDs(bio)	186.4
1.0CDs/CdS QDs(bio)	200.2

Table 5.5. Turbidity of CDs/CdS QDs(bio) composite.

Catalyst concentration (g/L)	Turbidity (NTU)
0.25	132
0.50	168
0.75	195
1.0	215
1.25	240

Table 5.6. Formic acid formation in the present and earlier studies.

Photocatalysts	Synthesis method	Reaction solvent	Light source	Performance (μmol/g·h)	Source
0.4CDs/CdS QDs(bio) composite	Facile deposition method	H_2O	250W, Metal halide lamp, λ>420 nm	439.51	**Present work**
(Mo-bi)sx/CdS	Hydrothermal	MeCN/[Bmim] BF_4/TEOA	Visible light (λ = 420–780 nm	208	[47]
MPA&MUA CdS QDs	-	H_2O/TEOA	LED, λ=400 nm	280	[48]
CdS/Mn_2O_3	Electrochemical deposition		Sunlight	139.2	[49]
CdS(commercial)	-	H_2O	Medium-pressure mercury lamp	0.265	[50]
		H_2O/TMACI		1.079	
CdS(commercial)	-	H_2O	Medium-pressure Hg arc lamps	9.87×10^{-7}	[51]
		H_2O/TMACI		2.39×10^{-7}	
CdS(commercial)	-	H_2O/propanol	500 W high-pressure mercury arc lamp	5.65	[52]

TEOA: Triethanolamine; MeCN: Acetonitrile; TMACI: tetramethylammonium chloride; MPA: 3-mercaptopronic acid; MUA:11-mercaptoalkanoic acid; BMIM-BF4:1-Butyl-3-methylimidazolium tetrafluoroborate; QDs: Quantum dots

5.2.4 Stability of CDs/CdS QDs(bio) composites

The XPS survey spectra (**Figure 5.17a**) validate the existence of C, S, and Cd elements in the 0.4CDs/CdS QDs (bio)/used composite, whereas only Cd was identified in CdS

QDs(bio)/used. The HR spectra of 0.4CDs/CdS QDs (bio)/used (**Figures 5.17b-5.17e**) exhibit similar binding energies before and after PCO_2RR. In contrast, for CdS QDs (bio)/used) (**Figures 5.17b-5.17c**), The S 2p peak binding energy exhibits an additional peak at 168.6 eV (S^{6+}), indicating sulfur oxidation (photocorrosion) and the formation of SO_4^{2-} [53,54].

XRD and FETEM analyses were carried out of 0.4CDs/CdS QDs(bio) composites before and after PCO_2RR to evaluate their structural and morphological characteristics. The XRD pattern of CDs/CdS QDs(bio) and 0.4CDs/CdS QDs(bio/used) (**Figure 5.18a**) exhibited no significant alterations in the lattice structure of CDs/CdS QDs(bio/used), with the crystallite size remaining consistent at 2.9-2.95 nm. Furthermore, the FETEM image of CDs/CdS QDs(bio/used) (**Figure 5.18b**) indicated no discernible changes in morphology compared to the initial CDs/CdS QDs(bio) (**Figure 5.1c**).

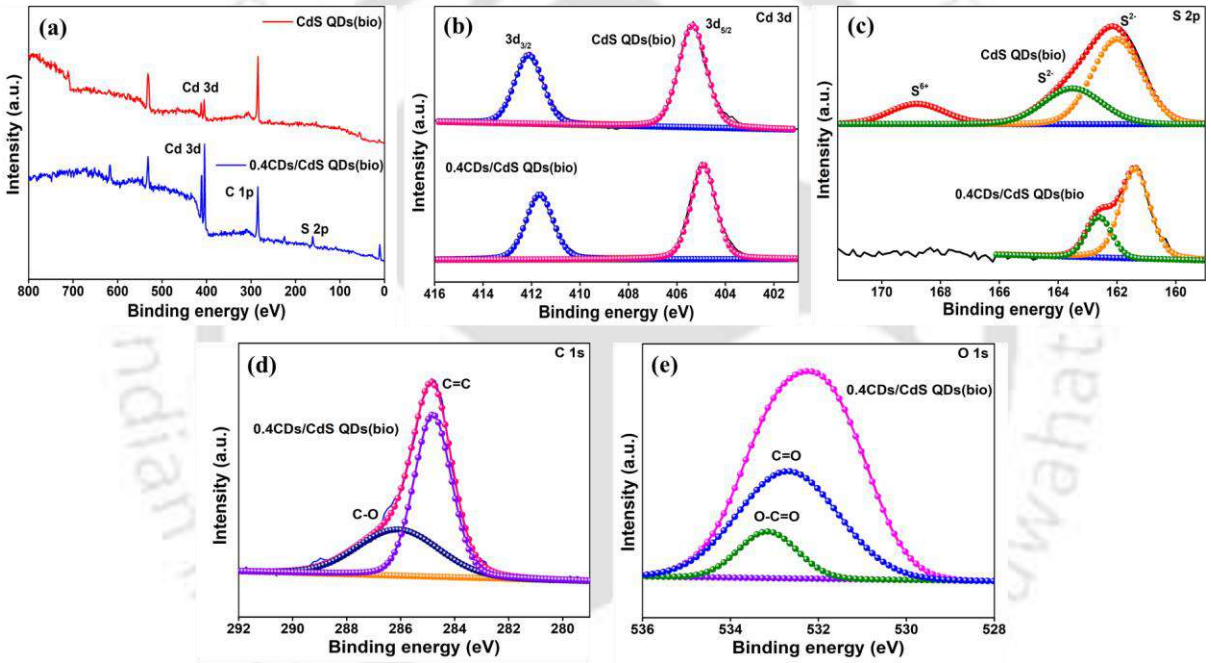

Figure 5.17. (a) XPS survey spectra and HR spectra of (b) Cd 3d, (c) S 2p for CdS QDs(bio)/used and 0.4CDs/CdS QDs(bio)/used, and (d) C 1s, (e) O 1s of 0.4CDs/CdS QDs(bio)/used.

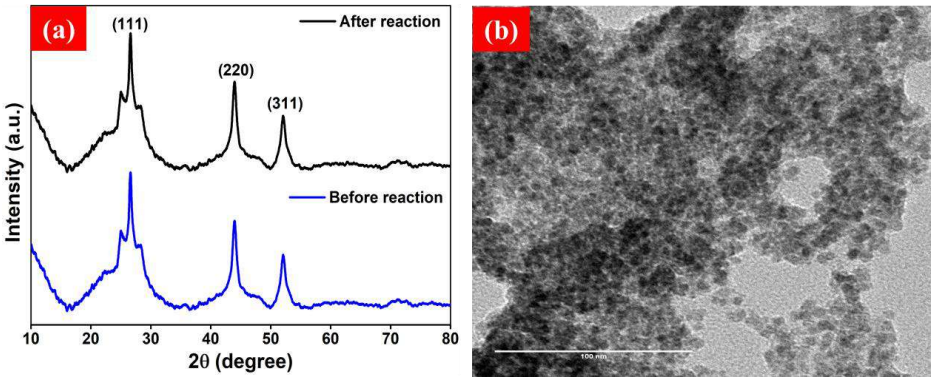

Figure 5.18. (a) XRD patterns of 0.4CDs/CdS QDs(bio) before and after PCO_2RR, and (b) FETEM of 0.4CDs/CdS QDs(bio)/used.

5.2.5 Band bending and charge transfer over CDs/CdS QDs(bio) composites

UPS VB and band position analysis indicate that CDs(bio) possess a higher work function and lower Fermi level, whereas CdS QDs(bio) exhibit the opposite traits. Upon interfacial contact, electrons from CdS QDs(bio) spontaneously transfer to CDs(bio) until Fermi level equilibrium is achieved. As a result, CdS QDs(bio) exhibit downward band bending with positive charge accumulation at the interface, while CDs(bio) undergo upward band bending, acquiring a negative charge, thereby forming an internal electric field (IEF) [2,32,55]. Under light illumination, the IEF and Coulomb effect drive photogenerated electrons from the CB of CDs(bio) to CdS QDs(bio), while holes migrate from the VB of CdS QDs(bio) to the VB of CDs(bio). As a result, electrons in the CB of CdS QDs(bio) drive CO_2 reduction to formic acid, while holes in the VB of CDs(bio) oxidize H_2O, generating protons (H^+) and hydroxyl radicals (•OH), completing the photocatalytic redox cycle (**Figure 5.19**).

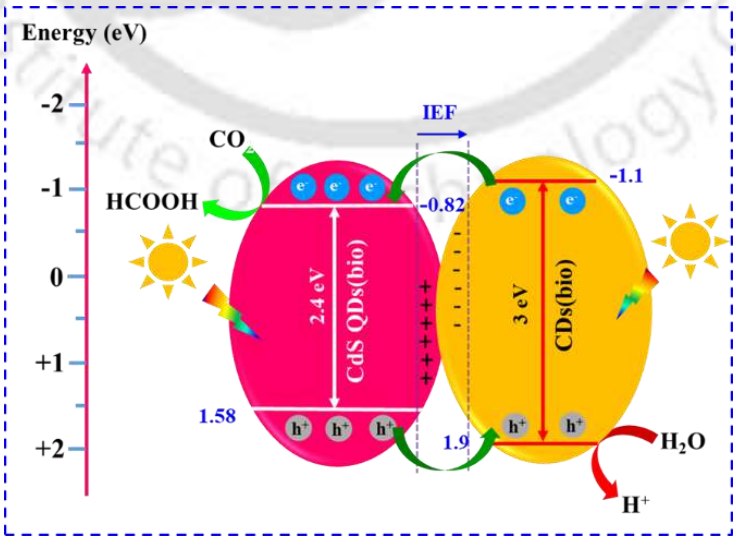

Figure 5.19. Proposed band bending and charge transfer mechanism in CDs/CdS QDs(bio) composite for photocatalytic CO_2 reduction.

5.2.6 DFT calculations for PCO$_2$RR Mechanism

To gain insights into the reactivity of CDs/CdS QDs composites for CO_2 reduction reactions, we performed periodic DFT calculations. Prior to exploring direct CO_2 activation, the CDs/CdS QDs composite was optimized, comprising zero-dimensional CDs and the CdS QDs (111) surface, with an interlayer distance of 3.36 Å (**Figure 5.20a (i)**). Subsequently, linear CO_2 molecules were adsorbed onto the CDs/CdS QDs composite, yielding a binding energy of -0.67 eV. As expected, CO_2 typically exhibits weak binding to catalytic surfaces due to its high-lying lowest unoccupied molecular orbital (LUMO) [56]. The calculated distance between CO_2 and CDs is 3.48 Å (**Figure 5.20a (ii)**), indicative of physisorption. To activate the CO_2 molecule on the composite catalyst, an electron (e^-)-coupled proton (H^+) transfer ($H^+ + e^-$) was introduced following the computational hydrogen electrode (CHE) model. According to previous studies, hydrogen can be added at either the carbon center, leading to HCOOH formation, or at the oxygen center, resulting in CO production. Our calculations revealed that the free energy changes (ΔG) for the formation of the intermediates HCOO* and COOH* were 1.99 eV and 1.94 eV, respectively, as seen in **Figure 5.20b**. These comparable energies suggest that both intermediates could form after the initial proton-coupled electron transfer. As depicted in **Figures 5.20a(iii-vi)**, the HCOO* intermediate adopts a V-shaped configuration, with both oxygen atoms of CO_2 oriented toward the CDs surface, while the COOH* intermediate aligns nearly parallel to the CDs layer. Further proton-coupled electron transfer results in the final products, HCOOH and CO, with ΔG values of -1.79 and -1.08 eV, respectively. The reaction profile indicates that the formation of HCOOH is energetically favored over CO by -0.71 eV, which is consistent with experimental observations.

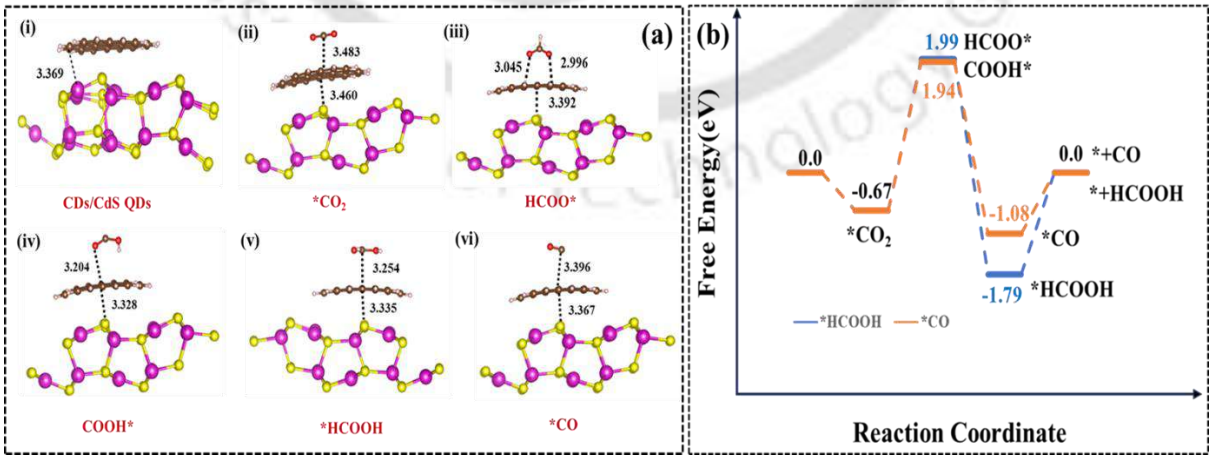

Figure 5.20. CO_2 reduction reactions over the CDs/CdS QDs composite systems (a) Optimized structures, and (b) Computed Gibbs free energy reaction profile for the formation of HCOOH and CO.

Density of states (DOS) analysis, shown in **Figures 5.21a-5.21d**, reveals that sulfur atoms in the CDs/CdS QDs composite predominantly contribute to the valence band near the Fermi level. Upon examining the projected density of states (PDOS) for CO_2 adsorption, we found that the valence band is primarily occupied by sulfur, while the conduction band contributions from carbon and oxygen are significantly distant from the Fermi level, indicating that CO_2 is physisorbed rather than chemisorbed on the composite. After proton-coupled electron transfer to CO_2, distinct PDOS profiles arise for the HCOO* and COOH* intermediates. A comparison of these intermediates shows a greater contribution of carbon and oxygen orbitals near the Fermi level in HCOO* than in COOH*, suggesting stronger electronic interactions for HCOO*. Based on the reaction profile and electronic structure analysis, it is evident that the formation of formic acid is thermodynamically more favorable than carbon monoxide production.

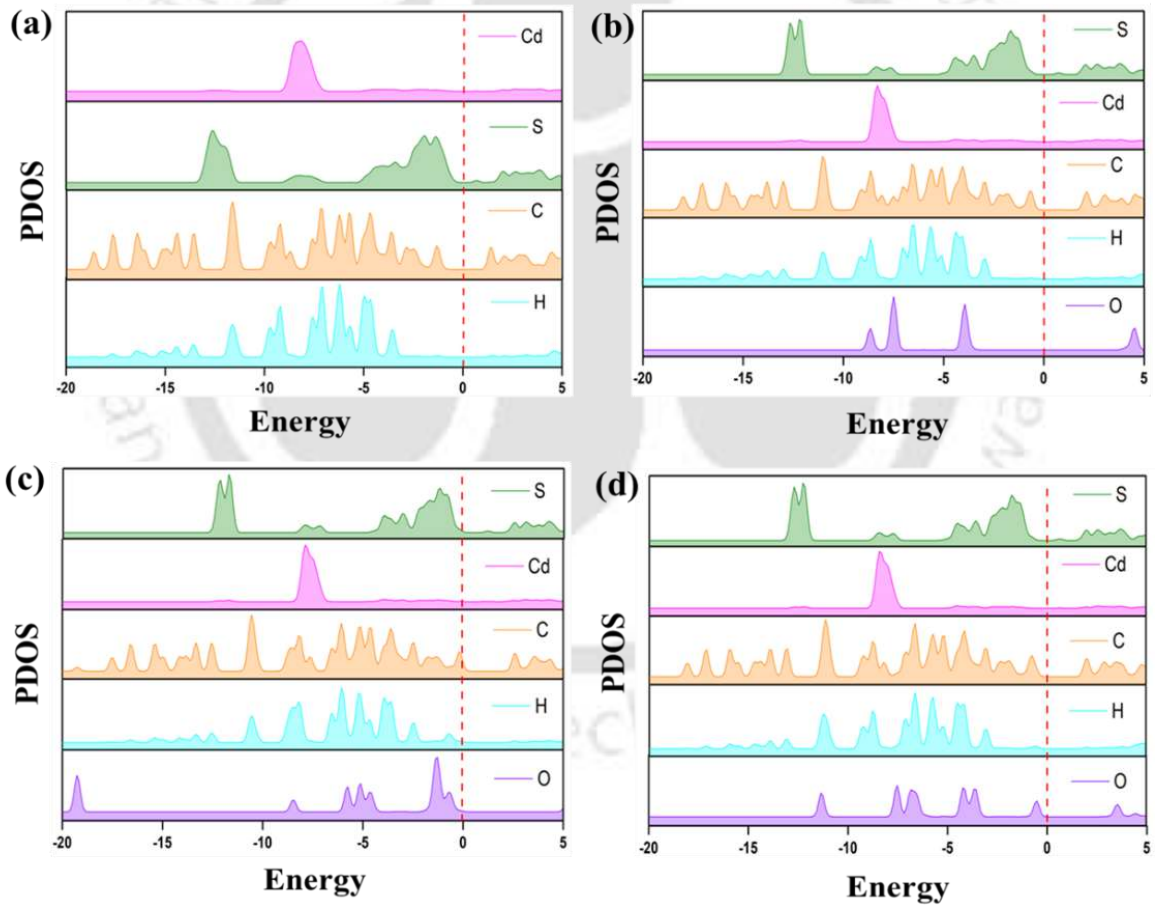

Figure 5.21. Projected density of states for (a) CDs/CdS QDs composite, (b) CO_2 adsorbed on CDs/CdS QDs composites, (c) HCOO* intermediate, and (d) COOH* intermediate.

5.3 Major findings

In this study, 0D CDs/CdS QDs composites with abundant SVs vacancies were successfully synthesized using natural precursors, including *orange peels* and phytochemicals from *Aegle marmelos*. The CDs/CdS QDs(bio) composites exhibited a significantly longer decay lifetime, superior CO_2 adsorption affinity, and higher photocurrent response than CdS QDs(bio). Notably, 0.4CDs/CdS QDs(bio) composites achieved a remarkable HCOOH rate of 439.51 μmol/g·h (AQY 3.81%) without sacrificial agent. The composites were stable with no noticeable changes in morphology and crystallite size owing to CDs incorporation onto CdS QDs(bio), preventing its photo-corrosion and inhibiting charge recombination. DFT analysis validated the preferential HCOOH formation over CO with a free energy difference of -0.71 eV. DOS revealed strong carbon-oxygen orbital interactions near the Fermi level, enhancing HCOO* intermediate stabilization and promoting HCOOH production. *However, CDs/CdS QDs exhibited narrow product selectivity towards HCOOH. To overcome this, the fourth objective introduced Z-scheme SnO_2/CdS QDs heterostructures, which combined spatial charge separation, strong redox potential alignment, and high product selectivity. DFT study was used to reveal the underlying mechanism of improved charge transfer and its role in improving photocatalytic performance.*

References

[1] J. Xue, Y. Yu, C. Yang, K. Zhang, X. Zhan, J. Song, J. Gui, Y. Li, X. Jin, S. Gao, Y. Xie, Developing Atomically Thin $Li_{1.81}H_{0.19}Ti_2O_5 \cdot 2H_2O$ Nanosheets for Selective Photocatalytic CO_2 Reduction to CO, Langmuir. 38 (2022) 523–530. https://doi.org/10.1021/acs.langmuir.1c02944.

[2] P.M. Gawal, A.K. Golder, Plant-Based Phytochemicals for Synthesis of Z-Scheme In_2O_3/CdS Heterostructures: DFT Analysis and Photocatalytic CO_2 Reduction to HCOOH and CO, Langmuir. 40 (2024) 13538–13549. https://doi.org/10.1021/acs.langmuir.4c01015.

[3] X. Li, J. Yu, M. Jaroniec, X. Chen, Cocatalysts for selective photoreduction of CO_2 into solar fuels, Chem. Rev. 119 (2019) 3962–4179. https://doi.org/10.1021/acs.chemrev.8b00400.

[4] Ž. Kovačič, B. Likozar, M. Huš, Photocatalytic CO2Reduction: A Review of Ab Initio Mechanism, Kinetics, and Multiscale Modeling Simulations, ACS Catal. (2020) 14984–15007. https://doi.org/10.1021/acscatal.0c02557.

[5] H. Shen, T. Peppel, J. Strunk, Z. Sun, Photocatalytic Reduction of CO_2 by Metal-Free-Based Materials: Recent Advances and Future Perspective, Sol. RRL. 4 (2020) 1900546. https://doi.org/10.1002/solr.201900546.

[6] K. Yang, Z. Yang, C. Zhang, Y. Gu, J. Wei, Z. Li, C. Ma, X. Yang, K. Song, Y. Li, Q. Fang, J. Zhou, Recent advances in CdS-based photocatalysts for CO_2 photocatalytic conversion, Chem. Eng. J. 418 (2021) 129344. https://doi.org/10.1016/j.cej.2021.129344.

[7] S. Wang, X. Wang, Photocatalytic CO_2 reduction by CdS promoted with a zeolitic imidazolate framework, Appl. Catal. B Environ. 162 (2015) 494–500. https://doi.org/10.1016/j.apcatb.2014.07.026.

[8] L. Cheng, Q. Xiang, Y. Liao, H. Zhang, CdS-Based photocatalysts, Energy Environ. Sci. 11 (2018) 1362–1391. https://doi.org/10.1039/c7ee03640j.

[9] J.A. Nasir, Z.U. Rehman, S.N.A. Shah, A. Khan, I.S. Butler, C.R.A. Catlow, Recent developments and perspectives in CdS-based photocatalysts for water splitting, J. Mater. Chem. A. 8 (2020) 20752–20780. https://doi.org/10.1039/d0ta05834c.

[10] L. Zhu, Y. Liu, X. Peng, Y. Li, Y.-L. Men, P. Liu, Y.-X. Pan, Noble-metal-free CdS nanoparticle-coated graphene oxide nanosheets favoring electron transfer for efficient photoreduction of CO_2, ACS Appl. Mater. Interfaces. 12 (2020) 12892–12900. https://doi.org/10.1021/acsami.0c00163.

[11] Y.-X. Feng, H.-J. Wang, J.-W. Wang, W. Zhang, M. Zhang, T.-B. Lu, Stand-alone CdS nanocrystals for photocatalytic CO_2 reduction with high efficiency and selectivity, ACS Appl. Mater. Interfaces. 13 (2021) 26573–26580. https://doi.org/10.1021/acsami.1c03606.

[12] M. Zhou, S. Wang, P. Yang, C. Huang, X. Wang, Boron Carbon Nitride Semiconductors Decorated with CdS Nanoparticles for Photocatalytic Reduction of CO_2, ACS Catal. 8 (2018) 4928–4936. https://doi.org/10.1021/acscatal.8b00104.

[13] K.M. Cho, K.H. Kim, K. Park, C. Kim, S. Kim, A. Al-Saggaf, I. Gereige, H.-T. Jung, Amine-Functionalized Graphene/CdS Composite for Photocatalytic Reduction of CO_2, ACS Catal. 7 (2017) 7064–7069. https://doi.org/10.1021/acscatal.7b01908.

[14] B. Su, L. Huang, Z. Xiong, Y. Yang, Y. Hou, Z. Ding, S. Wang, Branch-like ZnS-DETA/CdS hierarchical heterostructures as an efficient photocatalyst for visible light CO_2 reduction, J. Mater. Chem. A. 7 (2019) 26877–26883. https://doi.org/10.1039/c9ta10470d.

[15] C. Bhan, A. Kumar Golder, Bio-based hierarchical vertically aligned 2D ZnO

nanostructures for ultra selective electrochemical sensing of p-Chloroaniline, Chem. Eng. J. 475 (2023) 146122. https://doi.org/10.1016/j.cej.2023.146122.

[16] R. Ravi, A.K. Golder, Bio-based Au Doping with Dominant Oxygen Vacancies and Ti^{3+} Defects on Photocatalytic Functionalities of TiO_2, Ind. Eng. Chem. Res. 62 (2023) 20702–20715. https://doi.org/10.1021/acs.iecr.3c02850.

[17] P.M. Gawal, A.K. Golder, Vegetal route for synthesis of CQDs/CdS nanocomposites for photocatalytic reduction of CO_2 to methanol under visible light, Colloids Surfaces A Physicochem. Eng. Asp. 683 (2024) 133068. https://doi.org/10.1016/j.colsurfa.2023.133068.

[18] A. Chowdhury, N.R. Peela, A.K. Golder, Synthesis of Cu_2O NPs using bioanalytes present in Sechium edule: Mechanistic insights and application in electrocatalytic CO_2 reduction to formate, J. CO2 Util. 51 (2021) 2–13. https://doi.org/10.1016/j.jcou.2021.101622.

[19] S.J. Phang, L.L. Tan, Recent advances in carbon quantum dot (CQD)-based two dimensional materials for photocatalytic applications, Catal. Sci. Technol. 9 (2019) 5882–5905. https://doi.org/10.1039/c9cy01452g.

[20] Y. Yao, H. Zhang, K. Hu, G. Nie, Y. Yang, Y. Wang, X. Duan, S. Wang, Carbon dots based photocatalysis for environmental applications, J. Environ. Chem. Eng. 10 (2022) 107336. https://doi.org/10.1016/j.jece.2022.107336.

[21] S. Sharma, V. Dutta, P. Singh, P. Raizada, A. Rahmani-Sani, A. Hosseini-Bandegharaei, V.K. Thakur, Carbon quantum dot supported semiconductor photocatalysts for efficient degradation of organic pollutants in water: A review, J. Clean. Prod. 228 (2019) 755–769. https://doi.org/10.1016/j.jclepro.2019.04.292.

[22] H. Jung, V.S. Sapner, A. Adhikari, B.R. Sathe, R. Patel, Recent Progress on Carbon Quantum Dots Based Photocatalysis, Front. Chem. 10 (2022) 1–28. https://doi.org/10.3389/fchem.2022.881495.

[23] M. Kurian, A. Paul, Recent trends in the use of green sources for carbon dot synthesis–A short review, Carbon Trends. 3 (2021). https://doi.org/10.1016/j.cartre.2021.100032.

[24] S. Chahal, J.R. Macairan, N. Yousefi, N. Tufenkji, R. Naccache, Green synthesis of carbon dots and their applications, RSC Adv. 11 (2021) 25354–25363. https://doi.org/10.1039/d1ra04718c.

[25] S.R. Dash, S.S. Bag, A.K. Golder, Carbon dots derived from waste Psidium guajava leaves for electrocatalytic sensing of chlorpyrifos, Electroanalysis. 34 (2022) 1141–1149.

[26] D. Gogoi, R. Koyani, A.K. Golder, N.R. Peela, Enhanced photocatalytic hydrogen evolution using green carbon quantum dots modified 1-D CdS nanowires under visible light irradiation, Sol. Energy. 208 (2020) 966–977. https://doi.org/10.1016/j.solener.2020.08.061.

[27] A. Prasannan, T. Imae, One-pot synthesis of fluorescent carbon dots from orange waste peels, Ind. Eng. Chem. Res. 52 (2013) 15673–15678. https://doi.org/10.1021/ie402421s.

[28] J. Zhang, J. Xu, F. Tao, Interface Modification of TiO_2 Nanotubes by Biomass-Derived Carbon Quantum Dots for Enhanced Photocatalytic Reduction of CO_2, ACS Appl. Energy Mater. 4 (2021) 13120–13131. https://doi.org/10.1021/acsaem.1c02760.

[29] Y. Liu, Y.X. Yu, W. De Zhang, Carbon quantum dots-doped CdS microspheres with enhanced photocatalytic performance, J. Alloys Compd. 569 (2013) 102–110. https://doi.org/10.1016/j.jallcom.2013.03.202.

[30] C. Zhu, C. Liu, Y. Zhou, Y. Fu, S. Guo, H. Li, S. Zhao, H. Huang, Y. Liu, Z. Kang, Carbon dots enhance the stability of CdS for visible-light-driven overall water splitting, Appl. Catal. B Environ. 216 (2017) 114–121. https://doi.org/10.1016/j.apcatb.2017.05.049.

[31] C. Liu, Y. Zhang, T. Shi, Q. Liang, Z. Chen, Hierarchical hollow-microsphere cadmium sulfide-carbon dots composites with enhancing charge transfer efficiency for photocatalytic CO_2 reduction, J. Alloys Compd. 936 (2023) 168286. https://doi.org/10.1016/j.jallcom.2022.168286.

[32] H. Ren, F. Qi, A. Labidi, J. Zhao, H. Wang, Y. Xin, J. Luo, C. Wang, Chemically bonded carbon quantum dots/Bi_2WO_6 S-scheme heterojunction for boosted photocatalytic antibiotic degradation: Interfacial engineering and mechanism insight, Appl. Catal. B Environ. 330 (2023) 122587. https://doi.org/10.1016/j.apcatb.2023.122587.

[33] Y. Zhang, Y. Wu, L. Wan, H. Ding, H. Li, X. Wang, W. Zhang, Hollow core–shell Co_9S_8@$ZnIn_2S_4$/CdS nanoreactor for efficient photothermal effect and CO2 photoreduction, Appl. Catal. B Environ. 311 (2022) 121255. https://doi.org/10.1016/j.apcatb.2022.121255.

[34] M.G. Ashritha, S.R. Rondiya, R.W. Cross, N.Y. Dzade, S.D. Dhole, K. Hareesh, D. V. Sunitha, Experimental and computational studies of sonochemical assisted anchoring of carbon quantum dots on reduced graphene oxide sheets towards the photocatalytic activity, Appl. Surf. Sci. 545 (2021) 148962. https://doi.org/10.1016/j.apsusc.2021.148962.

[35] D. Borah, P. Saikia, P. Sarmah, D. Gogoi, A. Das, J. Rout, N.N. Ghosh, P. Pandey, C.R.

Bhattacharjee, Photocatalytic and Antibacterial Activity of Fluorescent CdS Quantum Dots Synthesized Using Aqueous Extract of Cyanobacterium Nostoc carneum, Bionanoscience. 13 (2023) 650–666. https://doi.org/10.1007/s12668-023-01115-z.

[36] S.M. Chaudhari, P.M. Gawal, P.K. Sane, S.M. Sontakke, P.R. Nemade, Solar light-assisted photocatalytic degradation of methylene blue with Mo/TiO_2: a comparison with Cr- and Ni-doped TiO_2, Res. Chem. Intermed. 44 (2018) 3115–3134. https://doi.org/10.1007/s11164-018-3296-1.

[37] J. V Rojas, M. Toro-Gonzalez, M.C. Molina-Higgins, C.E. Castano, Facile radiolytic synthesis of ruthenium nanoparticles on graphene oxide and carbon nanotubes, Mater. Sci. Eng. B. 205 (2016) 28–35. https://doi.org/https://doi.org/10.1016/j.mseb.2015.12.005.

[38] Y. Wang, J. Chen, L. Liu, X. Xi, Y. Li, Z. Geng, G. Jiang, Z. Zhao, Novel metal doped carbon quantum dots/CdS composites for efficient photocatalytic hydrogen evolution, Nanoscale. 11 (2019) 1618–1625. https://doi.org/10.1039/C8NR05807E.

[39] C. Jiang, X. Xu, M. Mei, F.N. Shi, Coordination Polymer Derived Sulfur Vacancies Rich CdS Composite Photocatalyst with Nitrogen Doped Carbon as Matrix for H_2 Production, ACS Sustain. Chem. Eng. 6 (2018) 854–861. https://doi.org/10.1021/acssuschemeng.7b03201.

[40] T. Grünleitner, A. Henning, M. Bissolo, M. Zengerle, L. Gregoratti, M. Amati, P. Zeller, J. Eichhorn, A. V. Stier, A.W. Holleitner, J.J. Finley, I.D. Sharp, Real-Time Investigation of Sulfur Vacancy Generation and Passivation in Monolayer Molybdenum Disulfide via in situ X-ray Photoelectron Spectromicroscopy, ACS Nano. 16 (2022) 20364–20375. https://doi.org/10.1021/acsnano.2c06317.

[41] T. Tian, X. Jin, N. Guo, H. Li, Y. Han, Y. Yuan, CdS/ethylenediamine nanowires 3D photocatalyst with rich sulfur vacancies for efficient syngas production from CO_2 photoreduction, Appl. Catal. B Environ. 308 (2022) 121227. https://doi.org/10.1016/j.apcatb.2022.121227.

[42] H. Liu, J. Peng, X. Zhang, K. Zheng, L. Zheng, K. Lv, Q. Li, P. Zhou, Engineering atomic Pt-N_3 sites on CdS nanorods for overcoming the rate-determining organic dehydrogenation in photocatalytic coproduction of HThe detection method used was HPLC, with details provided in Section 2.3. In this study, only a single, Chem. Eng. J. 504 (2025) 158618. https://doi.org/10.1016/j.cej.2024.158618.

[43] R. Ravi, A.K. Golder, A tuneable bioinspired process of Pt-doping in TiO_2 for improved photoelectrochemical and photocatalytic functionalities, Colloids Surfaces A

Physicochem. Eng. Asp. 663 (2023) 131034. https://doi.org/10.1016/j.colsurfa.2023.131034.

[44] C. Bhan, A.K. Golder, ZnO Nanorods Aligned in a Vertical Configuration for Targeted Electrochemical Detection of Aniline, ACS Appl. Bio Mater. 7 (2024) 7413–7428. https://doi.org/10.1021/acsabm.4c01050.

[45] S. Guiyuan, Novel metal doped carbon quantum dots/CdS composites for efficient photocatalytic hydrogen evolution, Nanoscale. 11 (2019) 1618–1625. https://doi.org/10.1039/c8nr05807e.

[46] T. Kulandaivalu, S. Abdul Rashid, N. Sabli, T.L. Tan, Visible light assisted photocatalytic reduction of CO_2 to ethane using CQDs/Cu_2O nanocomposite photocatalyst, Diam. Relat. Mater. 91 (2019) 64–73. https://doi.org/10.1016/j.diamond.2018.11.002.

[47] B. Zhou, J. Song, C. Xie, C. Chen, Q. Qian, B. Han, Mo–Bi–Cd Ternary Metal Chalcogenides: Highly Efficient Photocatalyst for CO_2 Reduction to Formic Acid Under Visible Light, ACS Sustain. Chem. Eng. 6 (2018) 5754–5759. https://doi.org/10.1021/acssuschemeng.8b00956.

[48] H.Y. Wang, R. Hu, Y.J. Lei, Z.Y. Jia, G.L. Hu, C.B. Li, Q. Gu, Highly efficient and selective photocatalytic CO_2 reduction based on water-soluble CdS QDs modified by the mixed ligands in one pot, Catal. Sci. Technol. 10 (2020) 2821–2829. https://doi.org/10.1039/d0cy00308e.

[49] M.M. Kandy, V.G. Gaikar, Enhanced photocatalytic reduction of CO_2 using CdS/Mn_2O_3 nanocomposite photocatalysts on porous anodic alumina support with solar concentrators, Renew. Energy. 139 (2019) 915–923. https://doi.org/10.1016/j.renene.2019.03.002.

[50] B.R. Eggins, P.K.J. Robertson, E.P. Murphy, E. Woods, J.T.S. Irvine, Factors affecting the photoelectrochemical fixation of carbon dioxide with semiconductor colloids, J. Photochem. Photobiol. A Chem. 118 (1998) 31–40. https://doi.org/10.1016/S1010-6030(98)00356-6.

[51] J.T.S. Irvine, B.R. Eggins, J. Grimshaw, Solar energy fixation of carbon dioxide via cadmium sulphide and other semiconductor photocatalysts, Sol. Energy. 45 (1990) 27–33. https://doi.org/10.1016/0038-092X(90)90063-I.

[52] B.-J. Liu, T. Torimoto, H. Yoneyama, Photocatalytic reduction of CO_2 using surface-modified CdS photocatalysts in organic solvents, J. Photochem. Photobiol. A Chem. 113 (1998) 93–97.

[53] L. Wei, Z. Guo, X. Jia, Probing Photocorrosion Mechanism of CdS Films and Enhancing Photoelectrocatalytic Activity via Cocatalyst, Catal. Letters. 151 (2021) 56–66. https://doi.org/10.1007/s10562-020-03275-z.

[54] D. Meissner, C. Benndorf, R. Memming, Photocorrosion of cadmium sulfide: Analysis by photoelectron spectroscopy, Appl. Surf. Sci. 27 (1987) 423–436. https://doi.org/10.1016/0169-4332(87)90152-8.

[55] Z. Qi, J. Chen, Q. Li, N. Wang, S.A.C. Carabineiro, K. Lv, Increasing the Photocatalytic Hydrogen Generation Activity of CdS Nanorods by Introducing Interfacial and Polarization Electric Fields, Small. 19 (2023) 1–9. https://doi.org/10.1002/smll.202303318.

[56] I. V. Chernyshova, S. Ponnurangam, Activation of CO_2 at the electrode–electrolyte interface by a co-adsorbed cation and an electric field, Phys. Chem. Chem. Phys. 21 (2019) 8797–8807. https://doi.org/10.1039/C8CP07807F.

CHAPTER 6

Green Synthesis of Z-Scheme SnO_2/CdS heterostructure: DFT Calculation and Photocatalytic CO_2 Reduction to Methanol and Hydrogen

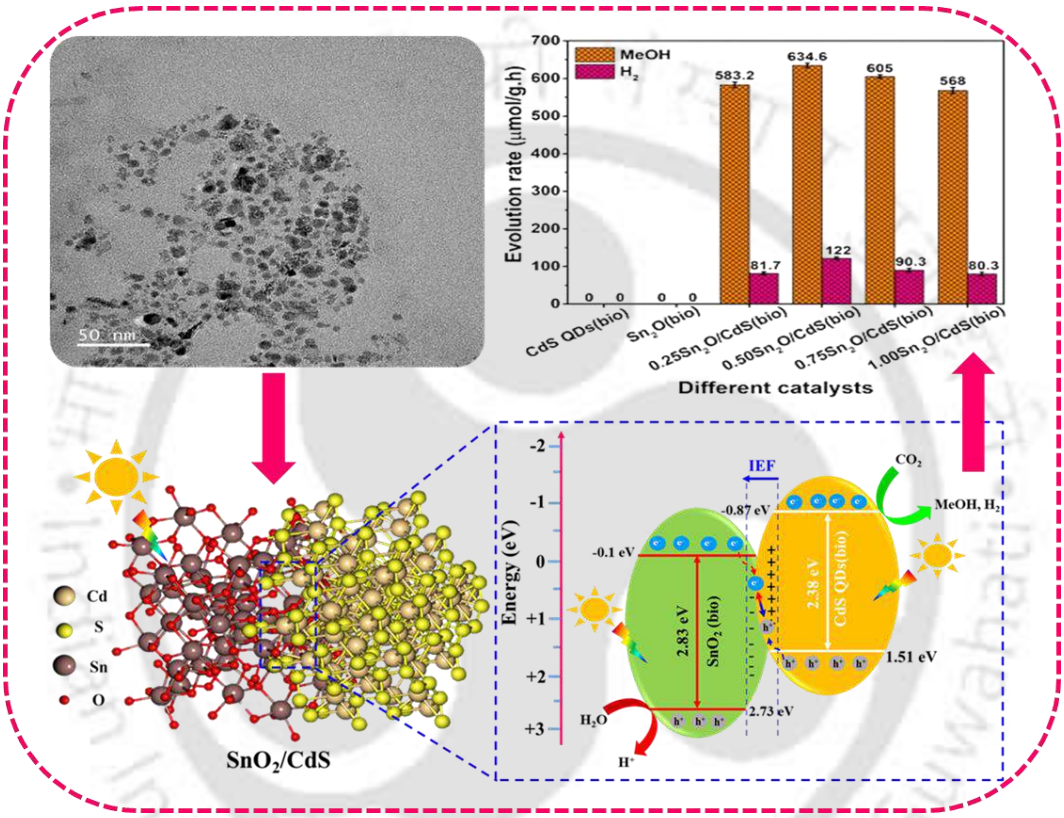

Chapter highlights

- CdS QDs(bio) and SnO_2(bio) NPs synthesized using plant-based phytochemicals
- SnO_2/CdS QDs(bio) heterostructures inhibits CdS QDs(bio) photocorrosion
- Z-scheme heterojunction enhances charge separation and suppresses recombination
- MeOH/H_2 production of 675.9/139.5 μmol/g·h over SnO_2/CdS QDs(bio)
- DFT confirms DOS modifications in CdS, enhancing charge transport at interfaces
- Internal electric field aids charge transfer, boosting photocatalytic performance

6.1 Introduction

The rapid industrialization and extensive use of fossil fuels have significantly increased CO_2 emissions, contributing to global warming and environmental degradation. As a major greenhouse gas, CO_2 not only intensifies climate change, but its emission is also related to the accelerated depletion of petroleum resources [1,2]. To address such challenges, the conversion of CO_2 into valuable carbon-based fuels such as CO, CH_4, HCOOH, and CH_3OH has gained significant research attention. Among various CO_2 utilization technologies, photocatalytic CO_2 reduction (PCO_2R) takes place in a sustainable and environmentally friendly approach by harnessing abundant solar energy to drive chemical transformations [3,4]. However, the process faces critical challenges, including slow CO_2 reduction kinetics, limited light-harvesting capabilities, rapid charge recombination, and competing side reactions [5,6]. Developing efficient semiconductor-based photocatalysts with enhanced light harvesting, improved charge separation, and high selectivity is crucial for industrial applications targeting carbon neutrality and renewable fuel production [7,8].

Various semiconductor nanoparticles (NPs), including quantum dots (QDs), have been studied for PCO_2R. However, CdS QDs attract interest due to their narrow band gap (2.42 eV), efficient solar energy conversion, exceptional charge carrier transport properties, multiexciton generation, large surface area (~100 m^2/g), and favorable conduction band(CB) position (-0.95 eV)[9,10]. However, CdS QDs face challenges such as photocorrosion of sulfur forming SO_4^{2-} and rapid recombination of electron (e^-)/hole(h^+) pairs, hindering their applications [11,12]. Various strategies have been explored to address these limitations of CdS QDs for PCO_2R, including morphology control, co-catalyst formation, and heterostructure construction. Notable examples such as In_2O_3/CdS [4], CQDs/CdS [12], ZnO/CdS [13], and CdS/A-GO [14] have demonstrated enhanced charge separation, reduced recombination, and suppression of the photocorrosion, enhancing overall photocatalytic performance.

SnO_2 is an n-type semiconductor with a ~3.6 eV band gap, featuring excellent electronic properties, chemical stability, and nontoxicity. Therefore, it has attracted significant attention for PCO_2R [15,16]. However, its relatively fast recombination rate of photogenerated charge carriers limits its performance. SnO_2 is commonly used as a co-catalyst in photocatalysts to improve electron transfer efficiency through heterostructure formation. Various hybrid SnO_2-based photocatalysts have been explored for PCO_2R, including such as $CsPbBr_3$/CdS [17], SnO_2/BiOI [18], SnO_2/$Cs_3Bi_2Br_9$ [19], exhibiting enhanced charge carrier separation and superior photocatalytic performance compared to single photocatalyst. Considering these

advantages, coupling SnO_2 with CdS presents a promising approach for better charge separation, minimization of recombination, and photocorrosion suppression, resulting in improved photocatalytic activity compared to individual CdS and SnO_2 catalysts.

Bio-based methods utilizing bio-precursors for synthesizing NPs/QDs are eco-friendly and cost-effective [20,21]. Such catalysts could be applied in PCO_2R to control industrial CO_2 emissions [4,22]. The diverse tropical plants found in Northeastern states of India, are rich in bio-precursors, which can be applied as capping and reducing agents for efficient NP/QDs synthesis. Additionally, combining microwave irradiation with bio-based processes can significantly increase NP/QDs formation rates [12].

Chapter 6 investigates on biomass-based SnO_2/CdS heterostructure formation using plant-derived phytochemicals from *Aegle marmelos* along with short microwave irradiation. The *Aegle marmelos* contains phytochemicals, such as flavonoids, alkaloids, tannins, phenols, and saponins, which could act as reducing and capping agents [4,12]. The synthesized catalysts were comprehensively characterized using spectroscopy, microscopy, diffraction, and electrochemical techniques. The bandgap and charge separation of catalysts were examined using density functional theory (DFT) by analyzing the band structure and density of state (DOS). The synthesized catalysts were evaluated for PCO_2R under visible light irradiation, producing MeOH and H_2. Furthermore, the stability and reusability of the heterostructure were evaluated. This study introduces a novel bio-based synthesis strategy for heterostructures to enhance the efficiency of PCO_2R, with a focus on producing MeOH and H_2.

6.2 Results and discussion

6.2.1. Photocatalyst characterizations

Morphological analyses: The positively charged surface of CdS QDs(bio), as confirmed by the zeta potential value at pH 7.5 (**Table 6.1**), enables the electrostatic adsorption of negatively charged Sn^{4+} ions. These ions react with an oxygen source to form SnO_2 on the surface of CdS QDs, resulting in the formation of the SnO_2/CdS QDs(bio) heterostructure. Microwave irradiation is then employed to enhance the interaction between the SnO_2(bio) and CdS QDs(bio).

Table 6.1. Hydrodynamic diameter and Zeta potential of CdS QDs(bio), CuO QDs(bio), and SnO_2/CdS QDs(bio) heterostructures.

Catalysts	Hydrodynamic diameter (nm)	Zeta potential (mV)

CdS QDs(bio)	212.2	15.9
SnO_2(bio)	238.7	-13.5
0.25SnO_2/CdS (bio)	247.3	-16.2
0.50SnO_2/CdS(bio)	276.2	-20.8
0.75SnO_2/CdS(bio)	298.1	-24.4
1.00SnO_2/CdS(bio)	312.3	-26.9

Figures 6.1a-6.1c shows the TEM images of CdS QDs(bio), SnO_2(bio), and 0.50SnO_2/CdS QDs(bio) heterostructure with their average particle size of 4.85, 8.06, and 5.70 nm, respectively. The HRTEM image (**Figure 6.1d**) of the 0.50SnO_2/CdS QDs(bio) heterostructure reveals lattice fringes with a d-spacing of 0.338 nm, corresponding to the (111) plane of CdS QDs(bio) and 0.334 nm, associated with the (110) plane of SnO_2(bio), confirming the coexistence of CdS and SnO_2 in the heterostructure. The same d-spacing values are observed in the individual CdS QDs(bio) and SnO_2(bio) (**Figure 6.2**). The SAED pattern (**Figure 6.1d**(inset)) of 0.50SnO_2/CdS QDs(bio) heterostructure exhibits a polycrystalline nature. EDX analysis (**Figure 6.1e**) of heterostructure confirms the presence of Cd, Sn, S, and O with their respective percentage of 31.1, 38.7, 9.0, and 21.1%. Elemental mapping (**Figure 6.1f**) further confirms the uniform dispersion of these elements in the heterostructure.

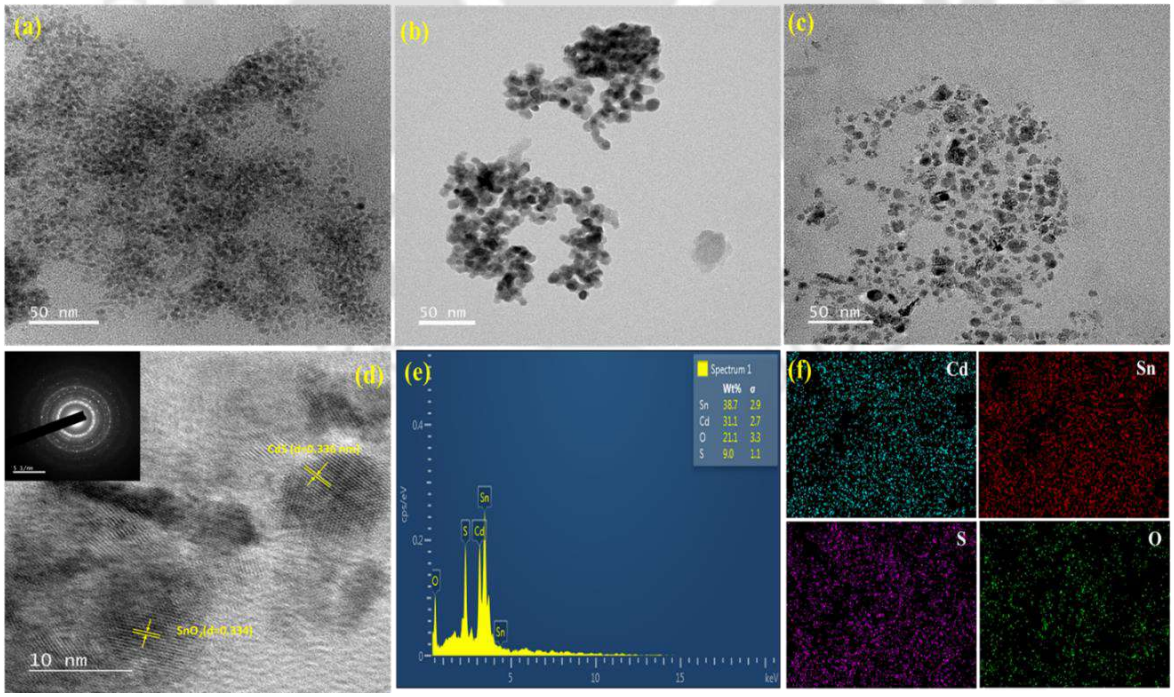

Figure 6.1. TEM images of (a) CdS QDs(bio), (b) SnO_2(bio), and 0.50SnO_2/CdS QDs(bio) heterostructure, (d) HR-TEM image and (inset) SAED pattern, (e) EDX spectrum, and (f) Elemental mapping of 0.50SnO_2/CdS QDs(bio) heterostructure.

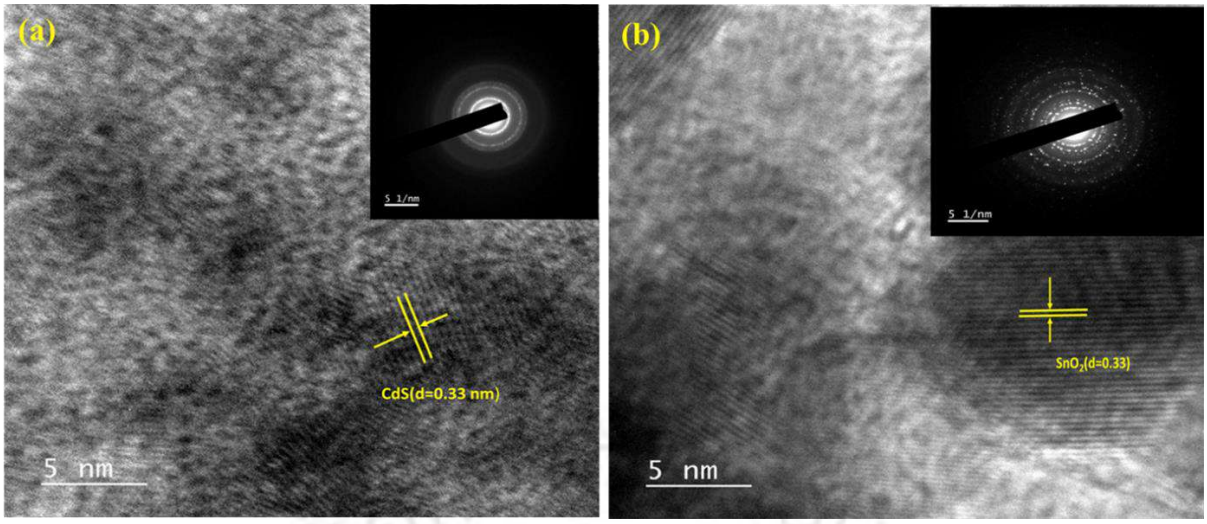

Figure 6.2. HRTEM images and (inset) SAED patterns of (a) CdS QDs(bio) and (b)SnO_2(bio).

Determination of energy levels: The absorption spectra of the synthesized catalyst are presented in **Figure 6.3a**. CdS QDs(bio) exhibit an absorption edge at 520 nm [4], while SnO_2(bio) is at 370 nm [23]. SnO_2(bio) has a limited visible light range than the CdS QDs(bio). The absorption edge of the 0.50SnO_2/CdS QDs(bio) heterostructure exhibited a red shift, thereby improving their light absorption in the visible spectrum [4,23]. The bandgap of the catalysts was determined using Tauc's relation, as illustrated in **Figure 6.3b**. The calculated bandgap values for CdS QDs(bio), SnO_2(bio), and the 0.50SnO_2/CdS QDs(bio) heterostructure were 2.38, 2.83, and 2.16 eV, respectively. The bandgap values for SnO_2(bio) and CdS QDs(bio) align with those reported in the literature [12,24].

Figure 6.3c presents the minimum valence band (VB) energies of CdS QDs(bio), SnO_2(bio), and the 0.50SnO_2/CdS QDs(bio) heterostructure, measured as 1.51, 2.73, and 1.20 eV, respectively. **Figure 6.3d** illustrates the energy level diagram of the catalysts, showing the calculated maximum conduction band energies of -0.87, -0.1, and -0.96 eV for CdS QDs(bio), SnO_2(bio), and the 0.50SnO_2/CdS QDs(bio) heterostructure, respectively. These results indicate that the heterostructure exhibits favourable maximum conduction band (CB) energies, which suggests an enhanced rate of MeOH and H_2 production. The work function (φ) is determined using the equation $\varphi = h\nu - E_{cutoff}$ [25], where $h\nu$ represents the energy of the monochromatic ionizing light (21.22 eV), and $E_{cut\text{-}off}$ is the threshold energy for secondary electrons obtained through linear extrapolation of the ultraviolet photoelectron spectroscopy (UPS) VB spectrum. The E_F is calculated using the relation $E_F = -\varphi$ [4]. The UPS VB spectra for secondary electrons are shown in **Figure 6.4**. The measured secondary electron cut-off energies for CdS QDs(bio), SnO_2(bio), and the 0.50SnO_2/CdS QDs(bio) heterostructure are

16.71, 15.7, and 16.13 eV, respectively, corresponding to work function values of 4.51, 5.52, and 5.09 eV. The E_F for CdS QDs(bio), SnO_2(bio), and the 0.50SnO_2/CdS QDs(bio) heterostructure are calculated as -4.51, -5.52, and -5.09 eV, respectively, aligning with previously reported literature values [26,27].

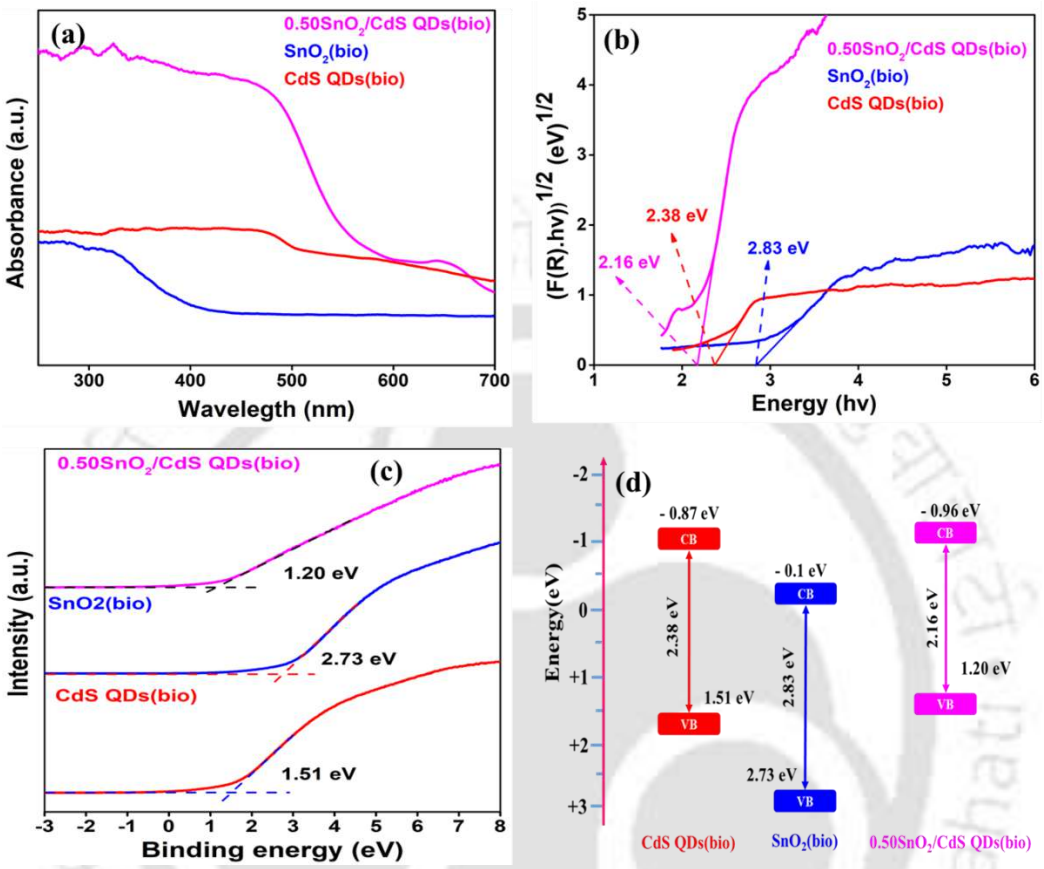

Figure 6.3. (a) UV-Vis absorption spectra, (b) Bandgap calculation, (c) UPS VB spectra, and (d) Energy level diagram of CdS QDs(bio), SnO_2(bio), and 0.50SnO_2/CdS QDs(bio) heterostructure.

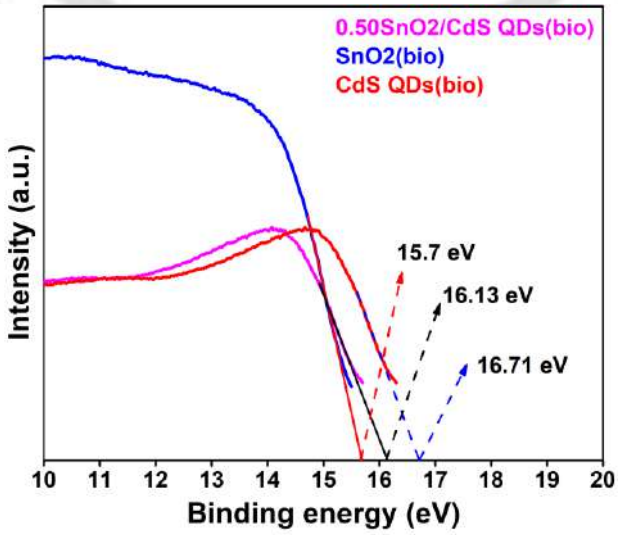

Figure 6.4. UPS VB spectra for secondary electron onset.

XRD analysis: The XRD pattern of synthesized catalysts is illustrated in **Figure 6.5**. For CdS QDs(bio), the peak positions at 2θ= 26.5° (111), 43.9° (220), and 51.9° (311) correspond to a cubic structure (JCPDF: 00-002-0454) [12]. For SnO_2(bio), the peak position at 2θ=26.67° (110), 33.93° (101), 38.10° (200), 52.23° (211),54.94° (220), 58.36° (002), 62.26° (310), 64.68° (112), 66.23° (301), 71.40° (202), 79.08° (321) attributed to the tetragonal phase (JCPDF: 00-001-0657) [28]. The diffraction pattern of the SnO_2/CdS(bio) heterostructure closely resembles that of CdS, while the characteristic peaks of SnO_2 corresponding to the (110), (101), and (211) planes are also observed. Notably, the SnO_2 peaks at 2θ = 26.67° and 52.23° overlap with the CdS peaks at 26.5° and 51.9°, respectively. This overlap arises from the nearly identical 2θ positions of the diffraction peaks for both semiconductors [29,30]. This confirms the successful coupling between SnO_2 NPs and CdS QDs. The average crystallite size was determined using Debye Scherrer's equation [4]. The average crystallite size of CdS QDs(bio), SnO_2(bio), and 0.50SnO_2/CdS QDs(bio) heterostructure was calculated to be 4.26, 8.4, and 5.39 nm, respectively.

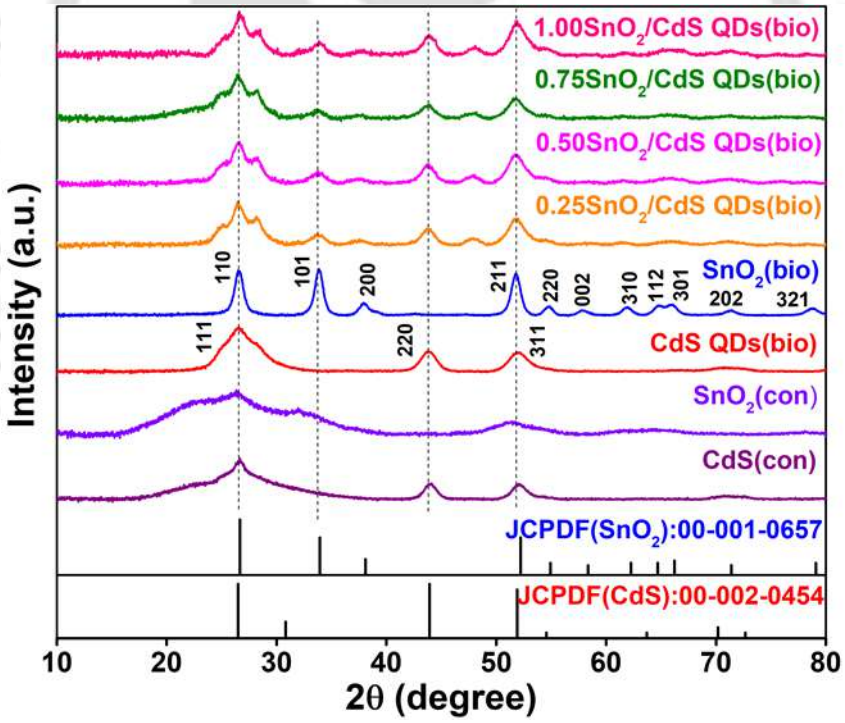

Figure 6.5. XRD patterns of CdS QDs(bio), CdS(con), SnO_2(bio), SnO_2(con), and SnO_2/CdS QDs(bio) heterostructures at different molar ratios (0.25-1.0) of SnO_2 and CdS QDs.

XPS analysis: The survey spectra of synthesized catalysts confirm the Cd, S, Sn, and O elements (**Figure 6.6a**). Cd 3d spectra (**Figure 6.6b**) of CdS QDs(bio) showed peaks at 412.1 eV($3d_{3/2}$) and 405.3 eV ($3d_{5/2}$), representing Cd^{2+} in CdS QDs(bio) [4]. Sn 3d spectra (**Figure**

6.6c) of SnO_2(bio) show the peaks at 496.35 eV($3d_{3/2}$) and 487.88 eV($3d_{5/2}$), respectively, indicating Sn^{4+} in SnO_2(bio) NPs [28]. S 2p spectra (**Figure 6.6d**) exhibited peaks at 163.1eV($2p_{1/2}$) and 161.86 eV($2p_{3/2}$), indicating the S^{2-} valence state in CdS QDs(bio) [12]. O 1s spectra of SnO_2(bio) (**Figure 6.6e**) exhibit the two peaks at 531.7 and 530.32 eV corresponding to the adsorbed oxygen (O_H) and lattice oxygen (O_L) [31]. The Sn 3d, Cd 3d, O 1s, and S 2p spectra of the 0.50SnO_2/CdS QDs(bio) heterostructure showed a similar trend. A blue shift in the binding energy of Sn 3d, Cd 3d, O 1s, and S 2p was observed, revealing the strong interaction between CdS and SnO_2, confirming the formation of heterostructure [23,32].

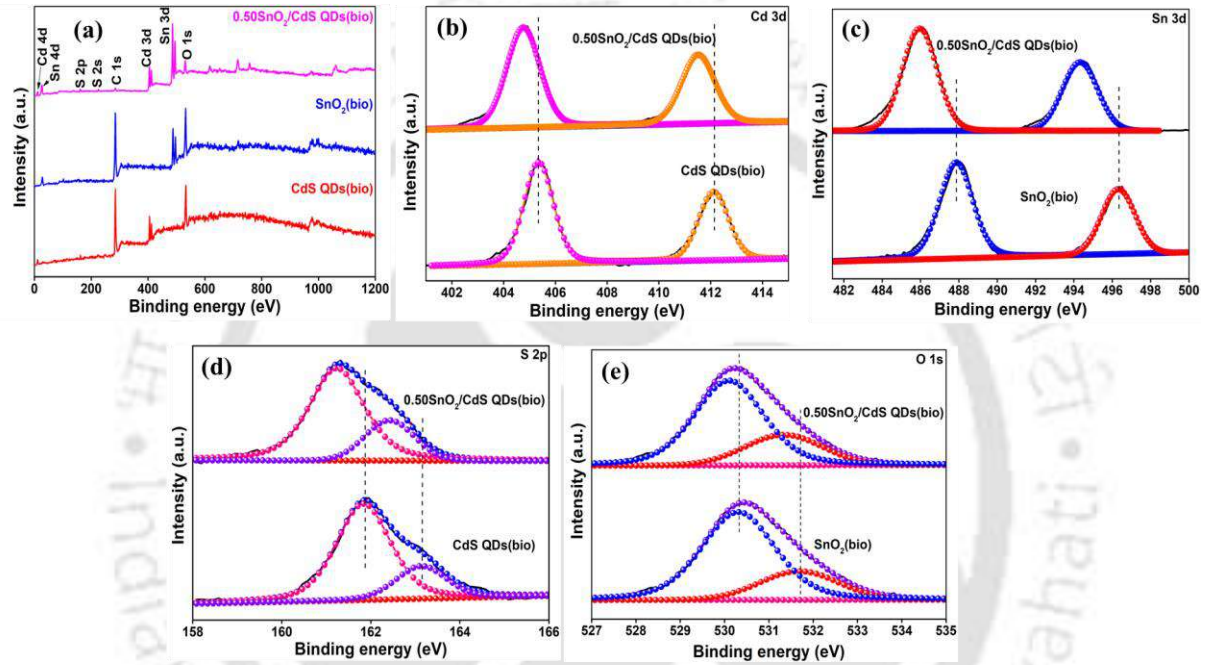

Figure 6.6. (a) XPS survey spectra, and high-resolution spectra of (b) Cd 3d, (c) Sn 3d, (d) S 2p, and O 1s of CdS QDs(bio), SnO_2(bio), and 0.50SnO_2/CdS QDs(bio) heterostructure.

Charge trapping and recombination: The PL spectra (**Figure 6.7a**) were obtained at the excitation wavelength of 360 nm for CdS QDs(bio) and SnO_2/CdS(bio) heterostructure and at 350 nm for SnO_2(bio). The prominent emission was observed at 493 nm for CdS QDs(bio) and the SnO_2/CdS QDs(bio) heterostructure, while SnO_2(bio) exhibited a peak at 466 nm. The PL intensity of heterostructure was decreased compared to the CdS QDs(bio) and SnO_2(bio), indicating reduced charge carrier recombination. This implies that heterojunction formation improves the separation of e^-/h^+ pairs [4,23].

The TRPL spectra were performed to understand the charge carrier dynamics (**Figure 6.7b** and **Table 6.2)**. The excitation and emission wavelengths were 375 nm and 528 nm for CdS QDs(bio) and the SnO_2/CdS QDs(bio) heterostructure, whereas for SnO_2(bio), they were

375 nm and 450 nm with 1000 counts. The TRPL decay curves were analyzed by fitting them with a bi-exponential decay function. The average lifetimes of SnO_2(bio), CdS QDs(bio), and 0.50SnO_2/CdS QDs(bio) heterostructure were calculated as 2.18, 2.74, and 5.37 ns, respectively. The longer average lifetime of the SnO_2/CdS QDs(bio) heterostructure compared to CdS QDs(bio) and SnO_2(bio) indicates enhanced charge separation efficiency within the heterostructure [4,31].

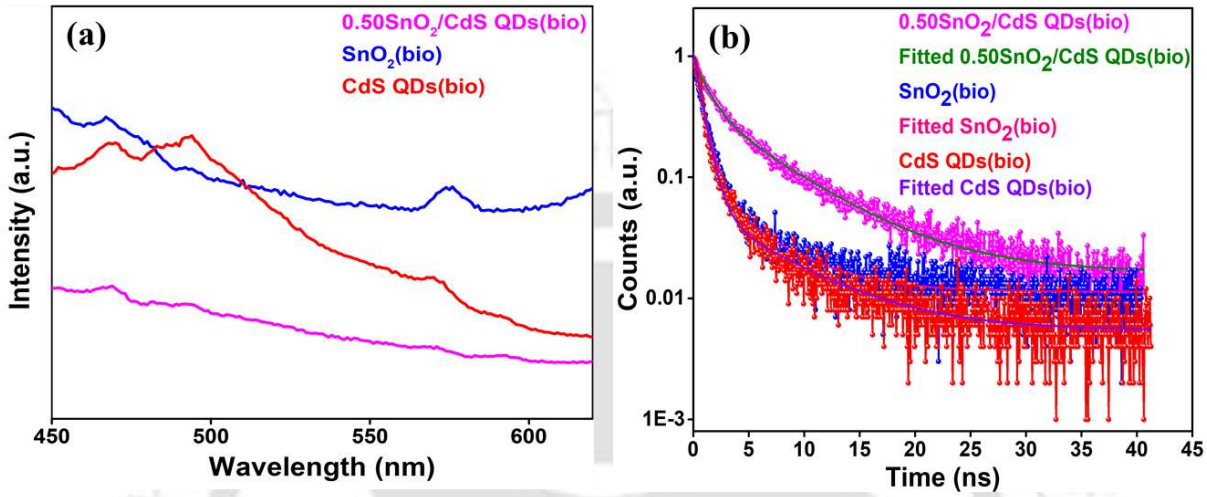

Figure 6.7. (a) PL and (b) TRPL spectra of synthesized catalysts.

Table 6.2. TRPL data of synthesized catalysts.

Photocatalyst	**A_1 (%)**	**A_2 (%)**	**τ_1 (ns)**	**τ_2 (ns)**	**τ_{ave} (ns)**
SnO_2(bio)	0.08596	1.0132	4.9092	0.8373	2.18
CdS QDs(bio)	0.0536	0.9862	6.8714	0.7886	2.74
0.50SnO_2/CdS QDs(bio)	0.3827	0.6029	6.6316	1.3	5.37

BET surface area analysis: The surface area and pore size of the synthesized catalyst were calculated using N_2 sorption analysis (**Table 6.3**). The N_2 sorption (**Figure 6.8a**) indicating CdS QDs(bio), SnO_2(bio), and 0.50SnO_2/CdS QDs(bio) heterostructure exhibit type IV isotherms with an H2, H2, H3 hysteresis loop, respectively, because of it mesoporous characteristics. The surface area and average pore diameter of SnO_2(bio), CdS QDs(bio), and SnO_2/CdS QDs(bio) heterostructure were 62.42, 69.52, and 120.66 m^2/g and 4.12, 6.28, and 9.45 nm, respectively. The heterostructure has a high surface area and porous properties, offering more catalytic active sites for redox reactions [28,33]. Additionally, the CO_2 adsorption ability of 0.50SnO_2/CdS QDs(bio) heterostructure (0.40 mmol/g) surpasses that of

CdS QDs(bio) (0.102 mmol/g) and SnO_2(bio) (0.09 mmol/g) (**Table 6.3**). The TGA analysis is presented in **Figure 6.8b**. The residual carbon content, as shown in **Table 6.4**, was measured within the temperature range of 300–500°C [7], revealing that the heterostructure contains 2.28% (w/w) carbon.

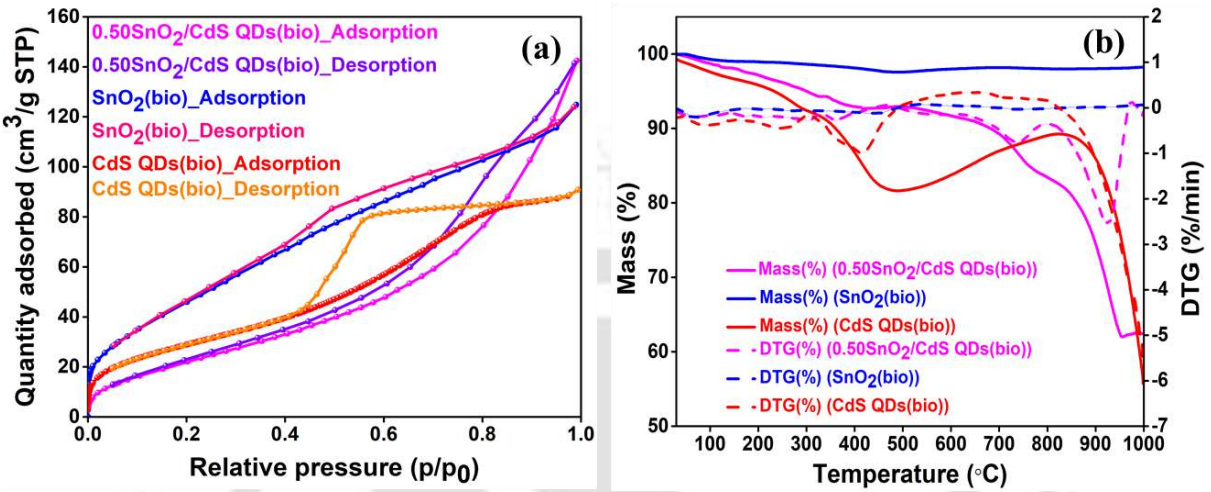

Figure 6.8. (a) N_2 sorption isotherms, and (b) TGA & DTG analysis of CdS QDs(bio), SnO_2 QDs(bio), and 0.50SnO_2/CdS QDs(bio) heterostructure.

Table 6.3. Physical characteristics of synthesized catalysts.

Catalyst	Bandgap (eV)	Crystallite size (nm)	BET surface area (m^2/g)	Average pore (nm)	Pore volume (cm^3/g)	CO_2 Adsorption (mmol/g)
CdS QDs(bio)	2.38	3.5	69.52	6.28	0.11	0.102
SnO_2(bio)	2.83	8.4	62.42	4.12	0.193	0.08
SnO_2/CdS(bio) heterostructure	2.16	5.39	120.6	9.45	0.22	0.40

Table 6.4. Residual carbon content calculation in catalyst samples from TGA.

Catalysts	Temperature range of carbon % calculation (°C)	Carbon (%)
CdS QDs(bio)	300 to 500	11
SnO_2(bio)	300 to 500	1.14
0.50SnO_2/CdS QDs(bio)	300 to 500	2.28

6.2.2 Photoelectrochemical response

The chronoamperometry study (i-t) was performed under visible light irradiation with alternating light on/off cycles at 25 s intervals (**Figure 6.9a**). The average photocurrent density of SnO_2/CdS QDs(bio) reaches 0.74 μA/cm^2, surpassing that of SnO_2(bio) by 9 times and CdS QDs(bio) by 7 times. This highlights the enhanced charge separation efficiency of the SnO_2/CdS QDs(bio) heterostructure [4,34].

The charge transfer resistance (Rp) at the photoelectrode-electrolyte interface was evaluated using EIS under both dark and light conditions (**Figure 6.9b**). The heterostructure exhibits a smaller arc radius compared to SnO_2(bio) and CdS QDs(bio), suggesting enhanced charge separation and lower Rp. The EIS-fitted parameters are summarized in **Table 6.5**, with the equivalent circuit illustrated in **Figure 6.9b**(inset). Under light conditions, the Rp values for SnO_2(bio), CdS QDs(bio), and SnO_2/CdS(bio) were 11.28, 13.2, and 9.45 MΩ, respectively. In dark conditions, the values were 15.55, 14.8, and 11.12 MΩ, respectively. The smaller arc radius and reduced resistance indicate improved conductivity, faster charge carrier migration, and a lower charge recombination rate [21,35]. This finding suggests enhanced charge carrier separation and transfer in the 0.50SnO_2/CdS QDs(bio) heterostructure, constituent with the results from photocurrent and PL study.

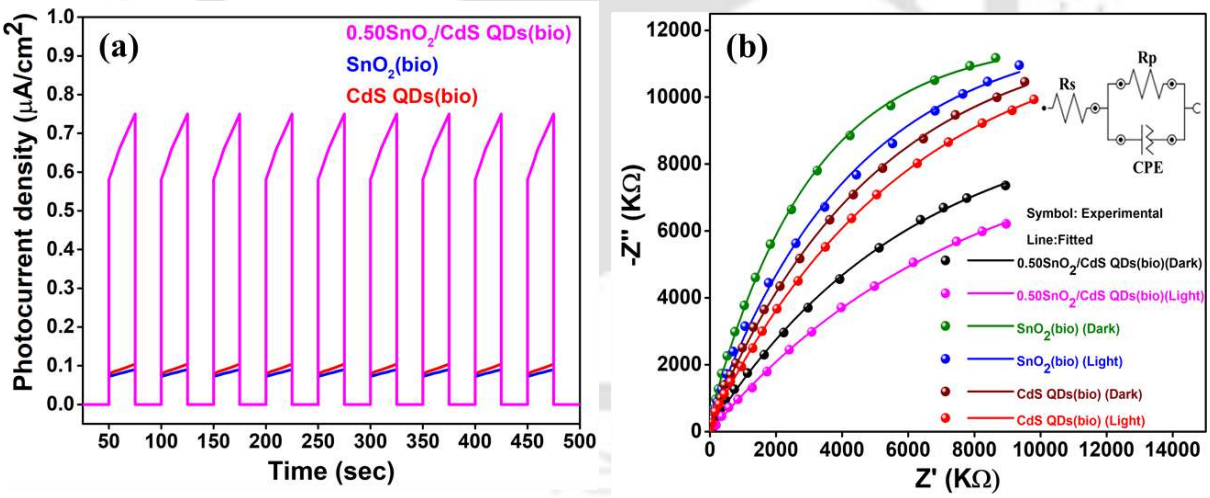

Figure 6.9. (a) Chronoamperometry study (i-t) and (b) Nyquist plots (EIS) under light and dark conditions (equivalent circuit is in inset) used for fitting of EIS data.

Table 6.5. Parameters of equivalent circuit used for fitting of EIS data.

Catalyst	Rs (KΩ)	Rp (MΩ)	CPE
CdS QDs(bio) (Dark)	6.23	14.8	Y_0=188nMho×S^N

			N=0.566
CdS QDs(bio) (Light)	4.83	13.2	Y_0=221nMho×S^N N=0.574
SnO_2(bio) (Dark)	7.25	15.55	Y_0=241nMho×S^N N=0.574
SnO_2(bio) (Light)	5.04	11.28	Y_0=253nMho×S^N N=0.589
SnO_2/CdS QDs(bio) (Dark)	5.75	11.12	Y_0=272nMho×S^N N=0.592
SnO_2/CdS QDs(bio) (Light)	3.5	9.45	Y_0=281nMho×S^N N=0.596

6.2.3 DFT calculation

DFT calculations were conducted to analyze the band structure and DOS of the synthesized catalysts. The optimized models for the CdS QDs, SnO_2, and the SnO_2/CdS heterostructure are presented in **Figures 6.10a–6.10c**, with the corresponding lattice parameters summarized in **Table 6.6**. Using the GGA+U approach in DFT with Hubbard parameters Ud=4.4 and Up=4.1 for CdS QDs, and Up=7.0 and Ud=9 for SnO_2, the calculated band structure (**Figures 6.11a–6.11c**) reveals bandgaps of 2.38, 2.8, and 2.15 eV for CdS QDs, SnO_2, and the SnO_2/CdS QDs heterostructure, respectively. These values are in close agreement with the experimental bandgaps of 2.38, 2.83, and 2.15 eV, respectively. The band structure of the 0.50SnO_2/CdS QDs heterostructure notably reveals overlapping electronic bands near the E_F due to the incorporation of SnO_2. This overlap introduces additional electronic states within the CdS bandgap, thereby effectively reducing the bandgap [36], as further supported by UV-DRS analysis. The DOS for CdS QDs, SnO_2, and SnO_2/CdS is illustrated in **Figures 6.11d–6.11f**. Notably, the DOS of the SnO_2/CdS heterostructure in the CB is shifted closer to the E_F compared to CdS QDs, indicating a higher density of electronic states near the E_F [37]. A similar phenomenon was reported for the $Bi_2S_3/Ti_3C_2T_x$ MXene composite and the In_2O_3/CdS heterostructure [7,28]. This feature enhances electron transport in the SnO_2/CdS QDs heterostructure compared to CdS QDs, indicating improved photocatalytic performance.

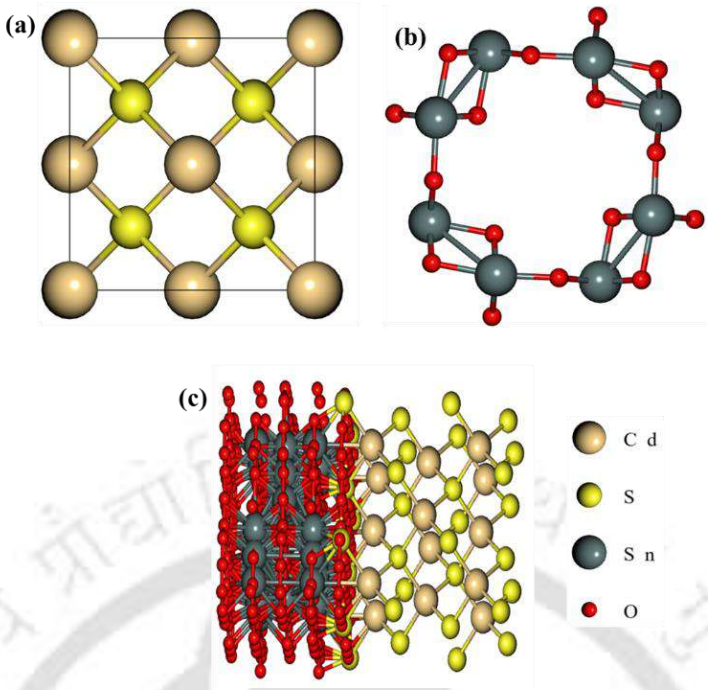

Figure 6.10. DFT model optimization of (a) CdS QDs, (b) SnO_2, and (c) SnO_2/CdS QDs heterostructure.

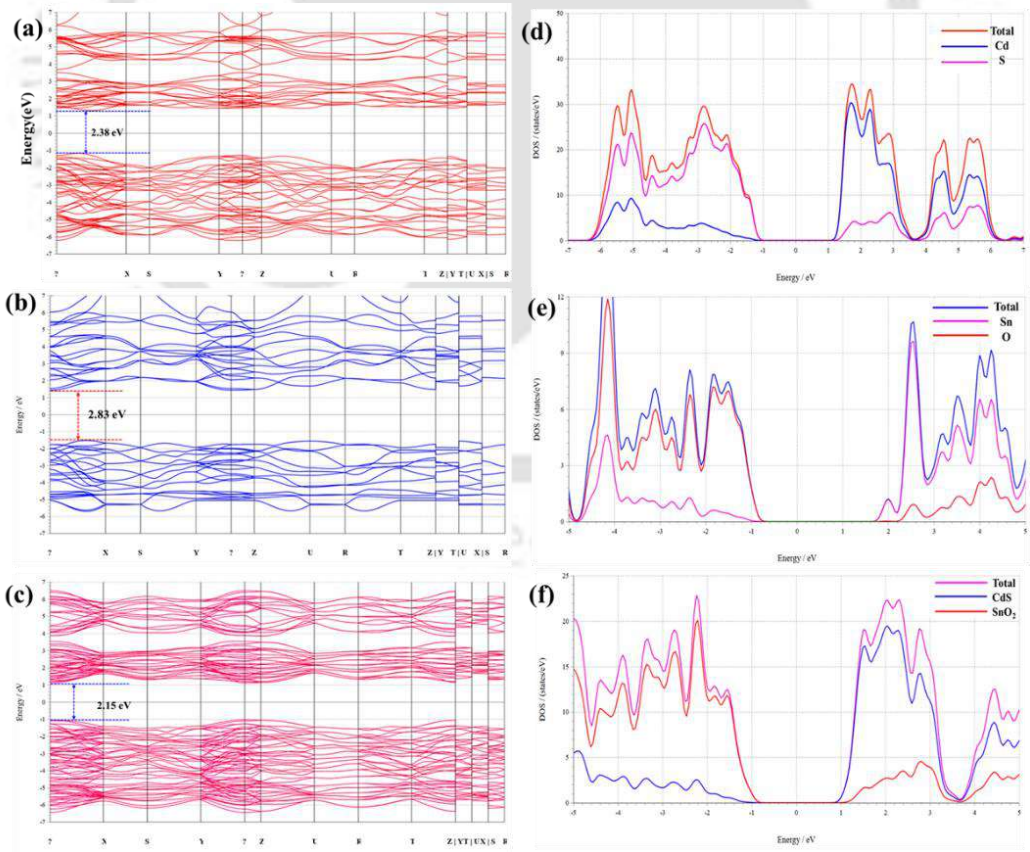

Figure 6.11. DFT calculation of (a-c) Band structure and (d-f) Density of state of CdS QDs, SnO_2, and SnO_2/CdS QDs heterostructure.

Table 6.6. Optimized crystal structure parameters of CdS(bio), SnO_2 QDs(bio), and CuO/CdS QDs (bio) heterostructures considered for DFT calculation.

Catalyst	a (Å)	b (Å)	c (Å)
CdS QDs(bio)	5.88	5.88	5.88
SnO_2(bio)	4.72	4.72	3.17
SnO_2/CdS QDs(bio)	20.6	24.2	42

6.2.4 Photocatalytic CO_2 reduction evaluation

The synthesized catalysts were evaluated for PCO_2R to MeOH/H_2 under visible light illumination. In this study, only two products were formed, namely, MeOH and H_2. The calibration curve for MeOH and H_2 standards are presented in **Figure 6.12,** while chromatograms of both standard and resulting product are shown in **Figure 6.13**. Neither MeOH nor H_2 was detected in the absence of the catalyst or light illumination. To determine the carbon source contributing to MeOH and H_2 formation, three control experiments were conducted under optimal conditions, each with one component absent as: (i) CO_2, (ii) lamp, and (iii) catalyst. In all cases, no MeOH or H_2 was detected (**Figure 6.14**), confirming that these products originate from the CO_2 feedstock in the system. Additionally, a control experiment using N_2 instead of CO_2 yielded no detectable reduction products (**Figure 6.15**), ruling out the influence of organic contaminant photodegradation and verifying that the observed activity is solely due to PCO_2R.

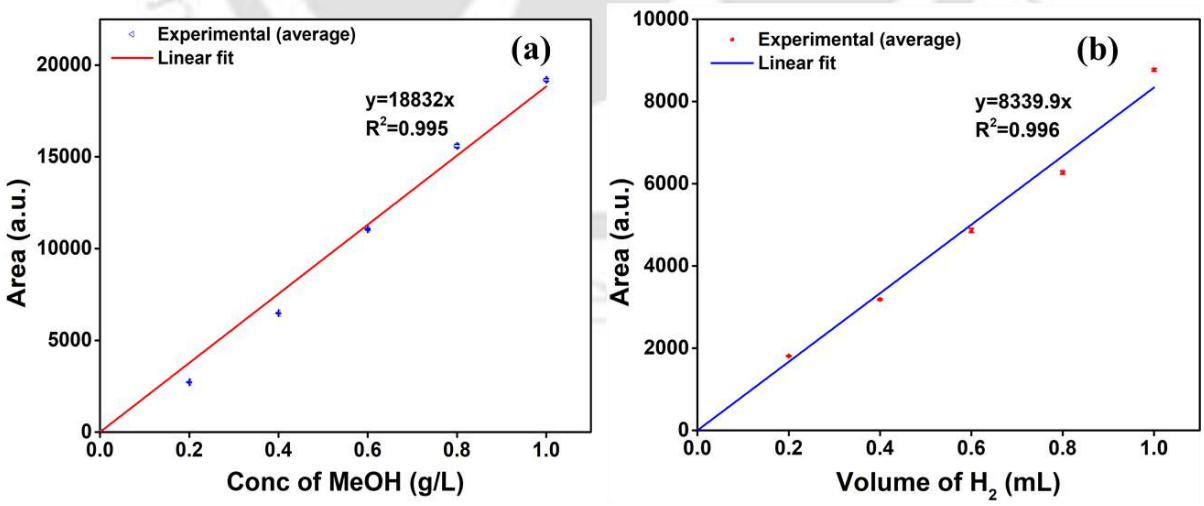

Figure 6.12. Calibration curves of (a) MeOH and (b) H_2.

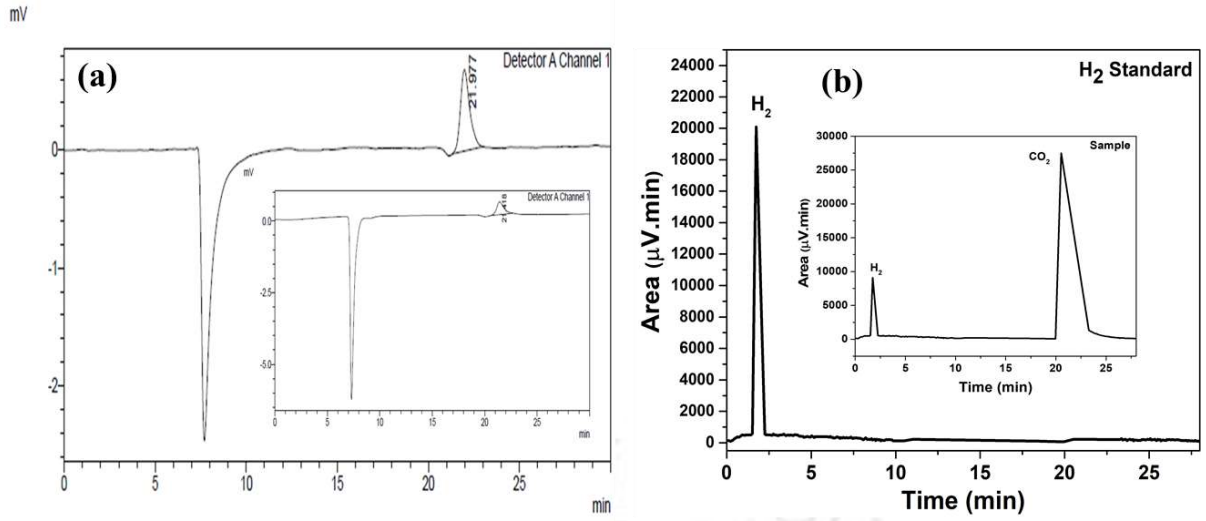

Figure 6.13. (a) HPLC chromatograms of standard 1 g/L MeOH and (inset) solution after 5 h of CO_2 reduction, and (b) GC chromatograms of standard 1 mL H_2 and (inset) solution after 5 h of CO_2 reduction.

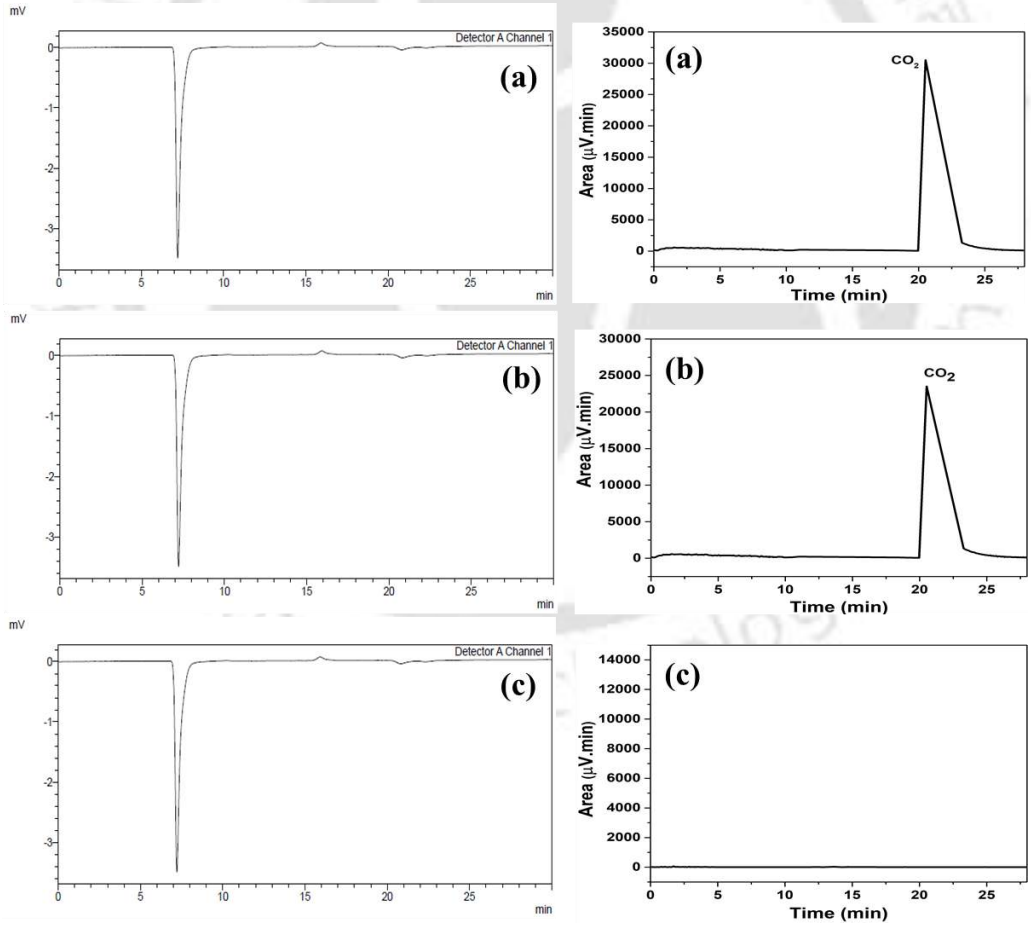

Figure 6.14. HPLC (left side) and GC (right side) chromatograms following 300 s of CO_2 reduction (a) CO_2 purge + DI water + light irradiation, (b) 0.50CuO/CdS QDs(bio) heterostructure + DI water + CO_2 purge, and (c) 0.50CuO/CdS QDs(bio) heterostructure + DI water + light irradiation.

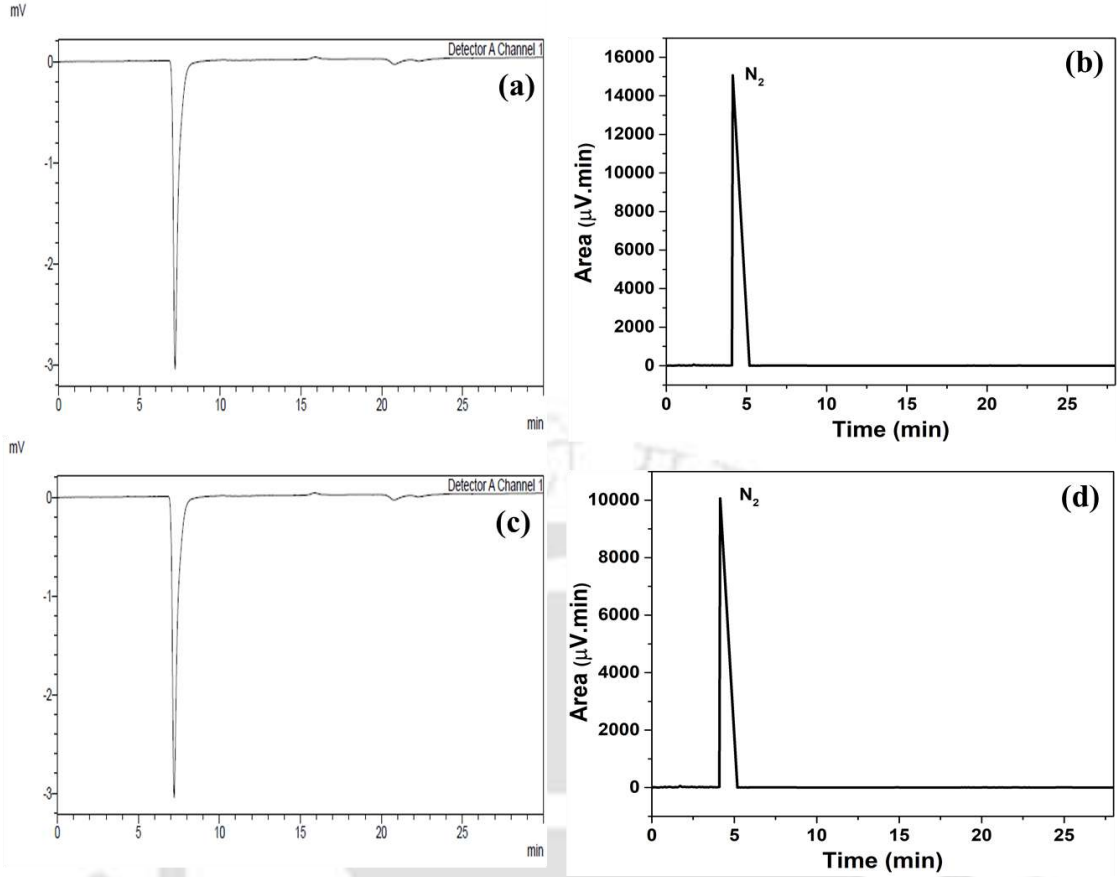

Figure 6.15. (a) HPLC, (b) GC chromatograms after 5 h of the control experiments, (c) HPLC, and (d) GC chromatograms after 10 h of the control experiments using N_2 instead of CO_2.

Figure 6.16a illustrates the formation rates of MeOH/H_2 using SnO_2(bio), CdS QDs(bio), and SnO_2/CdS QDs(bio) heterostructure at different loading ratios (0.25, 0.50, 0.75, and 1.00 molar). CdS QDs(bio) and SnO_2(bio) failed to produce any detectable products, attributed to rapid e^-/h^+ pairs recombination and photocorrosion of CdS, as confirmed by PL and XPS and PL studies (**Figure 6.7a** and **Figure 6.17**). This indicates their inefficiency as catalysts for PCO_2R to MeOH/H_2 [12,32]. MeOH and H_2 formation was detected by SnO_2/CdS QDs(bio) heterostructure, with yield increasing as the SnO_2 loading ratio increased. The highest production rates were observed at a 0.50 molar SnO_2 loading, reaching 634.6 μmol/g·h for MeOH and 122 μmol/g·h for H_2. However, a further increase in SnO_2 loading led to a significant decline in the formation rates of MeOH and H_2. This decline is attributed to particle aggregation and the blockage of active sites on CdS QDs(bio), which hinder light absorption [12]. Dynamic light scattering (DLS) analysis (**Table 6.1**) showed that when SnO_2(bio) loading exceeded 0.50, the particle size increased from 276.2 to 312.3 nm because of agglomeration.

Therefore, the optimal SnO_2 loading for the SnO_2/CdS QDs(bio) heterostructure catalyst was identified as 0.50.

Figure 6.16b depicts the formation rates of MeOH and H_2 at varying concentrations of the 0.50SnO_2/CdS QDs(bio) heterostructure (0.25, 0.40, 0.75, 1.0, 1.25 g/L). The maximum MeOH and H_2 production rates were achieved at a photocatalyst concentration of 0.75 g/L, yielding 675.9 and 13.5 μmol/g·h, respectively, with apparent quantum yield (AQY) of 3.51 and 0.24 % (AQY calculation provided in **Table A4**). The selectivity of MeOH and H_2 is found to be 46.44 and 53.55 %, respectively. However, higher photocatalyst concentrations led to increased turbidity in the solution, reducing the efficiency of light irradiation [12,38]. **Table 6.7** presents turbidity assessments for different photocatalyst concentrations, showing a 24.21% increase in turbidity when exceeding 0.75 g/L. A comparison of the MeOH and H_2 formation rates obtained in this study with reported literature values (**Table 6.8**) highlights the superior performance of the bio-based SnO_2/CdS QDs(bio) heterostructure.

Figure 6.16c illustrates the evaluation of the functional stability of the 0.50SnO_2/CdS QDs(bio) heterostructure through repeated cycles of time-dependent PCO_2R to MeOH and H_2 production. Over five consecutive cycles, the heterostructure demonstrated consistent photocatalytic activity with only a marginal 1.97% for MeOH and a 10 % for H_2 decline in their performance. This slight decline is attributed to the unavoidable loss of catalysts during the recovery process. This remarkable stability indicates that incorporating SnO_2(bio) onto CdS QDs(bio) effectively mitigates photocorrosion and suppresses the recombination of e^-/h^+ pairs, enhancing the overall stability of the heterostructure [4,39].

Table 6.7. Turbidity of 0.50SnO_2/CdS QDs(bio) heterostructure.

Catalyst concentration (g/L)	Turbidity (NTU)
0.25	140
0.50	155
0.75	190
1.0	236
1.25	289

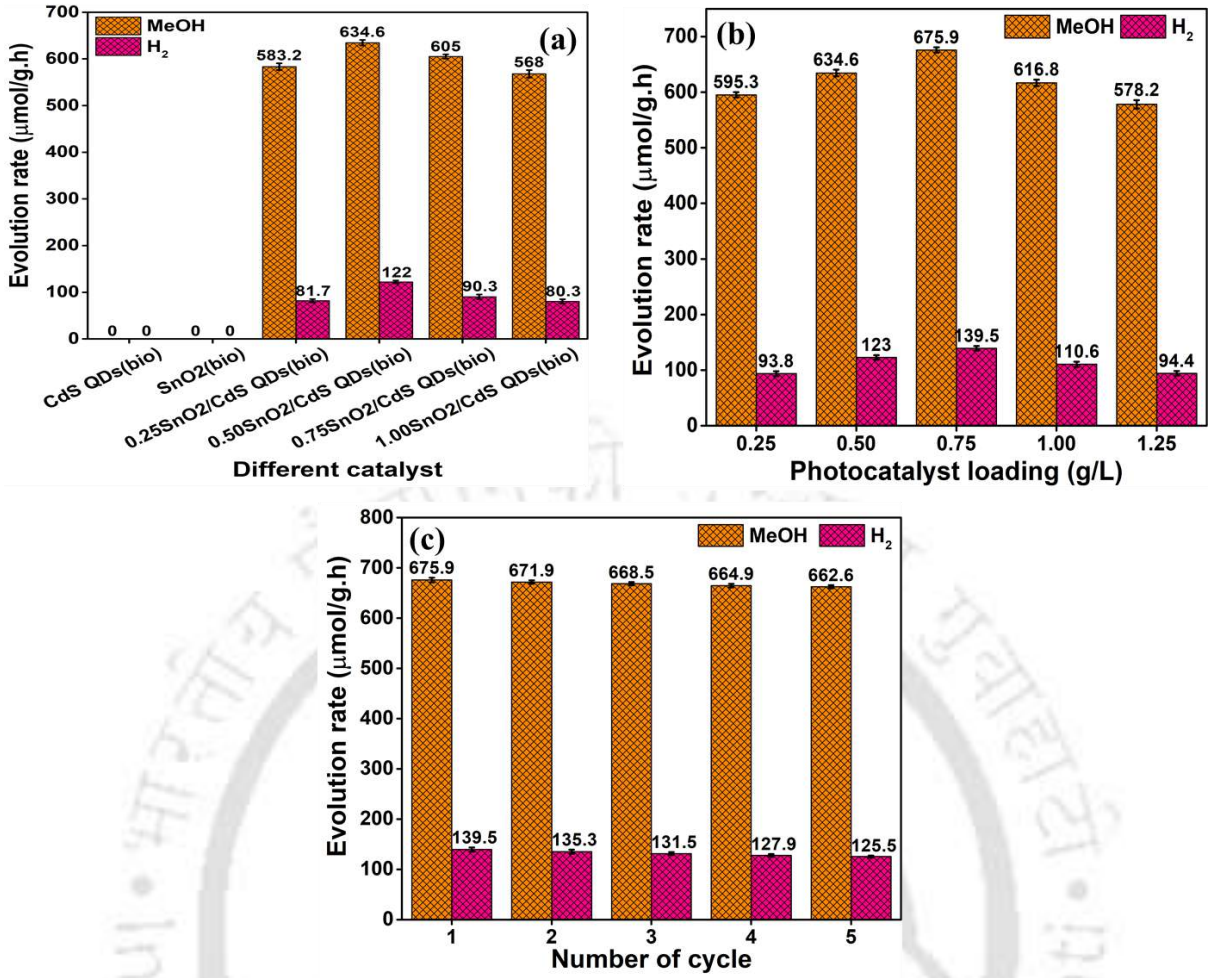

Figure 6.16. (a) Photocatalytic CO_2 reduction using bio-based catalysts, (b) Effect of photocatalyst loading, and (c) Functional stability study of $0.50SnO_2$/CdS QDs(bio) heterostructure.

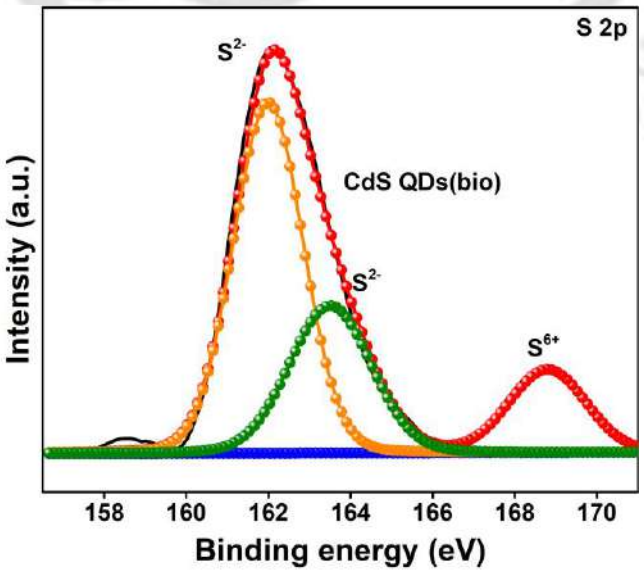

Figure 6.17. XPS HR spectra of S 2p of CdS QDs(bio/used).

Table 6.8. Comparison of the MeOH and H_2 rate with the earlier report.

Photocatalyst	Synthesis method	Reaction solvent	Light source	Products (µmol/g·h)		Sources
				MeOH	H_2	
SnO_2/CdS(bio) heterostructure	Microwave irradiation	Water	250 W Metal halide lamp, λ> 420 nm	675.9	139.5	**Present Work**
CdS/PAA	SILAR	Water vapour	10 W LED lamp	114.5		[40]
CdS/TiO_2	Direct precipitation reaction	0.1 NaOH/ 0.1 M Na_2SO_3 /H_2O	500 W Xenon lamp, λ>400 nm	31.9		[41]
Bi_2S_3/CdS	Hydrothermal	0.1M NaOH, 0.1M Na_2SO_3, H_2O	500 W Xenon lamp, λ=400-700 nm	122.6		[42]
CdS/A-GO	Ultrasonication	TEOA/H_2O	350W Xenon lamp, λ>420 nm	662.5		[14]
RGO/CdS/PAA	SILAR	Water vapour	Sunlight	157.3		[43]
CdS@CeO_2 core/shell composite	Two-step chemical	Milli-Q water	300W Xenon lamp, λ>420 nm	138		[44]
CdS@CeO_2 heterojunction	Electrostatic interaction	DMF/H_2O/TEA (2:2:1)	300 W Xenon lamp, λ>420 nm	153.4		[45]

TEOA: Triethanolamine; PAA: Porous anodic alumina; SBA: Santa barbara amorphous; TEA: trimethylamine; DMF: N, N-dimethylformamide; SILAR: Successive ionic layer adsorption and reaction

6.2.5 Stability of SnO_2/CdS QDs(bio) heterostructures

Figure 6.18 displays the XPS spectra of 0.50SnO_2/CdS QDs(bio) heterostructure before and after PCO_2R. The survey spectra (**Figure 6.18a**) verify the existence of Sn, Cd, O, and S in the heterostructure. High-resolution spectra of 0.50SnO_2/CdS QDs(bio) (**Figures 6.18b-18e**) reveal consistent peak intensities before and after PCO_2R, demonstrating the structural stability of the heterostructure. In contrast, for CdS QDs (bio/used) (**Figure 6.17**), the S 2p peak binding energy shows an additional peak at 168.6 eV (S^{6+}), suggesting sulfur oxidation (photocorrosion) and the formation of SO_4^{2-} [22,46].

XRD and TEM analyses were performed on SnO_2/CdS QDs(bio) heterostructure before and after PCO_2R to evaluate its structural and morphological properties. The XRD spectra of 0.50SnO_2/CdS QDs(bio) and 0.50SnO_2/CdS QDs(bio/used) (**Figure 6.19a**) reveal no significant changes in the lattice structure after the reaction, indicating structural stability. The crystallite size showed minimal variation, measuring 4.38 nm for 0.50SnO_2/CdS QDs(bio/used) compared to 4.40 nm for 0.50SnO_2/CdS QDs(bio). Likewise, the TEM image of 0.50SnO_2/CdS(bio/used) (**Figure 6.19b**) reveals an average particle size of 5.65 nm, exhibits no significant morphological changes compared to the initial 5.70 nm of 0.50SnO_2/CdS QDs(bio) with a size of 5.70 nm (**Figure 6.1c**).

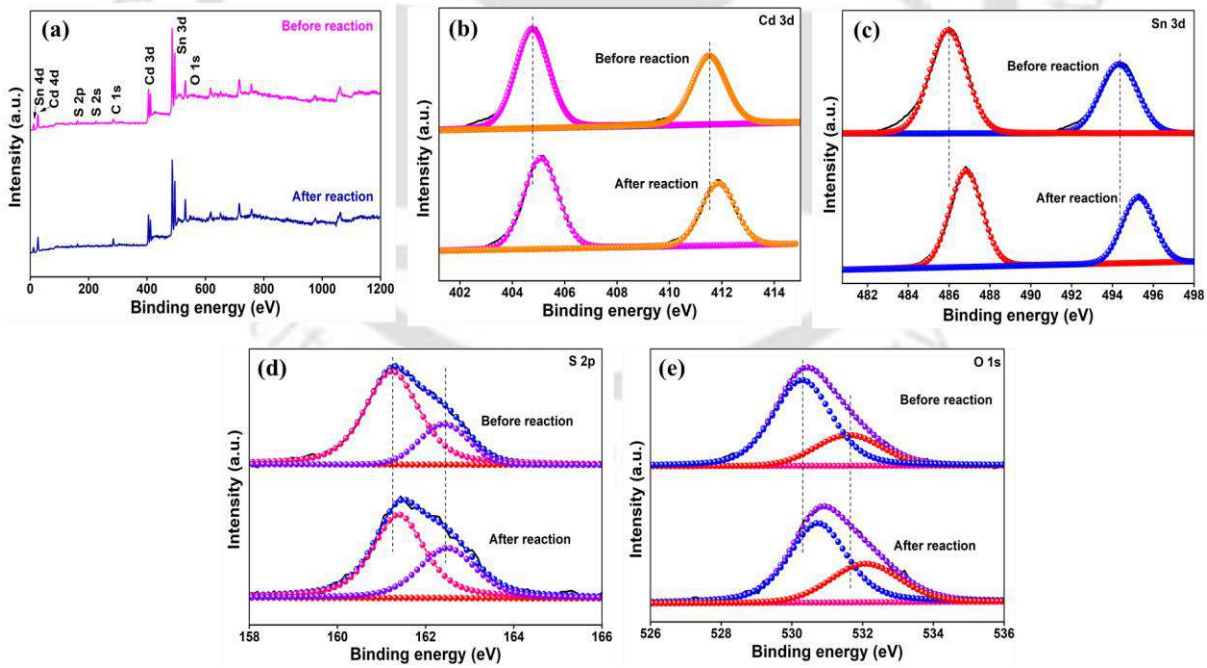

Figure 6.18. (a) XPS survey spectra, (b) Cd 3d, (c) Sn 3d, (d) S 2p, (e) O 1s of 0.50SnO_2/CdS QDs(bio) heterostructure before and after PCO_2R.

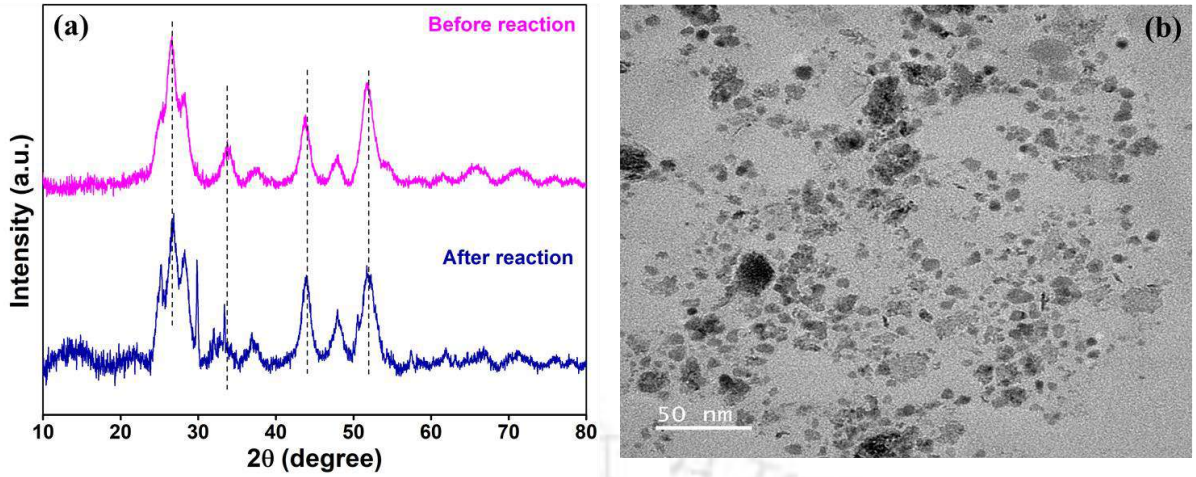

Figure 6.19. (a) XRD patterns of SnO_2/CdS QDs(bio) heterostructure before and after PCO_2R, and (b) FETEM of SnO_2/CdS QDs(bio)/used.

6.2.6 Mechanism of PCO_2R catalysed by SnO_2/CdS QDs(bio) heterostructure

The CdS QDs(bio), with a smaller φ value and higher $E_{F,}$ function as the reduction catalyst, whereas SnO_2(bio), possessing a larger φ value and lower E_F, acts as the oxidation catalyst. When these two semiconductors interact, the e^- of CdS QDs(bio) spontaneously transfer to SnO_2(bio) until their E_F level reaches equilibrium. As a result, SnO_2(bio) undergoes the downward band bending, accumulating negative charge at the interface, while CdS QDs(bio) experience upward band bending, developing positive charges. This charge redistribution leads to the development of an internal electric field (IEF)[4,17]. Under light illumination, the catalysts generate e^-/h^+ pairs (Eq. 6.1). Driven by band edge bending, the IEF and Coulomb interactions, e^- in the CB of SnO_2(bio) migrate across the interface and recombine with the h^+ in the VB of CdS QDs(bio). This process enables the e^- in the CB of CdS QDs(bio) with strong reduction capability, while the h^+ in the VB of SnO_2(bio) possesses strong oxidation capability. The h^+ in the VB of SnO_2(bio) oxidizes H_2O to produce a proton (H^+) and hydroxyl radical ($^{\cdot}OH$) (Eq. 6.2), while high potential e^- in CB of CdS QDs(bio) drives the CO_2 reduction reaction to MeOH and H_2. For H_2 production, the photogenerated e^- reduces H^+ to form H_2 (Eq. 6.3) [47]. The detailed reaction mechanism for MeOH formation is illustrated in **Scheme I**. Thus, the full redox cycle of the photocatalytic system is completed (**Figure 6.20**).

$$SnO_2/CdS\ QDs(bio) + hv \rightarrow h^+ + e^- \quad (6.1)$$

$$H_2O + h^+ \rightarrow H^+ + {}^{\cdot}OH \quad (6.2)$$

$$2H^+ + 2e^- \rightarrow H_2 \quad (6.3)$$

The photocatalytic reduction of CO_2 to MeOH proceeds through a multi-step process, each involving H^+ and e^-. Initially, CO_2 is reduced to formate ($HCOO^-$) (Eq. 6.4), which then gains another H^+/e^- pair to form formic acid (HCOOH) (Eq. 6.5), a key intermediate in CO_2 conversion. HCOOH is further reduced to the hydroxycarbene (HCO) with the release of H_2O (Eq. 6.6). Subsequent reduction of HCO yields formaldehyde (CH_2O) (Eq. 6.7), which is finally converted to methanol (CH_3OH) (Eq. 6.8). Overall, the reduction of 1 mole of CO_2 requires 6 e^- and 6 moles of H^+, producing one mole each of CH_3OH and H_2O (Eq. 6.9) [42].

Scheme I

$$CO_2 + H^+ + e^- \rightarrow HCOO^- \quad (6.4)$$

$$HCOO^- + H^+ + e^- \rightarrow HCOOH \quad (6.5)$$

$$HCOOH + H^+ + e^- \rightarrow HCO + H_2O \quad (6.6)$$

$$HCO + H^+ + e^- \rightarrow CH_2O \quad (6.7)$$

$$HCHO + H^+ + e^- \rightarrow CH_3OH \quad (6.8)$$

$$CO_2 + 6H^+ + 6e^- \rightarrow CH_3OH + H_2O \quad (6.9)$$

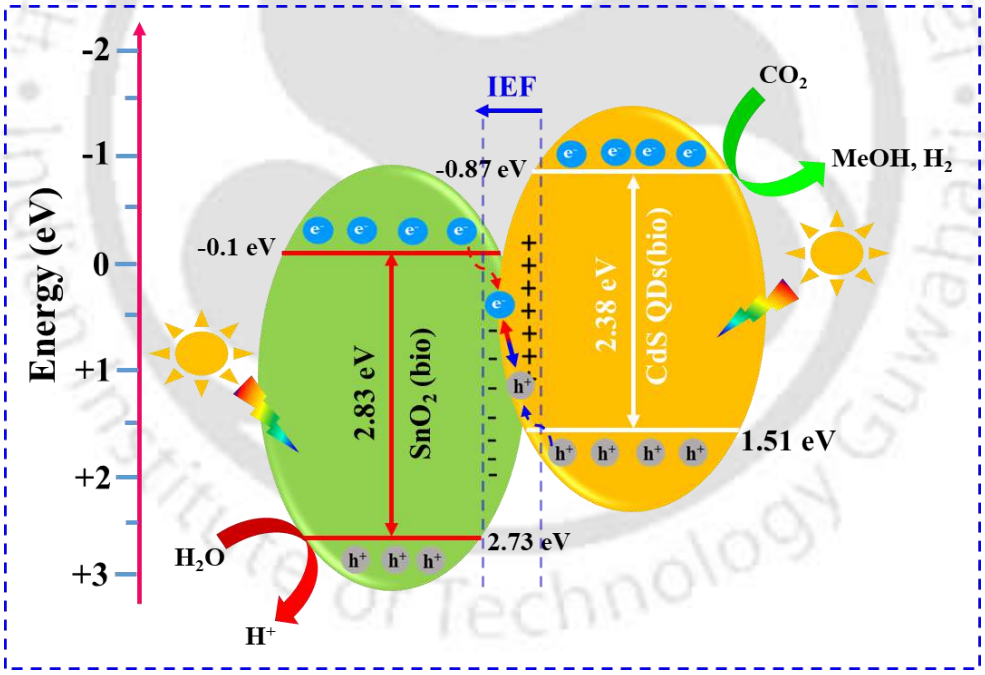

Figure 6.20. Possible reaction mechanism of PCO_2R over Z-scheme SnO_2/CdS QDs(bio) heterostructure.

6.3 Major findings

A bio-based Z-scheme SnO_2/CdS QDs heterostructure (average particle size 5.7 nm and surface area 120.6 m^2/g) is successfully synthesized using bio-analytes present in *Aegle marmelos* plant extract assisted by microwave irradiation. Its photocatalytic activity was evaluated for PCO_2R to MeOH and H_2 under visible light. The bandgap of CdS QDs, SnO_2, and SnO_2/CdS QDs heterostructure calculated using DFT closely agrees with the experimental determinations. The incorporation of SnO_2 (0.5 molar ratio) could reduce the CdS QDs(bio) bandgap from 2.38 to 2.16 eV. DOS analysis reveals that SnO_2 introduces an additional electronic state within the CdS QDs bandgap, enhancing charge separation and transport at the heterojunction. The SnO_2/CdS QDs(bio) heterostructure exhibits a prolonged decay lifetime of 5.37 ns, which is 1.95 and 2.45 times longer than that of CdS QDs(bio) and SnO_2(bio), respectively. It also shows a 4-5-fold increase in CO_2 adsorption (0.40 mmol/g). About 7- and 9-times enhancement in photocurrent response was achieved compared to CdS QDs(bio) and SnO_2(bio). Notably, SnO_2/CdS QDs(bio) achieves a remarkable MeOH and H_2 formation rate of 675.9/139.5 μmol/g·h (AQY 3.51/0.24%) without a sacrificial agent. The heterostructures demonstrated excellent stability (tested for 25 h), retaining its morphology (0.87% variation in particle size) and crystal structure (0.45% variation in crystallite size), and it could effectively prevent photocorrosion and suppress e^-/h^+ pair recombination. *However, the competing hydrogen evolution reaction (HER) lowered CO_2 reduction selectivity and affected multi-electron conversion pathways. The fifth objective focused on synthesizing p-n junction CuO/CdS QD heterostructures to form ethanol (C2 hydrocarbon) and to suppress HER. The experimental studies, in combination with DFT analysis, elucidated the mechanism of enhanced charge transfer that leads to the formation of ethanol.*

References

[1] J. Wu, L. Zhao, X. Gao, Y. Li, Multiscale structural regulation of Two-Dimensional materials for photocatalytic reduction of CO_2, Prog. Mater. Sci. 148 (2025) 101386. https://doi.org/10.1016/j.pmatsci.2024.101386.

[2] K. Tang, Z. Zhang, D. Zhou, J. Xu, H. Cui, F. Li, X. Zhang, J. Lei, L. Tang, N. Liu, Bimetallic materials as catalysts for photocatalytic CO_2 reduction to value-added chemicals: A review, Sep. Purif. Technol. 356 (2025) 129952. https://doi.org/10.1016/j.seppur.2024.129952.

[3] Y. Ma, Y. Zhang, G. Xie, Z. Huang, L. Peng, C. Yu, X. Xie, S. Qu, N. Zhang, Isolated

Cu Sites in CdS Hollow Nanocubes with Doping-Location-Dependent Performance for Photocatalytic CO_2 Reduction, ACS Catal. 14 (2024) 1468–1479. https://doi.org/10.1021/acscatal.3c05412.

[4] P.M. Gawal, A.K. Golder, Plant-Based Phytochemicals for Synthesis of Z-Scheme In_2O_3/CdS Heterostructures: DFT Analysis and Photocatalytic CO_2 Reduction to HCOOH and CO, Langmuir. 40 (2024) 13538–13549. https://doi.org/10.1021/acs.langmuir.4c01015.

[5] S.S.A. Shah, M.A. Nazir, K. Khan, I. Hussain, M. Tayyab, S.S. Alarfaji, A.M. Hassan, M. Sohail, M.S. Javed, T. Najam, Solar energy storage to chemical: Photocatalytic CO_2 reduction over pristine metal-organic frameworks with mechanistic studies, J. Energy Storage. 75 (2024) 109725. https://doi.org/10.1016/j.est.2023.109725.

[6] A.M. Sadanandan, J.H. Yang, V. Devtade, G. Singh, N. Panangattu Dharmarajan, M. Fawaz, J. Mee Lee, E. Tavakkoli, C.H. Jeon, P. Kumar, A. Vinu, Carbon nitride based nanoarchitectonics for nature-inspired photocatalytic CO_2 reduction, Prog. Mater. Sci. 142 (2024) 101242. https://doi.org/10.1016/j.pmatsci.2024.101242.

[7] K. Yang, Z. Yang, C. Zhang, Y. Gu, J. Wei, Z. Li, C. Ma, X. Yang, K. Song, Y. Li, Q. Fang, J. Zhou, Recent advances in CdS-based photocatalysts for CO_2 photocatalytic conversion, Chem. Eng. J. 418 (2021) 129344. https://doi.org/10.1016/j.cej.2021.129344.

[8] H. Shen, T. Peppel, J. Strunk, Z. Sun, Photocatalytic Reduction of CO_2 by Metal-Free-Based Materials: Recent Advances and Future Perspective, Sol. RRL. 4 (2020) 1900546. https://doi.org/10.1002/solr.201900546.

[9] M. Zhang, Z. Liu, J. Wang, Z. Chen, G. Jiang, Q. Zhang, Z. Li, Generating Long-Lived Charge Carriers in CdS Quantum Dots by Cu-Doping for Photocatalytic CO_2 Reduction, Inorg. Chem. 63 (2024) 2234–2240. https://doi.org/10.1021/acs.inorgchem.3c04196.

[10] X. Liang, X. Wang, X. Zhang, S. Lin, M. Ji, Q. Liu, M. Wang, Generation of Lattice Strain in CdS Promotes Photocatalytic Reduction of CO_2, ACS Catal. 14 (2024) 4648–4655. https://doi.org/10.1021/acscatal.4c00016.

[11] W. Boonta, W. Sangkhun, C. Suppaso, N. Chantanop, W. Panchan, K. Chainok, P. Thamyongkit, T. Sudyoadsuk, K. Maeda, T. Butburee, J. Unruangsri, Rhenium(I) Complex-Containing Amphiphilic Metallopolymer Stabilizing CdS Quantum Dots for Synergistically Boosting Photoreduction of CO_2, ACS Catal. 13 (2023) 12391–12402. https://doi.org/10.1021/acscatal.3c01979.

[12] P.M. Gawal, A.K. Golder, Vegetal route for synthesis of CQDs/CdS nanocomposites

for photocatalytic reduction of CO_2 to methanol under visible light, Colloids Surfaces A Physicochem. Eng. Asp. 683 (2024) 133068. https://doi.org/10.1016/j.colsurfa.2023.133068.

[13] L. Zhang, L. Zhang, Y. Chen, Y. Zheng, J. Guo, S. Wan, S. Wang, C.K. Ngaw, J. Lin, Y. Wang, CdS/ZnO: A Multipronged Approach for Efficient Reduction of Carbon Dioxide under Visible Light Irradiation, ACS Sustain. Chem. Eng. 8 (2020) 5270–5277. https://doi.org/10.1021/acssuschemeng.0c00190.

[14] L. Zhu, Y. Liu, X. Peng, Y. Li, Y.-L. Men, P. Liu, Y.-X. Pan, Noble-metal-free CdS nanoparticle-coated graphene oxide nanosheets favoring electron transfer for efficient photoreduction of CO_2, ACS Appl. Mater. Interfaces. 12 (2020) 12892–12900. https://doi.org/10.1021/acsami.0c00163.

[15] N. Ojha, A. Bajpai, S. Kumar, Enriched oxygen vacancies of $Cu_2O/SnS_2/SnO_2$ heterostructure for enhanced photocatalytic reduction of CO_2 by water and nitrogen fixation, J. Colloid Interface Sci. 585 (2021) 764–777. https://doi.org/10.1016/j.jcis.2020.10.056.

[16] F. You, Y. Zhou, D. Li, H. Zhang, D. Gao, X. Ma, R. Hao, J. Liu, Construction of a flower-like SnS_2/SnO_2 junction for efficient photocatalytic CO_2 reduction, J. Colloid Interface Sci. 629 (2023) 871–877. https://doi.org/10.1016/j.jcis.2022.09.134.

[17] Z. Dong, Y. Shi, Y. Jiang, C. Yao, Z. Zhang, In situ growth of $CsPbBr_3$ quantum dots in mesoporous SnO_2 frameworks as an efficient CO_2-reduction photocatalyst, J. CO2 Util. 72 (2023) 102480. https://doi.org/10.1016/j.jcou.2023.102480.

[18] Y. Xiao, A. Abulizi, K. Okitsu, T. Ren, Facile fabrication of SnO_2 modified hierarchical BiOI S-scheme heterojunction photocatalyst with efficient activity for carbon dioxide reduction, J. Ind. Eng. Chem. 125 (2023) 317–324. https://doi.org/10.1016/j.jiec.2023.05.041.

[19] P. Hu, G. Liang, B. Zhu, W. Macyk, J. Yu, F. Xu, Highly Selective Photoconversion of CO_2 to CH_4 over $SnO_2/Cs_3Bi_2Br_9$ Heterojunctions Assisted by S-Scheme Charge Separation, ACS Catal. 13 (2023) 12623–12633. https://doi.org/10.1021/acscatal.3c03095.

[20] P.M. Gawal, J. Ishrat, K. Bhattacharyya, A.K. Golder, Experimental and Theoretical Studies on Photocatalytic CO_2 Reduction to HCOOH by Biomass-Derived Carbon Dots Embedded Phytochemical-Based CdS Quantum Dots, Langmuir. 41 (2025) 11161–11172. https://doi.org/10.1021/acs.langmuir.5c01002.

[21] R. Ravi, A.K. Golder, A tuneable bioinspired process of Pt-doping in TiO_2 for improved

photoelectrochemical and photocatalytic functionalities, Colloids Surfaces A Physicochem. Eng. Asp. 663 (2023) 131034. https://doi.org/10.1016/j.colsurfa.2023.131034.

[22] P.M. Gawal, A.K. Golder, Plant-Derived Phytochemicals for the Synthesis of p–n Junction CuO/CdS Heterostructures for Photocatalytic Carbon Dioxide Reduction to Ethanol and Carbon Monoxide, ACS Appl. Energy Mater. 8 (2025) 6087–6099. https://doi.org/10.1021/acsaem.5c00497.

[23] L. Zhang, C.G. Niu, C. Liang, X.J. Wen, D.W. Huang, H. Guo, X.F. Zhao, G.M. Zeng, One-step in situ synthesis of CdS/SnO_2 heterostructure with excellent photocatalytic performance for Cr(VI) reduction and tetracycline degradation, Chem. Eng. J. 352 (2018) 863–875. https://doi.org/10.1016/j.cej.2018.07.102.

[24] H. Khallaf, C.T. Chen, L.B. Chang, O. Lupan, A. Dutta, H. Heinrich, F. Haque, E. Del Barco, L. Chow, Chemical bath deposition of SnO_2 and Cd_2 SnO_4 thin films, Appl. Surf. Sci. 258 (2012) 6069–6074. https://doi.org/10.1016/j.apsusc.2012.03.004.

[25] B. Su, L. Huang, Z. Xiong, Y. Yang, Y. Hou, Z. Ding, S. Wang, Branch-like ZnS-DETA/CdS hierarchical heterostructures as an efficient photocatalyst for visible light CO_2 reduction, J. Mater. Chem. A. 7 (2019) 26877–26883. https://doi.org/10.1039/c9ta10470d.

[26] E. Ching-Prado, C.A. Samudio, J. Santiago-Aviles, S. Velumani, Electronic structure and optical properties of SnO_2:F from PBE0 hybrid functional calculations, J. Mater. Sci. Mater. Electron. 29 (2018) 15423–15435. https://doi.org/10.1007/s10854-018-9067-3.

[27] H. Ren, F. Qi, A. Labidi, J. Zhao, H. Wang, Y. Xin, J. Luo, C. Wang, Chemically bonded carbon quantum dots/Bi_2WO_6 S-scheme heterojunction for boosted photocatalytic antibiotic degradation: Interfacial engineering and mechanism insight, Appl. Catal. B Environ. 330 (2023) 122587. https://doi.org/10.1016/j.apcatb.2023.122587.

[28] A. Chowdhury, C. Bhan, N.R. Peela, A.K. Golder, A tunable bioinspired process of SnO_2 NPs synthesis for electrochemical CO_2-into-formate conversion, J. CO2 Util. 66 (2022) 102263. https://doi.org/10.1016/j.jcou.2022.102263.

[29] S.G. Ghugal, S.S. Umare, R. Sasikala, A stable, efficient and reusable CdS-SnO_2 heterostructured photocatalyst for the mineralization of Acid Violet 7 dye, Appl. Catal. A Gen. 496 (2015) 25–31. https://doi.org/10.1016/j.apcata.2015.02.035.

[30] S. Shabna, S.C. Jeyakumar, M.R. Joel, S.S.J. Dhas, S. Aswathappa, R.S. Kumar, A.I. Almansour, A. Aravind, L.M. Jose, C.S. Biju, Structural, optical and photocatalytic

investigations of cauliflower like SnO_2/CdS nanocomposite prepared by the sol-gel method, J. Sol-Gel Sci. Technol. (2024). https://doi.org/10.1007/s10971-024-06365-1.

[31] Y. Liu, P. Zhang, B. Tian, J. Zhang, Core-Shell Structural CdS@SnO_2 Nanorods with Excellent Visible-Light Photocatalytic Activity for the Selective Oxidation of Benzyl Alcohol to Benzaldehyde, ACS Appl. Mater. Interfaces. 7 (2015) 13849–13858. https://doi.org/10.1021/acsami.5b04128.

[32] E.E. El-Katori, M.A. Ahmed, A.A. El-Bindary, A.M. Oraby, Impact of CdS/SnO_2 heterostructured nanoparticle as visible light active photocatalyst for the removal methylene blue dye, J. Photochem. Photobiol. A Chem. 392 (2020) 112403. https://doi.org/10.1016/j.jphotochem.2020.112403.

[33] S.M. Chaudhari, P.M. Gawal, P.K. Sane, S.M. Sontakke, P.R. Nemade, Solar light-assisted photocatalytic degradation of methylene blue with Mo/TiO2: a comparison with Cr- and Ni-doped TiO2, Res. Chem. Intermed. 44 (2018) 3115–3134. https://doi.org/10.1007/s11164-018-3296-1.

[34] D. Gogoi, A.K. Shah, P. Rambabu, M. Qureshi, A.K. Golder, N.R. Peela, Step-Scheme Heterojunction between CdS Nanowires and Facet-Selective Assembly of MnOx - $BiVO_4$ for an Efficient Visible-Light-Driven Overall Water Splitting, ACS Appl. Mater. Interfaces. 13 (2021) 45475–45487. https://doi.org/10.1021/acsami.1c11740.

[35] C. Bhan, A.K. Golder, ZnO Nanorods Aligned in a Vertical Configuration for Targeted Electrochemical Detection of Aniline, ACS Appl. Bio Mater. 7 (2024) 7413–7428. https://doi.org/10.1021/acsabm.4c01050.

[36] Y. Zhang, Y. Wu, L. Wan, H. Ding, H. Li, X. Wang, W. Zhang, Hollow core–shell Co_9S_8@$ZnIn_2S_4$/CdS nanoreactor for efficient photothermal effect and CO2 photoreduction, Appl. Catal. B Environ. 311 (2022) 121255. https://doi.org/10.1016/j.apcatb.2022.121255.

[37] L. Li, C. Guo, J. Ning, Y. Zhong, D. Chen, Y. Hu, Oxygen-vacancy-assisted construction of FeOOH/CdS heterostructure as an efficient bifunctional photocatalyst for CO_2 conversion and water oxidation, Appl. Catal. B Environ. 293 (2021) 120203. https://doi.org/10.1016/j.apcatb.2021.120203.

[38] D. Gogoi, R. Koyani, A.K. Golder, N.R. Peela, Enhanced photocatalytic hydrogen evolution using green carbon quantum dots modified 1-D CdS nanowires under visible light irradiation, Sol. Energy. 208 (2020) 966–977. https://doi.org/10.1016/j.solener.2020.08.061.

[39] L. Wang, Y. Dong, J. Zhang, F. Tao, J. Xu, Construction of NiO/g-C_3N_4 p-n

heterojunctions for enhanced photocatalytic CO_2 reduction, J. Solid State Chem. 308 (2022) 122878. https://doi.org/10.1016/j.jssc.2022.122878.

[40] M.M. Kandy, V.G. Gaikar, Photocatalytic reduction of CO_2 using CdS nanorods on porous anodic alumina support, Mater. Res. Bull. 102 (2018) 440–449. https://doi.org/10.1016/j.materresbull.2018.02.054.

[41] X. Li, H. Liu, D. Luo, J. Li, Y. Huang, H. Li, Y. Fang, Y. Xu, L. Zhu, Adsorption of CO_2 on heterostructure CdS(Bi_2S_3)/TiO_2 nanotube photocatalysts and their photocatalytic activities in the reduction of CO_2 to methanol under visible light irradiation, Chem. Eng. J. 180 (2012) 151–158. https://doi.org/10.1016/j.cej.2011.11.029.

[42] X. Li, J. Chen, H. Li, J. Li, Y. Xu, Y. Liu, J. Zhou, Photoreduction of CO_2 to methanol over Bi_2S_3/CdS photocatalyst under visible light irradiation, J. Nat. Gas Chem. 20 (2011) 413–417. https://doi.org/10.1016/S1003-9953(10)60212-5.

[43] M.M. Kandy, V.G. Gaikar, Continuous photocatalytic reduction of CO_2 using nanoporous reduced graphene oxide (RGO)/cadmium sulfide (CdS) as catalyst on porous anodic alumina (PAA)/aluminum support, J. Nanosci. Nanotechnol. 19 (2019) 5323–5331. https://doi.org/10.1166/jnn.2019.16817.

[44] S. Ijaz, M.F. Ehsan, M.N. Ashiq, N. Karamat, T. He, Preparation of CdS@CeO_2 core/shell composite for photocatalytic reduction of CO_2 under visible-light irradiation, Appl. Surf. Sci. 390 (2016) 550–559. https://doi.org/10.1016/j.apsusc.2016.08.098.

[45] Q. Mou, Z. Guo, Y. Chai, B. Liu, C. Liu, Visible light assisted production of methanol from CO_2 using CdS@CeO_2 heterojunction, J. Photochem. Photobiol. B Biol. 219 (2021) 112205. https://doi.org/10.1016/j.jphotobiol.2021.112205.

[46] P.M. Gawal, A.K. Golder, Plant-Based Phytochemicals for Synthesis of Z-Scheme In_2O_3/CdS Heterostructures: DFT Analysis and Photocatalytic CO_2 Reduction to HCOOH and CO, Langmuir. 40 (2024) 13538–13549. https://doi.org/10.1021/acs.langmuir.4c01015.

[47] M.M. Kandy, V.G. Gaikar, Enhanced photocatalytic reduction of CO_2 using CdS/Mn_2O_3 nanocomposite photocatalysts on porous anodic alumina support with solar concentrators, Renew. Energy. 139 (2019) 915–923. https://doi.org/10.1016/j.renene.2019.03.002.

CHAPTER 7

Phytochemicals for Synthesis of p-n Junction CuO/CdS Heterostructures for Photocatalytic Carbon Dioxide Reduction to Ethanol and Carbon Monoxide

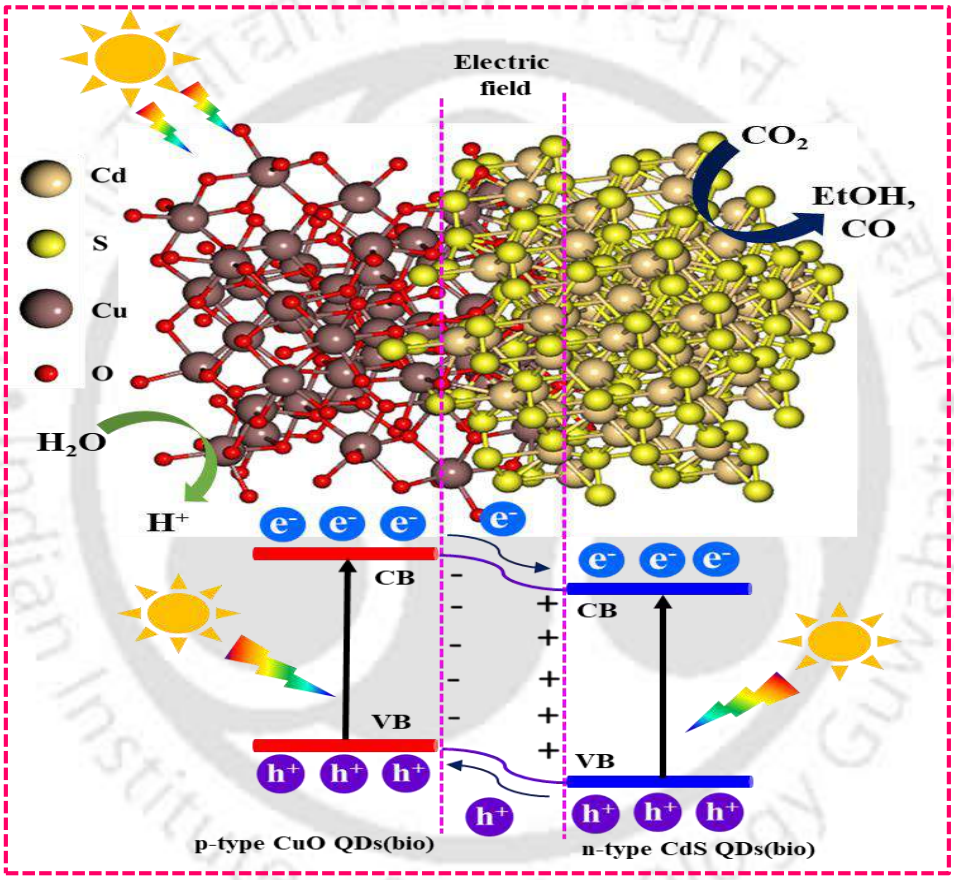

Chapter highlights

- CdS QDs(bio) and CuO QDs(bio) synthesized using plant-based phytochemicals
- CuO/CdS QDs(bio) heterostructures inhibited CdS QDs(bio) photocorrosion
- Band overlapping of CuO/CdS heterostructures near Fermi level reducing its bandgap
- CuO QDs(bio) incorporation in heterostructures conducive to CO_2 adsorption by 6-fold
- EtOH/CO production of 158.48/182.68 µmol/g·h over CuO/CdS QDs(bio)

7.1 Introduction

Photocatalytic CO_2 reduction into value-added products is a promising strategy for sustainable energy and greenhouse gas mitigation [1,2]. However, the reaction rate is slow due to the chemical inertness of CO_2, complex reaction pathways, and a variety of potential products [3,4]. Over the past decade, significant efforts have focused on developing cost-effective photocatalysts with high efficiency and selectivity. Semiconductor nanoparticles (NPs) have demonstrated potential in artificial photosynthesis due to their excellent light harvesting, tunable band alignment, multiple exciton generation, and abundant surface binding sites [5–7]. Semiconducting materials, including g-C_3N_4 [8], TiO_2 [5], CdS [9], Cu_2O [10], ZnO [11], WO_3 [12], MOFs [13], BiOBr [14], and In_2O_3 [15], have been employed as photocatalysts for CO_2 reduction. However, their pristine forms generally exhibit low performance due to low charge separation, high recombination of electron (e^-)/hole (h^+) pairs, photocorrosion, limited visible light absorption, inadequate CO_2 adsorption, and stability issues [16–18]. To overcome these limitations, heterostructures and co-catalyst integration are widely employed to enhance photocatalytic efficiency [19–21].

CdS, an n-type semiconductor, is widely studied for photocatalytic CO_2 reduction due to its narrow band gap (2.42 eV), strong solar absorption, negative conduction band position (-0.95 V), chemical and thermal stability, excellent charge transport, and tunable morphology [16,22]. However, its low photocatalytic activity is hindered by low charge separation and photocorrosion (oxidation of S^{2-} to SO_4^{2-}), limiting its application. Studies show that forming a heterostructure with semiconductors having suitable band structures significantly improves charge separation and photocorrosion resistance, enhancing CdS's photocatalytic performance [11,23]. The p-n junction improves photocatalytic activity by creating an internal electric field that effectively separates e^-/h^+ pairs and photostability [24,25]. For example, the NiO/g-C_3N_4 heterostructure has shown improved CO_2 reduction efficiency and photostability due to the effective separation of e^-/h^+ pairs facilitated by the p-n junction formed between NiO and g-C_3N_4 [26].

On the other hand, CuO is a p-type semiconductor with a 1.2-1.9 eV band gap, excellent visible light absorption, and a favorable band structure for CO_2 reduction [27,28]. However, its efficiency is limited by high e^-/h^+ pairs recombination. CuO NPs are frequently used in the fabrication of heterogeneous photocatalysts by integrating them with other semiconductors to improve photocatalytic efficiency [29,30]. Combining p-type CuO with n-type CdS forms a p-n heterojunction, reducing photocorrosion and suppressing charge recombination. Their well-

aligned conduction and valence bands further improve charge separation, addressing the limitations of both materials [27,31].

Bio-based synthesis of quantum dots (QDs) is eco-friendly and cost-effective, utilizing bio-based precursors [32,33]. A green approach for synthesizing QDs and their application in photocatalytic CO_2 reduction could help control industrial CO_2 emissions [34,35]. Northeastern states of India, abundant in diverse tropical plants, offer potential as sources for capping and reducing agents in efficient QDs synthesis. Additionally, combining microwave irradiation with bioinspired processes can significantly increase QDs formation rates [9].

In this work, a nature-inspired route was explored for the formation of p-n junction CuO/CdS heterostructure using plant-derived phytochemicals from *Aegle marmelos* assisted by a microwave irradiation method. *Aegle marmelos* contains phytochemicals, such as flavonoids, alkaloids, tannins, phenols, and saponins, acted as strong reducing and capping agents [9,34]. The synthesized catalysts were characterized using spectroscopy, microscopy, diffraction, and electrochemical techniques. The bandgap and charge separation of catalysts were calculated using DFT by analyzing the band structure and DOS. Photocatalytic CO_2 reduction under visible light produced ethanol (EtOH) and CO, and the heterostructures' stability and reusability were evaluated. This study presents a novel bio-based synthesis approach for heterostructures designed to enhance the efficiency of photocatalytic CO_2 reduction, with a focus on producing EtOH and CO.

7.2 Results and discussions

7.2.1 Photocatalyst characterization

XRD analysis: The XRD pattern of the synthesized catalyst is shown in **Figure 7.1**. The peaks at 2θ of 26.5°, 43.9°, and 51.9° for CdS QDs(bio) correspond to crystal planes (111), (220), and (311), confirming its cubic structure (JCPDF: 00-002-0454). For CuO QDs(bio), peak positions at 2θ of 32.52°, 35.45°,38.73°,48.76°, 53.41°, 58.32°, 61.57°, 66.23°, 68.14°, 72.42°, 75.02° correspond to crystal plane (110), (002), (111), ($\bar{2}$02), (020), (202), ($\bar{1}$13), ($\bar{3}$11), (220), (311), and (004), confirming monoclinic structure (JCPDF: 00-005-0661). The peak positions of both catalysts were perfectly matched with the reported literature [31,34]. For the CuO/CdS QDs(bio) heterostructure, the diffraction peaks corresponding to CdS QDs(bio) are observed, while no peaks are associated with CuO QDs(bio). This absence of CuO diffraction peaks is likely attributed to the low loading content (<1 molar ratio) and indicates a uniform distribution and small particle size. The average crystallite size was determined by Debye

Scherrer's equation [36]. The average crystallite size of CdS QDs(bio), CuO QDs(bio), and 0.50CuO/CdS QDs(bio) heterostructures was calculated to be 3.5, 5.2, and 4.40 nm, respectively.

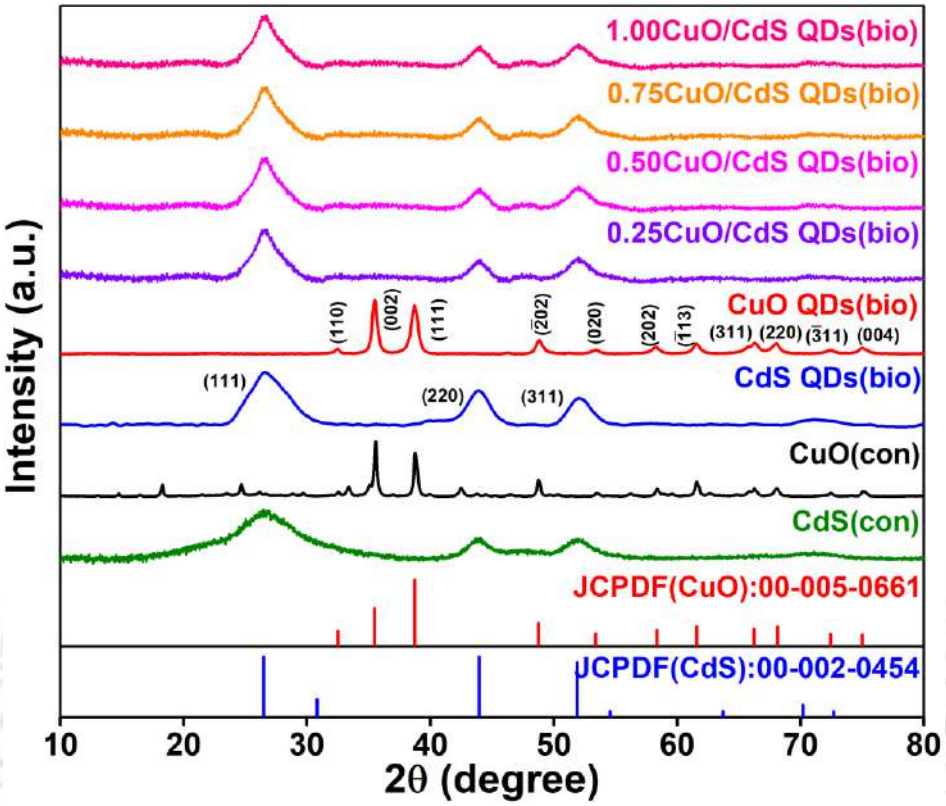

Figure 7.1. XRD diffractograms of CdS(con), CuO(con), CdS QDs(bio), CuO QDs(bio), and CuO/CdS QDs(bio) heterostructure at different molar ratios (0.25-1.0) of CuO and CdS QDs.

XPS analysis: The survey spectra of synthesized catalysts confirm the Cd, S, Cu, and O elements (**Figure 7.2a**). Cd 3d spectra (**Figure 7.2b**) of CdS QDs(bio) showed peaks at 412.1 eV($3d_{3/2}$) and 405.3 eV ($3d_{5/2}$), representing Cd^{2+} in CdS QDs(bio). S 2p spectra (**Figure 7.2c**) exhibited peaks at 160.1eV($2p_{1/2}$) and 158.88 eV($2p_{3/2}$), indicating the S^{2-} valence state in CdS QDs(bio) [34] . Cu 2p spectra (**Figure 7.2d**) of CuO QDs(bio) show the peaks at 962.3 eV($2p_{1/2}$), 953.9 eV ($2p_{1/2}$), and 934 eV (Cu $2p_{3/2}$), while two peaks at 941.5 and 943.85 eV represent the satellite peak of Cu, confirming the Cu^{2+} in the CuO (bio) [31]. O 1s spectra (**Figure 7.2e**) of CuO QDs(bio) show the peaks at 531.9 and 529.9 eV corresponding to the adsorbed oxygen and lattice oxygen, respectively [27]. The Cu 2p, Cd 3d, O 1s, and S 2p spectra of CuO/CdS QDs(bio) heterostructure exhibited a similar trend. In S 2p, a new characteristic peak appears at 168.46 eV, corresponding to the Cu-S bond and the sulfate group. The positive shift of Cu 2p and O 1s compared to CuO QDs(bio) indicates the strong chemical interaction between CuO and CdS in the CuO/CdS heterostructure [27,31].

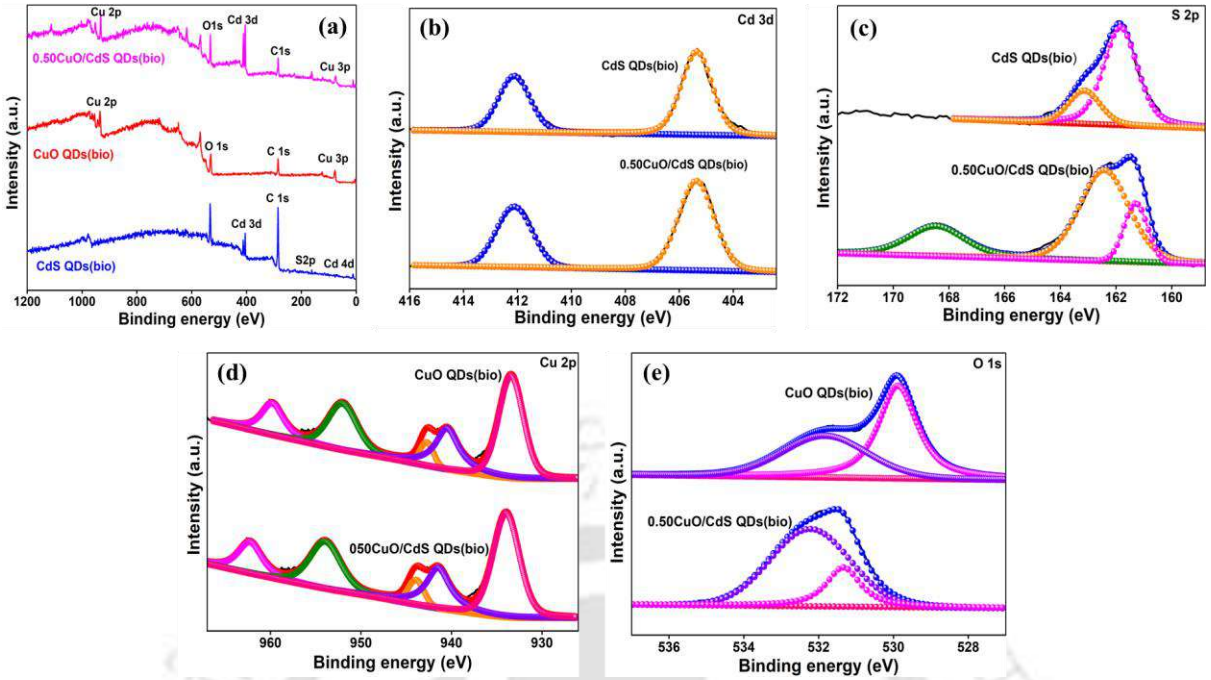

Figure 7.2. (a) XPS survey spectra, (b, c) Cd 3d and S 2p spectra of CdS QDs(bio) and CuO/CdS QDs(bio) heterostructure, and (d, e) Cu 2p and O 1s of CuO QDs(bio) and CuO/CdS QDs(bio) heterostructure.

Determination of energy: The absorption spectra of the synthesized catalyst are shown in **Figure 7.3a**. CdS QDs(bio) show a notable absorption edge at 520 nm, while CuO QDs(bio) at 600 nm. Both catalysts work in the visible range. In CuO/CdS QDs(bio) heterostructure, the red shift in the absorption edge was noted, enhancing the light absorption in the visible range [9]. The bandgap of catalysts was calculated by Tauc's relation, shown in **Figure 7.3b.** The bandgap of CdS QDs(bio), CuO QDs(bio), and 0.50CuO/CdS QDs(bio) heterostructure were calculated to be 2.39, 1.75, and 2.25 eV, respectively. The bandgap of CuO QDs(bio) and CdS QDs(bio) matches with the reported literature [37,38].

Figure 7.3c shows the minimum valence band energies of CdS QDs(bio), CuO QDs(bio), and 0.50CuO/CdS QDs(bio) heterostructure, which are 1.51, 0.68, and 1.13 eV, respectively. In **Figure 7.3d**, the energy level diagram of the catalysts gives the calculated maximum conduction band energies of -0.88, -1.07, and -1.12 eV for CdS QDs(bio), CuO QDs(bio), and 0.50CuO/CdS QDs(bio) heterostructure, respectively. This indicates that the 0.50CuO/CdS QDs(bio) heterostructure possesses favourable maximum CB energies, suggesting an enhanced rate of EtOH and CO production [34]. The work function (φ) is calculated using the equation $\varphi = hv - E_{cutoff}$ [9], where hv is the energy of the monochromatic ionizing light (21.22 eV), and $E_{cut\text{-}off}$ denotes the threshold energy for the secondary electron

obtained from the linear extrapolation of the UPS VB spectrum. The Fermi level (E_F) is determined by the relation $E_F = -\varphi$ [9]. The UPS VB spectra for secondary electrons are presented in **Figure 7.4**. The measured secondary electron cut-off energies for CdS QDs(bio), CuO QDs(bio), and 0.50CuO/CdS QDs(bio) heterostructure are 17.01, 16.52, and 16.62 eV, respectively, with corresponding work function values of 4.21, 4.7, and 4.6 eV. The E_F of CdS QDs(bio), CuO QDs(bio), and 0.50CuO/CdS QDs(bio) heterostructure are calculated as -4.21, -4.7, and -4.6 eV, respectively match with reported literature [39,40].

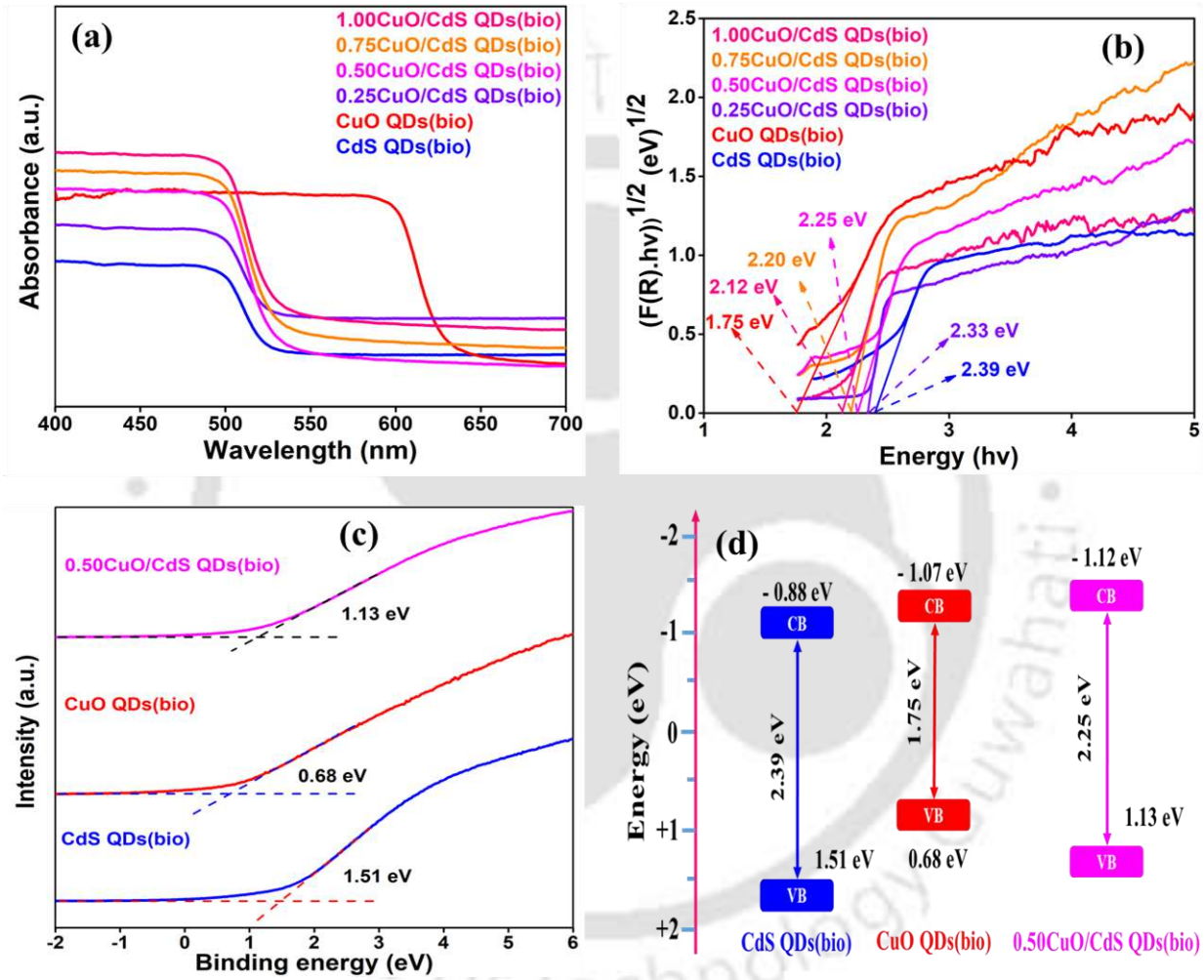

Figure 7.3. (a) Absorption spectra, (b) Bandgap calculation, (c) UPS VB spectra, and (d) Energy band diagram of CdS QDs(bio), CuO QDs(bio), and CuO/CdS QDs(bio) heterostructures.

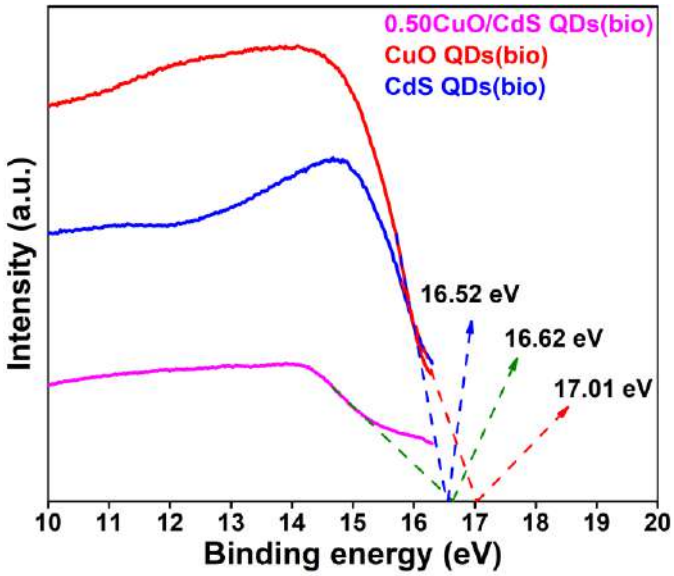

Figure 7.4. UPS VB spectra for secondary electron onset.

Synthesis and morphology: The surface of CdS QDs(bio) exhibits a positive charge, as confirmed by the zeta potential value at pH 7.5 (**Table 7.1**), enabling the electrostatic adsorption of negatively charged Cu^{2+} ions. These ions then react with an oxygen source to form CuO QDs on the surface of CdS QDs, forming CuO/CdS QDs(bio) heterostructure. Subsequently, microwave irradiation is applied to enhance the interaction between the CuO QDs (bio) and CdS QDs(bio).

Table 7.1. Hydrodynamic diameter and zeta potential of CdS QDs(bio), CuO QDs(bio), and CuO/CdS QDs(bio) heterostructures.

Catalysts	Hydrodynamic diameter (nm)	Zeta potential (mV)
CdS QDs(bio)	212.2	15.9
CuO QDs(bio)	265.7	-19.9
0.25CuO/CdS QDs(bio)	217.1	-15.3
0.50CuO/CdS QDs(bio)	248.7	-21.5
0.75CuO/CdS QDs(bio)	288.5	-26.56
1.00CuO/CdS QDs(bio)	318.6	-29.4

The FETEM images of the synthesized catalyst are presented in **Figures 7.5a-7.5c**. The well-defined quantum dot or nanocrystal structures of CdS QDs(bio), CuO QDs(bio), and CuO/CdS QDs(bio) heterostructure are clearly visible, with average particle sizes of 4.85 nm, 5.14 nm, and 7.2 nm, respectively. All particles are under 10 nm, classifying them as quantum

dots [41]. The HRTEM analysis (**Figure 7.5d**) of the 0.5CuO/CdS QDs(bio) heterostructure reveals the distinct (111) planes of CdS (cubic) and CuO (monoclinic) with d-spacing's of lattice fringes of 0.33 nm and 0.23 nm, respectively, confirming the coexistence of both CdS and CuO phases in the heterostructure. Additionally, the SAED pattern (**Figure 7.5e**) of heterostructure exhibited a polycrystalline nature with rings corresponding to the (111), (220), and (311) crystalline planes of CdS QDs(bio) and (002) and ($\bar{2}$02) of CuO QDs(bio), supporting the formation of CuO/CdS QDs(bio) heterostructure. Furthermore, the distribution of elements of CuO/CdS QDs(bio) heterostructure was confirmed by EDX elemental mapping (**Figure 7.5f**). The elements of Cu, Cd, O, and S are uniformly distributed in the CuO/CdS QDs(bio) heterostructure, indicating the successful anchoring of CuO onto CdS and the formation of a p-n junction.

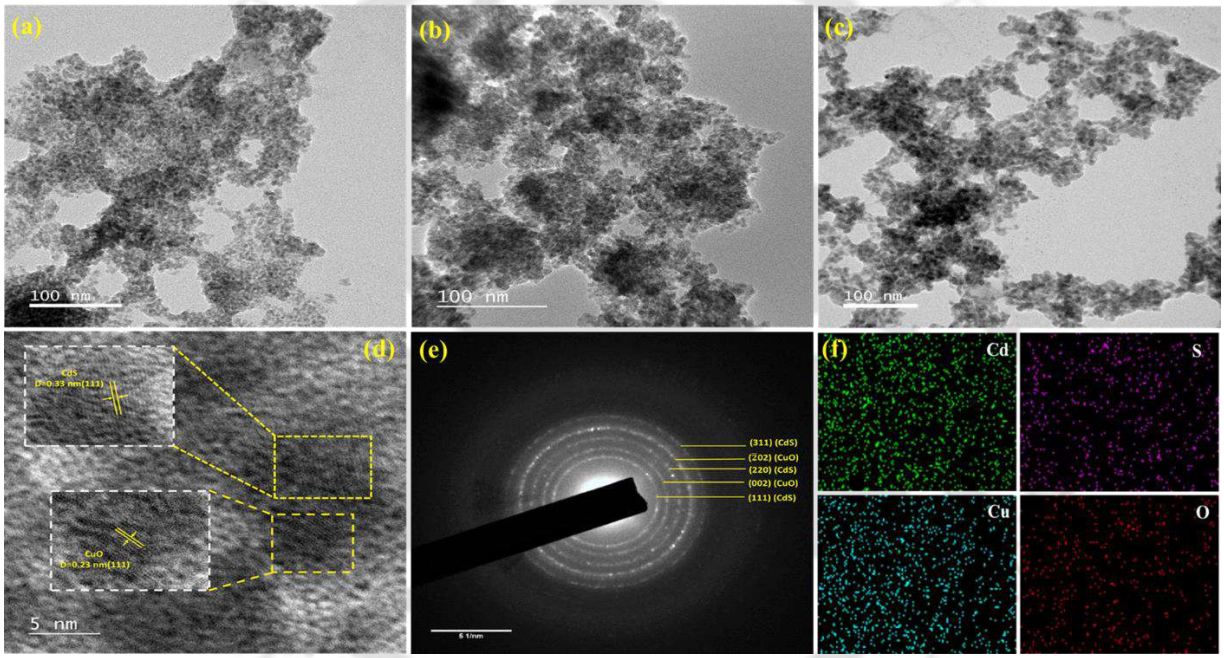

Figure 7.5. TEM images of (a) CdS QDs(bio), (b) CuO QDs(bio), (c) 0.50CuO/CdS QDs(bio) heterostructure, (d) HRTEM image, (e) SAED pattern, and (f) Elemental mapping with 10 μm scale of 0.50CuO/CdS QDs(bio) heterostructure.

Charge trapping and recombination: To examine the separation and transfer behavior of photoinduced e^-/h^+ pairs in the photocatalysts, PL spectra were recorded for CdS QDs(bio) and 0.50CuO/CdS(bio) heterostructure at the excitation wavelength of 360 nm and CuO QDs(bio) at 300 nm (**Figure 7.6a**). The CdS QDs(bio), CuO QDs(bio), and 0.50CuO/CdS QDs(bio) heterostructure each exhibited a prominent emission peak at 460 nm. The PL intensity of heterostructure was lower than that of CdS QDs(bio) and CuO QDs(bio), indicating

a lower charge carrier recombination. This suggests that the formation of the heterostructure enhances the separation of e^-/h^+ pairs.

TRPL spectra (**Figure 7.6b**) of synthesized catalyst were recorded with excitation and emission wavelengths of 405 and 450 nm, with 5000 counts to examine charge transfer behavior. The TRPL decay curves were analysed by fitting them with a bi-exponential decay function. The average lifetimes of charge carriers of CdS QDs(bio), CuO QDs(bio), and 0.50CuO/CdS QDs(bio) heterostructure were found to be 1.82, 2.05, and 3.16 ns, respectively. The heterostructure exhibits a longer lifetime of charge carriers than the CdS QDs(bio) and CuO QDs(bio), indicating that 0.50CuO/CdS QDs(bio) heterostructure demonstrates better efficiency in separation of e^-/h^+ pairs [42,43].

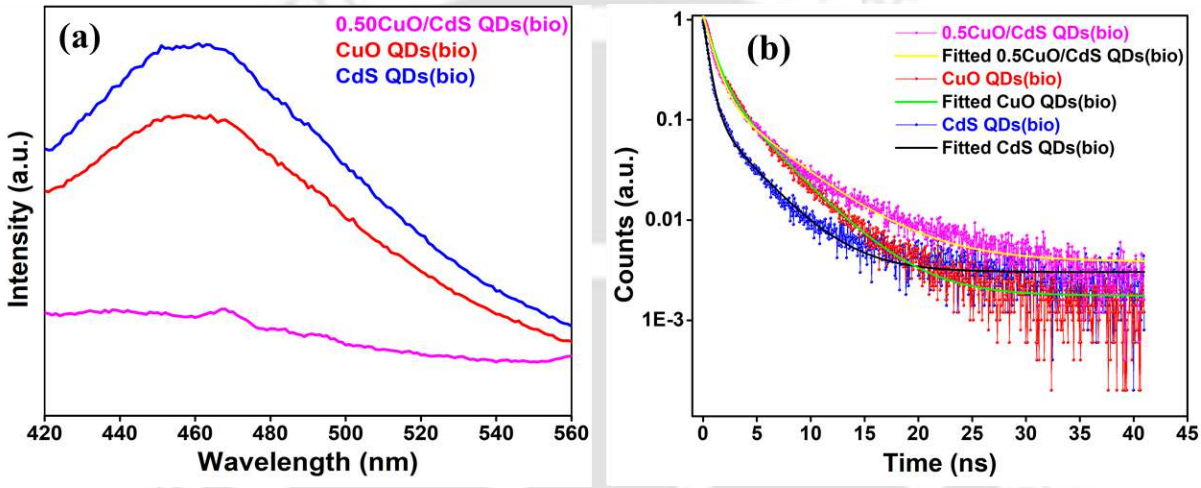

Figure 7.6. (a) PL and (b) TRPL spectra of synthesized catalysts.

Raman analysis: The Raman spectra of the synthesized catalysts are shown in **Figure 7.7**. For CdS QDs, two distinct peaks are observed at 295.8 and 593.5 cm^{-1}, corresponding to the longitudinal optical (1LO) phonon mode and its overtone (2LO), respectively [44]. The first- and second-order LO phonon peaks exhibit a shift to lower frequencies and are asymmetrically broadened towards the lower-frequency side. This phonon softening and peak broadening can be attributed to the phonon confinement effect [28]. The Raman peaks of the 0.50CuO/CdS QDs (bio) heterostructure can be attributed to the surface coverage by CuO [44]. For CuO QDs(bio), phonon modes 113, 147, and 212 cm^{-1} correspond to the scattering from phonons of symmetry Γ^-_{12}, Γ^-_{15}, and $2\Gamma^-_{12}$, respectively. The peak at 613 cm^{-1} is the contribution of the phonon mode Γ^-_{15} [45].

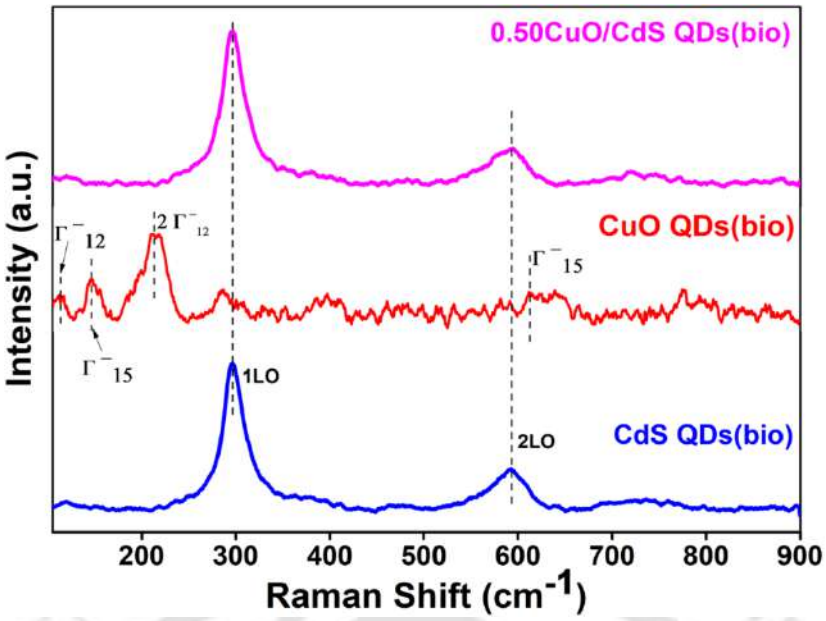

Figure 7.7. Raman spectra of CdS QDs(bio), CuO QDs(bio), and 0.50CuO/CdS QDs(bio) heterostructure.

BET surface area analysis: N_2 sorption analysis was performed to assess the surface area and pore properties of the synthesized catalyst, with the result depicted in **Table 7.2**. N_2 sorption isotherms (**Figure 7.8a**) recorded with CdS QDs(bio), CuO QDs(bio), and CuO/CdS QDs(bio) heterostructure exhibit type IV isotherms with an H1, H3, and H3 hysteresis loop, respectively, indicating its mesoporous characteristics. The surface area and average pore diameter of CdS QDs(bio), CuO QDs(bio), and CuO/CdS QDs(bio) heterostructure were 69.52, 64.73, and 136.65 m^2/g and 6.28, 6.94, and 13.65 nm, respectively. The p-n junction heterostructure has substantial surface area and porous properties, offering numerous catalytically active sites for redox reactions [25,31]. Additionally, the CO_2 adsorption ability of 0.5CuO/CdS QDs(bio) heterostructure (0.643 mmol/g) surpasses that of CdS QDs(bio) (0.102 mmol/g) and CuO QDs(bio) (0.123 mmol/g), as indicated in **Table 7.2.** The TGA analysis is shown in **Figure 7.8b**. The residual carbon content (**Table 7.3**) is determined within the temperature range of 300-500°C [9], and heterostructure was found to contain 7% (w/w) carbon.

Table 7.2. Physical characteristics of synthesized catalysts.

Catalyst	**Bandgap (eV)**	**Crystallite size (nm)**	**BET surface area (m^2/g)**	**Average pore (nm)**	**Pore volume (cm^3/g)**	**CO_2 Adsorption (mmol/g)**
CdS QDs(bio)	2.39	3.5	69.52	6.28	0.11	0.102

CuO QDs(bio)	1.75	5.2	64.73	6.94	0.106	0.123
0.50CuO/CdS QDs(bio) heterostructure	2.25	4.40	136.65	13.65	0.32	0.643

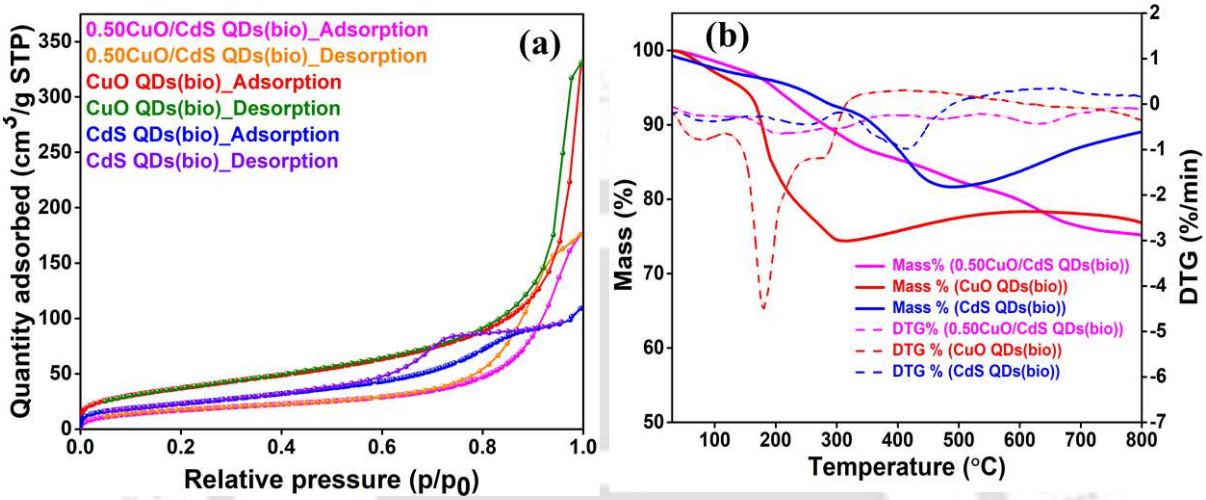

Figure 7.8. (a) N_2 sorption isotherms, and TGA & DTG analysis of CdS QDs(bio), CuO QDs(bio), and 0.50CuO/CdS QDs(bio) heterostructure.

Table 7.3. Residual carbon content calculation in catalysts from TGA plot.

Catalysts	Temperature range of carbon % calculation (°C)	Carbon (%)
CdS QDs(bio)	300 to 500	11
CuO QDs(bio)	300 to 500	0
0.50CuO/CdS QDs(bio)	300 to 500	7

7.2.2 Photo-electrochemical response

The electrochemical characteristics of the synthesized catalyst were investigated through photocurrent measurements and EIS studies. In chronoamperometry (**Figure 7.9a**), the average photocurrent density of 0.50CuO/CdS QDs(bio) heterostructure reached 0.94 μA/cm^2, approximately nine and eight-fold higher than that of CdS QDs(bio), and CuO QDs(bio), respectively. This suggests the effective separation of photogenerated e^-/h^+ pairs due to p-n heterojunction formation between CuO QDs(bio) and CdS QDs(bio) [25].

In the EIS spectra (**Figure 7.9b**) under visible light, a reduced arc radius was observed for 0.50CuO/CdS QDs(bio) heterostructure, implying enhanced charge separation and transfer

efficacy. The EIS-fitted parameters are listed in **Table 7.4**, and the equivalent circuit is depicted in **Figure 7.10**. Charge transfer resistance (Rp) values for CdS QDs (bio), CuO QDs(bio), and 0.50CuO/CdS QDs(bio) under light conditions were 13.2, 10.48, and 9.26 MΩ, respectively, and under dark conditions, they were 14.8, 2.34, and 10.12 MΩ, respectively. The smaller arc radius and lower resistance are because of enhanced conductivity, faster charge carrier migration, and decreased charge recombination rate [46,47]. This finding indicates enhanced charge carrier separation and transfer in the CuO/CdS QDs(bio) heterostructures, which aligned well with photocurrent and PL analysis results.

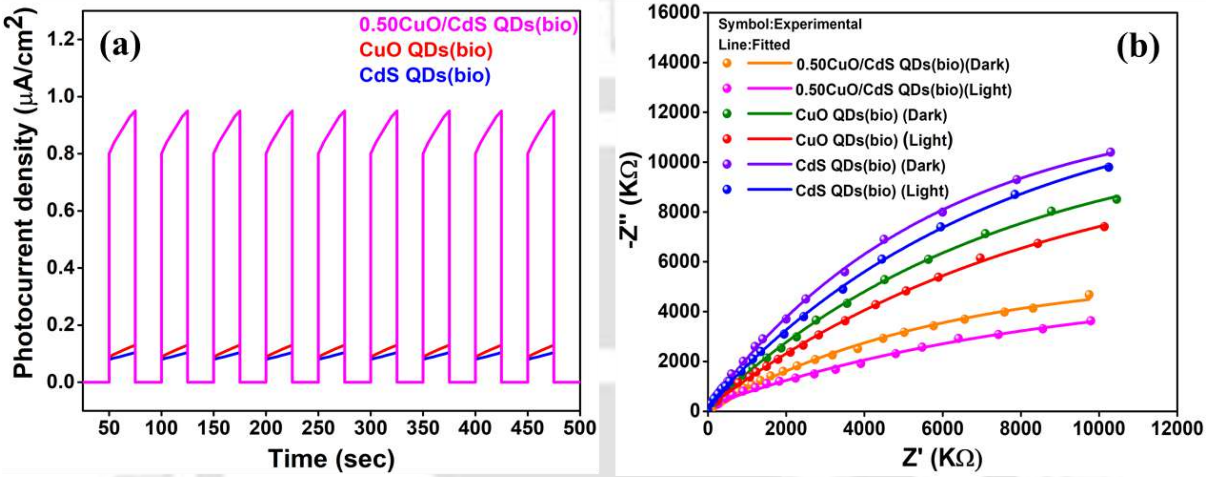

Figure 7.9. (a) Chronamperometry study and (b) Nyquist plots (EIS) under light and dark conditions.

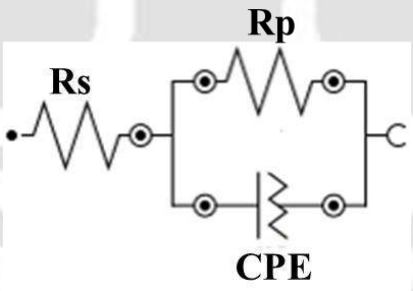

Figure 7.10. Equivalent circuit used for fitting of EIS data (Rs: Electrolytes resistance; Rp: Polarization resistance; CPE: Constant phase element).

Table 7.4. Parameters of equivalent circuit used for fitting of EIS data.

Catalyst	**Rs (KΩ)**	**Rp (MΩ)**	**CPE**
CdS QDs(bio) (Dark)	6.23	14.8	Y_0=188nMho×S^N N=0.566
CdS QDs(bio) (Light)	4.83	13.2	Y_0=221nMho×S^N N=0.574
CuO QDs(bio) (Dark)	5.64	12.34	Y_0=232nMho×S^N

			N=0.552
CuO QDs(bio) (Light)	4.12	10.48	Y_0=248nMho×S^N N=0.549
0.50CuO/CdS QDs(bio) (Dark)	5.36	10.12	Y_0=264nMho×S^N N=0.542
0.50CuO/CdS QDs(bio) (Light)	3.10	9.26	Y_0=276nMho×S^N N=0.52.6

7.2.3 DFT calculations

DFT calculations were performed to elucidate the band structure and DOS of synthesized catalysts. The optimized models of CdS QDs (111) surface, CuO QDs (111) surface, and CuO/CdS QDs heterostructure are depicted in **Figures 7.11a-7.116c**, with lattice parameters detailed in **Table 7.5**. Applying GGA+U in DFT with Hubbard parameters Ud=4.4 and Up=4.1 for CdS QDs, while Ud=7 for CuO QDs, the band structure (**Figures 7.12a-7.12c**) reveals bandgaps of 2.38, 1.75, and 2.22 eV for CdS QDs, CuO QDs, and CuO/CdS QDs heterostructure, respectively, closely aligned with experimental values of 2.39, 1.75, and 2.25 eV, respectively. Notably, the band structure of 0.50CuO/CdS QDs heterostructure displays overlapping electronic bands near the E_F due to the introduction of CuO, introducing additional electronic states within the CdS bandgap and effectively reducing its bandgap [40], as observed in UV-DRS analysis. The DOS for CdS QDs, CuO QDs, and CuO/CdS QDs is depicted in **Figures 7.12d-7.12f**, with the CuO/CdS QDs heterostructure DOS in the CB moved closer to the E_F compared to CdS QDs, indicating a higher density of electronic states near the E_F [48]. A similar observation was observed in the Bi_2S_3/Ti_3C_2Tx MXene composite and In_2O_3/CdS heterostructure [9,49]. This characteristic facilitates faster electron transport in CuO/CdS QDs heterostructure compared to CdS QDs, suggesting superior photocatalytic performance.

Table 7.5. Optimized crystal structure parameters of CdS(bio), CuO QDs(bio), and CuO/CdS QDs (bio) heterostructures considered for DFT calculation.

Catalyst	a (Å)	b (Å)	c (Å)
CdS QDs(bio)	7.20	4.16	0.19
CuO QDs(bio)	6.01	2.93	7.69
CuO/CdS QDs(bio)	15.1	8.7	30

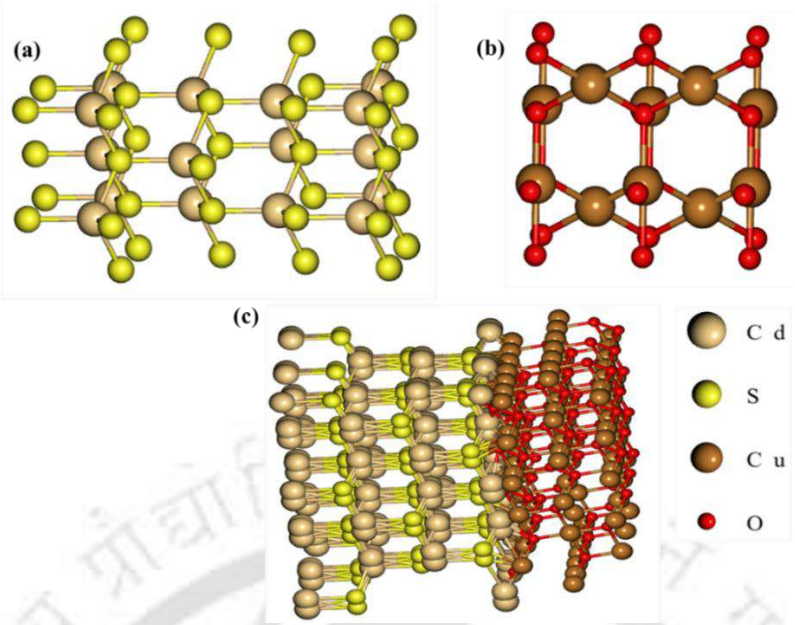

Figure 7.11. DFT model optimization of (a) CdS QDs (111) surface, (b) CuO QDs (111) surface, and (c) CuO /CdS QDs heterostructure.

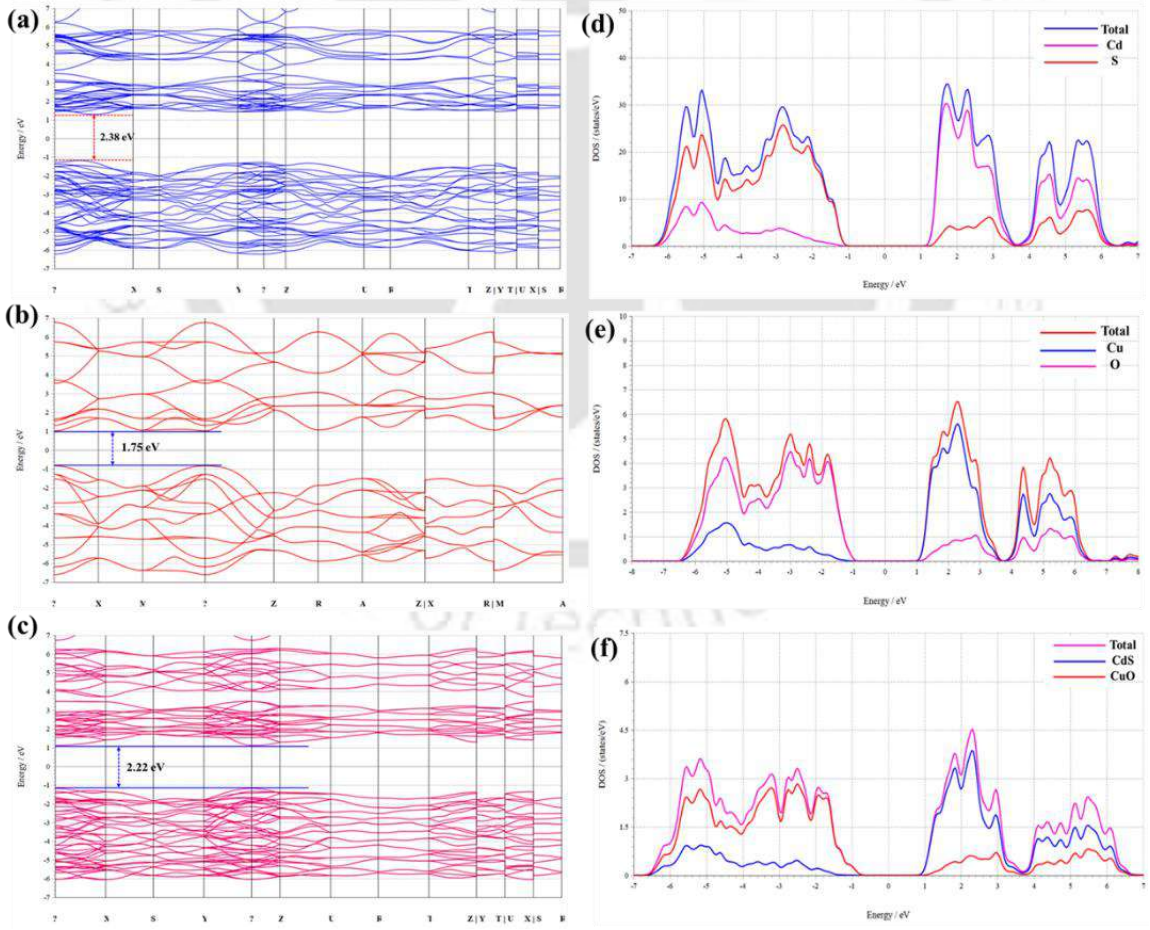

Figure 7.12. DFT calculation of (a-c) Band structure and (d-f) Density of state of CdS QDs, CuO QDs, and CuO/CdS QDs heterostructure.

7.2.4 Photocatalytic CO_2 reduction evaluation

The synthesized catalysts were tested for photocatalytic CO_2 reduction under visible light illumination. In this study, only EtOH and CO were formed. The calibration graphs of EtOH and CO standard are shown in **Figure 7.13,** and chromatograms of both standard and resulting product are shown in **Figure 7.14**. No ethanol or CO was observed in the absence of a catalyst or light illumination. To identify the carbon source involved in EtOH and CO formation, three control experiments were conducted under optimal conditions, each with one component absent: (i) CO_2, (ii) lamp, and (iii) catalyst. Notably, no EtOH and CO were generated in any of these control tests (**Figure 7.15**), indicating that EtOH and CO originate from the CO_2 feedstock in the system. To verify the photocatalytic CO_2 reduction activity and exclude the possibility of organic contaminants photo-degradation, a control experiment using N_2 instead of CO_2 showed no detectable CO_2 reduction products (**Figure 7.16**), confirming the exclusive origin from photocatalytic CO_2 reduction.

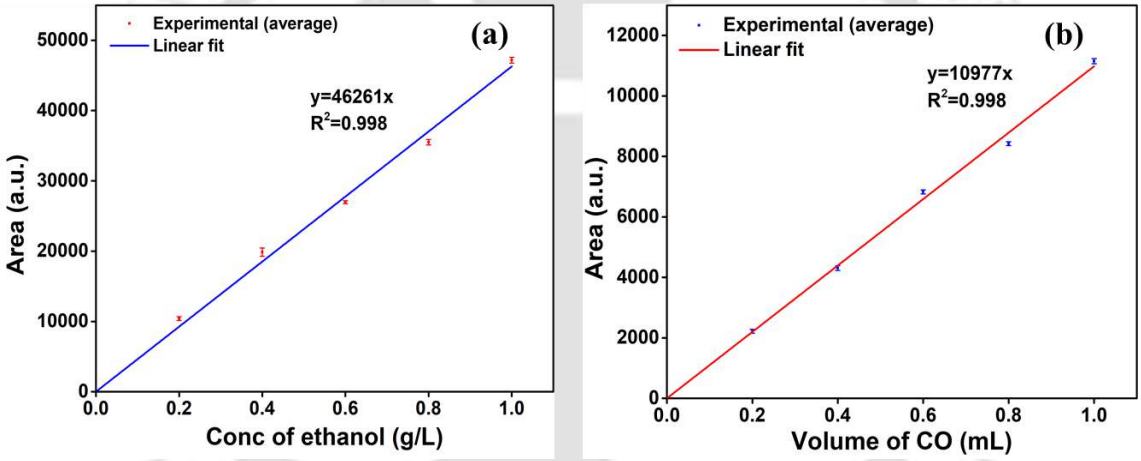

Figure 7.13. Calibration curve of (a) Ethanol and (b) Carbon monoxide.

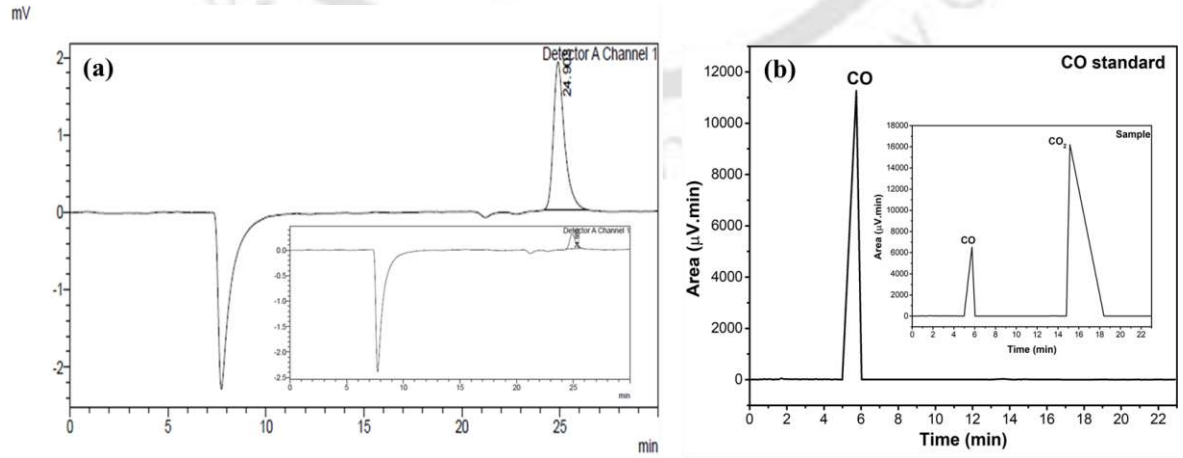

Figure 7.14. (a) HPLC chromatograms of standard 1 g/L EtOH and (inset) solution after 5 h of CO_2 reduction, and (b) GC chromatograms of standard 1 mL CO and (inset) solution after 5 h of CO_2 reduction.

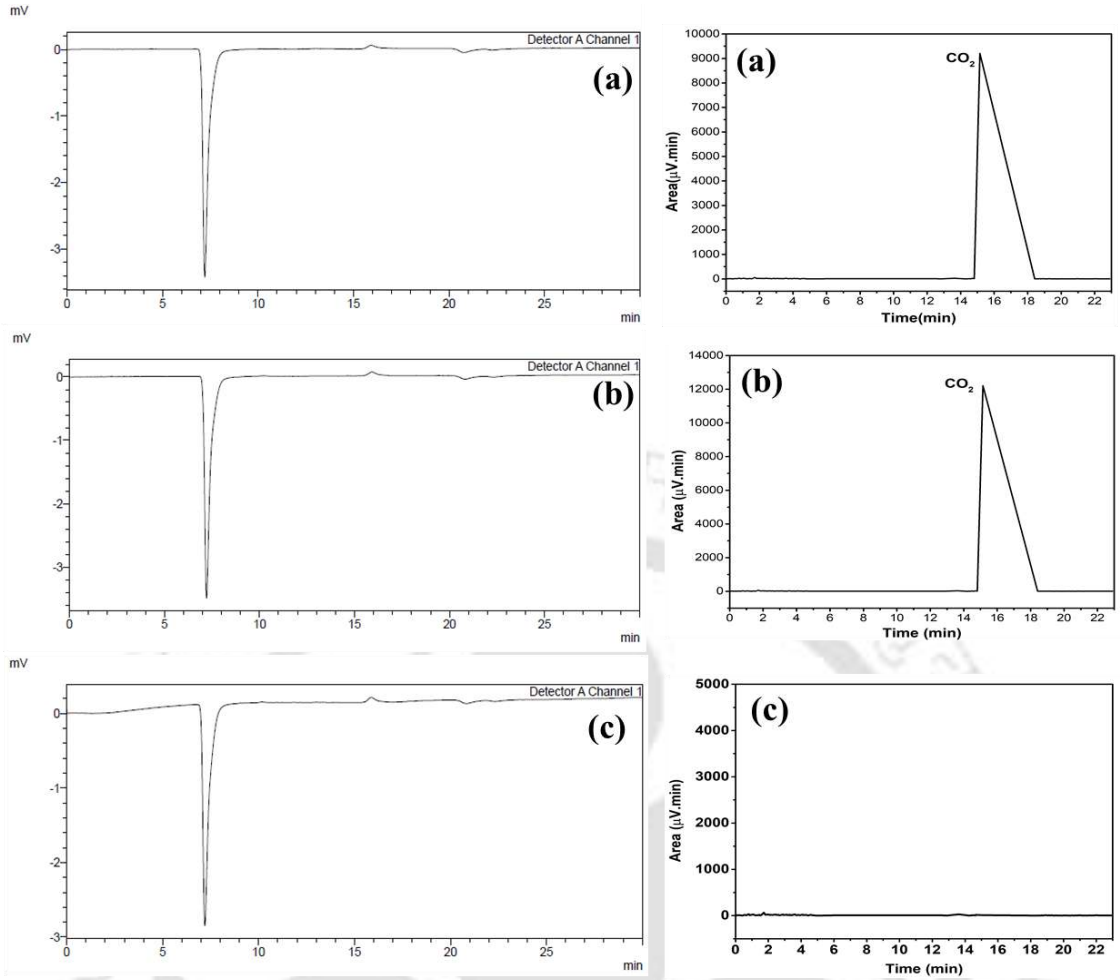

Figure 7.15. HPLC (left side) and GC (right side) chromatograms of 300 s of CO_2 reduction (a) 0.50CuO/CdS QDs(bio) heterostructure + DI water + CO_2 purge, (b) CO_2 purge + DI water + light irradiation, and (c) 0.50CuO/CdS QDs(bio) + DI water + light irradiation.

Figure 7.17a shows the rate of EtOH and CO formation using CdS QDs(bio), CuO QDs(bio), and CuO/CdS QDs(bio) heterostructure at varying loading percentages (0.25, 0.50, 0.75, 0.8, and 1.00 molar ratio). CdS QDs(bio) and CuO QDs(bio) didn't produce any product due to the rapid e^-/h^+ pairs recombination and photocorrosion of CdS, as evidenced by PL and XPS and PL studies (**Figure 7.6a** and **Figure 7.19c**), inferring its inefficiency as a catalyst for photocatalytic CO_2 reduction to EtOH and CO[9,27]. EtOH and CO formation was observed in CuO/CdS QDs(bio) heterostructure, showing an increasing trend with increasing CuO loading percentage, peaking at 0.50 molar CuO loading, yielding 144.99 and 168.98 µmol/g·h, respectively. However, further increases in CuO loading significantly decreased the EtOH and CO formation rate. This reduction is caused by particle aggregation and blockage of active sites on CdS QDs(bio), which hinder light absorption [34]. Dynamic light scattering (DLS) analysis (**Table 7.1**) indicated that particle size increased from 248.7 to 318.6 nm when CuO(bio)

loading exceeded 0.50, resulting in particle agglomeration. Thus, optimal CuO loading for the CuO/CdS QDs(bio) heterostructure catalyst was determined to be 0.50.

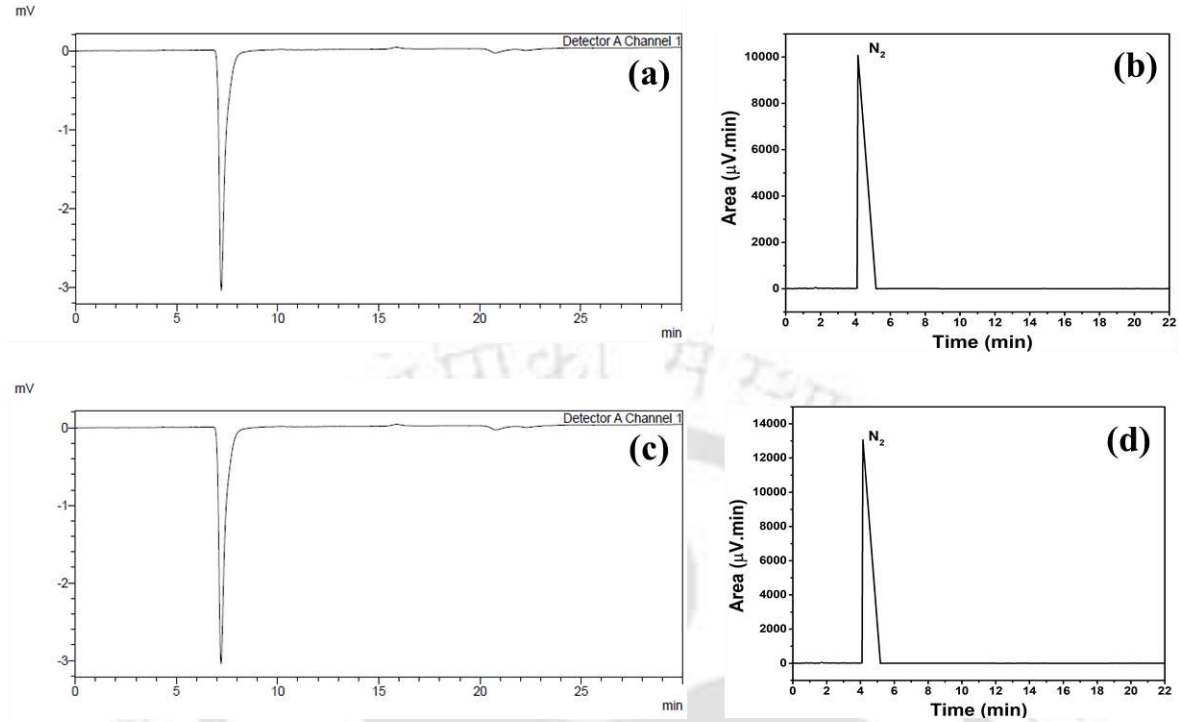

Figure 7.16. (a) HPLC, (b) GC chromatograms after 5 h of the control experiments, (c) HPLC, and (d) GC chromatograms after 10 h of the control experiments using N_2 instead of CO_2.

Figure 7.17b illustrates the EtOH and CO formation rate using different concentrations of 0.50CuO/CdS QDs(bio) heterostructure (0.25, 0.40, 0.75, 1.0, 1.25 g/L). The highest EtOH and CO production rate was attained at a 0.75 g/L photocatalyst concentration, yielding 158.48 and 182.68 µmol/g·h, respectively, with apparent quantum yield (AQY) of 8.24 and 1.58 % (AQY calculation provided in **Table A5**). However, increased photocatalyst concentrations resulted in turbidity in the solution, impeding efficient light irradiation [9]. Turbidity assessments for various photocatalyst concentrations are outlined in **Table 7.6**, indicating a 21.1% increase in turbidity beyond 0.75 g/L. A comparison of the achieved EtOH and CO formation rate in this study with reported literature values (**Table 7.7**), the bio-based CuO/CdS QDs(bio) heterostructure demonstrated a clear superiority.

Figure 7.17c illustrates the evaluation of the functional stability of the 0.50CuO/CdS QDs(bio) heterostructure through repeated cycles of time-dependent photocatalytic CO_2 reduction to EtOH and CO production. Over five consecutive cycles, the heterostructures demonstrated consistent photocatalytic activity with only a marginal 3.5% decline in their performance. This minor decrease is attributed to the unavoidable loss of catalysts during the

recovery process. This exceptional stability suggests that integrating CuO QDs(bio) onto CdS QDs(bio) helps mitigate photocorrosion and inhibits the e^-/h^+ pairs recombination, leading to the improved overall stability of the heterostructure [9,26].

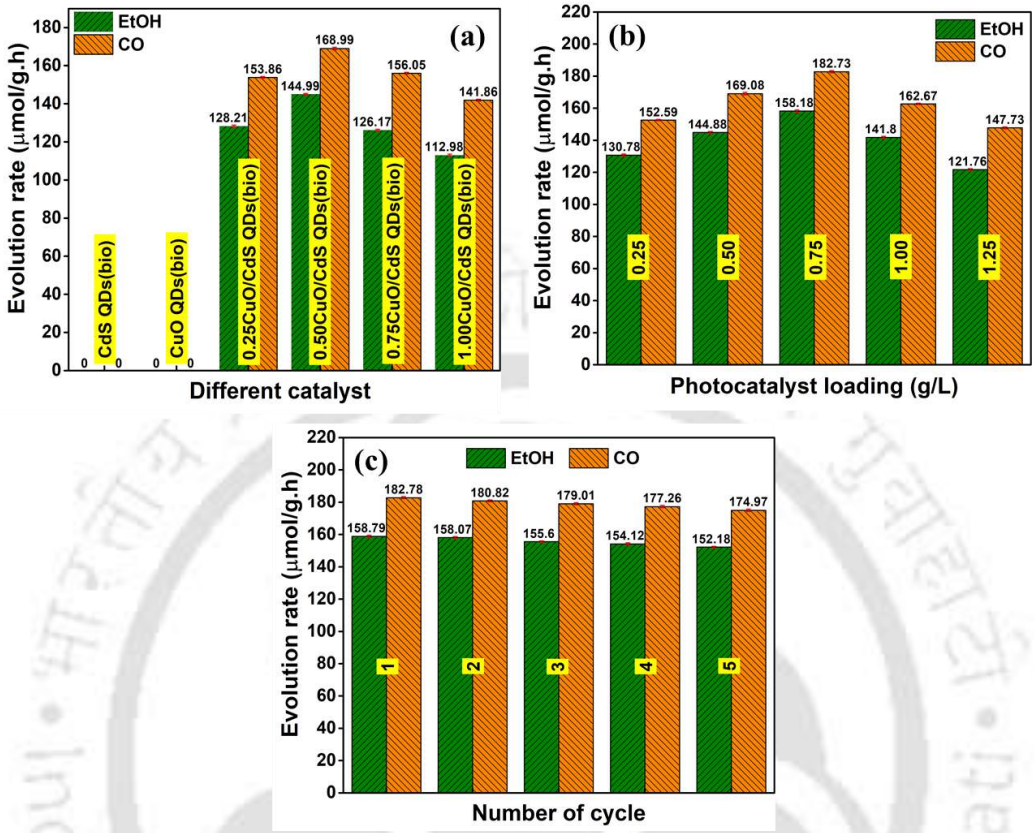

Figure 7.17. (a) Photocatalytic CO_2 reduction using various bio-based catalysts, (b) Effect of photocatalyst loading, and (c) Functional stability study of 0.50CuO/CdS QDs(bio) heterostructure.

Table 7.6. Turbidity of 0.50CuO/CdS QDs(bio) heterostructure.

Catalyst concentration (g/L)	Turbidity (NTU)
0.25	158
0.50	187
0.75	218
1.0	264
1.25	318

Table 7.7. Comparison of the ethanol and carbon monoxide rates with the earlier report.

Photocatalyst	Synthesis method	Reaction solvent	Light source	Products (µmol/g·h)		Source
				EtOH	CO	
CuO/CdS QDs(bio) heterostructure	Microwave irradiation	H_2O	250 W, metal halide lamp (λ>420 nm)	158.48	182.68	**Present work**
CdS-Cu^{2+}/TiO_2	SILAR	-	300 W Xenon lamp	109.12	-	[50]
CdS/Mn_2O_3	Electrochemical deposition	-	Sunlight	52.2	-	[51]
CdS/Ni_9S_8/Al_2O_3		H_2O/TEOA	300 W Xe lamp (λ > 420 nm)	-	121	[52]
CdS/ethylenediamine	Solvothermal route	MeCN/H_2O/ TEOA	300 W Xe lamp (λ > 420 nm)	-	115.6	[53]
CdS/FeTCPP	Hydrothermal	MeCN/H_2O/ TEOA	300 W Xe lamp, λ = 420-780 nm	-	7.46	[54]
CdS/ZnO	Solvothermal method	H_2O	500 W Hg lamp (λ > 400 nm)	-	35.2	[11]
CdS/NH_2-UiO-66/Chitosan	Solvent evaporation technique	MeCN/ H_2O/ TEOA	300 W Xe lamp, λ = 400-760 nm	-	86.98	[55]
CdS/TiO_2	Photodeposition	H_2O (vapor)	300 W Xe arc lamp (λ = 300-800 nm)	-	3.62	[56]
CdS/$CdWO_4$	Chemical deposition	H_2O/TEOA	300 W xenon lamp (λ > 420nm)	-	1.39	[57]
CdS/MIL-101	Double solvent method	H_2O (vapor)	300 W Xe lamp (λ > 420 nm)	-	16.35	[58]
CUGAS_2/CdS	Ultrasonic dispersion	H_2O/K_2SO_3/KHCO_3	300 W Xe lamp	-	0.75	[59]

SILAR: Successive ionic layer adsorption and reaction; TEOA: Triethanolamine; MeCN: Acetonitrile; FeTCPP: tetra(4-carboxyphenyl) porphyrin iron (III) chloride

7.2.5 Stability of CuO/CdS QDs(bio) heterostructure

Figure 7.18 presents the XPS spectra of 0.50CuO/CdS QDs(bio) heterostructure before and after photocatalytic CO_2 reduction. The survey spectra (**Figure 7.18a**) confirm the presence of Cu, Cd, O, and S in the heterostructure. The high-resolution (HR) spectra of 0.50CuO/CdS QDs (**Figures 7.18b-7.18e**) show consistent peak intensities before and after photocatalytic CO_2 reduction, indicating structural stability. The survey and HR spectra of individual CdS QDs(bio) and CuO QDs(bio) before and after photocatalytic CO_2 reduction are presented in **Figure 7.19**. The HR spectra of CuO QDs(bio) exhibit consistent peak intensities before and after the reaction. In the case of CdS QDs(bio)/used (**Figure 7.19c**), the S 2p peak binding energy shows an additional peak at 168.6 eV (S^{6+}), indicating sulfur oxidation (photocorrosion) and the formation of SO_4^{2-} [9,60]. The heterostructure could successfully mitigate the photocorrosion issue of CdS QDs(bio). The PL intensity of 0.50CuO/CdS QDs(bio)/used heterostructure was lowered by 58 and 48% for CdS QDs(bio)/used and CuO QDs(bio)/used, respectively (**Figure 7.20**), indicating a lower charge carrier recombination.

XRD and FETEM analyses were performed on CuO/CdS QDs(bio) heterostructure before and after photocatalytic CO_2 reduction to assess their structural and morphological properties. The XRD spectra of 0.50CuO/CdS QDs(bio) and 0.50CuO/CdS QDs(bio/used) (**Figure 7.21a**) show no significant changes in the lattice structure after the reaction. The crystallite size remained nearly unchanged, measured at 4.38 nm for 0.50CuO/CdS QDs(bio/used) compared to 4.40 nm for 0.50CuO/CdS QDs(bio). Similarly, the FETEM image of 0.50CuO/CdS(bio/used) (**Figure 7.21b**) reveals no noticeable morphological differences when compared to the initial CuO/CdS QDs(bio) (**Figure 7.5c**).

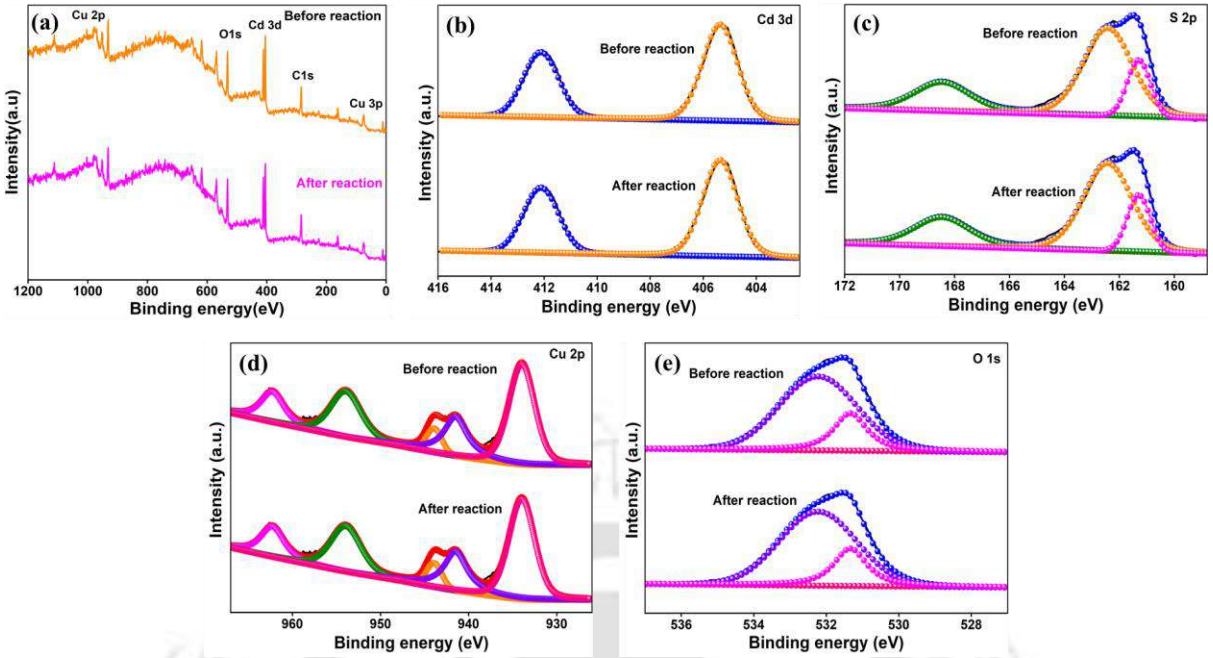

Figure 7.18. (a) XPS survey spectra, (b) Cd 3d, (c) S 2p, (d) Cu 2p, (e) O 1s of 0.50CuO/CdS QDs(bio) heterostructure before and after photocatalytic CO_2 reduction.

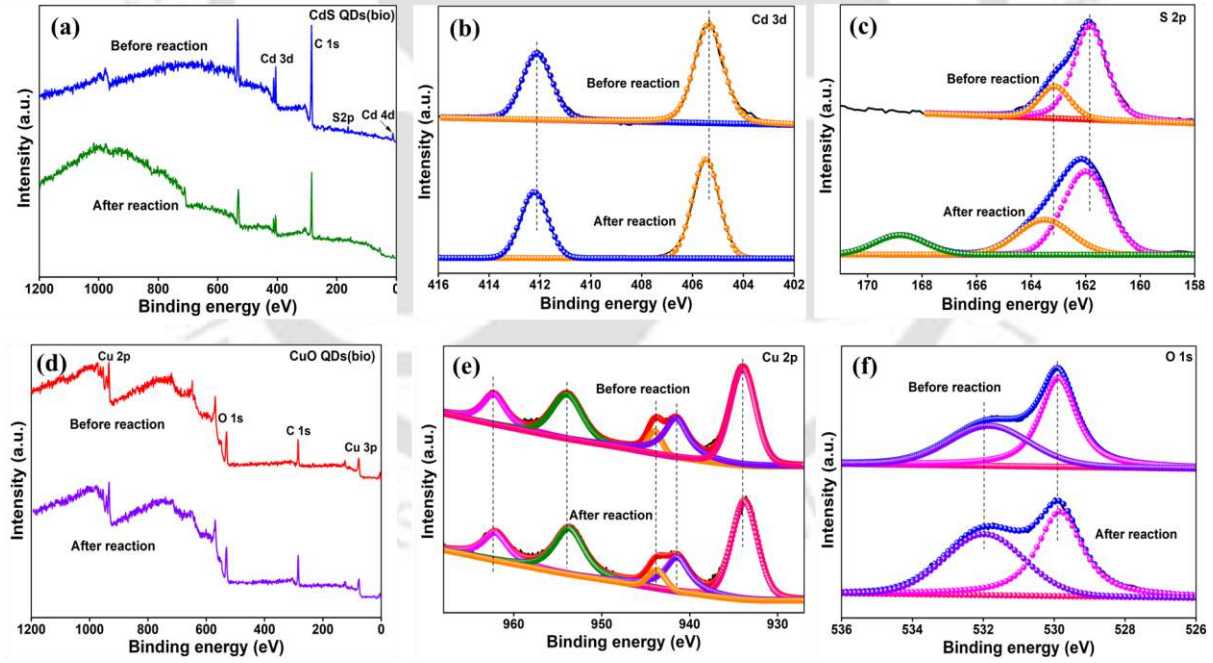

Figure 7.19. (a) XPS survey spectra, (b) Cd 3d and (c) S 2p of CdS QDs(bio), (d) survey spectra, (e) Cu 2p, and O 1s of CuO QDs(bio).

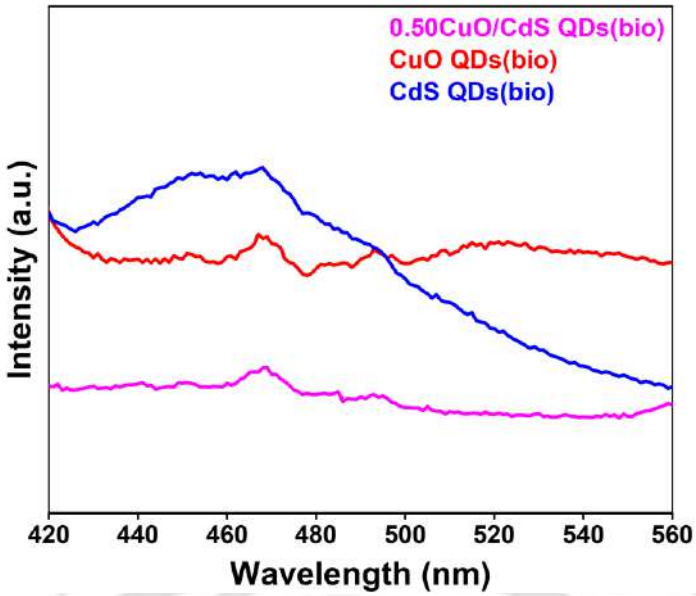

Figure 7.20. PL spectra of CdS QDs(bio)/used, CuO QDs(bio)/used, and 0.50CuO/CdS QDs(bio)/used heterostructure.

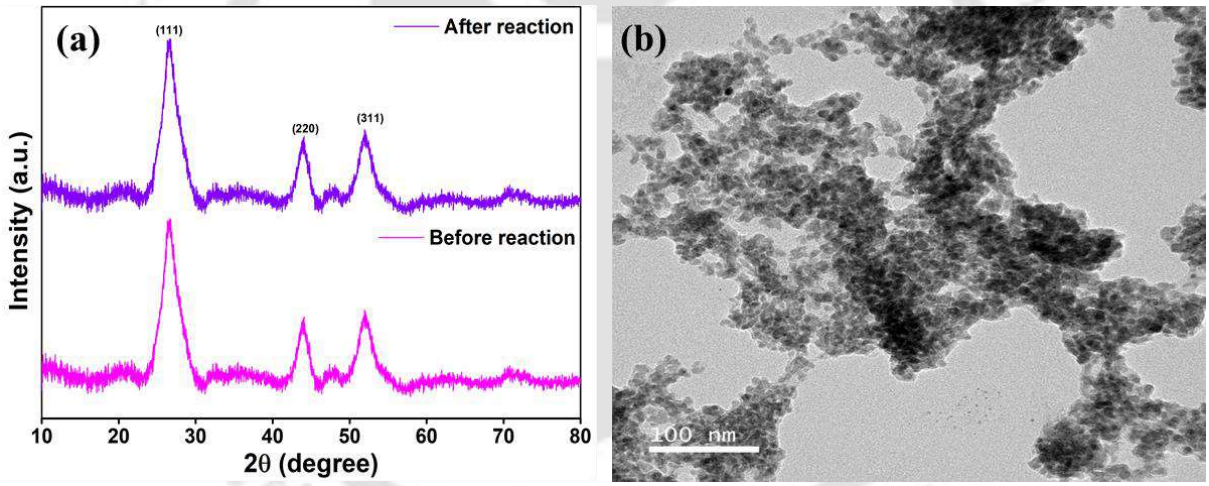

Figure 7.21. (a) XRD patterns of 0.50CuO/CdS QDs(bio) heterostructure before and after photocatalytic CO_2 reduction, and (b) FETEM of 0.50CuO/CdS QDs(bio)/used.

7.2.6 Mechanism of photocatalytic CO_2 reduction catalyzed by CuO/CdS QDs(bio) heterostructure

The UPS VB spectra and band positions of the catalyst indicate that CuO QDs(bio) have a higher φ and a lower E_F, while CdS QDs(bio) possess a smaller φ and a higher E_F. When CuO QDs(bio) come into interfacial contact with CdS QDs(bio), e^- spontaneously flow from CdS QDs(bio) to CuO QDs(bio) until their Fermi levels equilibrate. As a result, CdS QDs(bio) undergo downward band bending and accumulate positive charges at the interface, whereas

CuO QDs(bio) experience upward band bending and develop negative charges at the interface, thereby generating an internal electric field (IEF) [61–63]. Under light illumination, the catalysts generate photogenerated e^-/h^+ pairs (Eq. 7.1). Under the influence of IEF and Coulomb effect, e^- in the CB of CuO QDs can transfer to CdS QDs, while h^+ in the VB of CdS QDs migrate to the VB of CuO QDs (**Figure 7.22**). Simultaneously, the h^+ in the VB of CuO QDs oxidize H_2O to produce a proton (H^+) and hydroxyl radical ($^{\cdot}OH$) (Eq. 7.2), and the e^- in the CB of CdS QDs reduce CO_2 to produce EtOH and CO. The details of the reaction mechanism are illustrated in **scheme I** for CO formation and **scheme II** for EtOH formation. Thus, a full redox cycle of the photocatalytic system is completed.

$$CuO/CdS\ QDs(bio) + hv \rightarrow h^+ + e^- \quad (7.1)$$

$$H_2O + h^+ \rightarrow H^+ + {}^{\cdot}OH \quad (7.2)$$

The photocatalytic reduction of CO_2 to CO over CuO/CdS QDs(bio) proceeds through a series of reaction steps, as outlined in Eqs. 3-7 (where * denotes species adsorbed on the surface of the photocatalyst). Firstly, CO_2 molecules are adsorbed onto the CuO/CdS QDs(bio) surface, leading to their activation (Eq. 7.3). The activated CO_2* then undergoes reduction through the addition of a photogenerated e^-/H^+ pair, forming the COOH* intermediate (Eq. 7.4). Further reduction, involving another e^-/H^+ pair, converts COOH* into the adsorbed CO* species (Eq. 7.5). Finally, CO is released from the CuO/CdS QDs(bio) surface as the final product (Eq. 7.6). Overall, the reduction of 1 mole of CO_2 with 2 photogenerated e^- and 2 moles of H^+ results in the formation of 1 mole of CO and 1 mole of H_2O (Eq. 7.7) [64,65].

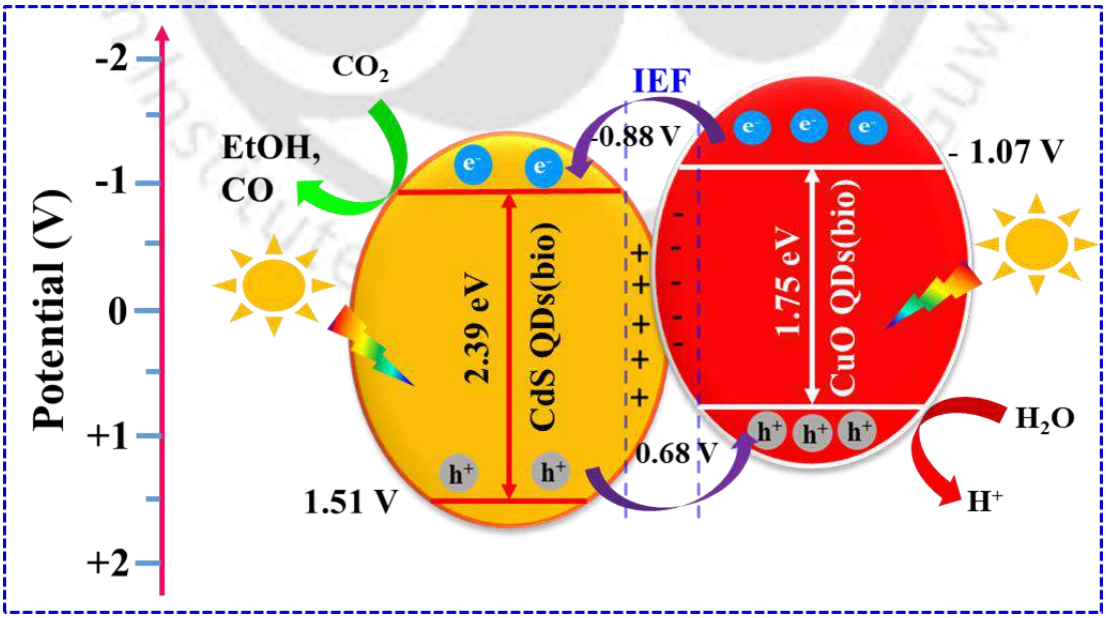

Figure 7.22. Possible reaction mechanism of photocatalytic CO_2 reduction over p-n junction CuO/CdS QDs(bio) heterostructure.

Scheme I:

$$CO_2 + e^- \rightarrow CO_2^* \quad (7.3)$$

$$CO_2^* + e^- + H^+ \rightarrow COOH^* \quad (7.4)$$

$$COOH^* + e^- + H^+ \rightarrow CO^* + H_2O \quad (7.5)$$

$$CO^* \rightarrow CO \quad (7.6)$$

$$CO_2 + 2e^- + 2H^+ \rightarrow CO + H_2O \quad (7.7)$$

The formation of ETOH via photocatalytic CO_2 reduction follows a multistep reaction pathway [66,67]. Initially, $2CO_2$ first reacts with $2e^-$ to generate a 2^*CO_2 intermediate (Eq. 7.8). The $2^*CO_2^-$ species then recombines with $2H^+$ assisted by the e^- to form 2HCOO* intermediate (Eq. 7.9). Further, the 2HCOO* intermediate dissociate into two *CO intermediates (Eq. 7.10), and then one intermediate of *CO is reduced to generate *CHO (Eq. 7.11). The *CHO intermediate is further reduced to the $^*CH_2OH$ intermediate (Eq. 7.12), which then reacts with H^+ and e^- to produce CH_3OH (Eq. 7.13). Then, CH_3OH undergoes reduction in the presence of the remaining *CO intermediate, leading to the formation of the $^*CH_3COH$ intermediate (Eq. 7.14). Finally, $^*CH_3COH$ recombines with $2H^+$ through successive reduction steps (Eqs. 7.15 and 7.16), selectively producing ethanol (C_2H_5OH). Overall, the reduction of 2 moles of CO_2 with 12 photogenerated e^- and 12 moles of H^+ results in the formation of 1 mole of EtOH and 3 moles of H_2O (Eq. 7.17).

Scheme II:

$$2CO_2 + 2e^- \rightarrow 2^*CO_2^- \quad (7.8)$$

$$2^*CO_2^- + e^- + 2H^+ \rightarrow 2HCOO^* \quad (7.9)$$

$$2HCOO^* + 2e^- + 2H^+ \rightarrow 2^*CO + 2H_2O \quad (7.10)$$

$$2^*CO + e^- + H^+ \rightarrow {}^*CHO + {}^*CO \quad (7.11)$$

$$^*CHO + {}^*CO + e^- + 2H^+ \rightarrow {}^*CH_2OH + {}^*CO \quad (7.12)$$

$$^*CH_2OH + {}^*CO + e^- + H^+ \rightarrow CH_3OH + {}^*CO \quad (7.13)$$

$$CH_3OH + {}^*CO + 2e^- + 2H^+ \rightarrow {}^*CH_3COH + H_2O \quad (7.14)$$

$$^*CH_3COH + e^- + H^+ \rightarrow {}^*CH_3CH_2O \quad (7.15)$$

$$^*CH_3CH_2O + e^- + H^+ \rightarrow CH_3CH_2OH \quad (7.16)$$

$$2CO_2 + 12e^- + 12H^+ \rightarrow C_2H_5OH + 3H_2O \quad (7.17)$$

7.3 Major findings

We have successfully synthesized bio-based p-n junction 0D/0D CuO/CdS QDs heterostructure using bio-analytes present in *Aegle marmelos* plant extract via microwave

irradiation. The photocatalytic study of CuO/CdS QDs(bio) heterostructure was evaluated for CO_2R to EtOH and CO under visible light. The DFT calculations yielded bandgap values for CdS QDs, CuO QDs, and the CuO/CdS QDs heterostructure, closely aligned with the experimental determinations. The incorporation of CuO (0.5 molar ratio) reduced the CdS QDs(bio) bandgap from 2.39 eV to 2.25 eV. DOS analysis revealed that CuO QDs could introduce an additional electronic state in the bandgap region of CdS QDs, enhancing charge separation and transport at the local junctions. The decay lifetime of CuO/CdS QDs(bio) heterostructure (3.16 ns) was 1.74 and 1.54 times longer than that of CdS QDs(bio) and CuO QDs(bio), respectively. It exhibited a 6- and 7-fold increase in CO_2 adsorption (0.643 mmol/g) and a photocurrent response 9 and 8 times higher compared to CdS QDs(bio) and CuO QDs(bio), respectively. Notably, CuO/CdS QDs(bio) achieved a remarkable EtOH and CO formation rate of 158.48/182.68 μmol/g·h (AQY 8.24/1.58%) without a sacrificial agent. The heterostructure demonstrated excellent stability, retaining its morphology and crystal structure, and it could effectively prevent photocorrosion and suppress e^-/h^+ pair recombination.

References

[1] Z. Chen, G. Ding, Z. Wang, Y. Xiao, X. Liu, L. Chen, C. Li, H. Huang, G. Liao, Precision Molecular Engineering of Carbon Nitride for Efficient and Selective Photoreduction of CO_2 to C_2H_6 in Pure Water, Adv. Funct. Mater. 2423213 (2025) 1–10. https://doi.org/10.1002/adfm.202423213.

[2] G. Liao, G. Ding, B. Yang, C. Li, Challenges in Photocatalytic Carbon Dioxide Reduction, Precis. Chem. 2 (2024) 49–56. https://doi.org/10.1021/prechem.3c00112.

[3] J. Fu, K. Jiang, X. Qiu, J. Yu, M. Liu, Product selectivity of photocatalytic CO_2 reduction reactions, Mater. Today. 32 (2020) 222–243. https://doi.org/10.1016/j.mattod.2019.06.009.

[4] I. Arora, S. Garg, A. Sapi, P.P. Ingole, A. Chandra, Insights into photocatalytic CO_2 reduction reaction pathway: Catalytic modification for enhanced solar fuel production, J. Ind. Eng. Chem. 137 (2024) 1–28. https://doi.org/10.1016/j.jiec.2024.03.011.

[5] H.-N. Wang, Y.-H. Zou, H.-X. Sun, Y. Chen, S.-L. Li, Y.-Q. Lan, Recent progress and perspectives in heterogeneous photocatalytic CO_2 reduction through a solid–gas mode, Coord. Chem. Rev. 438 (2021) 213906. https://doi.org/10.1016/j.ccr.2021.213906.

[6] U. Ghosh, A. Majumdar, A. Pal, Photocatalytic CO_2 reduction over g-C_3N_4 based heterostructures: Recent progress and prospects, J. Environ. Chem. Eng. 9 (2021)

104631. https://doi.org/10.1016/j.jece.2020.104631.

[7] Y. Wang, Z. Fan, Y. Wan, M. Xu, J. Li, Y. Ling, Y. Xie, K. Yang, X. Li, Facilitating CO_2 activation and photoreduction through Lewis basic sites of hydroxyl-bonded MXene on BiOBr, Appl. Catal. B Environ. 366 (2025) 125017. https://doi.org/10.1016/j.apcatb.2024.125017.

[8] L. Ma, Z. Li, Z. Jiang, X. Wu, S. Chang, S.A.C. Carabineiro, K. Lv, Effect of precursors on the structure and photocatalytic performance of g-C_3N_4 for NO oxidation and CO_2 reduction, Chinese J. Struct. Chem. 43 (2024) 100416. https://doi.org/10.1016/j.cjsc.2024.100416.

[9] P.M. Gawal, A.K. Golder, Plant-Based Phytochemicals for Synthesis of Z-Scheme In_2O_3/CdS Heterostructures: DFT Analysis and Photocatalytic CO_2 Reduction to HCOOH and CO, Langmuir. 40 (2024) 13538–13549. https://doi.org/10.1021/acs.langmuir.4c01015.

[10] Z. Zhao, H. Wang, Q. Yu, S. Roy, X. Yu, Photo-/electrocatalytic approaches to CO_2 conversion on Cu_2O-based catalysts, Appl. Catal. A Gen. 667 (2023) 119445. https://doi.org/10.1016/j.apcata.2023.119445.

[11] L. Zhang, L. Zhang, Y. Chen, Y. Zheng, J. Guo, S. Wan, S. Wang, C.K. Ngaw, J. Lin, Y. Wang, CdS/ZnO: A Multipronged Approach for Efficient Reduction of Carbon Dioxide under Visible Light Irradiation, ACS Sustain. Chem. Eng. 8 (2020) 5270–5277. https://doi.org/10.1021/acssuschemeng.0c00190.

[12] J. Jin, J. Yu, D. Guo, C. Cui, W. Ho, A Hierarchical Z-Scheme CdS-WO_3 Photocatalyst with Enhanced CO_2 Reduction Activity, Small. 11 (2015) 5262–5271. https://doi.org/10.1002/smll.201500926.

[13] G. Ding, C. Li, L. Chen, G. Liao, Porphyrin-based metal-organic frameworks for photo(electro)catalytic CO_2 reduction, Energy Environ. Sci. 17 (2024) 5311–5335. https://doi.org/10.1039/d4ee01748j.

[14] X. Li, K. Li, D. Ding, J. Yan, C. Wang, S.A.C. Carabineiro, Y. Liu, K. Lv, Effect of oxygen vacancies on the photocatalytic activity of flower-like BiOBr microspheres towards NO oxidation and CO_2 reduction, Sep. Purif. Technol. 309 (2023) 123054. https://doi.org/10.1016/j.seppur.2022.123054.

[15] P. Chang, Y. Wang, Y. Wang, Y. Zhu, Current trends on In_2O_3 based heterojunction photocatalytic systems in photocatalytic application, Chem. Eng. J. 450 (2022) 137804. https://doi.org/10.1016/j.cej.2022.137804.

[16] K. Yang, Z. Yang, C. Zhang, Y. Gu, J. Wei, Z. Li, C. Ma, X. Yang, K. Song, Y. Li, Q.

Fang, J. Zhou, Recent advances in CdS-based photocatalysts for CO_2 photocatalytic conversion, Chem. Eng. J. 418 (2021) 129344. https://doi.org/10.1016/j.cej.2021.129344.

[17] H. Shen, T. Peppel, J. Strunk, Z. Sun, Photocatalytic Reduction of CO_2 by Metal-Free-Based Materials: Recent Advances and Future Perspective, Sol. RRL. 4 (2020) 1900546. https://doi.org/10.1002/solr.201900546.

[18] J. Ye, M. Ren, J. Qian, X. Li, Q. Chen, Advances in graphene quantum dots-based photocatalysts for enhanced charge transfer in photocatalytic reactions, Chinese Chem. Lett. (2025) 110857. https://doi.org/10.1016/j.cclet.2025.110857.

[19] C. Li, H. Lu, G. Ding, Q. Li, G. Liao, Recent advances on g-C_3N_4-based Z-scheme photocatalysts for organic pollutant removal, Catal. Sci. Technol. 13 (2023) 2877–2898. https://doi.org/10.1039/d3cy00242j.

[20] C. Li, H. Lu, G. Ding, T. Ma, S. Liu, L. Zhang, G. Liao, Interfacial coordination bonds accelerate charge separation for unprecedented hydrogen evolution over S-scheme heterojunction, Chinese J. Catal. 65 (2024) 174–184. https://doi.org/10.1016/S1872-2067(24)60108-7.

[21] C. Li, B. Cheng, H. Lu, G. Ding, Z. Jiang, G. Liao, Kinetically and Thermodynamically Favorable Ni-Al Layered Double Hydroxide/Ni-Doped $Zn_{0.5}Cd_{0.5}S$ S-Scheme Heterojunction Triggering Photocatalytic H_2 Evolution, Inorg. Chem. 62 (2023) 6843–6850. https://doi.org/10.1021/acs.inorgchem.3c00613.

[22] L. Cheng, Q. Xiang, Y. Liao, H. Zhang, CdS-Based photocatalysts, Energy Environ. Sci. 11 (2018) 1362–1391. https://doi.org/10.1039/c7ee03640j.

[23] M.Y. Qi, Q. Lin, Z.R. Tang, Y.J. Xu, Photoredox coupling of benzyl alcohol oxidation with CO_2 reduction over CdS/TiO_2 heterostructure under visible light irradiation, Appl. Catal. B Environ. 307 (2022) 121158. https://doi.org/10.1016/j.apcatb.2022.121158.

[24] F. Tian, X. Wu, S. Liu, Y. Gu, Z. Lin, H. Zhang, X. Yan, G. Liao, Boosting photocatalytic H_2 evolution through interfacial manipulation on a lotus seedpod shaped Cu_2O/g-C_3N_4 p-n heterojunction, Sustain. Energy Fuels. 7 (2022) 786–796. https://doi.org/10.1039/d2se01634f.

[25] L. Wang, W. Wang, Y. Chen, L. Yao, X. Zhao, H. Shi, M. Cao, Y. Liang, Heterogeneous p-n Junction CdS/Cu_2O Nanorod Arrays: Synthesis and Superior Visible-Light-Driven Photoelectrochemical Performance for Hydrogen Evolution, ACS Appl. Mater. Interfaces. 10 (2018) 11652–11662. https://doi.org/10.1021/acsami.7b19530.

[26] L. Wang, Y. Dong, J. Zhang, F. Tao, J. Xu, Construction of NiO/g-C_3N_4 p-n

heterojunctions for enhanced photocatalytic CO_2 reduction, J. Solid State Chem. 308 (2022) 122878. https://doi.org/10.1016/j.jssc.2022.122878.

[27] C. Yan, M. Xu, J. Li, B. Chang, Q. Chen, W. Cao, W. Xiao, H. Wang, P. Huo, Rational Construction of CuO/CdS for Highly Selective CO_2 to CO Conversion with S-Scheme Photocatalysts, Energy Technol. 2401137 (2024) 1–11. https://doi.org/10.1002/ente.202401137.

[28] A.E. Nogueira, J.A. Oliveira, G.T.S.T. da Silva, C. Ribeiro, Insights into the role of CuO_2 in the CO_2 photoreduction process, Sci. Rep. 9 (2019) 1–11. https://doi.org/10.1038/s41598-018-36683-8.

[29] W. Septina, R.R. Prabhakar, R. Wick, T. Moehl, S.D. Tilley, Stabilized Solar Hydrogen Production with CuO/CdS Heterojunction Thin Film Photocathodes, Chem. Mater. 29 (2017) 1735–1743. https://doi.org/10.1021/acs.chemmater.6b05248.

[30] D. Jiang, J. Xue, L. Wu, W. Zhou, Y. Zhang, X. Li, Photocatalytic performance enhancement of CuO/Cu_2O heterostructures for photodegradation of organic dyes: Effects of CuO morphology, Appl. Catal. B Environ. 211 (2017) 199–204. https://doi.org/10.1016/j.apcatb.2017.04.034.

[31] S.S. Hossain, M. Tarek, T.D. Munusamy, K.M. Rezaul Karim, S.M. Roopan, S.M. Sarkar, C.K. Cheng, M.M. Rahman Khan, Facile synthesis of CuO/CdS heterostructure photocatalyst for the effective degradation of dye under visible light, Environ. Res. 188 (2020) 109803. https://doi.org/10.1016/j.envres.2020.109803.

[32] R. Ravi, A.K. Golder, A tuneable bioinspired process of Pt-doping in TiO_2 for improved photoelectrochemical and photocatalytic functionalities, Colloids Surfaces A Physicochem. Eng. Asp. 663 (2023) 131034. https://doi.org/10.1016/j.colsurfa.2023.131034.

[33] C. Bhan, A. Kumar Golder, Bio-based hierarchical vertically aligned 2D ZnO nanostructures for ultra selective electrochemical sensing of p-Chloroaniline, Chem. Eng. J. 475 (2023) 146122. https://doi.org/10.1016/j.cej.2023.146122.

[34] P.M. Gawal, A.K. Golder, Vegetal route for synthesis of CQDs/CdS nanocomposites for photocatalytic reduction of CO_2 to methanol under visible light, Colloids Surfaces A Physicochem. Eng. Asp. 683 (2024) 133068. https://doi.org/10.1016/j.colsurfa.2023.133068.

[35] A. Chowdhury, N.R. Peela, A.K. Golder, Synthesis of Cu_2O NPs using bioanalytes present in Sechium edule: Mechanistic insights and application in electrocatalytic CO_2 reduction to formate, J. CO2 Util. 51 (2021) 2–13.

https://doi.org/10.1016/j.jcou.2021.101622.

[36] S.M. Chaudhari, P.M. Gawal, P.K. Sane, S.M. Sontakke, P.R. Nemade, Solar light-assisted photocatalytic degradation of methylene blue with Mo/TiO_2: a comparison with Cr- and Ni-doped TiO_2, Res. Chem. Intermed. 44 (2018) 3115–3134. https://doi.org/10.1007/s11164-018-3296-1.

[37] M. Vaseem, A.R. Hong, R.T. Kim, Y.B. Hahn, Copper oxide quantum dot ink for inkjet-driven digitally controlled high mobility field effect transistors, J. Mater. Chem. C. 1 (2013) 2112–2120. https://doi.org/10.1039/c3tc00869j.

[38] M. Arvand, S. Sayyar, S. Hemmati, Visible-light-driven polydopamine/CdS QDs hybrid materials with synergistic photocatalytic activity, J. Electroanal. Chem. 848 (2019) 113288. https://doi.org/10.1016/j.jelechem.2019.113288.

[39] A. Paruthi, J.M. Brown, E. Panda, A.R.S. Gautam, S. Singh, S.K. Misra, Transformation in band energetics of CuO nanoparticles as a function of solubility and its impact on cellular response, NanoImpact. 22 (2021) 100324. https://doi.org/10.1016/j.impact.2021.100324.

[40] Y. Zhang, Y. Wu, L. Wan, H. Ding, H. Li, X. Wang, W. Zhang, Hollow core–shell Co_9S_8@$ZnIn_2S_4$/CdS nanoreactor for efficient photothermal effect and CO2 photoreduction, Appl. Catal. B Environ. 311 (2022) 121255. https://doi.org/10.1016/j.apcatb.2022.121255.

[41] K. Shivaji, S. Mani, P. Ponmurugan, C.S. De Castro, M. Lloyd Davies, M.G. Balasubramanian, S. Pitchaimuthu, Green-Synthesis-Derived CdS Quantum Dots Using Tea Leaf Extract: Antimicrobial, Bioimaging, and Therapeutic Applications in Lung Cancer Cells, ACS Appl. Nano Mater. 1 (2018) 1683–1693. https://doi.org/10.1021/acsanm.8b00147.

[42] B. Su, L. Huang, Z. Xiong, Y. Yang, Y. Hou, Z. Ding, S. Wang, Branch-like ZnS-DETA/CdS hierarchical heterostructures as an efficient photocatalyst for visible light CO_2 reduction, J. Mater. Chem. A. 7 (2019) 26877–26883. https://doi.org/10.1039/c9ta10470d.

[43] B. Pan, J. Qin, X. Wang, W. Su, Efficient self-assembly synthesis of $LaPO_4$/CdS hierarchical heterostructure with enhanced visible-light photocatalytic CO_2 reduction, Appl. Surf. Sci. 504 (2020) 144379. https://doi.org/10.1016/j.apsusc.2019.144379.

[44] D. Gogoi, R. Koyani, A.K. Golder, N.R. Peela, Enhanced photocatalytic hydrogen evolution using green carbon quantum dots modified 1-D CdS nanowires under visible light irradiation, Sol. Energy. 208 (2020) 966–977.

https://doi.org/10.1016/j.solener.2020.08.061.

[45] M. Shaji, K.K. Markose, K.J. Saji, M.K. Jayaraj, Investigation on the improved electrical and optical properties of trivalent boron-doped Cu_2O thin film and fabrication of Cu_2O:B/c-Si heterojunction diode, J. Mater. Sci. Mater. Electron. 31 (2020) 10724–10730. https://doi.org/10.1007/s10854-020-03622-1.

[46] R. Ravi, A.K. Golder, Bio-based Au Doping with Dominant Oxygen Vacancies and Ti^{3+} Defects on Photocatalytic Functionalities of TiO_2, Ind. Eng. Chem. Res. 62 (2023) 20702–20715. https://doi.org/10.1021/acs.iecr.3c02850.

[47] C. Bhan, A.K. Golder, ZnO Nanorods Aligned in a Vertical Configuration for Targeted Electrochemical Detection of Aniline, ACS Appl. Bio Mater. 7 (2024) 7413–7428. https://doi.org/10.1021/acsabm.4c01050.

[48] L. Li, C. Guo, J. Ning, Y. Zhong, D. Chen, Y. Hu, Oxygen-vacancy-assisted construction of FeOOH/CdS heterostructure as an efficient bifunctional photocatalyst for CO_2 conversion and water oxidation, Appl. Catal. B Environ. 293 (2021) 120203. https://doi.org/10.1016/j.apcatb.2021.120203.

[49] K. Ghosh, P.K. Giri, Experimental and theoretical study on the role of 2D Ti_3C_2Tx MXenes on superior charge transport and ultra-broadband photodetection in MXene/Bi_2S_3 nanorod composite through local Schottky junctions, Carbon N. Y. 216 (2024) 118515. https://doi.org/10.1016/j.carbon.2023.118515.

[50] M. Cheng, S. Yang, R. Chen, X. Zhu, Q. Liao, Y. Huang, Visible light responsive CdS sensitized TiO_2 nanorod array films for efficient photocatalytic reduction of gas phase CO_2, Mol. Catal. 448 (2018) 185–194. https://doi.org/10.1016/j.mcat.2018.01.005.

[51] M.M. Kandy, V.G. Gaikar, Enhanced photocatalytic reduction of CO_2 using CdS/Mn_2O_3 nanocomposite photocatalysts on porous anodic alumina support with solar concentrators, Renew. Energy. 139 (2019) 915–923. https://doi.org/10.1016/j.renene.2019.03.002.

[52] S. Li, Q. Wang, X. Yan, H.Q. Zhuang, C. Yuan, J. Feng, M. Wang, R. Li, W. Li, Y.X. Pan, Al_2O_3 support triggering highly efficient photoreduction of CO_2 with H_2 on noble-metal-free CdS/Ni_9S_8/Al_2O_3, Appl. Catal. B Environ. 240 (2019) 174–181. https://doi.org/10.1016/j.apcatb.2018.08.060.

[53] T. Tian, X. Jin, N. Guo, H. Li, Y. Han, Y. Yuan, CdS/ethylenediamine nanowires 3D photocatalyst with rich sulfur vacancies for efficient syngas production from CO_2 photoreduction, Appl. Catal. B Environ. 308 (2022) 121227. https://doi.org/10.1016/j.apcatb.2022.121227.

[54] P. Li, C. Hou, X. Zhang, Y. Chen, T. He, Ethylenediamine-functionalized CdS/tetra(4-carboxyphenyl)porphyrin iron(III) chloride hybrid system for enhanced CO_2 photoreduction, Appl. Surf. Sci. 459 (2018) 292–299. https://doi.org/10.1016/j.apsusc.2018.08.002.

[55] H. Zhao, X. Yang, R. Xu, J. Li, S. Gao, R. Cao, CdS/NH_2 -UiO-66 hybrid membrane reactors for the efficient photocatalytic conversion of CO_2, J. Mater. Chem. A. 6 (2018) 20152–20160. https://doi.org/10.1039/C8TA05970E.

[56] X. Pan, Y.-J. Xu, Graphene-Templated Bottom-up Fabrication of Ultralarge Binary CdS–TiO_2 Nanosheets for Photocatalytic Selective Reduction, J. Phys. Chem. C. 119 (2015) 7184–7194. https://doi.org/10.1021/jp512797t.

[57] Y.Y. Li, Z.H. Wei, J. Bin Fan, Z.J. Li, H.C. Yao, Photocatalytic CO_2 reduction activity of Z-scheme CdS/$CdWO_4$ catalysts constructed by surface charge directed selective deposition of CdS, Appl. Surf. Sci. 483 (2019) 442–452. https://doi.org/10.1016/j.apsusc.2019.03.333.

[58] D. Ding, Z. Jiang, J. Jin, J. Li, D. Ji, Y. Zhang, L. Zan, Impregnation of semiconductor CdS NPs in MOFs cavities via double solvent method for effective photocatalytic CO_2 conversion, J. Catal. 375 (2019) 21–31. https://doi.org/10.1016/j.jcat.2019.05.015.

[59] S. Wu, H. Pang, W. Zhou, B. Yang, X. Meng, X. Qiu, G. Chen, L. Zhang, S. Wang, X. Liu, R. Ma, J. Ye, N. Zhang, Stabilizing $CuGaS_2$ by crystalline CdS through an interfacial Z-scheme charge transfer for enhanced photocatalytic CO_2 reduction under visible light, Nanoscale. 12 (2020) 8693–8700. https://doi.org/10.1039/D0NR00483A.

[60] D. Meissner, C. Benndorf, R. Memming, Photocorrosion of cadmium sulfide: Analysis by photoelectron spectroscopy, Appl. Surf. Sci. 27 (1987) 423–436. https://doi.org/10.1016/0169-4332(87)90152-8.

[61] X. Li, T. Han, Y. Zhou, M. Wang, Z. Tian, F. Deng, Y. Luo, Y. Xie, J. Huang, L. Han, Z. Chen, Z. Feng, W. Chen, Boosting photoelectrocatalytic hydrogen evolution of Bi@OV-BiOBr/Cu_3P high-low heterojunction with dual-channel charge transfer, Appl. Catal. B Environ. 350 (2024) 123913. https://doi.org/10.1016/j.apcatb.2024.123913.

[62] X. Li, T. Han, Y. Zhou, Y. Xie, Y. Luo, J. Huang, Z. Chen, F. Deng, Photoelectrocatalytic hydrogen evolution and synchronous degradation of organic pollutants by pg-C_3N_4/β-FeOOH S-scheme heterojunction, Sci. China Technol. Sci. 67 (2024) 1238–1252. https://doi.org/10.1007/s11431-023-2604-x.

[63] S. Shen, X. Li, Y. Zhou, L. Han, Y. Xie, F. Deng, J. Huang, Z. Chen, Z. Feng, J. Xu, F. Dong, Novel BiOBr/Bi_2S_3 high-low junction prepared by molten salt method for

boosting photocatalytic degradation and H_2O_2 production, J. Mater. Sci. Technol. 155 (2023) 148–159. https://doi.org/10.1016/j.jmst.2023.03.006.

[64] J. Zhou, X. Zha, Z. Chen, K. Li, H. Sun, J. Wang, K. Lv, S. Cong, Z. Zhao, Tailoring the coordination microenvironment of single-atom W for efficient photocatalytic CO_2 reduction, Appl. Catal. B Environ. 350 (2024) 123911. https://doi.org/10.1016/j.apcatb.2024.123911.

[65] J. Dong, J. Zhao, X. Yan, L. Li, G. Liu, M. Ji, B. Wang, Y. She, H. Li, J. Xia, Construction of carbonized polymer dots/potassium doped carbon nitride nanosheets Van der Waals heterojunction by ball milling method for facilitating photocatalytic CO_2 reduction performance in pure water, Appl. Catal. B Environ. 351 (2024) 123993. https://doi.org/10.1016/j.apcatb.2024.123993.

[66] A. Mandal, K. Kargupta, Cu-Doped 2D-Bi_2MoO_6 Nanoribbon/rGO Photocatalysts for Selective Ethanol Production by Photocatalytic CO_2 Reduction, ACS Appl. Nano Mater. 8 (2025) 3471–3486. https://doi.org/10.1021/acsanm.4c06608.

[67] G. Wang, H. Su, S. Chen, Y. Wang, Z. Chen, F. Chen, H. Yin, J. Li, Protective structure coupled dual electron transfer channels for enhancing the activity and stability of photocatalytic CO_2 reduction to C_2 liquid products, Appl. Catal. B Environ. 366 (2025) 124997. https://doi.org/10.1016/j.apcatb.2024.124997.

CHAPTER 8

Conclusions and Scopes for Future Studies

This chapter outlines the key findings of the overall work. It also presents suggestions and recommendations for future research based on the outcomes and shortcomings in the present study.

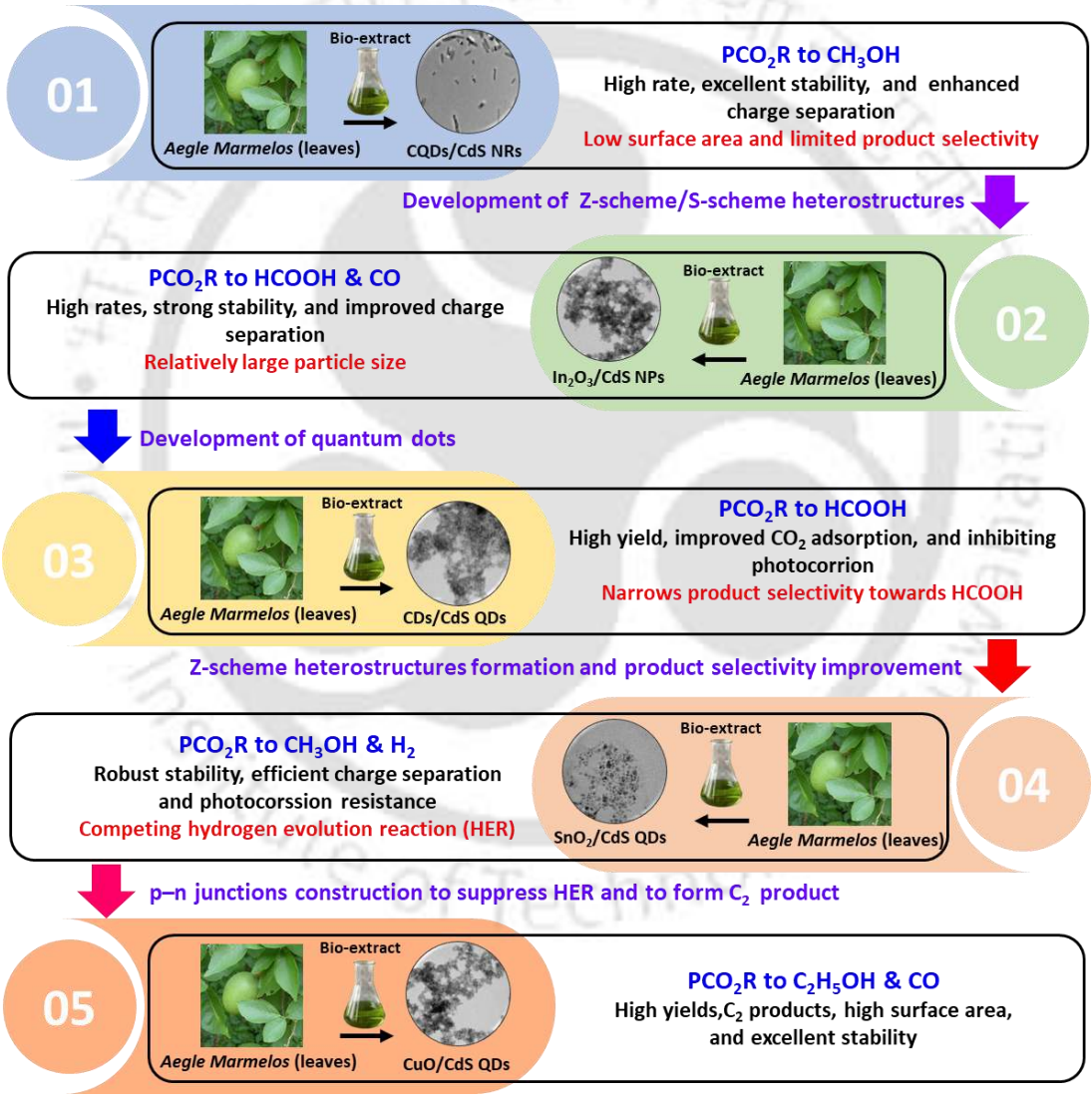

8.1 Overall Conclusions

This doctoral work investigates on bioinspired synthesis of tailor-made metal sulfide and metal oxide nanomaterials using reducing and capping agents present in the vegetal extract of *Aegle Marmelos* (bael). Catalyst modification, including nanocomposites and heterostructures formation, was successfully carried out through a bioinspired route. The resulting catalysts were effectively evaluated for photocatalytic CO_2 reduction (PCO_2R) to value-added chemicals under visible light irradiation.

The phytochemicals present in *Aegle Marmelos,* including flavonoids, alkaloids, tannins, phenols, and saponins, served as effective reducing and capping agents. A mass spectrum confirmed that the flavonoid fraction of 3,5-dihydroxy-6-methyl-2H-pyran-4(3H)-one was abundant in the bio-extract and could serve as a reducing and capping agent for synthesizing metal sulfide and metal oxide nanoparticle/quantum dots.

1. Bioinspired synthesis of CQDs/CdS nanocomposite for PCO_2R to methanol (Chapter 3):

This study demonstrates a sustainable and efficient approach for photocatalytic CO_2 reduction to methanol using bio-based CQDs/CdS nanocomposites. CdS nanorods were synthesized using *Aegle marmelos* phytochemicals and modified with carbon quantum dots derived from *orange peels*. The resulting CQDs/CdS(bio) composites exhibited enhanced charge separation, CO_2 adsorption, and visible-light-driven photocatalytic activity, achieving a high methanol yield of 1060.52 μmol/g·h with an apparent quantum yield (AQY) of 7% at optimal CQD loading (0.50% w/w), without sacrificial agents. The composites also showed excellent structural stability over multiple cycles. This work highlights a promising green route for developing bio-derived photocatalysts for CO_2 conversion into value-added fuels.

2. Z-scheme In_2O_3/CdS heterostructure for PCO_2R to HCOOH and CO (Chapter 4):

This study presents a green synthesis route for bio-based In_2O_3/CdS(bio) Z-scheme heterostructures using *Aegle marmelos* phytochemicals along with a short microwave irradiation. The incorporation of In_2O_3 enhanced charge separation, suppressed photocorrosion, and significantly improved CO_2 adsorption and photocurrent density. Density functional theory (DFT) analysis confirmed bandgap narrowing and favorable electronic interactions. The optimized $0.4In_2O_3$/CdS(bio) catalyst achieved outstanding PCO_2R to HCOOH and CO with yields of 514.4 and 162 μmol/g·h (AQY 4.44 and 2.45%), respectively, and demonstrated excellent stability. These findings highlight the potential of bio-derived heterostructures for efficient and sustainable CO_2 conversion.

3. Carbon dots embedded phytochemical-based CdS quantum dots for PCO_2R to HCOOH (Chapter 5):

This study demonstrates a sustainable strategy for PCO_2R to formic acid using bio-derived CDs/CdS QDs composites synthesized using carbon-rich *orange peels* and phytochemicals found in *Aegle marmelos*. The optimized 0.4% CDs/CdS QDs(bio) composite exhibited excellent photocatalytic activity, achieving a high HCOOH yield of 439.51 μmol/g·h (AQY 3.81%) under visible light without sacrificial agents. Structural stability, enhanced CO_2 adsorption, improved charge separation, and rich sulphur vacancies contributed to superior performance. DFT analysis confirmed the thermodynamic favourability of HCOOH formation via HCOO* intermediate. This work provides valuable mechanistic and practical insights into bio-based catalysts for efficient CO_2 conversion.

4. Z-scheme SnO_2/CdS heterostructure for PCO_2R to methanol and H_2 (Chapter 6):

This study demonstrates successful synthesis of bio-based Z-scheme SnO_2/CdS QDs heterostructure using *Aegle marmelos* phytochemicals and microwave irradiation. The optimized 0.50SnO_2/CdS QDs(bio) composite exhibited enhanced CO_2 adsorption, improved charge separation, and suppressed recombination, leading to exceptional photocatalytic activity for CO_2 reduction. It achieved methanol and hydrogen production rates of 675.9 and 139.5 μmol/g·h (AQY 3.51 and 0.24%) under visible light without a sacrificial agent. DFT analysis confirmed the role of SnO_2 in modifying the electronic structure of CdS, promoting efficient charge transport. This work reports a sustainable strategy for developing stable, efficient, and eco-friendly photocatalysts for CO_2-to-fuel conversion.

5. p-n junction CuO/CdS heterostructures for PCO_2R to ethanol and CO (Chapter 7):

This study presents a sustainable approach for PCO_2R using a bio-based 0D/0D p–n CuO/CdS QDs heterostructure synthesized from *Aegle marmelos* phytochemicals. The optimized 0.50CuO/CdS QDs(bio) composite exhibited enhanced CO_2 adsorption (0.643 mmol/g), improved charge separation, and excellent photocatalytic performance, achieving ethanol and CO yields of 158.48 and 182.68 μmol/g·h (AQY 8.24% and 1.58%) under visible light without sacrificial agents. DFT analysis confirmed the role of CuO in modifying the electronic structure and promoting charge transport. This work explores the potential of bio-derived p-n junctions for efficient and stable CO_2-to-fuel conversion.

8.2 Scopes for Future Studies

- In this study, PCO_2Rs were performed in a semi-batch reactor. The studies in a continuous reactor may be considered in the future.
- Integrating bioinspired photocatalysts into CCU systems for continuous CO_2 capture and conversion can be explored, particularly with simulated or real flue gases and industrial CO_2 sources.
- Developing scalable and cost-effective photocatalytic reactors that utilize solar irradiation is essential to bridge the gap between lab-scale CO_2 photoreduction and pilot-scale applications.
- Integration of in-situ/operando spectroscopy (e.g., FTIR, XPS, or XAS) during PCO_2R could offer deeper mechanistic insights into the reaction intermediates, surface chemistry, and degradation pathways.
- Separation of the liquid product from the reaction mixture was not within the scope of this study. Product separation would be an imperative objective of future investigations.
- The kinetics of PCO_2R using Langmuir–Hinshelwood–type rate expressions can be further investigated.
- Catalyst modifications for CdS-based PCO_2R, including oxide-derived Cu/Cu–CdS hybrid surfaces, facet/strain engineering, defect/vacancy tuning, alloying (e.g., Cu–Ag, Cu–Zn, Cu–Au), tandem architectures, surface functionalization, confinement effects, hydrophobic interfaces, operando reconstruction, and electrolyte/cation tuning, collectively stabilize key intermediates (CO, OCCO), promote C-C coupling, and enhance selectivity toward C_2/C_3 products, providing direction for further research.
- Comprehensive techno-economic analysis (TEA) and life cycle assessment (LCA) to quantitatively evaluate the economic feasibility, energy demand, environmental impact, and scalability of the developed bioinspired photocatalytic system are prudent research topics.
- Formation of a selective product through multiple CdS-based architectures to systematically compare structure-property-performance relationships and identify the most efficient design strategy should be given due consideration in future studies.
- Future studies should focus on improving long-term catalyst stability, preventing photocorrosion, optimizing catalyst immobilization and recovery, enhancing reactor design for light penetration, overcoming mass transfer limitations of CO_2 and products, and maintaining product selectivity in continuous operation.

Appendix

Table A1: Calculation of apparent quantum yield (AQY) for methanol (Chapter 3).

The energy of a photon with a wavelength of λ (nm) is expressed as:

$$E_{photon} = \frac{hc}{\lambda}$$

Planck's constant, h = 6.626 ×10^{-34} J·s

The speed of light, c = 3×10^{8} m·s^{-1}

The wavelength of the incident monochromatic light, λ= 420 nm

The total energy of the incident monochromatic light (E_{total}) is

$$E_{total} = PAt$$

The power intensity of the incident monochromatic light is given by, P= 2.02 W/m^2

The irradiation area, A= 0.0356 m^2

Photon Flux $= \frac{I \times \lambda}{h \times c}$= 4.2719×$10^{18}$ photons/m^2.s

Number of incident photons, $\frac{E_{total}}{E_{photon}} = \frac{PAt\lambda}{hc}$

The apparent quantum yield (AQY) was determined using the following equation.

$$AQY(\%) = \frac{6 \times \text{moles of methanol yield}}{\text{Number of incident photons}} \times 100$$

$$AQY\ (\%) = \frac{6 \times n_{methanol} \times N_A \times hc}{PAt\lambda} \times 100$$

Where n methanol is the mole of methanol (=10.60 μmol)

Avogadro's constant, Na= 6.022×10^{23} mol^{-1} ; t =3600 s

AQY (%) =7 %

Table A2: Calculation of AQY for formic acid and carbon monoxide (Chapter 4).

The energy of a photon with a wavelength of λ (nm) is expressed as:

$$E_{photon} = \frac{hc}{\lambda}$$

Planck's constant, h = 6.626 ×10^{-34} J·s

The speed of light, c = 3×10^{8} m·s^{-1}

The wavelength of the incident monochromatic light, λ= 460nm

The total energy of the incident monochromatic light (E_{total}) is

$$E_{total} = PAt$$

The power intensity of the incident monochromatic light is given by, P= 3.51 W/m^2

The irradiation area, A= 0.0356 m^2

Photon Flux $= \frac{P \times \lambda}{h \times c}$= 8.13×$10^{18}$ photons/m^2.s

Number of incident photons, $\frac{E_{total}}{E_{photon}} = \frac{PAt\lambda}{hc}$

The apparent quantum yield (AQY) was determined using the following equation.

$$AQY(\%) = \frac{2 \times \text{moles of HCOOH or CO yield}}{\text{Number of incident photons}} \times 100$$

$$AQY\ (\%) = \frac{2 \times n_{HCOOH/CO} \times N_A \times hc}{PAt\lambda} \times 100$$

Where n is the mole of formic acid or carbon monoxide (=38.49 &12.21 μmol)

Avogadro's constant, Na= 6.022×10^{23} mol^{-1} ; t =3600 s

AQY_{HCOOH} (%) =4.44 %

AQY_{CO} (%) =2.45%

Table A3: Calculation of AQY for formic acid (Chapter 5).

The energy of a photon with a wavelength of λ (nm) is expressed as:

$$E_{photon} = \frac{hc}{\lambda}$$

Planck's constant, h = 6.626 ×10^{-34} J·s

The speed of light, c = 3×10^8 m·s^{-1}

The wavelength of the incident monochromatic light, λ= 460 nm

The total energy of the incident monochromatic light (E_{total}) is

$$E_{total} = PAt$$

The irradiation area, A= 0.0356 m^2

The power intensity of the incident monochromatic light is given by P= 3.51 W/m^2

Photon Flux $= \frac{P \times \lambda}{h \times c}$= 8.12×$10^{18}$ photons/m^2.s

Number of incident photons, $\frac{E_{total}}{E_{photon}} = \frac{PAt\lambda}{hc}$

The apparent quantum yield (AQY) was determined using the following equation.

$$AQY(\%) = \frac{2 \times \text{moles of HCOOH yield}}{\text{Number of incident photons}} \times 100$$

$$AQY\ (\%) = \frac{2 \times n_{HCOOH} \times N_A \times hc}{PAt\lambda} \times 100$$

Where n is the mole of formic acid (=33.01μmol)

Avogadro's constant, Na= 6.022×10^{23} mol^{-1} ; t =3600 s

AQY_{HCOOH} (%) =3.81 %

Table A4: Calculation of AQY for methanol and hydrogen (Chapter 6).

The energy of a photon with a wavelength of λ (nm) is expressed as:

$$E_{photon} = \frac{hc}{\lambda}$$

Planck's constant, h = 6.626×10^{-34} J·s

The speed of light, c = 3×10^{8} $m\cdot s^{-1}$

The wavelength of the incident monochromatic light, λ= 460nm

The total energy of the incident monochromatic light (E_{total}) is

$$E_{total} = PAt$$

The power intensity of the incident monochromatic light is given by, P= 3.51 W/m^2

The irradiation area, A= 0.0356 m^2

Photon Flux $= \frac{P\times\lambda}{h\times c}$= 8.13×10^{18} photons/m^2.s

Number of incident photons, $\frac{E_{total}}{E_{photon}} = \frac{PAt\lambda}{hc}$

The apparent quantum yield (AQY) was determined using the following equation.

$$AQY(\%) = \frac{6\times\text{moles of MeOH yield}}{\text{Number of incident photons}}\times100$$

$$AQY(\%) = \frac{2\times\text{moles of H2 yield}}{\text{Number of incident photons}}\times100$$

$$AQY\ (\%) = \frac{6 \times n_{MeOH} \times N_A \times hc}{PAt\lambda} \times 100$$

$$AQY\ (\%) = \frac{2 \times n_{H_2} \times N_A \times hc}{PAt\lambda} \times 100$$

Where n is the mole of MeOH or H_2 (=11.88 & 13.7 μmol) in 5 hr

Avogadro's constant, Na= 6.022×10^{23} mol^{-1} ; t =18000 s

AQY_{MeOH} (%) =3.51 %

$$AQY_{H2}\ (\%) = 0.24\%$$

$$\text{Selectivity}(\%) = \frac{Number\ of\ mole\ of\ MeOH or\ H_2}{Total\ Mole\ of\ MeOH\ and\ H_2} \times 100$$

$$\text{Selectivity}_{MeOH}\ (\%) = 46.44\%$$

$$\text{Selectivity}_{H2}\ (\%) = 53.55\%$$

Table A5: Calculation of AQY for ethanol and carbon monoxide (Chapter 7).

The energy of a photon with a wavelength of λ (nm) is expressed as:

$$E_{photon} = \frac{hc}{\lambda}$$

Planck's constant, $h = 6.626 \times 10^{-34}$ J·s

Speed of light, $c = 3 \times 10^{8}$ m·s^{-1}

Wavelength of the incident monochromatic light, λ= 460nm

Total energy of the incident monochromatic light (E_{total}), E_{total} =PAt

Power intensity of the incident monochromatic light is given by, P= 3.51 W/m^2

Irradiation area, A= 0.0356 m^2

Photon Flux $= \frac{P \times \lambda}{h \times c} = 8.13 \times 10^{18}$ photons/m^2.s

Number of incident photons, $\frac{E_{total}}{E_{photon}} = \frac{PAt\lambda}{hc}$

Apparent quantum yield (AQY) was determined using the following equations.

$$AQY(\%) = \frac{12 \times \text{moles of EtOH yield}}{\text{Number of incident photons}} \times 100$$

$$AQY(\%) = \frac{2 \times \text{moles of CO yield}}{\text{Number of incident photons}} \times 100$$

$$AQY\ (\%) = \frac{12 \times n_{EtOH} \times N_A \times hc}{PAt\lambda} \times 100$$

$$AQY\ (\%) = \frac{2 \times n_{CO} \times N_A \times hc}{PAt\lambda} \times 100$$

Where, n is the mole of ethanol or carbon monoxide (=11.88 & 13.7 μmol)

Avogadro's constant, Na= 6.022×10^{23} mol^{-1} ; t =3600 s

$$AQY_{EtOH}\ (\%) = 8.24\ \%$$

$$AQY_{CO}\ (\%) = 1.58\%$$

RESEARCH OUTCOMES

Journal Publication (Thesis Work)

1. **P.M. Gawal**, A.K. Golder, Green Synthesis of Z-Scheme SnO_2/CdS Heterostructures: Density Functional Theory Calculation and Photocatalytic CO_2 Reduction to Methanol and Hydrogen, ***Langmuir***. 42 (2026) 3490–3502. https://doi.org/10.1021/acs.langmuir.5c05827.
2. **P.M. Gawal**, J. Ishrat, K. Bhattacharyya, A.K. Golder, Experimental and Theoretical Studies on Photocatalytic CO_2 Reduction to HCOOH by Biomass-Derived Carbon Dots Embedded Phytochemical-Based CdS Quantum Dots, ***Langmuir*** 41 (2025) 11161–11172. https://doi.org/10.1021/acs.langmuir.5c01002.
3. **P.M. Gawal**, A.K. Golder, Plant-Derived Phytochemicals for the Synthesis of p–n Junction CuO/CdS Heterostructures for Photocatalytic Carbon Dioxide Reduction to Ethanol and Carbon Monoxide, ***ACS Appl. Energy Mater***. 8 (2025) 6087–6099. https://doi.org/10.1021/acsaem.5c00497.
4. **P.M. Gawal**, A.K. Golder, Plant-Based Phytochemicals for Synthesis of Z-Scheme In_2O_3/CdS Heterostructures: DFT Analysis and Photocatalytic CO_2 Reduction to HCOOH and CO, ***Langmuir*** 40 (2024) 13538–13549. https://doi.org/10.1021/acs.langmuir.4c01015.
5. **P.M. Gawal**, A.K. Golder, Vegetal route for synthesis of CQDs/CdS nanocomposites for photocatalytic reduction of CO_2 to methanol under visible light, ***Colloids Surfaces A Physicochem. Eng. Asp.*** 683 (2024) 133068. https://doi.org/10.1016/j.colsurfa.2023.133068.
6. **P.M. Gawal**, A.K. Golder, CdS-based Catalysts for Photocatalytic Reduction of CO_2 to Value-added Chemicals: A Comprehensive Review of Recent Progress and Future Prospects (**Manuscript under preparation**)

Book Chapter

1. **P.M. Gawal**, A.K. Golder, Carbon Quantum Dots for Photocatalytic Application: A Mini Review, in: ***Curr. Prog. Eng. Sci.***, Springer Nature Singapore, Singapore, 2025: pp. 595–610. https://doi.org/10.1007/978-981-96-8753-4_39
2. **P.M. Gawal**, A.K. Golder, Nature-Based Synthesis and Characterization of CdS from *Aegle Marmelos* Leave Extract for Efficient Visible-Light-Driven Methylene Blue Degradation, in: ***Curr. Prog. Eng. Sci.***, Springer Nature Singapore, Singapore, 2025: pp.

611–618. https://doi.org/10.1007/978-981-96-8753-4_40

3. **P.M. Gawal**, A.K. Golder, Bioinspired synthesis and characterization of SnO_2 from *Aegle marmelos* leave extract for photocatalytic degradation of methylene blue. ***Research Industrial Conclave*** (2025) (**Under review**)
4. **P.M. Gawal**, A.K. Golder, Carbon Dioxide Conversion Processes for Value-added Chemicals, ***Research Industrial Conclave*** (2025) (**Under review**)

Journal Publication (Non-Thesis Work)

1. **P.M. Gawal**, A.K. Golder, Novel ternary Z-scheme nanocomposite: Biomass-derived carbon dots decorated on g-C_3N_4(T) -g-C_3N_4(U) heterostructures for the photocatalytic CO_2 reduction to CO and H_2, ***Int. J. Hydrogen Energy***. 199 (2026) 152856. https://doi.org/10.1016/j.ijhydene.2025.152856
2. **P.M. Gawal**, A.K. Golder, Recent Progress in Carbon Quantum Dots-Based Composite Photocatalysts for CO_2 Reduction to Solar Fuels: A Review (Manuscript under preparation)
3. **P.M. Gawal**, P. Bania, B.Mandal, A.K. Golder, Facile Synthesis of TiO_2/UiO-66/GO Ternary Composites for Visible-Light-Driven Water Splitting (Manuscript under preparation)

International Conference and Workshop

1. **P.M. Gawal**, A.K. Golder "Green Synthesis of Z-scheme SnO_2/CdS Heterostructure for Photocatalytic CO_2 Reduction to Methanol and Hydrogen" 8th International Conferences On CSR & Sustainable Development, Ho Chi Minh City, Vietnam, June 16-17,2025 (**Oral presentation**)
2. **P.M. Gawal**, A.K. Golder "Plant-based Phytochemicals for the Synthesis of p-n Junction CuO/CdS Heterostructures for Photocatalytic CO_2 Reduction to Ethanol and Carbon Monoxide" International Conference on Environmental Challenges, Opportunities, and Sustainable Solution, IIT Guwahati, Dec 9-11,2024 (**Oral presentation**)
3. **P.M. Gawal**, A.K. Golder "Phytochemicals-based Synthesis of Z-scheme In_2O_3/CdS Heterostructure: DFT Calculations and Photocatalytic CO_2 Reduction to Fuels" 8th Green and Sustainable Chemistry Conference (Green Chem 2024), Elsevier and Leuphana University of Lüneburg, Dresden, Germany, May 13-15, 2024 (**Poster presentation**)
4. **P.M. Gawal**, A.K. Golder "Bioinspired Synthesis of In_2O_3/CdS Z-Scheme Heterostructures for Solar-Driven CO_2 Reduction to Fuels" International Conference on Recent Advanced in Waste Minimization & Utilization (RAWMU), Lovely Professional

University, Punjab, April 23-24, 2024 (**Oral presentation**)

5. **P.M. Gawal**, A.K. Golder "Plant-based Phytochemicals for Synthesis of Z-scheme In_2O_3/CdS Heterostructure for Photocatalytic CO_2 Reduction to Fuels" International Conference on Advanced Nanomaterials & Nanotechnology (ICANN), IIT Guwahati, Nov 29- Dec 1, 2023 (**Oral presentation**)
6. **P.M. Gawal**, A.K. Golder "Plant-based Phytochemicals for Synthesis of Z-scheme In_2O_3/CdS Heterostructure for Photocatalytic CO_2 Reduction to Fuels" International Conference on Petroleum, Hydrogen, & Decarbonization (ICPHD), IIT Guwahati, Nov 3-5.,2023 (**Oral presentation**)
7. **P.M. Gawal**, A.K. Golder "Bioinspired Synthesis of CQDs/CdS Nanocomposites for Photocatalytic CO_2 Reduction to Value-added Chemicals" International Conference on Academic & Industrial Innovations in Engineering (ICAIIE), PP Savani University Surat, August 12-13,2023 (**Oral presentation**)
8. **P.M. Gawal**, A.K. Golder "Tuneable Bioinspired CdS/CQDs Nanocomposites for Photocatalytic Reduction of CO_2 to Value-added Chemical" International Chemical Engineering Conference(IChEC), IIT Patna, November 12-13, 2022 (**Oral presentation**)

National Conference and Workshop

1. **P.M. Gawal**, A.K. Golder "Green Synthesis of Z-scheme SnO_2/CdS Heterostructure for Photocatalytic CO_2 Reduction to Methanol and Hydrogen" Research and Industrial Conclave (RIC-2025), IIT Guwahati, October 10-12, 2025 (**Oral presentation**)
2. **P.M. Gawal**, A.K. Golder "Development of Bioinspired Nanostructured Materials for Photocatalytic CO_2 Reduction to Value-added Chemicals" Research and Industrial Conclave (RIC-2025), IIT Guwahati, October 10-12, 2025 (**Oral presentation**)
3. **P.M. Gawal**, A.K. Golder "Carbon Dioxide Conversion Processes for Value-added Chemicals" Research and Industrial Conclave (RIC-2025), IIT Guwahati, October 10-12, 2025 (**Poster presentation**)
4. **P.M. Gawal**, A.K. Golder "Green Synthesis of Z-scheme SnO_2/CdS Heterostructure for Photocatalytic CO_2 Reduction to Methanol and Hydrogen" Symposium on Ending Plastic Pollution, Center for the Environment, IIT Guwahati, June 5, 2025 (**Poster presentation**)
5. **P.M. Gawal**, A.K. Golder "Synthesis of Sulfur-vacancy-rich Carbon Dots/CdS Quantum Dots Composites for Enhanced Photocatalytic CO_2 Reduction to Formic Acid" Research and Industrial Conclave (RIC-2024), IIT Guwahati, August 9-11,2024 (**Oral presentation**)
6. **P.M. Gawal**, A.K. Golder "Carbon Quantum Dots-based Composites for Photocatalytic

CO_2 Reduction: A Comprehensive Review of Recent Progress and Future Prospects" Research and Industrial Conclave (RIC-2024), IIT Guwahati, August 9-11,2024 (**Oral presentation**)

7. **P.M. Gawal**, A.K. Golder "Green Synthesis of CDs Decorated CdS QDs with Rich Sulfur Vacancies for Photocatalytic CO_2 Reduction to HCOOH" Symposium on Environmental Challenges, Opportunities, and Sustainable Solution, Center for the Environment, IIT Guwahati, June 5, 2024 (**Poster presentation**)
8. **P.M. Gawal**, A.K. Golder "Photocatalytic Reduction of CO_2 to Value-added Chemicals Catalyzed by CdS/CQDs Nanocomposites." North-East Research Conclave(NERC), IIT Guwahati, INDIA, May 20-22,2022.
9. Participate in the DST-SERB-sponsored One-day workshop titled "Fuel Cell Technology: Advancement & Applications" organized by the Department of Chemical Engineering, IIT Guwahati on 17 March 2025
10. Participate in the 1st Hands-On-Training on Density Functional Theory Modelling of Advanced Materials (DFT-Advanced), organized by the Centre for Advanced Computational Research, Delhi from 10th June – 19th June 2024
11. Participate in the Next-Generation Atomistic Modelling and Simulation with AMS Software workshop organized by Nyro Research India Pvt Ltd, Sep 25–Oct 4, 2023.
12. Participate in the 1st workshop on Density Functional Theory Modeling of Materials (DFT-M) organized by the Center for Advanced Computational Studies, Delhi, Sep 7-13, 2023.
13. Participate in the workshop on Scientific Writing using LaTeX organized by the Student Academic Board, IIT Guwahati, Sept 9-10, 2023.

Awards

1. Best Poster Presentation Award at 8th Green and Sustainable Chemistry Conference (Green Chem 2024), Elsevier and Leuphana University of Lüneburg, Dresden, Germany, May 13-15, 2024.
2. Best Oral Presentation Awards at International Conference on Advanced Nanomaterials & Nanotechnology (ICANN), IIT Guwahati, Nov 29- Dec 1, 2023
3. Best Oral Presentation Awards at International Conference on Recent Advanced in Waste Minimization &Utilization (RAWMU), Lovely Professional University, Punjab, April 23-24, 2024
4. Best Oral Presentation Awards at International Conference on Academic & Industrial Innovations in Engineering (ICAIIE), PP Savani University Surat, August 12-13,2023